REPORT DOCUMENTATION PAGE

Form Approved OMB No. 0704-0188

Public reporting burden for this collection of information is estimated to average 1 hour per response, including the time for reviewing instructions, searching existing data sources, gathering and maintaining the data needed, and completing and reviewing the collection of information. Send comments regarding this burden estimate or any other aspect of this collection of information, including suggestions for reducing the burden, to Department of Defense, Washington Headquarters Services, Directorate for Information Operations and Reports (0704-0188), 1215 Jefferson Davis Highway, Suite 1204, Arlington, VA 22202-4302. Respondents should be aware that notwithstanding any other provision of law, no person shall be subject to any penalty for failing to comply with a collection of information if it does not display a currently valid OMB control number. **PLEASE DO NOT RETURN YOUR FORM TO THE ABOVE ADDRESS.**

1. REPORT DATE *(DD-MM-YYYY)* 15-02-2007	2. REPORT TYPE Final Report	3. DATES COVERED *(From – To)* 01-Mar-03 - 15-Feb-07

4. TITLE AND SUBTITLE Excitation Of Nuclei And Trapping Of Atoms In Optical Fields Of High Intensity	5a. CONTRACT NUMBER ISTC Registration No: 2651
	5b. GRANT NUMBER
	5c. PROGRAM ELEMENT NUMBER
6. AUTHOR(S) Professor Anatoli Andreev	5d. PROJECT NUMBER
	5d. TASK NUMBER
	5e. WORK UNIT NUMBER

7. PERFORMING ORGANIZATION NAME(S) AND ADDRESS(ES) Moscow State University Leninskie Gory Moscow 119899 Russia	8. PERFORMING ORGANIZATION REPORT NUMBER N/A

9. SPONSORING/MONITORING AGENCY NAME(S) AND ADDRESS(ES) EOARD PSC 821 BOX 14 FPO AE 09421-0014	10. SPONSOR/MONITOR'S ACRONYM(S)
	11. SPONSOR/MONITOR'S REPORT NUMBER(S) ISTC 01-7042

12. DISTRIBUTION/AVAILABILITY STATEMENT

Approved for public release; distribution is unlimited.

13. SUPPLEMENTARY NOTES

14. ABSTRACT

This report results from a contract tasking Moscow State University as follows: Exploration of methods to control the radiative gamma-processes in nuclei is currently one of the most promising investigation directions of the modern Quantum Nucleonics - a new realm of contemporary Physics which spreads the basic conceptual ideas and methods of optical Quantum Electronics of atoms and molecules to the gamma-ray range and atomic nuclei and even anti-particles. One of the most important problems in this field is the generation of coherent gamma-radiation by a Gamma-ray Lasing (GRL) process which makes use of excited nuclei as an amplifying medium. The most likely medium for gamma-ray lasers is an ensemble of metastable nuclear isomers. Direct excitation of these isomeric states by electrons or X-ray photons will also create a deeper understanding of nuclear structure and properties.

15. SUBJECT TERMS
EOARD, Physics, Nuclear Physics and Elementary Particle Physics

16. SECURITY CLASSIFICATION OF:			17. LIMITATION OF ABSTRACT	18, NUMBER OF PAGES	19a. NAME OF RESPONSIBLE PERSON DONALD J SMITH
a. REPORT UNCLAS	b. ABSTRACT UNCLAS	c. THIS PAGE UNCLAS	UL	148	19b. TELEPHONE NUMBER *(Include area code)* +44 (0)20 7514 4953

Standard Form 298 (Rev. 8/98)
Prescribed by ANSI Std. Z39-18

ISTC 2651

Final
Project Technical Report
of ISTC 2651

Excitation of nuclei and atoms trapping in
optical fields of high intensity

(From 1 March 2003 to 31 August 2006 for 14 months)

Anatoli Vasilievich Andreev
(Project Manager)
International Laser Centre
M.V.Lomonosov Moscow State University

November 2006

CONTENTS

TASK 1. GAMMA-RAY LASER WITH HIDDEN INVERSION OF NUCLEAR STATE POPULATIONS

INTRODUCTION

Objective

The objective of this project is to develop a new approach to gamma-ray laser (GRL) based on the concept of recoil assisted lasing in an active medium of free nuclei with hidden inversion of the nuclear states populations. The use of nuclear recoil opens up, contrary to the standard scheme of optical lasers, entirely new possibilities inherent to the processes with emission of hard photons. Our task (it is referred in the Work Plan of the project as the <u>Task 1</u>) is to accomplish the detailed theoretical studies of a set of separate key sub-problems of the recoil assisted gamma-ray lasing approach.

One of the main task of the version of GRL under consideration is overcoming of pernicious influence of Doppler line-broadening. This very important task could be accomplished by the well known present-day techniques for deep cooling of atomic ensembles by the light pressure of optical lasers. Therefore, the first key sub-problem of the Project is the development of criteria for the selection procedure of the most suitable candidate nuclides, which shall take into account both nuclear and atomic properties of the candidate. Another one is the analysis of hindrances of existing methods for creating extended filament-like confined beams with relatively high concentration of deeply cooled nuclei and proposals to overcome or bypass these hindrances. Solving these key sub-problems together with detailed theoretical study of the GRL process including rigorous quantum mechanical calculations (based on the perturbation theory subjected to some generalization in order to include into consideration the effect of nuclear recoil) of the probabilities and cross-sections for multi-quantum nuclear radiative transitions and development the work formulae for estimations the main GRL output parameters could pave the way to launch the primary demonstrative GRL experiment.

GRL process would introduce into practice a new type of nuclear reaction, namely, the chain reaction of stimulated nuclear radiative transitions with release of nuclear energy in a 'clean' way, as a burst of coherent gamma radiation without the production of radioactive by-products and the environment pollution. The motivation for proposed research is not only from the view of pure science but also from the perspective of possible applications of GRL process for nuclear energy production.

This project can be treated as the first stage at gathering together wide consortium of scientists from Russia, US and other countries to make collective efforts toward gamma lasing. It implies effective collaboration with AFOSR, YSU, joint experiments, workshops, etc.

It is worth noting, that dealing with nuclear excitation we are choosing methods and designs providing effective environmental protection and nuclear safety. Our methods do not lead to any hazardous pollution, or other undesired consequences. Furthermore successive resolution of the project tasks might allow further progress in novel and peaceful technologies.

Expected results

The expected results as described in the Work Plan include:

1. Development of criteria for the selection procedure of first suitable candidate nuclides for the GRL experiment, which shall take into account both nuclear and atomic candidate properties, and selection of a few most suitable candidate nuclides and compilation of tables of related parameters.
2. Rigorous quantum mechanical calculation of the probabilities and cross-sections of many-quantum processes of gamma-emission according to «two-level» and anti-Stokes recoil assisted lasing scheme.
3. Development of working formulae to estimate the main GRL output parameters for selected most suitable nuclides in the primary demonstrative experiment (gamma-photon beam intensity, radiation line-width, angular beam divergence, *etc.*).
4. Analysis of hindrances of existing methods of creating extended filament-like confined beams of deeply cooled nucleus bearing atoms with relatively high concentration and monokineticity, and proposal of methods to overcome or bypass the hindrances of creating extended filament-like cooled atom beams.
5. Analysis of availability of modern X-ray sources with extremely high spectral density and limited divergence of radiation to pump a nuclear medium with hidden inversion.
6. Experimental production in collaboration with LPI team an extended ensemble of ultracold atoms and finding the dependence of γ-density on power, frequency and geometry of laser beams and other parameters of the set-up (magnetic field, vacuum).
7. The possible absorption rate of γ-quanta will be evaluated by taking into account the last achievements in synchrotron-radiation sources.
8. Development in collaboration with LPI team of the system of master (diode) lasers and optical power amplifiers and the study of their limiting performance

Solving these problems can be considered as a first but very important step directed to launch the primary demonstrative GRL experiment. GRL process would be interesting not only from a physical perspective but very useful in many applications as diverse as radiation oncology, gamma-ray holography, nano-technology, nuclear energetic, etc. GRL process would introduce into practice a new type of nuclear reaction, namely, the chain reaction

of stimulated nuclear radiative transitions with release of nuclear energy in a 'clean' way, as a burst of coherent gamma radiation without the production of radioactive by-products.

Technical approach

Technical approach is based on the concept of recoil assisted lasing in an active medium of free nuclei with hidden inversion of the nuclear states populations. Coherent gamma radiation may be generated by a gamma-ray lasing process which makes use of excited nuclei as an amplifying medium. It is well known that to obtain a sufficiently high gamma-photon gain, care should be taken to increase two crucial factors of a nuclear medium: the linewidth ratio (e.g., the ratio of natural radiative linewidth of the lasing transition to the total linewidth caused by all possible broadening factors, including inhomogeneous broadening), and the degree of population inversion or, in more correct terms, the positive difference between the densities of the excited and unexcited nuclei. The Mössbauer effect, as a method for increasing the linewidth ratio, came to the attention of the authors even of the very first Soviet and American proposals of a nuclear gamma-ray laser Regrettably, this approach encounters the so-called (and insoluble) *GRL dilemma*. This expresses the impossibility of reconciling the requirements of a very intensive pump flux of any kind with maintaining the delicate Mössbauer conditions and has not furnished positive results even at the conceptual level during the past 40 years.

An alternative approach of recoil-assisted GRL in ensembles of free nuclei appears today to be much more promising. The use of nuclear recoil opens up, contrary to the standard scheme of optical lasers, entirely new possibilities possessed exclusively by radiative processes with sufficiently hard photons. Among them are:

- the possibility to establish a *hidden inversion* of state populations in an ensemble of free nuclei, which appears without excess of the number of excited nucleus over the number of unexcited ones;
- the possibility to achieve incoherent x-ray pumping of a nuclear ensemble in the so-called *two-level* scheme (which is similar to the well-known three-level scheme of optical lasers, but does not resort to a third, auxiliary level), as well as in an anti-Stokes scheme that uses for lasing the intranuclear energy of long-lived isomers.
- the possibility of anisotropic quantum amplification of a unidirectional gamma-photon flux without any reflecting mirrors; and many other attractive possibilities.

A salient feature of radiative processes in free nuclei is their recoil as a consequence of the laws of energy and momentum conservation in the emission or absorption of a gamma photon with a relatively large momentum. Thus, in any radiative transition a nucleus acquires a recoil kinetic energy equal approximately to 1 meV. In an emission process, this kinetic energy is drawn from the energy of a nuclear state and, in absorption, from *the* photon energy. This signifies that the absorption and emission spectral lines are shifted by the recoil energy relative to the transition energy and by twice the recoil energy relative to each other. This phenomenon and its more complex forms can conventionally be termed the kinematic shift and line splitting. An important conclusion is drawn from this kinematic shift: if the specified shift is comparable with the total linewidth, there arise prerequisite conditions for the formation of a so-called hidden inversion, because emitted photons have no possibility to be absorbed by unexcited nuclei. Thus, a total inversion is not required, i.e. the total number of excited nuclei need not be greater than the number of unexcited ones and consequently, in principle, the gain coefficient is positive for any finite population of upper state which is provided by sufficient incoherent x-ray pumping.

The above-listed and other remarkable features reveal themselves only in a laser with free nuclei. But this simultaneously creates a need for a radical reduction in the inhomogeneous Doppler broadening of the emission line to attain an acceptable linewidth ratio and gain coefficient for the photon flux. This very important task could be accomplished by the well known present-day techniques for deep cooling of atomic ensembles by the light pressure of optical lasers.

RECOIL-ACCOMPANIED NUCLEAR ELECTROMAGNETIC TRANSITIONS

This section reviews aspects of quantum nucleonics, as extensions of quantum electronics, that are essential to understanding specific types of recoil-accompanied nuclear electromagnetic transitions. The impact of recoil, and related inhomogeneous broadening, is critical to the feasibility a gamma-ray laser. These aspects have strong effects on reaction cross sections for the photon energies of interest, both for the driving x ray and for the emitted gamma rays. The situation is quite different, therefore, from that seen with atomic transitions for which recoil is typically ignored. Naturally, the largest cross sections are obtained at resonance between the energy of the incident photons and the energy of a specific nuclear transition. Thus, the types of transitions that are of greatest interest are recoil-accompanied resonance anti-Stokes scattering, taking the form of two-step (two-photon) depletion of isomers with spontaneous photon emission and two-step depletion of isomers with stimulated photon emission. Also important is recoil-accompanied nuclear resonance fluorescence with emission of spontaneous or stimulated gamma rays.

Single-photon nuclear transitions with recoil

The simplest case is that of single-photons transitions. The nucleus is initially described by a linear momentum $\mathbf{P}_0$ and is in an excited state $|i\rangle$ with energy $E_i = \hbar\omega_i$. The electromagnetic field is comprised by $n_{\mathbf{k}\sigma}$ photons having wavevector $\mathbf{k}$ and polarization σ. The complete initial state for the system of nucleus and radiation field is therefore represented by $|\mathbf{P}_0, i, n_{\mathbf{k}\sigma}\rangle$. The final state, represented by $|\mathbf{P}, f, n_{\mathbf{k}\sigma} + 1\rangle$, corresponds to the nucleus

with linear momentum $\mathbf{P}$ in a lower state $|f\rangle$, with energy $E_f = \hbar\omega_f$, accompanied by $n_{\mathbf{k}\sigma} + 1$ photons in the radiation field. Conventional perturbation theory gives the probability per unit time for a nuclear transition of multipolarity L:

$$P_{fi}^{(1)} = \frac{2\pi}{\hbar}\left(\frac{\omega}{c}\right)^{2L-1}\left|\left(V_{\mathbf{\kappa}\sigma}^{(L)*}\right)_{fi}\right|^2 (n_{\mathbf{k}\sigma} + 1) \times$$

$$\delta_{0,\mathbf{P}_0 - \mathbf{P} - \hbar\mathbf{k}}\,\delta(\hbar\omega + E_f + P^2/2M - E_i - P_0^2/2M) \tag{1}$$

in which the Kroniker delta $\langle \mathbf{P}|e^{-i\mathbf{k}R}|\mathbf{P}_0\rangle = \delta_{0,\mathbf{P}_0 - \mathbf{P} - \hbar\mathbf{k}}$ expresses linear momentum conservation of nucleus and emitted photon, while the Dirac delta function expresses energy conservation in the process of photon emission. The factor $n_{\mathbf{k}\sigma} + 1$ takes into account the contributions of either stimulated or spontaneous transitions. In accordance with the standard approach, the finite lifetimes of the nuclear states with energies E_i and E_f will be introduced phenomenologically by substituting $E_i \rightarrow E_i - i\Gamma_i/2$ and $E_f \rightarrow E_f + i\Gamma_f/2$ for the initial and final states, respectively. Also, the delta function will be replaced by a Lorentzian having a total energy width equal to $\Gamma_i + \Gamma_f$, the sum of the energy widths of the initial and final levels according to $\Gamma_i = \hbar\gamma_i$ and $\Gamma_f = \hbar\gamma_f$, respectively. The latter are given in terms of the frequency widths typically employed in quantum electronics and the corresponding inverse lifetimes of the levels are $\gamma_i = T_{1/2i}^{-1}\ln 2$ and $\gamma_f = T_{1/2f}^{-1}\ln 2$ where their halflives are $T_{1/2i}$ and $T_{1/2f}$. These halflives are considered the result of only radiative decays and possibly internal electron conversion. The Lorentzian $g_L(\omega - \omega_0)$ is written as

$$g_L(\omega - \omega_0) = \frac{1}{\pi}\frac{\gamma/2}{(\omega - \omega_0)^2 + \gamma^2/4}.$$

Assuming in Eq. (1) that the initial photon occupation $n_{\mathbf{k}\sigma} = 0$, and then summing over the final nuclear momentum $\mathbf{P}$, and the momentum $\hbar\mathbf{k}$ and polarization σ of the emitted photons, the probability per unit time for a spontaneous radiative nuclear transition is found to be

$$W_{sp}^{(1)} = \gamma_{if}^{(r)} = \frac{1}{(2\pi\hbar)^2 c}\left(\frac{\omega_{if}}{c}\right)^{2L+1}\sum_\sigma \int \left|(V_{\mathbf{\kappa}\sigma}^{(L)*})_{fi}\right|^2 d\Omega, \tag{2}$$

where the radiation (frequency) width of the transition is $\gamma_{if}^{(r)}$. From Eq. (2), it is then possible to obtain the matrix element of the nuclear transition, averaged over solid angle for the emitted photon and the two possible polarizations:

$$\left|(\widetilde{V}_{fi}^{(L)})^*\right|^2 = \frac{1}{2}\sum_\sigma\left(\frac{1}{4\pi}\int\left|(V_{\mathbf{\kappa}\sigma}^{(L)*})_{fi}\right|^2 d\Omega\right) = \frac{1}{8\pi}\frac{(2\pi\hbar)^2 c\gamma_{if}^{(r)}}{(\omega_{if}/c)^{2L+1}} \tag{3}$$

The probability per unit time for emission of a spontaneous gamma photon with a particular polarization σ into a differential spectral (dω) and solid angle (dΩ) intervals is determined by

$$dW_{sp}^{(1)} = \frac{1}{(2\pi\hbar)^2 c}\left(\frac{\omega}{c}\right)^{2L+1}\left|(V_{\mathbf{\kappa}\sigma}^{(L)*})_{fi}\right|^2 g(\omega - \omega_{if} - \frac{\omega_{if}}{c}(\mathbf{v}_0\mathbf{\kappa}) + \frac{E_{\text{rec}}}{\hbar})d\omega d\Omega \tag{4}$$

in which the Lorentzian function of total width $\gamma_i + \gamma_f$ reaches its maximum when the frequency, ω, of the emitted photon is shifted from the transition frequency, ω_{if}, by $(\omega_{if}/c)(\mathbf{v}_0\mathbf{\kappa}) - E_{\text{rec}}/\hbar$. The first term depends on the initial velocity $\mathbf{v}_0$ of the nucleus and describes the Doppler effect whereas the second term introduces the recoil reduction of the frequency of the emitted gamma ray. The nuclear recoil kinetic energy is $E_{\text{rec}} = (\hbar\omega_{if})^2/2Mc^2$. Since the orientations of nuclei are randomly distributed (without coherent excitation) relative to the direction of gamma emission, the matrix element in Eq. (4) must be replaced by its averaged value, $(\widetilde{V}_{fi}^{(L)})^*$. Summing over the photon polarizations, in the frequency range $|\omega - \omega_{if}| \ll \omega_{if}$ it is possible to obtain the following expression for the differential probability per unit time for spontaneous emission of a gamma ray:

$$dW_{sp}^{(1)} = \frac{\gamma_{if}^{(R)}}{4\pi}g_L(\omega - \omega_{if} - \frac{\omega_{if}}{c}(\mathbf{v}_0\mathbf{\kappa}) + \frac{E_{\text{rec}}}{\hbar})d\omega d\Omega \tag{5}$$

This differs from the conventional expression only by the terms in the argument of the Lorentzian that are related to the Doppler effect and recoil – nevertheless, these terms have a significant impact.

Based on this development, the cross section for spontaneous emission is given by

$$\sigma_{st} = \pi \lambda^2 \frac{dW_{sp}^{(1)}}{d\omega d\Omega} = \frac{\lambda^2}{4} \gamma_{if}^{(r)} g_L (\omega - \omega_{if} - \frac{\omega_{if}}{c}(\mathbf{v}_0 \mathbf{\kappa}) + \frac{E_{rec}}{\hbar}) \tag{6}$$

and the absorption cross section is

$$\sigma_{ab} = \frac{2J_i + 1}{2J_f + 1} \frac{\lambda^2}{4} \gamma_{if}^{(r)} g_L (\omega - \omega_{if} - \frac{\omega_{if}}{c}(\mathbf{v}_0 \mathbf{\kappa}) - \frac{E_{rec}}{\hbar}) \tag{7}$$

In Eqs. (6) and (7), $\lambda = 2\pi c / \omega$ is the wavelength of the emitted or absorbed photon and J_i and J_f are the angular momentum quanta of the upper and lower nuclear states, respectively (the ratio of $2J + 1$ terms is the same 'spin factor'). Again, these expressions differ from the conventional ones only in that the centers of emission and absorption lines are shifted away from the transition frequency due to the Doppler and recoil effects. This modification is nevertheless important since the relative displacement of the centers of emission and absorption lines is $2E_{rec}$, forming the basis of the Mössbauer effect.

Two-photon anti-Stokes nuclear transitions with recoil

In this scenario, a nucleus is initially in a long-lived isomeric level with excitation energy E_i. Under the influence of externally-produced x rays, two-photon transitions may be driven through an intermediate level of energy E_s to a lower level of energy E_f. (Fig. 1) Upconversion results if the final state is not only lower in energy than the intermediate state, but also lower than the isomer.

This process is accompanied by absorption of an x ray of energy $\hbar \omega_1$ (which, in general, may or may not be close to the transition energy, E_{si}) and simultaneous emission of a spontaneous or stimulated gamma ray having an energy $\hbar \omega_2$. The initial state of the combined system is described by $\left| \mathbf{P}_0, i, n_{\mathbf{k}_1 \sigma_1}, n_{\mathbf{k}_2 \sigma_2} \right\rangle$, where $\mathbf{P}_0$ is the linear momentum of the nucleus when in the isomeric state denoted by i, $n_{\mathbf{k}_1 \sigma_1}$ is the occupation number for incident x rays in a particular mode wavevector $\mathbf{k}_1$ and polarization σ_1, and $n_{\mathbf{k}_2 \sigma_2}$ is the occupation number for the emitted gamma ray with wavevector $\mathbf{k}_2$ and polarization σ_2. The intermediate level is represented as two states $\left| \mathbf{P}_s, s, n_{\mathbf{k}_1 \sigma_1} - 1, n_{\mathbf{k}_2 \sigma_2} \right\rangle$ and $\left| \mathbf{P}_s, s, n_{\mathbf{k}_1 \sigma_1}, n_{\mathbf{k}_2 \sigma_2} + 1 \right\rangle$, and the final state of the system is represented by $\left| \mathbf{P}, f, n_{\mathbf{k}_1 \sigma_1} - 1, n_{\mathbf{k}_2 \sigma_2} + 1 \right\rangle$.
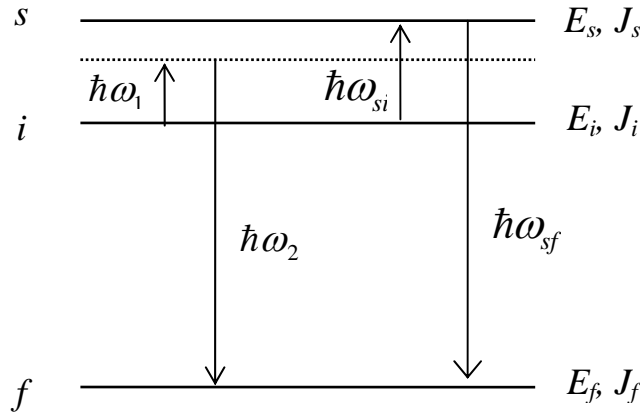

Fig. 1. *Anti-Stokes two-quantum transition from initial isomeric nuclear state i through an intermediate state s into final state f.*

The probability per unit time for this x-ray driven transition is given by

$$P_{fi}^{(2)} = \frac{2\pi}{\hbar} \left(\frac{\omega_1}{c} \right)^{2L-1} \left(\frac{\omega_2}{c} \right)^{2L'-1} \left| M_{fi}^{(L,L')} \right|^2 n_{\mathbf{k}_1 \sigma_1} (n_{\mathbf{k}_2 \sigma_2} + 1) \times$$
$$g_L (\hbar \omega_2 + E_f + P^2/2M - \hbar \omega_1 - E_i - P_0^2/2M), \tag{8}$$

where L and L' are the multipolarities of the corresponding nuclear transitions (absorption of the incident x ray and emission of the gamma ray, respectively). The matrix element contains of two terms

6

$$M_{fi}^{(L,L')} = \sum_{\mathbf{P}_s} \left[\frac{\delta_{0,\mathbf{P}_s-\mathbf{P}-\hbar\mathbf{k}_2}\delta_{0,\hbar\mathbf{k}_1+\mathbf{P}_0-\mathbf{P}_s}\langle f|V_{\kappa_2\sigma_2}^{(L')*}|s\rangle\langle s|V_{\kappa_1\sigma_1}^{(L)}|i\rangle}{E_i+\hbar\omega_1+P_0^2/2M-E_s-P_s^2/2M-i(\Gamma_i+\Gamma_s)/2} \right] +$$

$$\sum_{\mathbf{P}_s} \left[\frac{\delta_{0,\mathbf{P}_s+\hbar\mathbf{k}_1-\mathbf{P}}\delta_{0,\mathbf{P}_0-\hbar\mathbf{k}_2-\mathbf{P}_s}\langle f|V_{\kappa_1\sigma_1}^{(L)}|s\rangle\langle s|V_{\kappa_2\sigma_2}^{(L')*}|i\rangle}{E_i-\hbar\omega_2+P_0^2/2M-E_s-P_s^2/2M-i(\Gamma_i+\Gamma_s)/2} \right] \tag{9}$$

both of which reflect resonance behavior: the first term is large if the energy, $\hbar\omega_1$, for incident x rays is close to (E_s-E_i), taking place when an intermediate level s lies above the initial level i, while the second term is large if the energy, $\hbar\omega_2$, of the emitted gamma ray is close to (E_i-E_s). The latter occurs only when the intermediate level s lies lower than the final level f, provided it is not the ground state. For the situation under consideration in Fig. 1, the second term in Eq. (9) may be neglected.

The driving x-ray irradiation may be described by a spectral-angular photon flux density, $F(\omega_1,\kappa_1)$, in the direction assigned by the unit vector κ_1. The probability per unit time for anti-Stokes scattering with emission of spontaneous gamma photons is then

$$W_{\text{sp}}^{(2)} = \int \sigma_{sp}(\omega_1,\kappa_1)F(\omega_1,\kappa_1)d\omega_1 d\Omega_1 , \tag{10}$$

in which the cross section for spontaneous anti-Stokes scattering is determined by the expression

$$\sigma_{sp}(\omega_1,\kappa_1) = \frac{2J_s+1}{2J_i+1}\frac{\lambda_1^2}{4}\frac{\gamma_{si}^{(r)}\gamma_{sf}^{(r)}}{\gamma_i+\gamma_s}\left(\frac{\omega_1}{\omega_{si}}\right)^{2L+1}\left(\frac{\omega_{if}+\omega_1}{\omega_{sf}}\right)^{2L'+1} \times$$

$$g_L\left(\omega_1-\omega_{si}-\frac{\omega_1}{c}(\mathbf{v}_0\kappa_1)-\frac{1}{\hbar}\frac{(\hbar\omega_1)^2}{2Mc^2}\right). \tag{11}$$

Equation (11) generalizes the known result by adding into the argument of the Lorentzian the terms describing the frequency shifts due to the Doppler effect for a nucleus moving with an initial velocity v_0 and the recoil effect due to absorption of an x-ray photon with energy $\hbar\omega_1$.

In typical experiments, $F(\omega_1,\kappa_1)$ exhibits a broad spectral distribution around the transition frequency, ω_{si}, so that the spectral width is much greater than the width of the absorption line for the i-to-s transition. Also, the irradiating x rays are characterized by a narrow angular distribution, being concentrated within a solid angle much less than 4π around the direction assigned by the unit vector κ_1. Then the cross section for stimulated anti-Stokes scattering with emission of a stimulated gamma ray can be represented in the form

$$\sigma_{\text{st}} = \frac{2J_s+1}{2J_i+1}\frac{\lambda_{si}^2}{4}\frac{\lambda_{sf}^2}{4}\frac{\gamma_{si}^{(r)}\gamma_{sf}^{(r)}}{\gamma_i+\gamma_s}F(\omega_{si}) \times$$

$$g_L\left(\omega_2-\omega_{sf}-\frac{\omega_{sf}}{c}(\mathbf{v}_0\kappa_2)+\frac{E_{2\text{rec}}}{\hbar}\left(1-\frac{2E_{si}}{E_{sf}}(\kappa_1\kappa_2)\right)\right). \tag{12}$$

Here, the Lorentzian possesses a width $2\gamma_i+\gamma_s+\gamma_f$ and the unit vector κ_2 assigns the emission direction for a stimulated gamma ray. The nuclear recoil energy, determined from the momentum of the emitted gamma ray, is $E_{2\text{rec}}=(\hbar\omega_{sf})^2/2Mc^2$ and $F(\omega_{si})$ is the spectral photon flux density of the incident x-ray radiation evaluated at the transition frequency, ω_{si}.

Two-step depletion of isomers with spontaneous gamma emission

It is useful to estimate the rate, defined in Eq.(10), for conversion of incident x rays with a frequency close to the transition frequency, ω_{si}, into spontaneous (driven) gamma radiation from an ensemble of isomeric nuclei. First, the cross section for spontaneous anti-Stokes scattering of Eq. (11) must be averaged over the possible velocities of nuclei in the ensemble. To do so, Eq. (11) must be multiplied by the probability that the velocity projection $u=(\mathbf{v}_0\kappa_1)$ of a given nucleus on the propagation direction of the incident x rays falls within the interval from u to $u+\mathrm{d}u$, resulting in

$$f(u)du = \left(M/2\pi k_B T\right)^{1/2}\exp\left(-Mu^2/2k_B T\right)du , \tag{13}$$

where k_B is the Boltzmann constant, and then integrated over all possible nuclear velocity projections. The result of the integration depends on the width of the velocity distribution, i. e., on the temperature T of the nuclear ensemble. Strictly speaking, this must be the "longitudinal temperature" along the propagation direction of the x-ray beam.

The Doppler term in Eq. (11) goes as $(\omega_{si}/c)\sqrt{k_B T/M}$ and is therefore much smaller than the width of the Lorentzian function, $(\gamma_i + \gamma_s)$ at low temperatures (when $\sqrt{E_{1rec}kT} << \hbar(\gamma_i + \gamma_s)$, with $E_{1rec} = (\hbar\omega_{si})^2/2Mc^2$ being the nuclear recoil energy due to the momentum of an absorbed x ray). In this case, the Doppler term may be neglected and homogeneous broadening dominates over Doppler broadening. The averaged cross section for spontaneous anti-Stokes scattering in the limit $|\omega_1 - \omega_{si}| << \omega_{si}$ is then given by

$$\sigma_{sp}(\omega_1, \kappa_1) = \frac{2J_s + 1}{2J_i + 1} \frac{\lambda_1^2}{4} \frac{\gamma_{si}^{(r)}\gamma_{sf}^{(r)}}{\gamma_i + \gamma_s} \, g_L(\omega_1 - \omega_{si} - E_{1rec}/\hbar). \qquad (14)$$

In the opposite case of high temperatures, $\sqrt{E_{1rec}k_B T} >> \hbar(\gamma_i + \gamma_s)$, a Doppler broadened cross section results from an expression similar to Eq.(14), but with the Lorentzian function replaced by the Doppler function

$$g_D(\omega_1 - \omega_{si} - E_{1rec}/\hbar) = \frac{2}{\gamma_D}\left(\frac{\ln 2}{\pi}\right)^{\frac{1}{2}} \exp\left[-\left(\frac{2(\ln 2)^{\frac{1}{2}}(\omega_1 - \omega_{si} - E_{1rec}/\hbar)}{\gamma_D}\right)^2\right] \qquad (15)$$

with the frequency Doppler width $\gamma_D = (4/\hbar)(E_{1rec}k_B T \ln 2)^{1/2}$.

Equation (10) shows that the rate of upconversion is strongly dependent on whether the frequency of the driving x-ray radiation is centered on the transition energy. Also, it depends sensitively on the relative values for the spectral width of the x rays, the width of the intermediate level, the Doppler width due to the initial nuclear velocity distribution, and the frequency shift resulting from recoil. The width of the isomeric level can be neglected due to its long halflife. When $F(\omega_1, \kappa_1)$ represents a sufficiently broad spectral distribution around the transition frequency, ω_{si}, with a spectral width exceeding any of the above-mentioned widths, all nuclei may participate in the resonance upconversion process. Then for both homogeneously and Doppler broadened cases, the expression for the rate for two-step depopulation of isomeric nuclear states reduces to

$$W_{sp}^{(2)} = \frac{2J_s + 1}{2J_i + 1} \frac{\lambda_{si}^2}{4} \frac{\gamma_{si}^{(r)}\gamma_{sf}^{(r)}}{\gamma_i + \gamma_s} F(\omega_{si}) \qquad (16)$$

Here, λ_{si} is the transition wavelength from isomer to intermediate state. If the intermediate state, s, can also decay by internal electron conversion with coefficient α_{sf}, the total rate for two-step transitions is obtained by multiplying Eq. (16) by $(1 + \alpha_{sf})$.

There will be a critical spectral photon flux density for the triggering x-ray radiation above which the two-step depopulation rate will dominate the spontaneous isomer decay rate, γ_i, by direct radiative transitions and internal conversion. The critical value is given by

$$F_{cr}^{(sp)}(\omega_{si}) = \frac{2J_i + 1}{2J_s + 1} \frac{4}{\lambda_{si}^2} \frac{\gamma_i(\gamma_i + \gamma_s)}{\gamma_{si}^{(r)}\gamma_{sf}^{(r)}(1 + \alpha_{sf})}, \qquad (17)$$

assuming $\gamma_t << \gamma_s$. Of course, in addition to the anti-Stokes gamma ray, there will follow from the population of the final state of emission of spontaneous gamma rays in whatever cascade is necessary to reach the ground state. It is important to note that Eq. (17), being obtained from perturbation theory, is valid only if the rates of transitions into nuclear state s from the initial state i and of stimulated transitions going back from s to i, both going as $F(\omega_{si})\gamma_{si}^{(r)}\lambda_{si}^2/4$, are less than the rate of spontaneous decay, γ_s, of the intermediate state. This means that the spectral photon flux density cannot saturate the population in the intermediate state, a condition that may be written as

$$F(\omega_{si}) < F_{sat}(\omega_{si}) = \frac{4\gamma_s}{\lambda_{si}^2\gamma_{si}^{(r)}} \qquad (18)$$

Since for a long-lived isomer $\gamma_i << \gamma_{sf}^{(r)}(1 + \alpha_{sf})$, this restriction is naturally satisfied for the critical spectral photon flux density expressed in Eq. (17).

Two-step depletion of isomers with stimulated gamma emission

In order to estimate the gain coefficient of stimulated gamma radiation by an ensemble of free isomeric nuclei, it is necessary to consider two competing processes:

1.   two-photon conversion of the incident broadband x-ray radiation into stimulated gamma radiation with the cross section of Eq.(12), and

2.   back-resonance absorption of the stimulated gamma ray by nuclear transitions from the state f to the state s, with the cross section determined by Eq. (7) with the index i being replaced by s.

The cross sections for these processes must be averaged over the initial nuclear velocity distribution in Eq. (13). Clearly, the result will be dependent on the temperature T of the nuclear ensemble.

In the case where $\sqrt{E_{2rec}k_B T} << \hbar(\gamma_s + \gamma_f)$, and neglecting the width of the isomeric state since $\gamma_i << \gamma_s, \gamma_f$, the Doppler terms in Eqs. (12) and (7) may be omitted. Now homogeneous broadening dominates over Doppler broadening and all nuclei participate in the process of emission of stimulated gamma radiation. The gain coefficient is $G = \sigma_{st} n_i - \sigma_{ab} n_f$, where n_i and n_f are the concentrations of nuclei in the isomeric state, i, and in the final state, f, respectively. At the central frequency of the gamma emission line, , $\omega_2 = \omega_{sf} - (E_{2rec}/\hbar)[1 - (2E_{si}/E_{sf})(\kappa_1\kappa_2)]$, the gain coefficient is given by as

$$G = \frac{\lambda_{sf}^2}{2\pi} \frac{\gamma_{sf}^{(r)}}{\gamma_s + \gamma_f} \left[\frac{2J_s+1}{2J_i+1} \frac{\lambda_{si}^2}{4} \frac{\gamma_{si}^{(r)}}{\gamma_s} F(\omega_{si})n_i - \right.$$

$$\left. \frac{2J_s+1}{2J_f+1} n_f \frac{(\hbar(\gamma_s+\gamma_f)/2)^2}{\left(2E_{2rec}\left(1-(E_{si}/E_{sf})(\kappa_1\kappa_2)\right)\right)^2 + (\hbar(\gamma_s+\gamma_f)/2)^2} \right]. \quad (19)$$

If the spectral photon flux density of incident x-ray radiation is sufficiently high to satisfy the condition

$$F(\omega_{si}) > F_{th}^{(1)}(\omega_{si}) = \frac{2J_i+1}{2J_f+1} \frac{n_f}{n_i} \frac{4\gamma_s}{\lambda_{si}^2 \gamma_{si}^{(r)}} \times$$

$$\left[\frac{4E_{2rec}}{\hbar(\gamma_s+\gamma_f)} \left(1 - \frac{E_{si}}{E_{sf}}(\kappa_1\kappa_2) \right) + 1 \right]^{-1}, \quad (20)$$

then gain appears in the center of the emission line. This condition remains consistent with the application of perturbation theory in Eq. (18) if the populations in the initial and final states meet the requirement

$$\frac{2J_f+1}{2J_i+1} \frac{n_i}{n_f} > \left[\frac{4E_{2rec}}{\hbar(\gamma_s+\gamma_f)} \left(1 - \frac{E_{si}}{E_{sf}}(\kappa_1\kappa_2) \right) + 1 \right]^{-1}. \quad (21)$$

This expresses the well-known condition of hidden, or spectral-local, population inversion. Equation shows that when the recoil energy due to gamma emission is large enough to radically reduce the overlapping of emission and absorption lines, where $E_{2rec}\left(1-(E_{si}/E_{sf})(\kappa_1\kappa_2)\right) > \hbar(\gamma_s+\gamma_f)$, gain can be reached without an overall population inversion. Specifically, gain occurs without the concentration of nuclei in the upper isomeric state, n_i, exceeding that in the lower state, n_f (appropriately weighted by the 'spin factor').

In the opposite case for which $\sqrt{E_{2rec}kT} >> \hbar(\gamma_s + \gamma_f)$, Doppler broadening dominates over homogeneous broadening. Then the gain coefficient at the frequency of the emission line maximum is

$$G = \frac{\lambda_{sf}^2}{2\pi} \frac{\gamma_{sf}^{(r)}}{\gamma_D} (\pi \ln 2)^{1/2} \left[\frac{2J_s+1}{2J_i+1} \frac{\lambda_{si}^2}{4} \frac{\gamma_{si}^{(r)}}{\gamma_s} F(\omega_{si})n_i - \right.$$

$$\left. \frac{2J_s+1}{2J_f+1} n_f \exp\left(-\frac{E_{2rec}}{k_B T}\left(1 - \frac{E_{si}}{E_{sf}}(\kappa_1\kappa_2) \right)^2 \right) \right], \quad (22)$$

where $\hbar\gamma_D = 4(E_{2rec}k_B T \ln 2)^{1/2}$ gives the Doppler width of the emission line. Modern methods for cooling of atomic beams by laser light pressure allow a reduction of the Doppler broadening to the level of $\hbar\gamma_D < E_{2rec}(1-(E_{si}/E_{sf})(\kappa_1\kappa_2))$ or $k_B T < E_{2rec}(1-(\kappa_1\kappa_2)E_{si}/E_{sf})$. This is sufficient to radically suppress overlap between the emission and absorption lines and near the center of the emission line this allows a very large spectral photon flux density

$$F(\omega_{si}) > F_{th}^{(1)}(\omega_{si}) = \frac{2J_i+1}{2J_f+1} \frac{n_f}{n_i} \frac{4\gamma_s}{\lambda_{si}^2 \gamma_{si}^{(r)}} \exp\left(-\frac{E_{2rec}}{k_B T}\left(1 - \frac{E_{si}}{E_{sf}}(\kappa_1 \kappa_2)\right)^2\right) \qquad (23)$$

without any excess in the overall number of excited nuclei over unexcited ones under the condition for hidden population inversion:

$$\frac{2J_f+1}{2J_i+1} \frac{n_i}{n_f} > \exp\left(-\frac{E_{2rec}}{k_B T}\left(1 - \frac{E_{si}}{E_{sf}}(\kappa_1 \kappa_2)\right)^2\right) \qquad (24)$$

Non-resonant losses of stimulated gamma quanta occur mainly due to photoionization of atoms, Compton scattering by atomic electrons and even pair production if the gamma-ray energy is sufficiently large. The cross section for all non-resonant losses of stimulated gamma quanta will be denoted by χ. If the conditions for hidden inversion (Eqs. (21) or (24)) are maintained, the threshold spectral photon flux density, $F_{th}(\omega_{si})$, required to reach lasing of the stimulated gamma radiation is estimated by the sum of either $F_{th}^{(1)}(\omega_{si})$ from Eq. (20) and

$$F_{th}^{(2)}(\omega_{si}) = \frac{2J_i+1}{2J_s+1} \frac{8\pi\chi}{\lambda_{si}^2 \lambda_{sf}^2} \frac{\gamma_s(\gamma_s + \gamma_f)}{\gamma_{si}^{(r)} \gamma_{sf}^{(r)}}\left(1 + \frac{n_f}{n_i}\right) \qquad (25)$$

for a homogeneously broadened emission line, or $F_{th}^{(1)}(\omega_{si})$ from Eq. (23) and

$$F_{th}^{(2)}(\omega_{si}) = (\pi \ln 2)^{-1/2} \frac{2J_i+1}{2J_s+1} \frac{8\pi\chi}{\lambda_{si}^2 \lambda_{sf}^2} \frac{\gamma_s \gamma_D}{\gamma_{si}^{(r)} \gamma_{sf}^{(r)}}\left(1 + \frac{n_f}{n_i}\right) \qquad (26)$$

for an inhomogeneously, Doppler broadened emission line. The threshold spectral photon flux density for the latter is larger than the homogeneously-broadened case by about $\gamma_D/(\gamma_s + \gamma_f) \gg 1$.

Nuclear Rayleigh scattering with recoil

Nuclear Rayleigh scattering is the non-resonant scattering of a photon with energy $\hbar\omega_1$ into a spontaneous or stimulated gamma photon of energy $\hbar\omega_2$ by a transition from the nuclear ground state to a virtual intermediate state and then back to the ground state. If instead the mediating level is a bound nuclear state, this process is referred to as nuclear resonance fluorescence and is denoted as a (γ, γ) reaction. Obviously, Rayleigh scattering is similar to the anti-Stokes scattering discussed above, but with identical initial and final states. The cross section for spontaneous or stimulated Rayleigh scattering can then be formally obtained from Eqs. and by substituting the initial state i for the final state f. This cross section may be written in the form

$$\sigma_{sp}(\omega_1, \kappa_1) = \frac{2J_s+1}{2J_i+1} \frac{\lambda_1^2}{4}\left(\frac{\omega_1}{\omega_{si}}\right)^{4L+2} \frac{\left(\gamma_{si}^{(r)}\right)^2}{\gamma_i + \gamma_s} \times$$
$$g_L\left(\omega_1 - \omega_{si} - \frac{\omega_1}{c}(v_0 \kappa_1) - \frac{1}{\hbar}\frac{(\hbar\omega_1)^2}{2Mc^2}\right) \qquad (27)$$

and in the frequency range $|\omega_1 - \omega_{si}| \ll \omega_{si}$ reduces to the well-known expression for the cross section of resonance fluorescence, taking into account the Doppler and recoil terms in the argument of the Lorentzian.

Again, the spectral photon flux density of the incident radiation, $F(\omega_1, \kappa_1)$ typically has a broad distribution around the transition frequency, ω_{si}, such that the spectral width is greater than the absorption line width, and a relatively narrow angular distribution around the direction assigned by the unit vector κ_1. The cross section for stimulated resonance fluorescence is then

$$\sigma_{st} = \frac{2J_s+1}{2J_i+1}\left(\frac{\lambda_{si}}{2}\right)^4 \frac{\left(\gamma_{si}^{(r)}\right)^2}{\gamma_i + \gamma_s} F(\omega_{si}) \times$$
$$g_L\left(\omega_2 - \omega_{si} - \frac{\omega_{si}}{c}(v_0 \kappa_2) + \frac{E_{rec}}{\hbar}(1 - 2(\kappa_1 \kappa_2))\right) \qquad (28)$$

where $E_{rec} = (\hbar\omega_{si})^2/2Mc^2$.

Equations (27) and (28) show that for forward resonance scattering, with $\kappa_1 = \kappa_2$, the centers of the absorption and emission lines coincide, whereas for backward scattering, with $\kappa_1 = -\kappa_2$, they differ in energy by $4E_{\text{rec}}$. Since the forward-scattered gamma rays can be resonantly absorbed by the same nuclei in their ground states, the condition for hidden population inversion cannot be fulfilled. On the contrary, for backward-scattered gamma rays the conditions for hidden inversion can be reached, as expressed in Eqs. and with the index f replaced by i. This implies that $8E_{\text{rec}} > \hbar(\gamma_s + \gamma_i)$ for a homogeneously-broadened emission line and $2E_{\text{rec}} > k_B T$ for a Doppler-broadened emission line. With the availability of a hidden inversion, gain can be obtained in the center of the emission line, at the frequency $\omega_2 = \omega_{si} - 3E_{2\text{rec}}/\hbar$, when the pumping spectral photon flux densities exceed the threshold value of

$$F_{\text{th}}^{(1)}(\omega_{si}) = \frac{4\gamma_s}{\lambda_{si}^2 \gamma_{si}^{(r)}} \left[\frac{8E_{\text{rec}}}{\hbar(\gamma_s + \gamma_i)} + 1 \right]^{-1} \tag{29}$$

for a homogeneously broadened emission line (when $\sqrt{E_{\text{rec}} k_B T} << \hbar(\gamma_s + \gamma_i)$) or

$$F_{\text{th}}^{(1)}(\omega_{si}) = \frac{4\gamma_s}{\lambda_{si}^2 \gamma_{si}^{(r)}} \exp\left(-\frac{2E_{\text{rec}}}{k_B T} \right) \tag{30}$$

for an inhomogeneously broadened emission line (when $\sqrt{E_{\text{rec}} k_B T} >> \hbar(\gamma_s + \gamma_i)$).

To reach lasing for gamma radiation, the gain must overcome the nonresonance losses with cross section χ for the stimulated photons. To do so, the required threshold spectral photon flux density for a homogeneously-broadened emission line is the sum of $F_{\text{th}}^{(1)}(\omega_{si})$ of Eq. (29) with index f replaced by i, and

$$F_{\text{th}}^{(2)}(\omega_{si}) = \frac{2J_i + 1}{2J_s + 1} \frac{16\pi\chi}{\lambda_{si}^4} \frac{\gamma_s(\gamma_s + \gamma_i)}{\left(\gamma_{si}^{(r)}\right)^2}. \tag{31}$$

For an inhomogeneously-broadened emission line, the sum of $F_{\text{th}}^{(1)}(\omega_{si})$ of Eq. (30) and

$$F_{\text{th}}^{(2)}(\omega_{si}) = (\pi \ln 2)^{-1/2} \frac{2J_i + 1}{2J_s + 1} \frac{16\pi\chi}{\lambda_{si}^4} \frac{\gamma_s \gamma_D}{\left(\gamma_{si}^{(r)}\right)^2} \tag{32}$$

is required. If the intermediate state, s, is the first excited nuclear state, the substitution $\gamma_s = \gamma_{si}^{(r)}(1 + \alpha_{si})$ should be employed in the above equations, where α_{si} is the internal electron conversion coefficient of the transition.

IDENTIFICATION OF PRIME NUCLIDES FOR AN ACTIVE MEDIUM OF GAMMA-RAY LASER

Selection of nuclides which might be employed for an active medium of gamma-ray laser requires a detailed analysis both the internal nuclear structure and the atomic electron shell of a potential candidate. We discuss the problem of identification the most promising nuclides for two attractive schemes of gamma-ray laser [1] based on the concept of the recoil-assisted lasing with hidden inversion of nuclear state populations.

First scheme takes advantage of the energy-storage capability of isomeric nuclei. The excitation energy of such nuclei is stored for a long time in a metastable state and then may be released through an emission of gamma rays. Since direct electromagnetic transitions between the isomeric and ground states are unlikely, a controlled energy release could be accomplished through the two step process. At first, the nucleus is exited from initial isomeric state to reach an upper intermediate state by absorption of an incident photon of pumping radiation. Then, the intermediate state decays promptly to the ground state with emission of a gamma photon. Actually, this two step de-excitation can be regarded as the nuclear resonance anti-Stokes scattering [2] with up-conversion of the pump X-ray radiation into a flux of gamma photons and it is often termed as the X-ray driven gamma emission or the photon triggering of gamma emission or, simply, the triggering of an isomer [3].

The emitted gamma photon may be absorbed by a nucleus being in the ground state with a resonance transition back to the intermediate state. However, one can get such transitions off the resonance due to nuclear recoil from momentum of the emitted or absorbed gamma photon. The recoil effect leads to an opposite shifting of emission and absorption lines. A cooling of the atomic ensembles allows one to reduce Doppler line broadening to the extent which is sufficient to eliminate an overlap between the lines. In such conditions, the emitted gamma photon can no longer be absorbed by an unexcited nucleus, but it is still capable of stimulating de-excitation of an excited nucleus with emission of an identical quantum. This allows a gain of stimulated gamma quanta to occur in a particular frequency range near to the center of emission line. A total population inversion is not required for this gain, so that the total number of excited nuclei need not be greater than the number of unexcited nuclei.

The isomeric states are rather commonly found to exist in many different nuclides, with a wide range of stored energies and half-lives. Naturally, the major focus is on the isomers that are capable of storing an appreciable amount of energy for a long time. We screen such isomers in order to pick out the candidates with appropriate arrangement of the nuclear states. Then, the atomic electron shells of the selected isomers is explored to identify the nuclides that would provide optimal conditions for cooling with optical lasers. The most valuable isomers are collected into a table.

Another scheme of gamma-ray laser uses the opportunity, offered again by the nuclear recoil, to pump the first excited state of a nucleus directly from its ground state. The two-level pump approach, totally forbidden in typical optical lasers, might provide lasing in a cooled nuclear ensemble due to establishing a hidden inversion of the nuclear state populations. It is worth noting that the process of lasing can be classified as the nuclear resonance fluorescence scattering of the pump radiation into a flux of stimulated gamma photons [4].

There are a lot of stable or long-lived isotopes suitable for pumping the first excited nuclear state. A search for the most attractive nuclides among them should take into account the need to match the specific nuclear parameters (half-lives, transition energy, *etc*.) to the pump capabilities of the available sources of X rays (pulse duration, energy of X rays, degree of monochromaticity, angular divergence, *etc*.). Together with some further limitations arising from the demands to atomic electron shell, this reduces considerably the number of candidates which might be employed for an active medium of gamma-ray laser. Ranking of the selected candidates is accomplished in the order of ascending threshold spectral photon flux density of pumping radiation. The first-ranked isotopes potentially valuable to realizing a gamma-ray laser are collected into a table.

Candidate isomers for a gamma-ray laser.

We begin with a discussion of general requirements for specification of isomers that would provide an optimal active medium for a gamma-ray laser based on the trigger scheme of pumping.

First of all, we are interested in isomers, which are long enough lived to permit their accumulation in an appreciable amount. An appropriate range of half-lives is specified by the requirement to the decay rate of an isomer to be less than the rate of its production, that occurs typically by (n, γ) reaction of neutron capture. This approach requires a detailed analysis of the production conditions (neutron flux intensity, concentration of parent nuclides in a target, reaction cross section, *etc*.). We leave, however, this analysis for a future investigation and merely restrict our choice by the isomers with half-lives greater than 10 days. This period seems reasonable from the viewpoint of carrying out a gamma-ray laser experiment that should include the following stages: production and accumulation of an isomer, deliver the specimen to the place of experiment, cooling and trapping of the nuclear ensemble and, finally, pumping with a source of X-ray radiation.

Further, the preferable nuclear level scheme of an isomer should contain near to the isomeric level an upper intermediate level suitable for triggering of gamma emission. The simplest level scheme of this kind is represented in Fig. 1 with a lower level *f* that may be ground or not. A nucleus, being initially in the isomeric state *i*, is excited to reach an intermediate state *s* by absorption of an incident photon of pumping radiation. Then, the intermediate state decays to the lower laser state *f* with spontaneous or stimulated emission of a gamma-photon. Such a scheme allows one to use for lasing an intranuclear energy rather than the energy of pumping radiation. Indeed, in an ensemble of isomeric nuclei a population inversion between the isomeric and ground states is established automatically, so that the role of X-ray photons of an external radiation is reduced to transferring this population from the isomer to the intermediate level. Since the transition energy is small, the X-ray photons play the triggering rather than pumping role and the process of lasing can be regarded as a driven release of energy stored in the nuclear isomer. This is the most attractive feature of the trigger scheme of gamma-ray laser.

The question of feasibility of such a gamma-ray laser rests on the degree to which the properties of some real nuclear isomer approach those of the ideals described above. We have screened all known isomers in order to pick out the candidates with appropriate arrangement of the nuclear states. For the screening we have used the Table of Isotopes [5] and the most comprehensive nuclear structure database, ENSDF [6], maintained by the National Nuclear Data Center at Brookhaven National Laboratory.

Our search has identified 29 isomers with half-lives greater than 10 days. Then, following the above argumentation, we have sorted out the isomers with triggering energy less than 50 keV. This energy range is covered by the modern sources of X rays of high intensity. The amount of energy that may be released in the form of coherent gamma rays is also important. So that the nuclides with higher placed (relatively the lower laser nuclear level) isomeric and trigger levels are most interesting. After a comparative examination, the isomers ^{102}Rh^m, ^{110}Ag^m, ^{113}Cd^m, ^{174}Lu^m, ^{177}Lu^m, ^{178}Hf^{m2}, ^{179}Hf^{m2} and ^{242}Am^m have been chosen to be the most interesting candidates potentially valuable for a gamma-ray laser. It is noteworthy, that the last four isomers have been previously identified [3] to be the most promising candidates for the experiments on triggering of gamma emission.

The threshold condition for a gamma-ray lasing requires the gain of stimulated gamma quanta to be high enough to compensate all kind of their losses. Non-resonant losses of gamma quanta occur due to incoherent (Compton) scattering by atomic electrons, coherent (Rayleigh) scattering, photoelectric absorption and even pair production if the gamma-ray energy is sufficiently large. The primary source of the non-resonant losses of gamma quanta with energies less than 100 keV is the photoelectric absorption by the atomic electrons. A small value of the total cross section χ for all non-resonant photon losses is a general requirement to the atomic electron shell of a

candidate. More specific demands to the shell arrangement arise from the need for deep cooling of an active nuclear medium.

The temperature of nuclear medium, that ensure a hidden population inversion to occur, is strongly dependent (through the recoil energy) on the energy of laser nuclear transition. For an ensemble of nuclei with mass number A=100 the corresponding temperatures are in the range from a few of K for 10 keV transitions to hundreds of K for 100 keV nuclear transitions. Far deeper cooling is required to attain a gain of stimulated gamma quanta sufficient to beginning of gamma-ray lasing. The appropriate temperatures may approach some critical temperature for which the Doppler width of emission line is reduced to the decay width of the upper laser level. The critical temperatures, lying typically in μK or even in nK region, can be reached by present-day techniques [7] for deep cooling of atomic ensembles by the light pressure of optical lasers.

The threshold spectral photon flux density of pumping radiation at the photon energy equal to the energy of trigger transition E_{si} can be estimated by [2, 3]

$$F_{\text{th}} = 7.8 \times 10^{16} \frac{\chi(1+\alpha_{sf})E_{si}^2 E_{sf}^3}{G_{si}\Gamma_{si}^{(\text{r})}} \sqrt{\frac{T}{A}} \tag{33}$$

where F_{th} is expressed in photons/(cm^2 s keV), while the total atomic cross section of the photon losses, χ, is in barns, temperature T is in μK, the nuclear transition energies E_{si} and E_{sf} are in keV, A is the mass number of a nucleus, α_{sf} is the internal electron conversion coefficient of the laser transition and $G_{si}=(2J_s+1)/(2J_i+1)$ and $\Gamma_{si}^{(\text{r})}$ (measured in eV) are the spin factor and the radiative width of the trigger transition, respectively. As a rule, the later value is unfortunately unknown and the single-particle Weisskopf estimate [8] for $\Gamma_{si}^{(\text{r})}$ is used.

In derivation of the formula (1) we assumed that the most part of nuclei comprising an active medium are initially in an isomeric state. We also used the relation $\Gamma_s = (1+\alpha_{sf})\Gamma_{sf}^{(\text{r})}$ which is valid if the s-to-f nuclear transition is the most intensive one. In particular, this means that the isomer, being pumped into the intermediate state s, decays directly to the final state f rather than comes back to the initial isomeric state i - the requirement that seems quit reasonable for a level scheme of gamma-ray laser. All the above selected isomers meet this requirement.

Table 1 summarizes both nuclear and atomic data for the most interesting candidate isomers. We have used NIST Photon Cross Sections Database [9] to identify the total atomic cross sections χ for each isomer at the gamma-ray laser energy. An intensive line should be available in the optical domain of absorption atomic spectrum of each candidate to apply the laser cooling technique. A search for this line has been accomplished with the help of NIST Atomic Spectra Database [10]. We have restricted the search by the wavelength region of interest ranging from 0.3 to 1.8 μm. The wavelengths of the found lines are presented in the table. The corresponding atomic transition probabilities are also displayed where available.

Table 1 Nuclear and atomic data for the most interesting candidate isomers.

Isomer	Nuclear data						Atomic data			
	$T_{1/2}$	E_{si} [keV]	E_{sf} [keV]	G_{si}	$\Gamma_{si}^{(\text{r})}$ [eV]	α_{sf}	λ μm]	Transition probability [10^8s^{-1}]	χ [b]	F_{th} (T=10 μK) [$10^{35}\times$ ph/(cm^2 s keV)]
^{102}Rh$^{\text{m}}$	2.9 y	15.7	156.5	-	-	-	0.385	0.59	76.5	-
^{110}Ag$^{\text{m}}$	249.8d	1.13	118.7 117.6	7/13	8.5×10^{-33}	0.78 0.10	0.546	0.86	170.0	3.3×10^{22} 2.0×10^{22}
^{113}Cd$^{\text{m}}$	14.1 y	34.9	298.6	1/3	2.1×10^{-30}	0.03	0.643	0.59	29.5	3.2×10^{23}
^{174}Lu$^{\text{m}}$	142 d	29.5	88.5 155.6	9/13	1.1×10^{-12}	4.61 0.32	0.451	0.21	25.2	2.2×10^4 2.8×10^4
^{177}Lu$^{\text{m}}$	160.4d	15.1	716.7 544.4	7/12	4.6×10^{-40}	0.01 0.04	0.451	0.21	25.2	1.5×10^{33} 6.4×10^{32}
^{178}Hf$^{\text{m2}}$	31 y	39.2	626.2	25/33	1.5×10^{-29}	0.02	0.417	-	29.9	1.8×10^{23}
^{179}Hf$^{\text{m2}}$	25 d	0.07	1105.9 983.2 891.5	4/13	1.1×10^{-122}	0.01 0.01 0.01	0.417	-	29.9	1.1×10^{112} 7.5×10^{111} 5.6×10^{111}
^{242}Am$^{\text{m}}$	141 y	4.27	52.9	7/11	1.1×10^{-16}	4.3	0.605	-	4680	1.6×10^8

The right-most column of the table contains the estimates of the threshold spectral photon flux densities of pumping radiation for each candidate performed with the help of (1) at a temperature of active medium of 10μK. Since the expression (1) incorporates the most part of the key nuclear and atomic parameters, the value of F_{th} may

be regarded as a sort of relative numerical figure-of-merit of each isomer (strictly speaking, we should use the inverse value of F_{th}, since the lower the threshold flux, the better). However, the ranking of the candidates in such a manner is quit unreliable, since many of the nuclear parameters are poorly known at present. First of all it concerns the probabilities of trigger transitions of isomers. The empirical values of the trigger transition probabilities and, thus, the actual values of the threshold spectral photon flux densities may show significant departures from the above estimates based on the single-particle Weisskopf approximation. Therefore, for a true evaluation of the threshold fluxes it is extremely important to determine experimentally the probabilities of the nuclear transitions involved.

One can see, also, that the threshold fluxes of pumping radiation needed for a gamma-ray lasing are huge. The primary reason for this is the basic inherent contradiction within the trigger scheme of gamma-ray laser. Indeed, for an efficient lasing, both trigger and laser transitions should have large probabilities. This requires the change of the nuclear angular momentum J for both transitions to be small. Unfortunately, this requirement conflicts with the condition for a long lifetime of isomeric state, since the isomerism in the case of so-called *spin isomers* is due to a large change of the nuclear angular momentum for the decay transitions from the isomer.

Many nuclei have axially symmetric deformed shapes and upon the body-centered axis it becomes possible to define the projection of the angular momentum vector. The quantum number assigned to this projection is K and it reflects the relative orientation of the angular momentum vector. So-called *K isomers* derive their long lives from a large change of the orientation of angular momentum vector for the decay transitions. The inherent contradiction appearing within the nuclear level scheme in Fig. 1 takes place for *K isomers* as well.

This contradiction may be partly relaxed, if the mediating level s possesses a value of J (and perhaps K) intermediate between those of initial and final states. In principle, the contradiction might completely disappear if the single trigger level s in Fig. 1 is replaced by a band with a number of closely spaced levels having a small spin (or K projection) difference. A full spontaneous decay cascade inside this band can rid an isomer of its excess angular momentum (or K projection). In this case, the transitions between a bottom level of this band and the lower final level f might provide a gamma-ray lasing. The existence of such an isomer is the most intriguing question around a gamma-ray laser. Further investigation of this issue requires better experimental data than those obtained so far. Collected in the table 1 isomers are the first priority candidates for such experiments.

Candidate isotopes for a gamma-ray laser.

A search for the most attractive isotopes which might be employed for a gamma-ray laser based on the two-level pump scheme should take into account the following criteria and preferences. First of all, we are interested in isotopes offering the opportunity to pump the first excited nuclear state directly from the ground state. Naturally, stable isotopes are more preferable, but nuclides with sufficiently long-lived ground states are also possible. We restrict our search by the isotopes with half-lives of the ground state greater than 100 days. This period seems to be long enough to produce and accumulate the isotope in an appreciable amount sufficient to conducting a sequence of successive gamma-ray laser experiments with one and the same specimen.

Another search criterion is necessitated by the consideration of pump capabilities of the available sources of X rays [11]. Undulators and wigglers at modern synchrotrons can produce radiation with peak fluxes up to 10^{24} photons/(cm^2 s keV) at the photon energy from 1 to 50 keV. Larger fluxes with the photon energies from 5 to 10 keV can be supplied, in principle, by the coming X-ray free electron lasers. Intense fluxes of photons with the same energies are also possible from plasma sources of X rays. A way to obtain X rays of higher energies is to employ the resonant harmonic generation techniques. In this case, however, the fluxes decrease drastically by many orders of magnitude. Therefore, a search for preferable isotopes that are suitable for pumping with modern sources of X rays should be limited by nuclides with the first excited state laying below 100 keV. It is clear that the isotopes with the transition energy less than 50 keV are more preferable, so we sort out these isotopes apart of those which have the transition energies greater than 50 keV.

We have identified 85 isotopes having the first excited state energy less than 100 keV and half-life of the ground state greater than 100 days. Nuclear data were generally taken directly from the Table of Isotopes [5] and the ENSDF file [6]. Further selection of the most attractive nuclides among them is based on ranking of the candidates in the order of ascending threshold spectral photon flux density of pumping radiation. This very important value can be estimated, above the critical temperature, by [3, 4]

$$F_{th} = 1.7 \times 10^{23} \frac{\chi(1+\alpha)^2 E^5 T_{1/2}}{G} \sqrt{\frac{T}{A}}, \qquad (34)$$

where F_{th} is expressed in photons/(cm^2 s keV), when the total atomic cross section of the photon losses, χ, is in barns, temperature T is in μK, the nuclear transition energy, E, is in keV and the half-life of the first excited nuclear state, $T_{1/2}$, is in ns, A is the mass number of a nucleus, α and G are the internal electron conversion coefficient and the spin factor of the nuclear transition.

Some of the considered isotopes cannot be evaluated in this manner because of the lack of the data for half-lives of their first excited nuclear states in the available databases. The single-particle Weisskopf approximation has been used for them to estimate the threshold spectral photon flux density of pumping radiation. For several isotopes the

internal electron conversion coefficient of the nuclear transition is unknown. In this cases we have used the tabulated theoretical estimates for α summarized in references [12, 13].

Top 10 isotopes ensuring the lowest threshold fluxes of pumping radiation are presented in tables 2 and 3 (separately, for the nuclear transition energies below and above 50 keV). Survey of the selected isotopes reveals two outstanding nuclides of ^{40}K and ^{54}Mn distinguished by an exceptionally low value of the threshold spectral photon flux density of pumping radiation. For the nearest competitors, the value of F_{th} turns out to be higher by two orders of magnitude. The primary reason for this is a lucky combination of the very low internal conversion coefficient of the nuclear transition with the very low atomic cross section of the non-resonant gamma photon losses.

Table 2. Top 10 isotopes with the nuclear transition energies less than 50 keV (ordered by the value of the threshold spectral photon flux density of pumping radiation).

Nuclear data					Atomic data				
Isotope	E [keV]	Ground state half life [y]	$T_{1/2}$ [ns]	α	λ [μm]	Transition probability [10^8 s^{-1}]	χ [10^3 b]	T_{cr} [μK]	F_{th} (T=10μK) [$10^{35}\times$ph/ (cm^2 s keV)]
$^{40}_{19}$K	29.830	1.3×10^9	4.24	0.357	0.766491	0.387	0.23	1.03×10^{-3}	4.6×10^{-2}
$^{183}_{74}$W	46.483	1.1×10^{17}	0.188	8.63	0.400875	0.163	2.20	0.98	1.66
$^{81}_{36}$Kr	49.56	2.3×10^5	3.9	1.3	0.877675	0.27	0.65	8.89×10^{-4}	1.91
$^{119}_{50}$Sn	23.870	Stable	18.03	5.22	0.283999	1.7	2.62	2.63×10^{-4}	3.50
$^{161}_{66}$Dy	25.652	Stable	29.1	2.35	0.421172	2.08	6.63	1.18×10^{-4}	10.23
$^{129}_{54}$Xe	39.578	Stable	0.97	12.3	0.823163	-	4.95	3.59×10^{-2}	19.50
$^{125}_{52}$Te	35.492	Stable	1.48	14.0	0.972274	-	5.96	1.86×10^{-2}	26.94
$^{133}_{56}$Ba	12.327	10.51	7.0	70.3	0.705994	0.71	24.30	7.32×10^{-3}	57.53
$^{227}_{89}$Ac	27.36	21.77	38.3	4.5	0.417998	-	18.10	8.48×10^{-5}	65.39
$^{121}_{51}$Sb	37.138	Stable	3.46	11.11	0.326751	-	4.97	3.00×10^{-3}	65.49

Table 3. Top 10 isotopes with the nuclear transition energies greater than 50 keV (ordered by the value of the threshold spectral photon flux density of pumping radiation).

Nuclear data					Atomic data				
Isotope	E [keV]	Ground state half life [y]	$T_{1/2}$ [ns]	α	λ [μm]	Transition probability [10^8 s^{-1}]	χ [10^3 b]	T_{cr} [μK]	F_{th} (T=10μK) [$10^{35}\times$ph/ (cm^2 s keV)]
$^{54}_{25}$Mn	54.40	312.3d	0.049	0.212	0.403075	0.17	0.13	3.11	4.6×10^{-3}
$^{75}_{34}$Se	112.39	119.79d	0.690	0.121	0.47308	-	0.063	5.1×10^{-3}	0.47
$^{165}_{67}$Ho	94.70	Stable	0.022	3.13	0.416303	-	1.10	15.59	1.31
$^{159}_{65}$Tb	58.00	Stable	0.054	11.0	0.432643	-	3.52	6.65	5.12
$^{173}_{70}$Yb	78.63	Stable	0.046	7.01	0.398799	1.76	2.08	5.40	5.67
$^{131}_{54}$Xe	80.185	Stable	0.480	1.57	0.823163	-	0.79	3.6×10^{-2}	7.82
$^{167}_{68}$Er	79.322	Stable	0.115	5.74	0.400796	2.6	1.84	0.82	10.07
$^{157}_{64}$Gd	54.548	Stable	0.13	12.40	0.422585	-	3.93	1.28	12.71
$^{155}_{64}$Gd	60.008	Stable	0.193	9.36	0.422585	-	3.07	0.47	14.29
$^{159}_{66}$Dy	56.626	144.4d	0.21	13.19	0.421172	2.08	3.95	0.46	27.72

Comparative examination of these two isotopes shows that the employment of ^{40}K seems to be more advantageous, due to its practically stable ground state (half-life is 1.3×10^9y against 312.3d for ^{54}Mn) and a relatively low nuclear transition energy (29.83 keV against 54.4 keV for ^{54}Mn). Moreover, the atomic absorption spectrum of ^{40}K has an intensive line with the wavelength that seems to be more attractive for cooling with optical lasers (0.77μm against 0.40μm for ^{54}Mn). Additionally, the transition probability corresponding to this line of ^{40}K is twice as much than that of the line of ^{54}Mn (0.39×10^8 s^{-1} against 0.17×10^8 s^{-1}).

Finally, it is important to emphasize that the presented estimates for F_{th} has been made at 10 μK temperature of an active medium. Further cooling down to the critical temperature may result in a corresponding decrease of the value of F_{th}. For ^{54}Mn, with the critical temperature of 3.1 μK, this decrease is insignificant, whereas cooling of ^{40}K nuclear ensemble down to its critical temperature of 10^{-3} μK would allow one to reduce the threshold flux of pumping radiation by two orders of magnitude. In this case the value of F_{th} might approach the peak fluxes that can be supplied with the coming X-ray free electron laser sources.

ANALYSIS OF IMPACT OF X-RAY PUMPING ON A GAMMA-RAY LASER MEDIUM

Coherent gamma radiation may be generated by a gamma-ray lasing process which makes use of excited nuclei as an amplifying medium. It is well known that to obtain a sufficiently high gamma-photon gain, two crucial factors should be maximized for the nuclear medium: the ratio of the natural radiative linewidth of lasing transition to the total linewidth and the degree of population inversion. The primary source of emission line broadening, detracting the linewidth ratio is the chaotic thermal motion of atoms bearing the active nuclei through their Doppler line broadening. There are several ways to reduce the inhomogeneous broadening of the emission line or even to completely eliminate the influence of the Doppler line broadening.

The Mössbauer effect was proposed at the very beginning of the search for a gamma-ray laser [14 - 16] as a possible method for increasing the linewidth ratio. Regrettably, this solid-state approach encounters the so-called, and apparently insoluble, 'graser dilemma' [17]. The graser dilemma expresses the inability to reconcile the requirements of a very intensive pump flux of any kind (optical, X-ray, neutron, *etc.*) with the need to maintain the thermal conditions that allow the Mössbauer effect to occur. Recent experimental results demonstrating the general process of excitation of nuclei by plasma radiation [18-20] and the first experimental evidence for X-ray driven nuclear population inversion [21] reinforce the harsh demands on pumping to reach the threshold for gamma-ray lasing. One hope is that ideas of lasing-without-inversion might be successfully applied to nuclei [22-25], and thereby relax the critical intensities of pumping radiation. However, the survival of the Mössbauer effect under lasing-without-inversion conditions has yet to be demonstrated.

A concept that seems very promising, as an alternative to the solid-state approach, is that of a recoil-assisted gamma-ray laser in deeply-cooled ensembles of free nuclei [26]. This concept utilizes entirely new possibilities [27] revealing themselves only in radiative processes with hard photons in cooled ensembles of free nuclei. One of them is the possibility to use the nuclear recoil in the emission or absorption of gamma-photons to establish a *hidden inversion* of state populations. The hidden inversion ensures a gain of stimulated gamma radiation in a particular frequency range without an excess of the number of excited nuclei over the number of unexcited ones. This may result in a considerable reduction in the threshold flux of X-ray pumping radiation, since a total population inversion is not required for the gamma-ray lasing. Simultaneously, a sufficiently high linewidth ratio and gain coefficient for the output gamma-photon flux can be attained through deep cooling of atomic ensembles. The cooling can be accomplished by present-day or upcoming techniques [28-30] based on the light pressure of optical lasers. Together with some other attractive features (the opportunity to use the so-called 'two-level' scheme for X-ray pumping of a cooled nuclear ensemble, the possibility of anisotropic amplification of a unidirectional gamma-photon flux without any reflecting mirrors, *etc.*) the concept of recoil-assisted gamma-ray laser in deeply-cooled ensembles of free nuclei appears today to be the most promising.

The question remains, however, whether intensive flux of pumping radiation can destroy the conditions for hidden inversion of state populations in cooled nuclear ensembles. We discuss in this paper the destructive impact of X-ray pumping radiation on the active medium of cooled free nuclei and formulate a set of requirements to the pumping radiation and to the amplifying nuclear medium crucial to the development of recoil assisted gamma-ray lasing. We discuss, as well, the efficiency of pumping with modern sources of X-ray radiation.

Self-amplified spontaneous gamma emission

Since in gamma region of wavelengths neither mirrors nor gratings exist to reflect the radiation well enough to form a resonator cavity, the development of a gamma-ray laser source is likely to be based on self-amplified spontaneous emission principle. Spontaneous gamma radiation, propagating along the axis of cylindrically shaped nuclear ensemble with hidden inversion of populations of an upper 2 and a lower 1 nuclear states (which are assumed below to be the first excited and the stable ground ones), undergoes an amplification with the gain coefficient

$$g(\omega) = \sigma_{\text{st}}\, n_2 - \chi\, n\,, \tag{35}$$

where n and n_2 are the total and excited nuclear concentrations, respectively, and χ is the total atomic cross section of photon losses due to the photoelectric effect, Compton scattering, *etc*. The cross section for stimulated emission of gamma radiation with a frequency ω, is

$$\sigma_{\text{st}} = \left(\lambda_0^2 \big/ 4\right)\gamma_{21}^{(\text{r})} f(\omega - \omega') \tag{36}$$

where $\gamma_{21}^{(\text{r})} = T_{1/2}^{-1}(1+\alpha)^{-1}\ln 2$ is the radiation (frequency) width of the 2-to-1 nuclear transition with the half-life $T_{1/2}$ of the excited state and internal electron conversion coefficient α, $\lambda_0 = 2\pi c/\omega_0$ is the nuclear transition wavelength and $f(\omega - \omega')$ is a shape-factor of the emission line with a central frequency ω' and spectral linewidth γ. Due to chaotic thermal motion of atoms, the linewidth γ in an ensemble with temperature T is normally dominated by the Doppler width of $\gamma_{\text{D}} = (4/\hbar)\left(E_{\text{rec}}k_{\text{B}}T\ln 2\right)^{1/2}$, where $E_{\text{rec}} = \left(\hbar\omega_0\right)^2\big/2Mc^2$ gives the nuclear recoil energy.

As is well known, the centers of emission and absorption lines of a free nucleus are shifted in the opposite directions due to recoil momentum acquired by the nucleus in the radiative processes with hard photons. At low temperatures of a nuclear ensemble of free nuclei, $k_{\text{B}}T < E_{\text{rec}}$, sufficient for a radical reduction in an overlap between emission and absorption lines (the linewidth should be less then the distance between centers of the lines), a hidden inversion of state populations arises for the gamma-ray propagating opposite to the pumping X-ray [26, 31]. Since in this case the emitted gamma-quanta cannot be resonantly absorbed by unexcited nuclei, the population difference under conditions of hidden inversion is merely equal to the concentration of excited nuclei and, accordingly, the gain coefficient (35) does not depend at all on the concentration n_1 of unexcited nuclei.

If we assume that the pump pulse duration exceeds the time for single pass of gamma-radiation, L/c, along the axis of a cylindrical nuclear medium with length L (see fig. 2) or, alternatively, the pump is arranged in such a way that the traveling wave of nuclear excitation occurs in the direction of expected gamma-ray, then the output flux of self-amplified spontaneous emission into a solid angle $\Delta\Omega = \pi\left(R/L\right)^2$ (where R is a radius of the cylinder) could be collected from all over the length L.

The output density of amplified photon flux integrated over all frequencies of emitted gamma quanta is

$$F = \frac{\Delta\Omega}{4\pi}\int_0^\infty S_{\text{sp}}(\omega)\left[\int_0^L e^{g(L-z)}dz\right]d\omega \tag{37}$$

where $S_{\text{sp}}(\omega) = n_2\gamma_{21}^{(\text{r})} f(\omega - \omega')$ is the spectral density of spontaneous gamma emission rate into unit volume. With approximation for $f(\omega - \omega')$ by a constant value of γ^{-1} within the spectral bandwidth γ around the central frequency ω', the amplified photon flux density F (37) can be estimated, as compared to out-of-axis flux density of spontaneous gamma emission, F_0, by a factor of

$$\frac{F}{F_0} = \frac{G-1}{\ln G}\,, \tag{38}$$

where $G = \exp(gL)$ is the single-pass gain of coherent gamma-photons over the length L with the gain coefficient being

$$g \approx \left(\lambda_0^2\big/4\right)\left(\gamma_{21}^{(\text{r})}\big/\gamma\right)n_2 - \chi\, n\,. \tag{39}$$

Truly exponential amplification of spontaneous gamma emission or, in other words, gamma-ray lasing occurs for $gL \geq 1$, the condition which is assumed to be a starting point to determine in the next sections a set of requirements crucial to the recoil assisted gamma-ray lasing process.

Gamma-ray lasing medium

The request for $gL \geq 1$, with the gain coefficient g given by (39), brings to the requirement to the relative concentration of excited nuclei

$$\frac{n_2}{n} \geq \frac{4\left(\chi\big/\lambda_0^2 + 1\big/\lambda_0^2 nL\right)}{\gamma_{21}^{(\text{r})}\big/\gamma}\,. \tag{40}$$
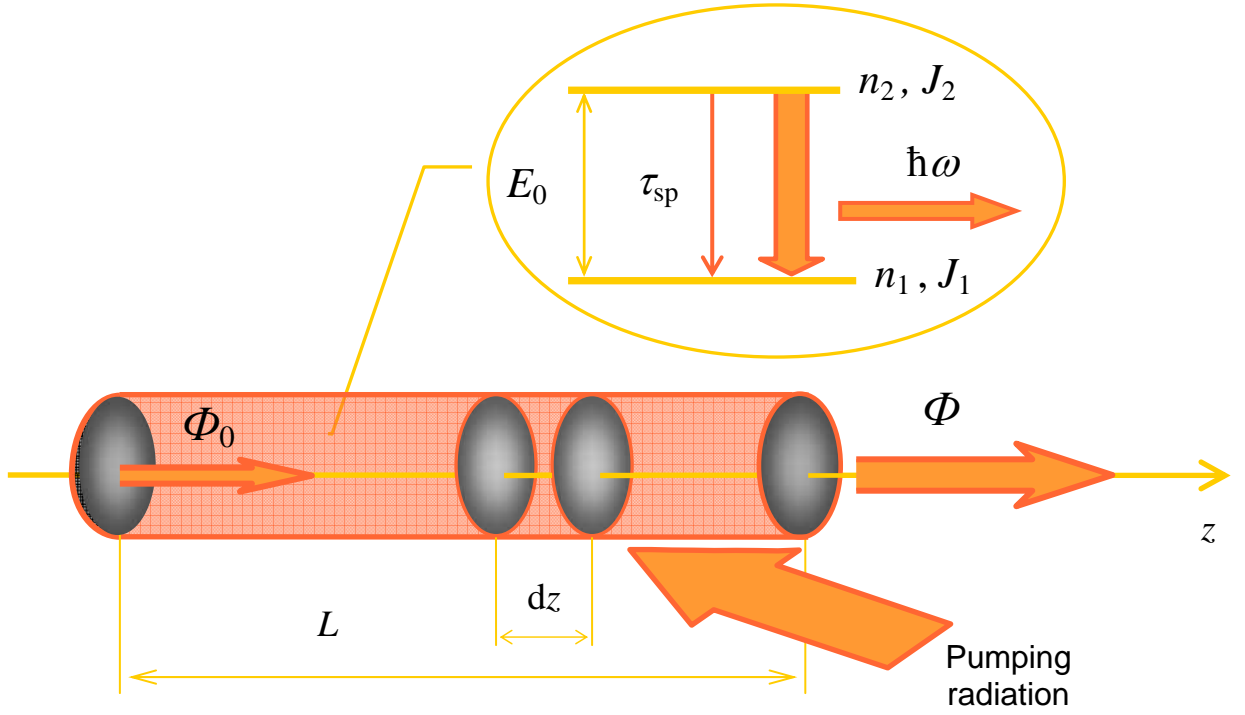
Fig. 2. *Schematic of a test experiment on gamma-ray lasing with pump by x-rays injected nearly antiparallel to the direction of expected gamma-ray.*

Taking into account that the concentration of excited nuclei, n_2 is obviously less then the total nuclear concentration, n, we obtain from (40) the following requirement to the linewidth ratio

$$\frac{\gamma_{21}^{(r)}}{\gamma} \geq 4\left(\frac{\chi}{\lambda_0^2} + \frac{1}{\lambda_0^2 nL}\right),$$

(41)

the condition which is, actually, to be considered as a demand on cooling degree of nuclear ensemble.

Even in deeply cooled nuclear ensembles the emission linewidth γ normally exceeds its minimum value equal to the decay width of the upper lasing state, $\gamma_2 = \gamma_{21}^{(r)}(1+\alpha)$, that may contains the contributions both from the radiative nuclear decay mode and the internal electron conversion decay mode. In combining with the requirement (41), this gives for the dimensionless parameter of gamma-ray lasing medium, $\varepsilon = \lambda_0^2 nL$, involved into relations (40) and (41), the following restriction

$$\varepsilon = \lambda_0^2 nL \geq \frac{1+\alpha}{1/4 - (1+\alpha)\chi/\lambda_0^2}.$$

(42)

For a numerical example we assume that the lasing nuclear transition has an energy of $E_0=10$ keV. The total losses of the gamma radiation with the corresponding wavelength of $\lambda_0 = 1.24$ Å, are mainly due to the photoelectric effect with atomic cross section within the range of $\chi = (10^{-21} \div 10^{-19})$ cm² (for example, $\chi = 1.14 \times 10^{-21}$ cm² for Al, 1.57×10^{-20} cm² for Fe, 4.32×10^{-20} cm² for Pb, 7.90×10^{-21} cm² for Rb, 5.55×10^{-21} cm² for Se, 2.82×10^{-20} cm² for W *etc.* [32]). Taking into account that $\chi/\lambda_0^2 \approx 6.5 \times (10^{-6} \div 10^{-4}) \ll 1$ we come from (42) to the requirement, $\varepsilon \geq \varepsilon_{min} = 4(1+\alpha)$, which gives $\varepsilon \geq 44$ for an internal electron conversion coefficient of $\alpha = 10$. In the case of the dimensionless parameter of $\varepsilon = 100$, the gamma-ray lasing medium might have the total concentrations of nuclei of $n=6.6 \times 10^{15}$ cm⁻³ or 1.3×10^{15} cm⁻³ for the lengths of amplification $L=1$ m or $L=5$ m, respectively.

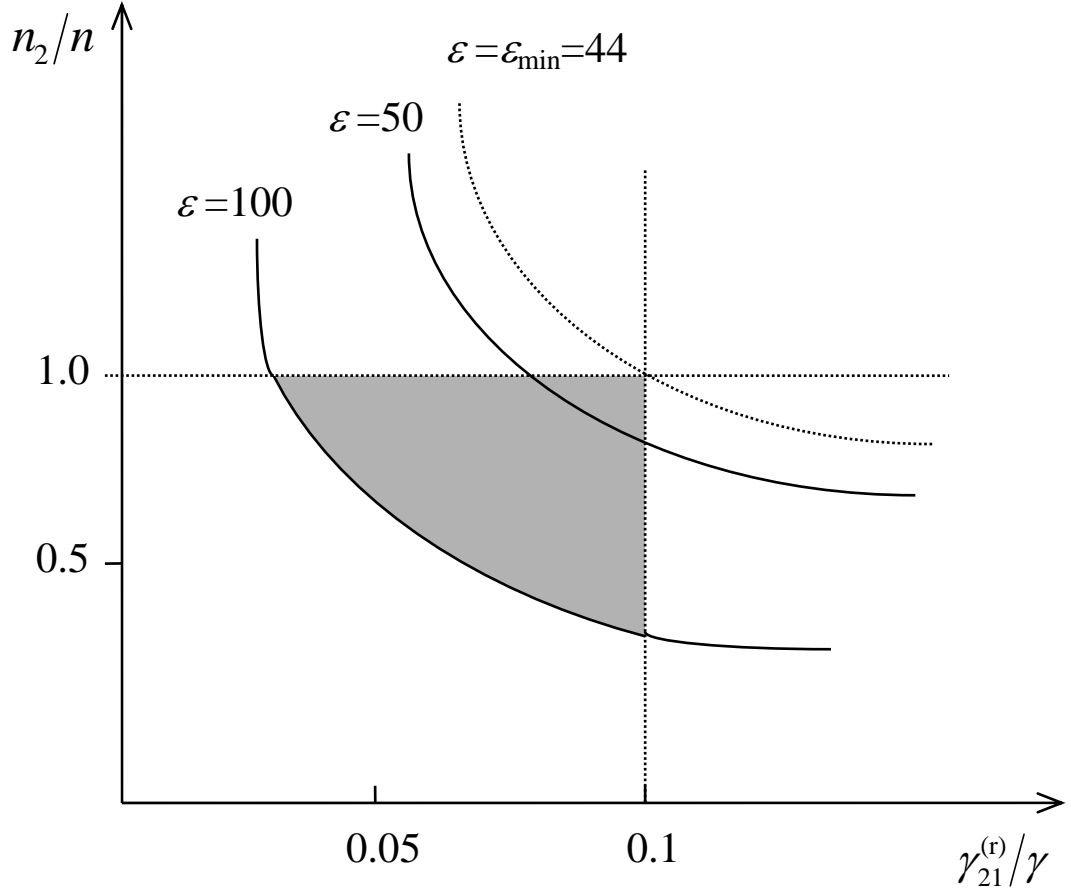Figure 3 shows the dependence of the relative concentration of excited nuclei, n_2/n, against the linewidth ratio $\gamma_{21}^{(r)}/\gamma$ with $\varepsilon = \lambda_0^2 nL$ taken as a parameter of a family of curves.

Gamma-ray lasing occurs for a set of nuclear medium parameters falling into a shaded domain in fig. 3 with the boundaries putted by the restrictions (40-42). In the case of $\varepsilon = \varepsilon_{min} = 4(1+\alpha)$ this domain consists of a single point (dashed curve in fig. 3), spreading gradually together with growth of ε above the minimum value. One can see from fig. 3 that the opportunity to use for gamma-ray lasing the lowest (for a given ε) concentration of excited nuclei,

$$n_{20}/n = \varepsilon_{min}/\varepsilon,$$

(43)

Fig. 3. *Relative concentration of excited nuclei, n_2/n, against the linewidth ratio $\gamma_{21}^{(r)}/\gamma$ with $\varepsilon = \lambda_0^2 nL$ taken as a parameter of a family of curves (the internal electron conversion coefficient is assumed to be $\alpha = 10$).*

is conditioned by the need of deep cooling of the atomic ensemble down to (or below) a temperature, T_0, for which the Doppler width γ_D of emission line is reduced to the decay width γ_2 of the upper laser level. This temperature expressed in μK can be estimated by

$$T_0 = \frac{0.41A}{(E_0 T_{1/2})^2},\qquad (44)$$

where A is the nuclear mass number, the gamma-ray transition energy, E_0, is in keV and the half-life of the upper lasing level, $T_{1/2}$, is in ns. For an ensemble of nuclei with A=100 and E_0=10 keV the estimate (44) gives T_0=13 μK for $T_{1/2} = 1$ ns and T_0=41 μK for $T_{1/2} = 0.1$ ns.

The higher temperatures of an atomic ensemble, the greater concentrations of excited nuclei are required and at the highest (for a given ε) temperature,

$$T_1 = T_0 \left(\varepsilon/\varepsilon_{\min}\right)^2,\qquad (45)$$

still suitable for development of the recoil assisted gamma-ray lasing, all the available nuclei of the atomic ensemble must be pumped into the excited state. In the case of α=10 and $\varepsilon = 100$ the estimate (45) gives T_1=5.2$T_0 = 67.6$ μK for $T_{1/2} = 1$ ns and T_1=213.2 μK for $T_{1/2} = 0.1$ ns. It is important to emphasize that the working temperatures of laser medium, ranging from T_0 to T_1, lie entirely within the temperature region, $T \leq E_{\mathrm{rec}}/k_B$, ($T \leq 6.15$ K for A=100 and E_0=10 keV) that allows a hidden inversion of state populations to occur.

X-ray pumping radiation

In attempting to propose any pump scheme (some key features of the pump scheme geometry can be seen in the fig. 2), it should be noted that the pumping radiation must interact with a previously-prepared cooled atomic ensemble. This is necessitated by the lifetime of the nuclear laser transition, which lies in the nanosecond and even

sub-nanosecond range, thereby precluding the reverse sequence of pumping and cooling operations. Therefore, the pump must not perturb the initial monokinetic quality of the cooled atomic ensemble. This imposes some restrictions on the pumping X-ray radiation.

First of all, it is important to note that the absorption of X-ray pump photons having the resonant energy E_0 and wave vectors directed parallel to the axis of atomic beam preserves initial monokinetic quality of the cooled nuclear medium, but through recoil only adds a new narrow line into the longitudinal velocity distribution. This extra line corresponds to a group of excited nuclei moving with the longitudinal velocities close to the nuclear recoil velocity $v_{rec} = E_0/Mc$. The velocity distribution of excited nuclei consisting this group is similar to that of the initial nuclear ensemble.

The pumping with a beam of photons having a broad energy distribution around the nuclear transition energy E_0 gives an additional velocity broadening of the line. This broadening is associated with dispersion of the nuclear recoil velocity,

$$\Delta v_{rec}^{(1)} = \hbar \gamma_D / Mc , \tag{46}$$

that appears because of the resonant photon absorption within the Doppler bandwidth γ_D. Accordingly, there is an additional Doppler broadening of the emission line

$$\gamma_{pump}^{(1)} = \frac{\omega_0}{c} \Delta v_{rec}^{(1)} = \frac{2E_{rec}}{E_0} \gamma_D , \tag{47}$$

associated with the nuclear velocity dispersion (46). It can be neglected, however, since $\gamma_{pump}^{(1)}$ is obviously far less then the initial Doppler linewidth γ_D.

It is important to emphasize, that in spite of an appreciable value of the nuclear recoil velocity, which is estimated to be 32 m/s for a nucleus with A=100 and $E_0 = 10$ keV, a pumped nucleus covers during its lifetime in excited state of 1 ns, a rather small distance 3×10^{-6} cm, which is less then the average distance between atoms for the concentrations up to 10^{16} cm^{-3}. Taking into account that the velocity of thermal atomic motion at T=10 μK is only 5 cm/s to be by three orders-of-magnitude less then the nuclear recoil velocity, it can be concluded that the inter-atomic collisions cannot destroy the monokineticity of the considered group of excited nuclei. This group creates a nuclear hidden inversion of states populations for a gamma-ray propagating opposite to the pump X-rays.

Angular divergence of the pumping X-ray radiation introduces an additional perturbation of the monokineticity into atomic medium. Providing that a pump photon beam is confined to a narrow cone with plane angle $\Delta\theta$ centered close to the axis of an atomic medium (see fig. 2), we obtain the estimates both for an additional dispersion of longitudinal velocities of the excited nuclei,

$$\Delta v_{rec}^{(2)} = \frac{E_0}{2Mc} \left(\frac{\Delta\theta}{2} \right)^2 , \tag{48}$$

and for an additional Doppler width

$$\gamma_{pump}^{(2)} = \frac{E_{rec}}{\hbar} \left(\frac{\Delta\theta}{2} \right)^2 . \tag{49}$$

To be unperturbed, the pump must meet the demand $\gamma_{pump}^{(2)} << \gamma_D$, which gives rise to the following requirement to the angular divergence of pumping radiation,

$$\Delta\theta << 4 \left(\frac{k_B T \ln 2}{E_{rec}} \right)^{1/4} . \tag{50}$$

For example, in the case of the nuclear medium with laser transition energy $E_0 = 10$ keV at the temperature T=10 μK, the pumping radiation must be concentrated into a cone with plane angle $\Delta\theta$ <<0.1 rad.

Among other processes introducing perturbations into the nuclear laser medium (coherent and incoherent X-ray scattering, X-ray absorption by atoms and nuclei, X-ray ionization of atomic electron shells, *etc.*), the atomic photoelectric absorption is likely to be the most destructive one. The recoil momentum acquired by a free excited nucleus in the process of atomic ionization knocks it out of the participants of the gamma-ray lasing process. Therefore, the pump can be considered as non-destructive if the rate of pumping into the upper laser level exceeds the rate of its devastation due to the photoelectric effect,

$$S\left(\lambda_0^2/4 \right) n_1 \gamma_{21}^{(r)} F(\omega_0) > n_2 \chi \Delta\omega_{pump} F(\omega_0) , \tag{51}$$

where $F(\omega_0)$ is the spectral photon flux density of pumping radiation on the nuclear transition frequency, $\Delta\omega_{pump}$ is the frequency bandwidth of pumping radiation and $S = (2J_2 + 1)/(2J_1 + 1)$ is the spin factor of the

nuclear transition. The demand of non-destructive pumping (17), with bearing in mind that $n_1 \approx n$, is consistent with the need to have concentrations of excited nuclei above the critical value of (43), only for the X-ray pumping radiation confined to a sufficiently narrow spectral bandwidth

$$\frac{\hbar \Delta \omega_{pump}}{E_0} < \frac{\ln 2}{32\pi} \frac{S}{(1+\alpha)^2} \frac{\lambda_0^3}{\chi c T_{1/2}} \varepsilon . \tag{52}$$

For a nuclear ensemble with $\varepsilon = \lambda_0^2 nL = 100$, $\lambda_0 = 1.24$ Å ($E_0 = 10$ keV), $\alpha = 10$, $S = 1$, $T_{1/2} = 10$ ps and $\chi = 10^{-22}$ cm^2 we obtain for the degree of monochromaticity of pumping radiation the value of $\hbar \Delta \omega_{pump} / E_0 <$ 4.3×10^{-4}.

Providing that the pumping X-ray radiation cannot saturate the population n_2 of the upper laser level, a condition that may be written as

$$F(\omega_0) < F_{sat}(\omega_0) = 4(1+\alpha)/\lambda_0^2 , \tag{53}$$

we can describe the growth of the concentration of excited nuclei by the relation

$$n_2 \approx nS(F/F_{sat})\left(1 - e^{-t/\tau}\right) \tag{54}$$

where $\tau = T_{1/2}/\ln 2$ gives the lifetime of the excited nuclear state. The critical concentration of excited nuclei (9) can be reached only with the help of intense pumping radiation of a high enough spectral photon flux density

$$F(\omega_0) \geq F_{cr}(\omega_0) = \frac{F_{sat}(\omega_0)}{S} \frac{\varepsilon_{min}}{\varepsilon} . \tag{55}$$

This equation expresses the critical spectral photon flux density $F_{cr}(\omega_0)$ in the units of cm^{-2}, whereas the same value expressed in photons/(cm^2 s keV) is given by $F_{cr}(\omega_0)/\hbar$ with $\hbar = 6.58 \times 10^{-19}$ keV s. For a nuclear ensemble with $\varepsilon = \lambda_0^2 nL = 100$, $\lambda_0 = 1.24$ Å, $\alpha = 10$ and $S = 1$ we obtain the value of $F_{cr}(\omega_0)/\hbar = 1.8 \times 10^{35}$ photons/(cm^2 s keV) that is consistent by order-of-magnitude with the estimates executed before for a number of selected nuclides

A practical question is what flux can be produced by modern sources of X-ray radiation. An average brightness of bremsstrahlung or synchrotron X-ray radiation consists 10^{12}-10^{14} photons/(mm^2 mrad^2 s 0.1% bandwidth). Radiation from undulators and wigglers at modern synchrotrons can produce a flux with average brightness of 10^{17}-10^{19} photons/(mm^2 mrad^2 s 0.1% bandwidth) at standard target positions in the energy range from 1 to 50 keV. Larger fluxes with average brightness up to 10^{23}-10^{26} photons/(mm^2 mrad^2 s 0.1% bandwidth) and peak brightness up to 10^{32}-10^{34} photons/(mm^2 mrad^2 s 0.1% bandwidth) can be supplied, in principle, by X-ray free electron lasers.

Intense fluxes are also possible from plasma sources of X-ray radiation. One way of creating a dense highly ionized plasma as a source of X-ray photons is by ablation of material exposed to pulses from terawatt, femtosecond optical lasers. Another possibility is the use of huge electric currents (tens millions amperes) to produce an ionized plasma, by vaporizing a spool-of-thread-sized array of hundreds wires. The currents produce powerful magnetic fields that surround the plasma, pinching it to densities and temperatures sufficient to generate intensive x rays. These processes are well-known to produce a large photon continuum on which is superimposed strong characteristic X-ray lines. The brightness of X-rays in the characteristic lines consists 10^{18}-10^{20} photons/(mm^2 mrad^2 s 0.01% bandwidth) to be orders-of magnitude larger then that of the continuum. The characteristic X-rays emitted from a hot plasma provide excellent opportunity to pump nuclei with the resonant transition energy.

At present, X-ray radiation of highest brightness that typically consists 10^{21}-10^{23} photons/(mm^2 mrad^2 s 0.01% bandwidth) is produced by X-ray plasma lasers. Unfortunately, they cover the range of very small photon energies from 0.03 to 0.3 keV.

Most significant radiation parameters of modern X-ray sources were collected in the Table 4. Instead of brightness we present here the estimates for spectral photon flux density of X-ray radiation expressed in the units of photons/(cm^2 s keV) more relevant to the analysis performed in this paper. These estimates are based on the assumption that X-rays hitting a target sample are confined to a cone with plane angle of 10 mrad.

Table 4. Modern sources of x-ray radiation

Source of x-ray radiation	Photon energy	Angular divergence	Degree of monochro-maticity	Spectral photon flux density
	(keV)	(mrad)		ph/(cm^2 s keV)
Plasma x-ray lasers	0.03-0.3	1-10	10^{-4}-10^{-5}	10^{31}-10^{32}
Laser plasma x-ray radiation (NIF, NOVA, NIKE)	0.1-20	10^3	10^{-3}-10^{-4}	10^{25}-10^{26}

Z-pinch plasma x-ray radiation (Sandia Z accelerator, Saturn)	0.1-20	10^3	10^{-3}-10^{-4}	10^{25}-10^{26}
X-ray free electron lasers (XFEL) (HASYLAB/DASY, LCLS/SLAC) *under construction*	5-10	10^{-2}-10^{-3}	10^{-3}-10^{-4}	10^{30}-10^{31}
Undulators, wigglers (HASYLAB/DASY, LCLS/SLAC) *under construction*	50-1000	0.1-1	10^{-2}-10^{-3}	10^{27}-10^{28}
Undulators, wigglers (ALS, SPEAR3)	1-10	1-10	10^{-2}-10^{-3}	10^{24}-10^{25}
Undulators, wigglers (APS, Spring-8, ESRF)	10-50	1-10	10^{-2}-10^{-3}	10^{23}-10^{24}
Bremsstrahlung x-ray radiation	1-300	10^3		10^{18}-10^{19}
Synchrotron x-ray radiation	1-20	1-10	10^{-1}-10^{-2}	10^{18}-10^{19}

One can see that the parameters requested for X-ray pumping radiation to develop gamma-ray lasing are far beyond that of available with current technology. First of all it concerns the degree of monochromaticity and the spectral photon flux density of X-ray radiation.

NUCLEAR GAMMA-RAY LASER WITH FABRY-PÉROT RESONATOR

Advent of Fabry-Pérot resonators for x-rays [33] opens up new possibilities for the development of new schemes for nuclear gamma-ray lasers. We consider a scheme for the recoil-assisted gamma-ray laser [34] which takes advantage of the resonator both for a pumping x-ray and for a stimulated gamma radiation.

Fig. 4 shows a Fabry-Pérot resonator built as a system of two sapphire crystal plates playing the role of Bragg back-reflecting mirrors for x-rays. The resonator cavity is filled with a gas of active nuclei. A pump x-ray, entering the cavity through the first mirror, bounces back and forth between the mirrors losing energy due to emerging radiation through the crystal mirrors and due to nuclear resonance absorption followed by excitation of the nuclei into an upper level. At a high enough concentration of the excited nuclei, a gain of stimulated gamma quanta can attain an acceptable value sufficient to beginning of gamma-ray lasing. It is important to emphasize, that at low temperatures, the nuclear recoil in the absorption or emission of gamma-photons ensures establishing a hidden inversion [34] of the nuclear state populations. As a result, a gain of stimulated gamma quanta may occur without excess of the number of excited nuclei over the number of unexcited ones.

In the scheme under consideration, the x-ray resonator serves as a means for accumulation of the pump energy inside the cavity. Also, the use of the resonator could enhance the pump efficiency due to an increase of the time of interaction between the pumping radiation and nuclei. At the same time, Fabry-Pérot resonator provides the opportunity for an efficient enlarging the length of interaction of stimulated gamma-radiation with active medium. Naturally, the x-ray cavity should meet the resonance condition that allow a standing wave of the stimulated gamma radiation to occur in the resonator.

In the paper we formulate a set of requirements to the pump x-ray radiation and to the nuclear medium crucial to achieving the threshold condition for the recoil assisted gamma-ray lasing. Comparison with a single-pass regime of the self-amplified spontaneous gamma emission is made.

Fabry-Pérot resonator for x-rays

Fabry-Pérot resonators are standard instruments in visible-light optics and laser physics. The main components of the Fabry-Pérot resonator are two highly reflecting plane mirrors parallel to each other. However, optical mirrors for the visible light are inefficient for x rays. Producing x-ray mirrors of high reflectivity is one of the main technical challenges in the realization of x-ray resonators.

Steyerl and Steinhauser [35] have proposed the idea of Fabry-Pérot resonator for x-rays with replacing the reflection from optical mirrors by the Bragg back reflection from silicon single crystals. Also, they have considered the problem of parasitic Bragg reflections occurring in silicon crystals at exact normal incidence of x-rays to reflecting atomic planes. They have pointed out that these parasitic reflections would reduce drastically the mirror reflectivity and aggravate the performance of the proposed device.

Cusatis et al. [36] were the first to observe x rays reflected backwards from a silicon (111) plate at the energy of 1.9 keV. Soon afterwards Kikuta et al. [37] reported the observation of suppression of the x-ray reflectivity at near normal incidence to silicon (991) crystal plates. It has been ascertained that, upon approaching exact backscattering, the reflectivity goes down and at exact normal incidence the parasitic diffraction effects may completely suppress the reflectivity in the back reflection channel. A similar drastic suppression of the reflectivity have been observed also in many other experiments (see [38] with extensive bibliography) on Bragg back reflection from different atomic planes of silicon crystals. Theoretical investigation [39] of this problem reveals this feature in Bragg backscattering for all the crystals with cubic symmetry.
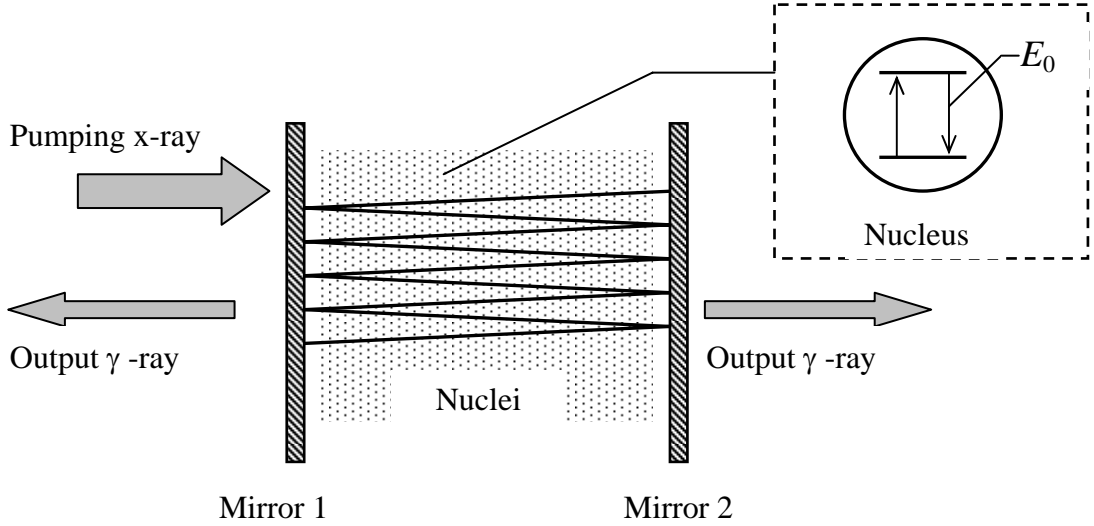
Fig. 4. Scheme of a gamma-ray laser with Fabry-Pérot resonator, which takes advantage of the resonator both for a pumping x-ray and for stimulated gamma-rays.

A practical issue of selecting materials for Bragg back-reflection mirrors have been made by Shvyd'ko and Gerdau [40]. They have noted that crystals with lower than silicon crystal symmetry allows one to avoid the problem of parasitic Bragg reflections. They have proposed sapphire, the crystal with rhombohedral lattice, for the role of normal incidence mirrors for x-ray resonators. Already first experiments with sapphire (α-Al$_2$O$_3$) single crystals [41] have demonstrated exact backscattering of high reflectivity for 14.4 keV Mössbauer radiation. Then, reflections with a peak reflectivity of more than 90% have been observed over a broad x-ray radiation spectral range from 5 to 35 keV. At low temperatures the high reflectivity range extends even more up to 45 keV. Performed comprehensive studies of Bragg diffraction in sapphire [38] definitively indicate that sapphire crystals are more suitable for normal incidence x-ray mirrors than silicon crystals.

The first attempt [42] to build an x-ray resonator by using Bragg backscattering from silicon single crystals confirms completely this statement. Though multiple Bragg reflections from the crystal mirrors have been observed, the intensity of reflected beams was very low, because of the low reflectivity of silicon crystals arising from parasitic Bragg reflections. As a result, after a few bounces between the resonator mirrors most of the x-ray radiation disappears.

Recently [33], direct evidences to a successful operation of a resonator for 14.3 keV x-rays with two back-reflecting sapphire crystal mirrors have been demonstrated. When the x-ray energy coincides with the crystal reflectivity maximum, more than 60 successive reflections have been observed in the x ray bouncing back and forth between the mirrors.

The performance of the x-ray resonator is similar to that of the optical Fabry-Pérot resonator. Both show a fine resonance structure in the transmission and reflection dependence. X-ray radiation entering a resonator through the first mirror experiences multiple reflections between the mirrors before it escapes through one of them. Like the multiple-beam interference effect underlying the theory of optical Fabry-Pérot resonators [43], the derivation of the expressions for the transmissivity and reflectivity of an x-ray resonator [38] uses the same geometrical approach based on summation of the amplitudes of all possible waves multiply-reflected from the crystal mirrors. Similar approach allows one to obtain expressions for the amplitudes of the resonance electromagnetic waves (modes) excited by an external x-ray radiation inside a Fabry-Pérot resonator cavity.

Fig. 5 is a schematic diagram showing the successive amplitudes of the electromagnetic waves reflected from and transmitted through the resonator mirrors spaced a distance d apart. The total amplitudes E_1 and E_2 of the waves incident inside the resonator on the first and on the second mirrors, respectively, are the sum of all partial amplitudes of multiply-reflected waves. The summation of the corresponding geometrical series gives the following expressions

$$E_1 = \frac{r\bar{t}E_{\text{ext}}e^{2ikd}}{1-r^2e^{2ikd}} \text{ and } E_2 = \frac{\bar{t}E_{\text{ext}}e^{ikd}}{1-r^2e^{2ikd}}, \tag{56}$$

where E_{ext} is the amplitude of a beam from an external source of radiation, $k = 2\pi/\lambda$ is the radiation wave number, r is the amplitude-reflection coefficients of the mirrors for a wave traveling from the cavity to the surrounding medium and $\bar{t}$ is the amplitude-transmission coefficient for a wave traveling into the cavity from the surrounding medium. For an empty resonator we can make no difference between the transmission (or reflection) coefficients for a wave traveling from or into the cavity.

Squaring the wave amplitudes E_1 and E_2 (1) at each mirror, we obtain the relations between the intensities P_1 and P_2 of the oppositely traveling waves inside resonator and the intensity P_{ext} of the external beam

$$P_1 = \frac{RTP_{\text{ext}}}{(1-R)^2 + 4R\sin^2(\varphi/2)} \quad \text{and} \quad P_2 = \frac{TP_{\text{ext}}}{(1-R)^2 + 4R\sin^2(\varphi/2)} \,, \tag{57}$$

where $R = |r|^2$ and $T = |t|^2$ are the mirror flux-reflection and transmission coefficients (defined as the ratio of the reflected or transmitted flux of radiation to the incident flux), $\varphi = \arg(r^2) + 2kd$ is the phase (it is termed the Airy phase) acquired by a beam in a round-trip circulation inside the resonator cavity, with the first term, $\arg(r^2) = 2\arg r$, being the sum of the phase jumps on reflection from each mirror.

Despite of the similarity between formulas describing the performance of an x-ray and optical Fabry-Pérot resonator, one should have in mind a number of significant differences [38]. First of all it concerns the Airy phase. The expression for the x-ray Airy phase differs from the above expression known from the theory of the optical Fabry-Pérot resonators. There are some additional terms in the x-ray Airy phase appearing due to internal structure of the crystal mirrors. The energy, incidence angle and temperature dependence of the x-ray Airy phase is expressed via the physical parameters included in these terms. Secondly, the crystal mirror reflection coefficient takes significant values only within the range of the Bragg back reflection peak and varies rapidly with x-ray energy, incidence angle, crystal temperature, *etc.*

The spectral width of the Bragg reflection peak for a crystal mirror is the reciprocal of the effective number of diffracting atomic planes contributing to Bragg diffraction. The higher the x-ray energy, the larger is the extinction length and therefore the smaller is the spectral width of the peak. Photo-absorption in the crystal mirrors and finite crystal thickness reduce the peak reflectivity and make the spectral curve of the reflectivity more broad. For example, according to Bragg diffraction dynamical theory calculations [1, 6], a peak reflectivity of 0.85 can be achieved within the region of 17.2 meV for 14.3 keV x-rays by using a 60μm thick sapphire crystal.
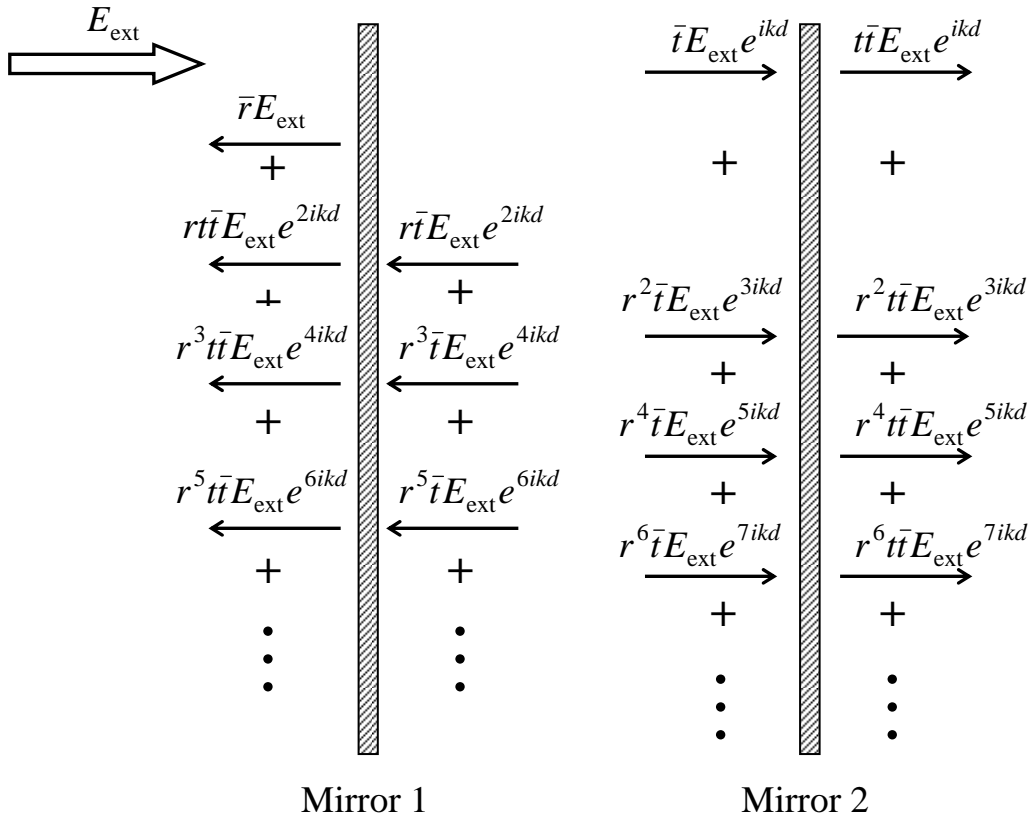
Fig. 5. *Schematic diagram showing the amplitudes of the waves reflected from and transmitted through the resonator mirrors.*

The intensities P_1 and P_2 (57) are periodic functions of the Airy phase φ and have sharp maxima when the phase φ is an integer multiple of 2π. Bearing in mind this resonance condition, one can conclude that in the case of excitation of an x-ray resonator with a broadband x-ray radiation, the electromagnetic field in the cavity can be described as a number of the resonant 'standing' waves with different wavelengths. Each of these 'standing' waves, termed as a mode of the resonator, is specified by an integer of $m = \varphi/2\pi$. Spectral photon flux density P in a mode of the resonator is the sum of the oppositely traveling fluxes constituting the mode. It is related with the spectral photon flux density P_{ext} of the external x-ray radiation with the corresponding wavelength by the expression

$$P = P_1 + P_2 = \frac{(1+R)TP_{\text{ext}}}{(1-R)^2}. \tag{58}$$

One can see that in the absence of absorption in the crystal mirrors, when $R+T=1$, the spectral photon flux density in a resonator mode scales as the external spectral photon flux density multiplied by $(1+R)/(1-R)$. For the crystal mirrors with $R=0.9$ the enhancement factor could reach the value of 20.

The decay of a mode due to emerging radiation through the resonator mirrors can be described by an exponential function $\sim \exp(-t/\tau)$. Taking into account that during the time of a round-trip circulation of a beam in the cavity, $t = 2d/c$, the beam intensity is decreased by a factor of R^2, we can write the expression for the lifetime of an x-ray photon inside the cavity as $\tau = (d/c)\ln^{-1}(1/R)$. This gives for the full energy width of a mode at half-maximum, Γ, the following estimate $\Gamma = \hbar/\tau = (\hbar c/d)\ln(1/R)$. Since the energy separation between the adjacent modes is determined by $\Delta E_{\text{f}} = \pi\hbar c/d$ (it is termed the free spectral range of the resonator), one can see that $\Delta E_{\text{f}} >> \Gamma$ at a closed to unit reflectivity R.

For a gap between mirrors of 5 cm the free spectral range is 12.4 μeV. With the reflection coefficient of $R=0.9$, the energy bandwidth of each modes will be 0.42 μeV, so that the modes of the resonator are well separated from each other on the energy scale. The lifetime of an x-ray photon in a mode of the resonator can be estimated as $\tau = 1.6$ ns. This corresponds to an order-of-magnitude enlargement of the path of an x-ray due to multiple reflections between mirrors. The number of modes exited by an external broadband radiation is determined by the spectral width of the high reflectivity region of the mirrors. For 10 keV x-rays this width is typically 10 meV, so we may have more than 800 modes being excited. This value can be reduced by monochromatization of the x-ray radiation to a narrow band less than 10 meV.

Nuclear hidden inversion

An important feature of radiative processes in free nuclei is the nuclear recoil due to energy and momentum conservation in the emission or absorption of gamma quanta. The recoil effect together with the Doppler effect fix the energy of a resonance photon,

$$E = E_0 + E_0 \text{v}/c \pm E_{\text{rec}}, \tag{59}$$

that could be absorbed (sign +) or emitted (sign -) by a nucleus moving with the velocity projection v on the photon propagation direction. The recoil kinetic energy E_{rec} acquired by a nucleus with mass M and the nuclear transition energy E_0 is $E_{\text{rec}} = E_0^2/2Mc^2$.

After being absorbed by a nucleus, an x-ray photon of pumping radiation with the energy E (4) transfers its momentum, E/c, to the nucleus. The recoil velocity acquired by the nucleus, additionally to the initial nuclear velocity, is

$$\text{v}_{\text{rec}} = \frac{E}{Mc} \approx \frac{E_0}{Mc}. \tag{60}$$

The recoil velocity determines, with the help of eq. (59), the energy of a photon that could be emitted by the pumped nucleus. This energy is dependent on the photon propagation direction. The co-propagated emitted and absorbed photons have the same energy $E = E_0 + E_0\text{v}_0/c + E_{\text{rec}}$, while the energy of a back-emitted photon is $E = E_0 - E_0\text{v}_0/c - 3E_{\text{rec}}$, where v_0 is the projection of the initial nuclear velocity on the direction of pumping x-ray.

Dispersion of the initial nuclear velocities v_0 leads to the Doppler broadening of the emission and absorption lines. One can see that the centers of the lines are shifted by the energies of $-3E_{\text{rec}}$ and $+E_{\text{rec}}$ relative to the nuclear transition energy E_0 and by the energy of $\Delta E = 4E_{\text{rec}}$ relative to each other (Fig. 6). A critical conclusion may be drawn from the presence of this shift: if the shift ΔE exceeds the Doppler linewidth, the backward emitted photons cannot be resonantly absorbed by unexcited nuclei but they are still capable to stimulate gamma emission of the excited nuclei. This allow a gain of stimulated gamma quanta to occur without total nuclear population inversion. A hidden inversion of the nuclear state population [2] is established in a particular energy range for a gamma-ray propagating oppositely to the direction of pumping x-ray.

The concentration n_2 of excited nuclei need not be greater than the concentration n_1 of unexcited ones. Indeed, it is sufficient to call for the gain of emitted gamma quanta to be greater than the losses of these quanta due to the non-resonant absorption by unexcited nuclei. This gives the requirement

$$\frac{n_2}{n_1} > S\frac{g_{\text{L}}(\Delta E)}{g_{\text{D}}(0)} \approx S(\pi\ln 2)^{-1/2}\frac{\Gamma_{\text{L}}}{\Gamma_{\text{D}}}\left(\frac{\Gamma_{\text{D}}}{2\Delta E}\right)^2 \tag{61}$$

with assumption that the Doppler broadening of the emission line, described by the function of $g_{\text{D}}(E)$ with the energy width Γ_{D}, dominates over Lorentz broadening described by the function of $g_{\text{L}}(E)$ with the energy width of Γ_{L}, that is $\Gamma_{\text{D}} > \Gamma_{\text{L}}$, and $S = (2J_2+1)/(2J_1+1)$ is the spin factor of a nuclear transition with angular momentum quanta J_2 and J_1 of the upper and lower nuclear states. We took into account in (61) that the wings of the nuclear

absorption line are described by the Lorentz rather than the Doppler function, since in the absorption energy domain under consideration, $|E - E_0 - E_{rec}| \gg \Gamma_D$, the Doppler function goes down far more faster than that of the Lorentz. Therefore, under condition of $\Delta E = 4E_{rec} \gg \Gamma_D$, it is appropriate to neglect the contribution of inhomogeneous Doppler broadening to the non-resonant absorption of photons with the energy of $E_0 - 3E_{rec}$.
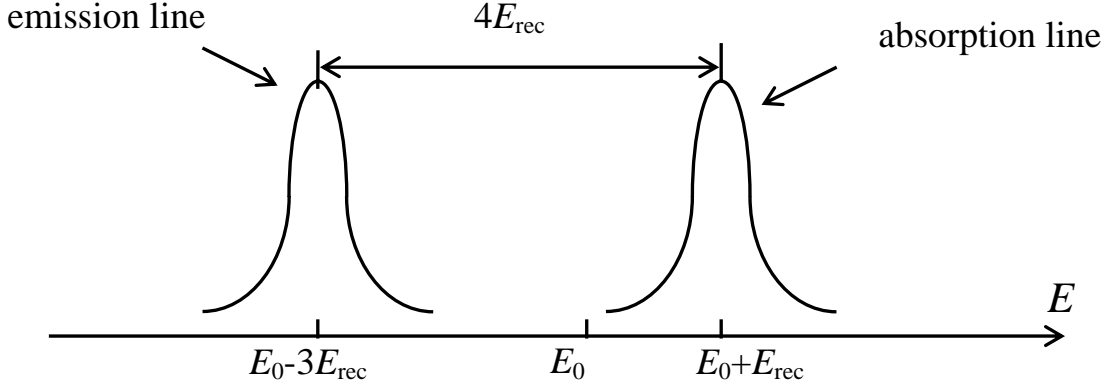

Fig. 6. Spectral splitting of emission and absorption lines in a cooled nuclear ensemble

The concentration n_2 of excited nuclei need not be greater than the concentration n_1 of unexcited ones. Indeed, it is sufficient to call for the gain of emitted gamma quanta to be greater than the losses of these quanta due to the non-resonant absorption by unexcited nuclei. This gives the requirement

$$\frac{n_2}{n_1} > S \frac{g_L(\Delta E)}{g_D(0)} \approx S(\pi \ln 2)^{-1/2} \frac{\Gamma_L}{\Gamma_D} \left(\frac{\Gamma_D}{2\Delta E} \right)^2 \tag{61}$$

with assumption that the Doppler broadening of the emission line, described by the function of $g_D(E)$ with the energy width Γ_D, dominates over Lorentz broadening described by the function of $g_L(E)$ with the energy width of Γ_L, that is $\Gamma_D > \Gamma_L$, and $S = (2J_2 + 1)/(2J_1 + 1)$ is the spin factor of a nuclear transition with angular momentum quanta J_2 and J_1 of the upper and lower nuclear states. We took into account in (61) that the wings of the nuclear absorption line are described by the Lorentz rather than the Doppler function, since in the absorption energy domain under consideration, $|E - E_0 - E_{rec}| \gg \Gamma_D$, the Doppler function goes down far more faster than that of the Lorentz. Therefore, under condition of $\Delta E = 4E_{rec} \gg \Gamma_D$, it is appropriate to neglect the contribution of inhomogeneous Doppler broadening to the non-resonant absorption of photons with the energy of $E_0 - 3E_{rec}$.

It is clear, that the use of hidden inversion creates a need for a considerable reduction in the Doppler broadening to the extent sufficient to a radical suppression of an overlap between emission and absorption lines. This may be accomplished by cooling of the nuclear ensemble down to a temperature $T \ll E_{rec}/k_B$, where $k_B = 8.62 \times 10^{-2}$ meV K^{-1} is the Boltzmann constant. Taking into account that for an ensemble of nuclei with the mass number of A the recoil energy can be estimated by $E_{rec} = 0.53 E_0^2/A$ (with E_{rec} in meV when the nuclear transition energy, E_0, is expressed in keV), we come to the following demand to the temperature $T \ll 6.2$ K, when $E_0 = 10$ keV and $A = 100$.

Far more deep cooling should be required in order to attain a gain of stimulated gamma quanta sufficient to beginning of gamma-ray lasing. The appropriate temperatures may approach the temperature T_0 for which the Doppler width of emission line, $\Gamma_D = 0.71 E_0 \sqrt{T/A}$ (with Γ_D in meV, when E_0 is in keV and temperature T in K), is reduced to the decay width of the upper nuclear laser level. This temperature expressed in μK can be estimated by

$$T_0 = \frac{0.41A}{(E_0 T_{1/2})^2} , \tag{62}$$

where the nuclear transition energy, E_0, is in keV and the half-life of an upper lasing level, $T_{1/2}$, is in ns. For an ensemble of nuclei with A=100 and E_0=10 keV the estimate gives T_0=13 μK for $T_{1/2} = 1$ ns and T_0=41 μK for $T_{1/2} = 0.1$ ns. This temperature region could be reached by present-day techniques [12] for deep cooling of atomic ensembles by the light pressure of optical lasers.

Nuclear pumping with x-ray radiation

A pump x-ray with the spectral photon flux density P_{ext}, entering a resonator cavity, experiences multiple reflections back and forth between the crystal mirrors. Due to the multiple-beam interference effect, the spectral photon flux density in a pumping mode of the resonator is increased with time. It could reach the value of $[(1+R)/(1-R)]P_{ext}$ during the photon storage time τ in the mode. However, the growth of the spectral photon flux density is restricted by emerging radiation through the crystal mirrors, by nuclear resonance absorption of the x-ray photons from the mode (the pumping mode frequency falls into the band of nuclear absorption) and by non-resonance photon losses due to the photoelectric effect, Compton scattering, *etc*. The dynamics of pumping of a nuclear ensemble inside the resonator cavity could be described by the following rate equations for the spectral photon flux density P_{pump} (measured in the units of photons/(cm^2 s keV)) of the pumping mode and for the concentration n_2 of excited nuclei

$$\frac{dP_{pump}}{dt} = \frac{[(1+R)/(1-R)]P_{ext} - P_{pump}}{\tau} - c\sigma_{abs}n_1 P_{pump} - c\chi n P_{pump} \tag{63}$$

$$\frac{dn_2}{dt} = -\frac{n_2 \ln 2}{T_{1/2}} + \sigma_{abs} n_1 \Gamma P_{pump}, \tag{64}$$

where n and n_1 are the total and unexcited nuclear concentrations, respectively, c is the speed of light,

$$\sigma_{abs} = \frac{S}{1+\alpha}\frac{\lambda_0^2}{4}\frac{\Gamma_n}{\Gamma_D} \tag{65}$$

is the nuclear resonance absorption cross section, S and α are the spin factor and internal electron conversion coefficient of the nuclear transition with wavelength λ_0 and decay width $\Gamma_n = \hbar \ln 2/T_{1/2}$, and χ is the total atomic cross section of non-resonance photon losses from the pumping mode. In Eq. (64) we assume that the energy bandwidth of the mode, $\Gamma = \hbar/\tau$, is less than the width Γ_D of the Doppler broadened nuclear absorption line, so that the total photon flux density of the mode, ΓP_{pump}, contributes to the process of nuclear pumping.

Among a variety of the non-resonant photon losses from the pumping mode, the atomic photoelectric absorption is considered to be the most intensive one. The photo-absorption atomic cross section [45] is within the range of $\chi = (10^{-21} \div 10^{-19})$ cm^2 for the photons with energy 10 keV. One can see that the rate of photo-absorption, $c\chi n P_{pump}$, is much less than the rate of photon losses, P_{pump}/τ, due to emerging radiation through the resonator mirrors up to the nuclear concentration 10^{16} cm^{-3}. Therefore this term in the equation (64) may be neglected.

Since the lifetime τ of a photon in the pumping mode is compared or even exceeds the half-life $T_{1/2}$ of active nuclei on the upper level ($\tau = 1.6$ ns for d=5 cm and R=0.9, while $T_{1/2}$ <1 ns), we can use a steady-state solution of the rate equations in order to estimate the concentration of pumped nuclei. With assumption that the concentration of unexcited nuclei n_1 is close to the total nuclear concentration n, we obtain

$$n_2 = \frac{1+R}{1-R}\frac{\Gamma}{\Gamma_n}\frac{c\tau n\sigma_{abs}}{1+c\tau n\sigma_{abs}}\frac{\Gamma P_{ext}}{c}. \tag{66}$$

Velocity distribution of the nuclei is of special interest. Fig. 7 shows the concentrations of excited and unexcited nuclei versus the projection of the nuclear velocity on the direction of an externally-produced pumping x-ray. The absorption of x-ray photons from the pumping mode of resonator creates, through recoil, two extra lines in the velocity distribution. These lines correspond to two groups of excited nuclei moving with the nuclear recoil velocity v_{rec} (60) in the opposite directions. The velocity distribution of excited nuclei is characterized by the width of $\Delta v = c\Gamma_n/E_0$, since the energy width of the pumping mode is less than the nuclear decay width ($\Gamma = \hbar/\tau$ =0.42μeV for d=5 cm and R=0.9, while $\Gamma_n = \hbar \ln 2/T_{1/2}$ =0.46μeV for $T_{1/2}$ =1ns, Γ_n = 4.6μeV for $T_{1/2}$ =0.1ns). The concentration of pumped nuclei in the groups are equal approximately to a half of n_2 (66). Accordingly, two holes burnt out by the pumping x-ray radiation are appeared in the curve of the velocity distribution of unexcited nuclei.

It is important to note, that in spite of an appreciable value of the nuclear recoil velocity (60), which is estimated to be 32 m/s for a nucleus with A=100 and $E_0 = 10$ keV, a pumped nucleus covers, during its lifetime of 1 ns in the excited state, a rather small path of 3×10^{-6} cm, which is less than the average distance between atoms up to the concentration 10^{16} cm^{-3}. Taking into account that the velocity of thermal atomic motion at T=10 μK is only 5 cm/s to be by three orders-of-magnitude less than the nuclear recoil velocity, one can be certain that the inter-atomic collisions cannot destroy the monokineticity of the considered groups of excited nuclei. Each of these groups of

pumped nuclei creates a hidden inversion of the states populations for a gamma-ray propagating oppositely to the recoil nuclear velocity of the group.
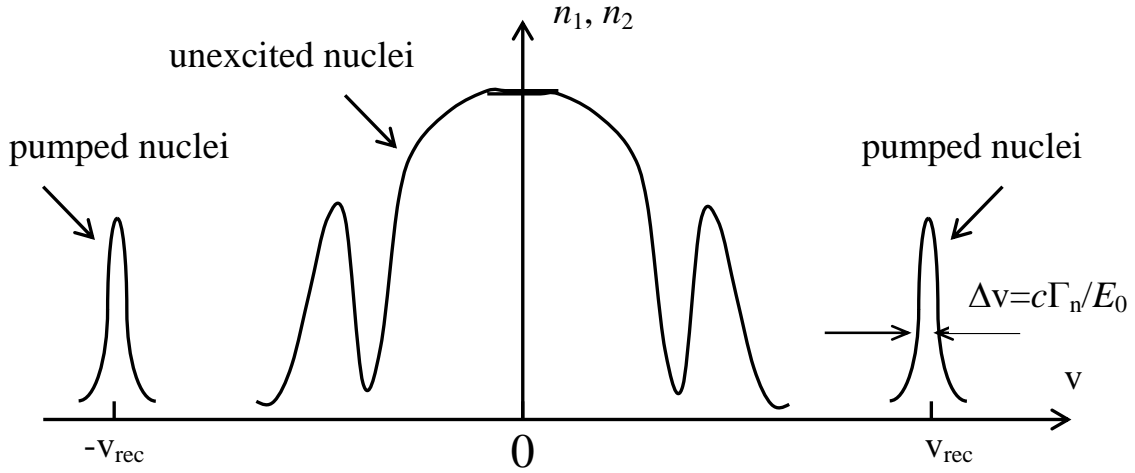

Fig. 7. *Concentrations of excited and unexcited nuclei versus the projection of the nuclear velocity on the direction of an externally-produced pumping x-ray.*

Threshold condition for gamma-ray lasing

Fig. 8 shows on the energy scale the Doppler broadened absorption line of a nuclear ensemble together with several modes of the resonator including the x-ray pumping mode with resonance energy falling into the band of nuclear absorption. The gamma emission line for the photons propagating oppositely to the recoil velocity of the pumped nuclei is shifted away from the pumping mode by the energy of $\Delta E = 4E_{rec}$.
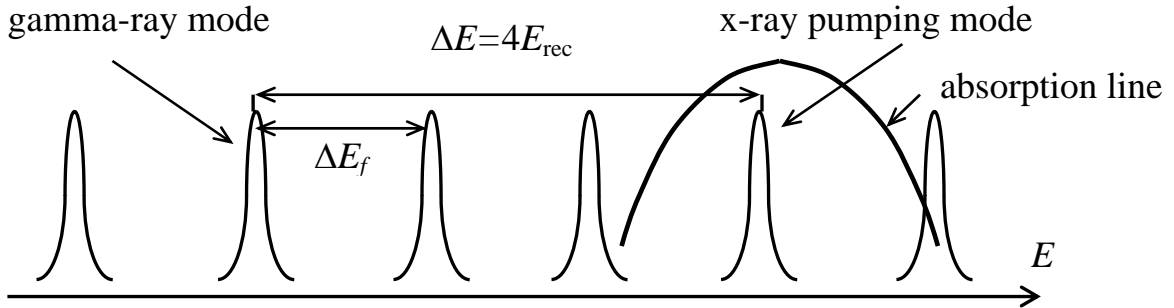
Fig. 8. *Several modes of the Fabry-Pérot resonator including the gamma-ray mode and the x-ray pumping mode with the resonance energy falling into the Doppler broadened absorption line of a nuclear ensemble.*

Energy width of this line is equal to the decay width of nuclear transition Γ_n, since the width of pumping mode Γ is less than Γ_n. Naturally, the concept of gamma-ray laser implies that the nuclear emission line should coincide with one of the mode of the resonator. To do so, the energy shift $\Delta E = 4E_{rec}$ has to be equal to an integer multiple of the resonator free spectral range $\Delta E_f = \pi \hbar c / d$. With $E_{rec}=0.53$ meV (for a nucleus with the mass number 100 and the transition energy 10 keV) this gives for the distance d between the resonator mirrors a number of acceptable values: 1.46, 2.92, 4.39, 5.85 cm. It is important to emphasize, that both the x-ray pumping and the gamma-ray modes of the resonator are within the spectral region of high reflectivity of the crystal mirrors, which is typically 15-20 meV for the photons with energy 10 keV.

Each of the traveling waves, constituting the standing wave of stimulated gamma radiation in the resonator, interacts separately with its own group of the pumped nuclei, that moves oppositely to the wave propagation direction. Stimulated gamma emission of the pumped nuclei keeps the gamma-ray mode in an excited state. Simultaneously, there are photon losses from this mode due to emerging radiation through the crystal mirrors of the

resonator and due to non-resonant scattering of the stimulated radiation by the nuclear medium. The rate equation for the spectral photon flux density P_γ of stimulated gamma radiation in the mode can be written as

$$\frac{dP_\gamma}{dt} = -\frac{P_\gamma}{\tau} + c\sigma_{st} n_2 P_\gamma - c\chi n P_\gamma, \qquad (67)$$

where $\sigma_{st} = \lambda_0^2 / 4(1+\alpha)$ is the cross section for stimulated gamma emission.

Since the nuclear population difference under condition of hidden inversion is merely equal to the concentration of excited nuclei n_2, the rate equation (67) does not contain the term with concentration of unexcited nuclei n_1, referring to the resonant nuclear absorption. Just like in eq. (63), the rate of photo-absorption, $c\chi n P_\gamma$, is much less than the rate of gamma-photon losses, P_γ/τ, due to emerging radiation through the resonator mirrors, so that this term in the equation (67) may be neglected.

The threshold condition, $dP_\gamma/dt = 0$, for beginning of gamma-ray lasing means that the gain of stimulated quanta in the gamma-ray mode compensates all kind of their losses from this mode. This gives the threshold concentration of pumped nuclei $n_2^{(th)} = 1/(c\tau\sigma_{st})$ and, with the help of eq. (66), the threshold spectral photon flux density of pumping x-ray radiation

$$P_{ext}^{(th)} = \frac{1-R}{1+R} \frac{\Gamma_D}{\Gamma} \frac{4(1+\alpha)}{\hbar\lambda_0^2} \frac{1 + (\Gamma_n/\Gamma_D) Sc\tau n \lambda_0^2 / 4(1+\alpha)}{Sc\tau n \lambda_0^2 / 4(1+\alpha)}. \qquad (68)$$

Assuming the ratio $\Gamma_D/\Gamma \sim \Gamma_n/\Gamma_D \sim 1$, spin factor $S\sim1$, $\lambda_0 = 1.24$ Å (E_0=10 keV), R=0.9, α=10, we come to the estimate $P_{ext}^{(th)} = 2.2 \times 10^{34}$ photons/(cm^2 s keV), which is by an order-of-magnitude less than that of obtained before [46] for the scheme of gamma-ray laser based on the self-amplified spontaneous gamma emission principle.

RESULTS

Two attractive schemes for a gamma-ray laser have been considered. Both schemes take advantage a hidden inversion of nuclear state populations which appears in cooled nuclear ensembles due to assistance of the nuclear recoil in emission and absorption of gamma quanta. Establishing a hidden inversion allows a gain of stimulated gamma radiation to occur in a particular frequency range without excess of the number of excited nuclei over the number of unexcited nuclei and results in a considerable reduction in the threshold intensity of x-ray pumping radiation.

First scheme is based on the energy-storage capability of isomeric nuclei. The excitation energy of such nuclei is stored for a long time in a metastable state and then may be released through an emission of gamma-rays in two step trigger transitions from the isomer. At the first step, the nucleus is exited from initial isomeric state to reach an upper intermediate state by absorption of an incident photon of driving radiation. Then, the intermediate state decays promptly to the ground state with emission of a gamma photon. The two step de-excitation of an isomer can be regarded as the nuclear resonance anti-Stokes scattering with up-conversion of incident radiation into a flux of spontaneous or stimulated gamma photons. We have estimated the gain coefficient which is expressed through the cross section for anti-Stokes scattering with conversion into stimulated gamma-quanta. Then we have formulated threshold condition for beginning of gamma-ray lasing process and estimated the threshold photon flux density of pumping radiation.

Second scheme of gamma-ray laser uses the opportunity, offered again by the nuclear recoil, to pump the first excited state of a nucleus directly from its ground state. The two-level pump scheme, totally forbidden in typical optical lasers, becomes possible now due to establishing a hidden inversion of the nuclear state populations. The process of amplification can be classified as the nuclear resonance fluorescence scattering of the pump radiation into a flux of stimulated gamma photons. As a result of such approach we have obtained the estimation for the threshold photon flux density of pumping radiation.

For both schemes, we have explored two regimes of laser generation: self-amplified spontaneous gamma emission without any mirrors or reflecting gratings and a gamma-ray lasing in a Fabry-Pérot resonator with Bragg back-reflecting mirrors. Advent of x-ray Fabry-Pérot resonators built of two sapphire single crystals serving as Bragg back-reflecting mirrors opens up new possibilities for the development of new approaches to a nuclear gamma-ray laser. We have proposed a scheme which takes advantage of the resonator both for x-ray pumping radiation and for output stimulated gamma-rays. The threshold conditions have been formulated for this scheme, which include the threshold concentration of pumped nuclei and the threshold spectral photon flux density of the external pumping radiation. We have estimated also the temperature of active nuclear ensemble required for establishing a hidden population inversion. The estimated threshold pump flux turns out to be by an order-of-magnitude less than that of appeared in the similar scheme based on the self-amplified spontaneous gamma emission principle.

All the estimates are based on the rigorous quantum mechanical calculations made in the project. We have obtained and presented expressions for the cross-sections for the recoil accompanied anti-Stokes scattering with up-conversion of the incident pumping radiation into a flux of spontaneous or stimulated gamma photons and for the nuclear resonance fluorescence scattering of the pump radiation into a flux of spontaneous or stimulated gamma photons. We have subjected the perturbation theory, used for the above calculations, to some generalization in order to include into consideration the effect of nuclear recoil. We have developed the work formulae which allow us to estimate the main parameters of gamma-ray lasing process for the selected nuclides most suitable in the primary demonstrative experiment (threshold flux of pumping radiation, temperature of active medium, concentration of active nuclei, conditions for establishing of hidden inversion, *etc.*)

We have discussed in the project the problem of identifying the most promising nuclides for an active medium of gamma-ray laser with hidden inversion of nuclear state populations and the pump capabilities of available sources of x-rays. We have formulated a set of requirements both to the internal structure of an active nucleus and to its atomic electron shell crucial to the recoil assisted gamma-ray lasing with hidden inversion of the nuclear state populations.

True identification of the best isomers for the anti-Stokes scheme of gamma-ray laser should be based on a complex weighing a variety of nuclear and atomic parameters of potential candidates. The task is complicated by the fact that neither the weighting factors nor the most part of the parameters are unknown at present. Nevertheless, the search criteria and preferences, formulated in the project, has allowed us to fix 8 attractive isomers potentially valuable to realizing a gamma-ray laser. Parameters of these isomers have been collected into a table together with our estimates for the threshold spectral photon flux density of pumping radiation.

Search for the most promising isotopes for the two-level pump scheme of gamma-ray laser has been made in the project. This search takes into account the need to match the specific nuclear parameters (half-lives, transition energy, *etc.*) to the pump capabilities of the available sources of X rays (pulse duration, energy of X rays, degree of monochromaticity, angular divergence, *etc.*). Together with some further limitations arising from the demands to atomic electron shell, we have reduced considerably the number of candidates which might be employed for an active medium of gamma-ray laser. On the first stage, the search has revealed 85 nuclides suitable, in principle, for pumping the first excited nuclear state directly from the ground state. Ranking of the selected candidates has been accomplished in the order of ascending threshold spectral photon flux density of pumping radiation. Parameters of the top ten isotopes potentially valuable to realizing a gamma-ray laser have been collected into a table. The first-ranked isotopes of ^{40}K and ^{54}Mn have been found by this procedure. They are distinguished by the exceptionally low threshold fluxes of pumping radiation. A comparative examination of these two isotopes has been made in the project to fix ^{40}K as the first priority candidate.

It is important to emphasize that only well established nuclear and atomic data have been used in the performed analysis (we have used Table of Isotopes and the Evaluated Nuclear Structure Data File (ENSDF), NIST Atomic Spectra Database, NIST Photon Cross Section Database). This makes the selection procedure well-grounded, enough to be certain in the results of our search. At the same time, it is clear that the final choice of the best candidate should be based on the comprehensive consideration of all features of the future gamma-ray laser experiment. Many details of this experiment are unknown at present and, naturally, could not be taken into account. Furthermore, several very important problems have been completely omitted in our analysis. In particular, the problem of production and accumulation of the selected isotopes has remained beyond the scope of our consideration. From this point of view the results of our search presented in this project should be considered only as a first-order approximation to an eventual identification of the best candidate.

CONCLUSION

Comparative analysis has been made of different schemes for a gamma-ray laser with hidden inversion of nuclear state populations. Among them are: (1) the trigger scheme and (2) the two-level pump scheme, based on the self-amplified spontaneous gamma emission principle and (3) the scheme with a Fabry-Pérot resonator, which takes advantage of the resonator both for a pumping x-ray and for stimulated gamma radiation

We have discussed the problem of identification the most promising nuclides for a gamma-ray laser based on the concept of hidden inversion of nuclear state populations. Two attractive schemes of pumping have been considered. First scheme takes advantage of the energy-storage capability of isomeric nuclei. True identification of the best isomers which might be employed for an active medium requires a complex weighing a variety of nuclear and atomic parameters of potential candidates. The task is further complicated by the fact that neither the weighting factors nor the most part of the parameters are unknown at present. Nevertheless, the search criteria and preferences, being formulated in this paper, has allowed us to fix a number of attractive isomers potentially valuable to realizing a gamma-ray laser.

Another approach to a gamma-ray laser is based on the opportunity, offered by the nuclear recoil, to employ the two-level scheme of pumping. A search for the promising isotopes has revealed 85 nuclides suitable, in principle, for pumping the first excited nuclear state directly from the ground state. Ranking of these isotopes has been accomplished in the order of ascending threshold spectral photon flux density of pumping radiation. The first-ranked isotopes of ^{40}K and ^{54}Mn distinguished by the exceptionally low threshold fluxes have been identified by this procedure. A comparative examination of these isotopes has been made to fix ^{40}K as the first priority candidate.

It is important to emphasize that only well established nuclear and atomic data have been used in the performed analysis. This makes the selection procedure well-grounded, enough to be certain in the results of our search. At the same time, it is clear that the final choice of the best candidates should be based on the comprehensive consideration of all features of the future gamma-ray laser experiment. Many details of this experiment are unknown at present and, naturally, could not be taken into account in this paper. Furthermore, several very important problems have been completely omitted in our analysis. In particular, the problem of production and accumulation of the selected isotopes has remained beyond the scope of our consideration. From this point of view the results of our search presented in this paper should be regarded only as a first-order approximation to an eventual identification of the best candidates.

We have formulated a set of requirements to the pumping radiation and to the amplifying nuclear medium crucial to the development of recoil assisted gamma-ray lasing. In particular, we have discussed the destructive impact of X-ray pumping radiation on the active medium of cooled free nuclei.

Performed analysis reveals several most significant parameters to be fixed for X-ray pumping radiation in order to reach a gamma-ray lasing in deeply cooled ensembles of free nuclei. Because of the necessity to preserve the initial monokinetic quality of cooled nuclear ensemble that allow a hidden inversion of state populations to occur, highly collimated X-ray photon beams should be employed for pumping. We have estimated the required angular divergence of the beams of pumping X-ray radiation.

A demand on the degree of monochromaticity of X-ray pumping radiation is conditioned by the aspiration to diminish a destructive influence of the X-ray pumping flux on the gamma-ray laser medium through the atomic photoelectric effect. We have determined the spectral bandwidth of the pumping radiation that could be considered as unperturbed

The need to reach the critical concentrations of excited nuclei that may consist an appreciable part of the total nuclear concentration in a cooled atomic ensemble, compels one to use for pumping very intense fluxes of X-ray radiation with hard-to-reach spectral photon flux densities. Although the considered scheme of gamma-ray lasers seems very promising, one can see that the requested spectral photon flux densities of pumping x-ray radiation are beyond that of available with current facilities . It appears that the lack of sources producing X-ray radiation of required spectral photon flux density and degree of monochromaticity is the primary impediment to realize the gamma-ray lasing process in a cooled nuclear ensemble.

We have considered a scheme of the recoil-assisted gamma-ray laser with Fabry-Pérot resonator, built of two sapphire crystal plates playing the role of Bragg back-reflecting mirrors for hard quanta. The proposed scheme takes advantage of the resonator both for a pumping x-ray and for a stimulated gamma radiation. Performed analysis has showed that the threshold spectral photon flux density of pumping x-ray radiation is by an order-of-magnitude less than that of appeared in the scheme of gamma-ray laser based on the self-amplified spontaneous gamma emission principle. For the scheme with a Fabry-Pérot resonator, the threshold spectral photon flux density of pumping radiation approach the peak fluxes that can be supplied with the upcoming x-ray free electron lasers (HASYLAB/DASY, Hamburg, Germany).

The performed analysis of general approaches to a future nuclear gamma-laser experiment revealed a number of difficulties common to all the above considered schemes for a gamma-ray laser. Among them are:

- the necessity of forming and maintaining a threadlike deeply cooled atomic ensemble of a considerable extension (up to a few meters).
- the necessity of obtaining a sufficiently large number of excited nuclei to form an active medium;
- the necessity of having a pump x-ray source with an extremely high brightness;
- the limited region of parameters for which successful gamma-ray laser experiments could be expected.

In addition, the possibility of using in a gamma-ray laser experiment the long-lived isomers as active nuclei for amplification of stimulated gamma radiation is not obvious at present and requires further investigation.

REFERENCES
1. L.A. Rivlin, Quantum Electronics, 6, 467 (1999).
2. A.A. Zadernovsky, Laser Physics, 11, 16 (2001).
3. J.J. Carroll, S.A. Karamian, L.A. Rivlin, A.A. Zadernovsky, Hyperfine Interactions, 135, 3 (2001).
4. A.A. Zadernovsky, Laser Physics, 12, 314 (2002).
5. R.B. Firestone. *Table of Isotopes*, 8th Edition: 1998 Update (Lawrence Berkeley National Laboratory, University of California).
6. Evaluated Nuclear Structure Data File (ENSDF): http://ie.lbl.gov/toi.html
7. H.J. Metcalf and P. van der Straten, *Laser Cooling and Trapping* (Springer, New York, 1999).
8. I.M. Eisenberg, W. Greiner, Excitation mechanisms of the nucleus, Amsterdam, North-Holland, 1988.
9. NIST Photon Cross Sections Database: http://physics.nist.gov
10. NIST Atomic Spectra Database: http://physics.nist.gov
11. A.A. Zadernovsky, Laser Physics, 13, 184 (2003).
12. I.M. Band, M.B. Trzhaskovskaya, and M.A. Listengarten, Atomic Data and Nuclear Data Tables 18, 433 (1976).
13. F. Rösel, H.M. Fries, K. Alder, and H.C. Pauli, Atomic Data and Nuclear Data Tables 21, 91 (1978); 21, 291 (1978).

14. Rivlin, L.A., 10 January, 1961, *Soviet Inventor's Certificate* No. 621265.
15. Vali, V. and Vali, W., 1963, *Proceedings IEEE*, 51, 182.
16. Baldwin, G.C., Neissel, J.P., and Tonks, L., 1963, *Proceedings IEEE*, 51, 1247.
17. Baldwin, G.C. and Solem, J.C., 1997, *Rev. Mod. Phys.*, 69, 1085.
18. Andreev, A.V., Volkov, R.V., Gordienko, V.M., Mikheev, P.M., Savel'ev, A.V., Tkalya, E.V., Chutko, O.V., Shashkov, A.A. and Dykhne, A.M., 1999, *JETP Lett.*, 69, 371.
19. Ledingham, K.W.D., Spencer, I., McCanny, T., Singhal, R.P., Santala, M.I.K., Clark, E., Watts, I., Beg, F.N., Zepf, M., Krushelnick, K., Tatarakis, M., Dangor, A.E., Norreys, P.A., Allott, R., Neely, D., Clark, R.J., Machacek, A.C., Wark, J.S., Cresswell, A.J., Sanderson, D.C.W., and Magill, J., 2000, *Phys. Rev. Lett.*, 84, 899.
20. Cowan, T.E., Hunt, A.W., Phillips T.W., Wilks, S.C., Perry, M.D., Brown, C., Fountain, W., Hatchett, S., Johnson, J., Key, M.H., Parnell, T., Pennington, D.M., Snavely, R.A. and Takahashi, Y., 2000, *Phys. Rev. Lett.*, 84, 903.
21. Stedile, F., Fill, E., Belic, D., von Brentano, P., Fransen, C., Gade, A., Kneissl, U., Kohstall, C., Linnemann, A., Matschinsky, P., Nord, A., Pietralla, N., Pitz, H. H., Scheck, M. and Werner, V., 2001, *Phys. Rev C*, 63, 024320.
22. Coussement, R., Vandenbergh, M., Sheeren, G., Neyens, G., Nouwen, R. and Boolchand, P., 1993, *Phys Rev. Lett.*, 71, 1824.
23. Odeurs, J. and Shakhmuratov, R.N., 2001, *Hyperfine Interactions*, 135, 215
24. Kocharovskaya, O., 1997, *Hyperfine Interactions*, 107, 187.
25. Rostovtsev, Yu. and Kocharovskaya, O., 2001, *Hyperfine Interactions*, 135, 233.
26. Rivlin, L.A., 1999, *Quantum Electronics*, 6, 467.
27. Carroll, J.J., Karamian, S.A., Rivlin, L.A. and Zadernovsky, A.A., 2001, *Hyperfine Interactions*, 135, 3.
28. Metcalf, H.J., van der Straten, P., 1999, *Laser cooling and trapping* (Springer, New York).
29. Adams,C.S., Riis, E., 1997, *Progr. Quant. Electron.*, 21, 1.
30. Vuletic, V. and Chu, S., 2000, *Phys Rev. Lett.*, 84, 3787.
31. Zadernovsky, A.A., 2002, *Laser Physics*, 12, 314.
32. NIST Photon Cross Sections Database: http://physics.nist.gov/
33. Shvyd'ko, Yu.V., Lerche, M., *et al.*, 10 January 2003, *Phys. Rev. Lett.*, 90, No 1.
34. Rivlin, L.A., 1999, *Quantum Electronics*, 6, 467.
35. Steyerl, A., Steinhauser, K.A., 1979, *Z. Phys.*, B34, 221.
36. Cusatis, C., Udron, D., Mazzaro, I., Giles, C., Tolentino, H., 1996, *Acta Cryst.*, A52, 614.
37. Kikuta, S., Imai, Y., Iizuka, T., Yoda, Y., Zhang, X.W., Hirano, K., 1998, *J. Synchrotron Rad.*, 5, 670.
38. Shvyd'ko, Yu.V., 2002, Habilitationsschrift, Universität Hamburg, DESY, Hamburg, (DESY-Thesis-2002-028, ISSN 1435-8085, www-library.desy.de/diss02.html).
39. Kohn, V.G., Kohn, I.V., Manykin, E.A., 1999, *JETP*, 89, 500.
40. Shvyd'ko, Y.V., Gerdau, E., 1999, *Hyp. Interact.*, 123/124, 741.
41. Shvyd'ko, Y.V., Gerdau, E., Jäschke, J., Leupold, O., Lucht, M., Rüter, H.D., 1998, *Phys. Rev.*, B57, 4968.
42. Liss, K.D., Hock, R., Gomm, M., Waibel, B., Magerl, A., Krisch, M., Tucoulou, R., 2000, *Nature*, 404, 371.
43. Born, M. and Wolf, E., 1980, *Principles of Optic*s (Pergamon Press).
44. Metcalf, H.J., van der Straten, P., 1999, *Laser cooling and trapping* (New York: Springer).
45. NIST Photon Cross Sections Database: http://physics.nist.gov/
46. Zadernovsky, A.A., 2003, *Laser Physics*, 13, 184.

TASK 2. EXTENDED ENSEMBLE OF MONOENERGETIC ATOMS

1. INTRODUCTION.

1.1 Target setting. The objective. Coherent gamma-radiation can be formed by stimulated emission of a nuclei ensemble with the inversion of population of nuclei levels. Two conditions are required for amplifying the flux of gamma-photons. The first is a reasonably high ratio of the natural width of the gamma transition to the total width caused by various broadening mechanisms (including inhomogeneous one). The second is a reasonable degree of population inversion. It has been shown that Moessbauer effect doesn't solve the problem (see the part of the report presented by "MIREA" group). There is a more perspective alternative approach [28, 29], which is based on the recoil effect in an ensemble of free nuclei. This approach reveals new opportunities which are relevant to the hard photons processes only. Particularly this effect opens the possibility of the velocity-selective population inversion in free nuclei and anisotropic quantum amplification of the unidirectional gamma-photon flux without reflecting mirrors.

The nice feature of the radiation processes in free nuclei is considerable recoil, as a result of a relatively big photon momentum. After any radiation transition a nucleus gets recoil energy of the order of 1 meV. In the case of photon absorption the recoil energy is taken from the photon energy while in the case of photon emission – from nucleus state energy. It leads to the shift of the spectral line which is equal to the recoil energy. This phenomenon and its derivatives are called kinematical shift or line splitting. From this it follows that in the case of the shift which is comparable with the natural linewidth of the nucleus transition it is possible to realize so-called hidden inversion, because emitted photons cannot be absorbed by the nuclei in the ground state. For instance see Fig. 1, where blue line shows (not in scale) the concentration of potassium or cesium atoms with nuclei in the lower state vs the projection of the velocity on the direction of the propagation of gamma-radiation. The red line shows the velocity distribution of the atoms (and their nuclei), which have absorbed the gamma-photons. Due to the recoil the speed of these atoms has changed by $V_{REC\gamma}$. Lower in the Fig. 1 there is a table with the most probable velocities of the atoms at room temperature, at the Doppler limit of temperature, and at the recoil limit of temperature of laser cooled atoms. The data demonstrate that at room temperature recoil velocity is comparable with thermal velocity. But in the case of Doppler cooling the velocity is by three orders of value smaller than the recoil velocity. If this velocity distribution is close to the Gaussian, the number of the nucleus remaining in the lower state and moving at $V_{REC\gamma}$ is negligible. Of coarse the recoil-limit temperature provides the same condition even better.

cm/s	^{133}Cs	^{40}K
$V_{REC\gamma}$	$1.96\cdot10^4$	$2.37\cdot10^4$
V_{MPB}	$1.92\cdot10^4$/298K	$3.49\cdot10^4$/ 298K
V_D	8.82 / 124μK	17.7 / 146μK
V_R	0.35 / 0.198μK	1.34 / 0.836μK
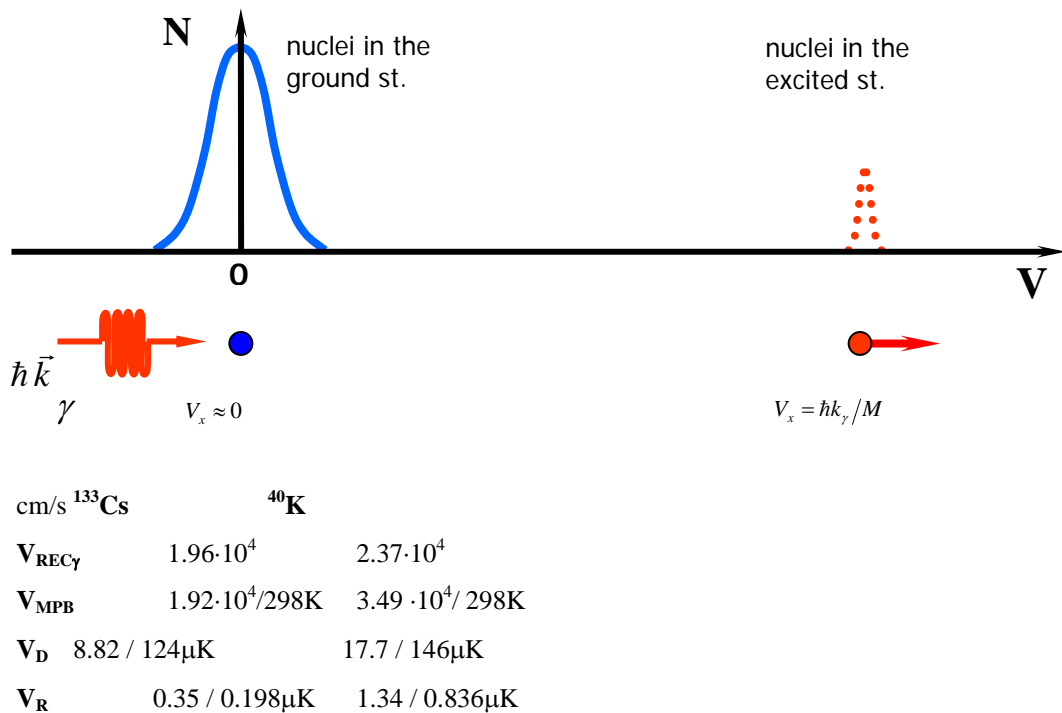
Fig. 1.

Hence, general inversion is not necessary, i.e. the total number of the excited nuclei should not be greater than the number of atoms in the lower state. Basically, the amplifying coefficient is positive at any non zero population of the upper nucleus state, excited by non coherent x-ray pumping.

The first natural step to this amplification is detecting the absorption of gamma radiation by the laser cooled ensemble of atoms. It is a challenging task because of a very small cross section of the resonant gamma-radiation

absorption. The goal is to build an ensemble, which gives the possibility to detect gamma-radiation absorption with $10^{-18} - 10^{-19}$ cm^2 cross section, using optical resonance radiation with the absorption cross-section of $\sim 10^{-10}$ cm^2.

Abovementioned peculiarities appear in the ensemble of free nuclei only. However, it requires a dramatic decreasing of the inhomogeneous Doppler broadening of the linewidth for reasonable linewidth ratio and amplification coefficient. This important problem must be solved by modern laser cooling techniques, which allow now decreasing the temperature of atoms by 10^8 times (from room temperature) [1, 2]. In that case the ratio of the homogeneous linewidth to the inhomogeneous (Doppler broadened) linewidth of the γ-transition increases by four orders of value. Nevertheless, for 10^{-2}-10^{-3} absorption of resonance gamma-radiation at record atom concentration of 10^{13}-10^{14} cm^{-3} [14, 32] the length of the ensemble must be ~ 1 m. Obviously, it is quite difficult to combine the record number of the atoms and the record low temperatures in the extended ensemble. So the practical goal is to determine the limit of the value

$$nL \Big/ \sqrt{T_{\parallel}} \qquad\qquad\qquad (2.1)$$

(n – nuclei concentration, L – length of the ensemble, $T_{\parallel}$ - "longitudinal" temperature) and to investigate its dependence on intensities, polarizations, diameters of the laser beams, vacuum level, magnetic field values, geometry, etc…

Gamma resonance detection on free nuclei or nuclei pumping requires gamma-radiation sources, like solid state Moessbauer source or a synchrotron. The advantage of the first one is a narrow spectrum; disadvantages are isotropic radiation (narrow beam must be formed by apertures, in that case the narrower is a beam, the lower is the source efficiency) and a requirement of high speed of the source relatively to the absorption target (for compensating the recoil effect). On account of the low gamma process cross-section and finite concentration of the cold atoms, the ensemble of atoms has to be a long thread, that doesn't match at all the isotropic radiation of the Moessbauer source. The advantages of the synchrotron radiation are a very small divergence and a high brightness. The disadvantage is relatively wide spectrum, although recent application of the crystal monochrometers led to significant narrowing of the spectrum down to ~ 1 meV. The important thing is a possibility of getting short powerful pulses for forming inversion in the gamma-transition. The gamma absorption on free nuclei experiment with synchrotron radiation is more realistic, so on developing the atomic ensemble we keep in mind this gamma-radiation source. It is important to fit the parameters of the atomic ensemble to the gamma-radiation properties; there is no sense to decrease the Doppler linewidth of nuclei absorption line much lower than the attainable linewidth limit of a gamma-radiation source.

The main task of this part of the project (Problem 2) is to investigate possibilities of creating extended monoenergetic ensembles of atoms, which might be used as a gamma-radiation absorption target, and to determine its limits: maximum length, maximum concentration, minimum temperature.

Expected results and possible applications.
1. Review of existing methods of creating thread-like high density cooled atomic beams.
2. Choosing an isotope by nucleus and atom properties.
3. Selecting the experimental setup scheme for forming the extended ensemble of cooled atoms.
4. Building laser system "master tunable diode laser – amplifier", studying the limits.
5. Experimental realization of the extended ensemble of ultra-cold atoms and measuring the dependence of the ratio of the total number of atoms to the transversal cross-section vs. power, detuning and geometry of laser beams and other parameters (magnetic field, vacuum).

1.2   Overview of atomic traps and bright atomic beams.
In the beginning we have analyzed the latest achievements in the world of traps and cooled atoms, especially linear traps and bright atomic beams. The remarkable sources are [1, 2, Tos89] reviews and "Laser cooling and trapping" book [22].

Transversal confinement of atoms in an extended ($\sim$1m) trap with resonance light pressure requires very large laser power. This method leads to additional noise and decreasing of the life time of the atoms in the trap because of collisions with excited atoms, therefore this method is not discussed here.

Another possibility is using dipole optical traps. Dipole moment of atoms (which is zero in the ground state) is induced by the light, and then the inhomogeneous laser field combined with the induced dipole moment produces the force acting on the atom. In other words, the force is produced because of changing potential energy of the atom in the inhomogeneous laser field due to AC Stark shift, which is proportional to the intensity of laser field. The light shift appears only in the case of non-zero detuning of the laser frequency from the atomic transition. The sign of the shift is negative for red detuning (longer wavelength) and is positive for blue detuning (shorter wavelength). Accordingly, in the case of red detuning atoms are attracted by maximum field [11], on the contrary, the blue detuning pushes atoms to the minimum of the laser field (so the transversal distribution of the laser field must be circular). Unfortunately, this method also requires very high laser power.

In [24] Rb atoms were trapped using the laser beam focused into the 10 μm waist at the power of at least 0.5 W. At 10% frequency detuning the depth of the potential well was 10 meV. Sharp focusing was required for significant gradient in both transversal and longitudinal directions so as to form a 3D-trap. In our case we need 2D-trap. For Cs atoms the 1.06 μm radiation of Nd laser is applicable. If the waist is 1 mm, its change is negligible in a

trap with a length of 1m. There is a disadvantage – atoms are trapped in the maximum field area, so optically shifted transition frequency makes probing and spectroscopic investigation difficult, especially in the presence of intensity fluctuations of the trap field. In any case this approach is rejected because of the finance limit and significant power fluctuations in the available Nd-laser. However, this method can be used in future.

Application of the blue detuned laser field requires hollow laser beams [14, 26]. This leads to a zero light shift on the trap axis, which is good, on the other hand forming such a hollow beams is not so easy on practice [2, 9, 30]. Basically, blue detuned laser beam may be used as a stopper in the end of the pure magnetic trap.

In the case of the total internal reflection on the border of glass and vacuum the field penetrates to the vacuum and its intensity goes down exponentially on the characteristic length $\lambda/2\pi$. It gives huge gradient and combined with blue detuned radiation forms significant repulsive force [6, 7, 16, 19]. Using such a light barrier on the internal surface of the capillary an extended trap may be realized. But in the method high laser power and small detuning are required for reasonable barrier value. For all that there are noticeable atomic light absorption and related leakages. There is another principle limit of the capillary length, which is connected with difficult vacuum support (big pumping resistance of the capillary).

The most perspective method is a pure magnetic trap. Many atoms, including alkali metal atoms, have constant magnetic dipole, so in the inhomogeneous magnetic field there is a force acting on the atom:

F = grad (μ·B) $\qquad\qquad\qquad\qquad\qquad\qquad\qquad\qquad\qquad$ (2.2)

It is possible to create a configuration of the magnetic field with a local minimum of its absolute value. Practically reasonable values of the magnetic field limit the potential well to $k_B \cdot 1K$. Only cooled atoms might be trapped in such a pure magnetic trap. That's why these traps were realized only recently. In one of the first works [23] the magnetic field was formed by a pair of coils in Helmholz configuration (with opposite currents). All three dimensions of the trap were similar, which is not applicable for the project task.

For gaunt geometry the Ioffe trap is applicable [10], which is formed by four linear parallel conductors with currents. In the transversal cross section conductors are placed in the corners of the square. Local minimum is located on the axis of the trap which is parallel to the conductor lines and goes through the center of the square. This geometry has translational symmetry, so atoms are allowed to move freely along the axis. In the classic scheme of the Ioffe trap additional coils are used on the both ends of the trap in order to stop the atoms.

The most important requirement of the trap is a long life time of the atoms in it. There are three major leaking mechanisms in a pure magnetic trap.

The first is non-adiabatic transitions of atoms from the so called low field seeking state. In this state an atom is attracted by the minimum of the magnetic field. If there is a transition to another state, in which an atom is attracted to the maximum of the field, the atom is kicked out from the trap. Additional longitude magnetic field should suppress such transitions on the trap axis, where the sign of the transversal magnetic field passes rapidly through zero.

The second mechanism is collisions of atoms in the ground state with the excited (in the P state) atoms. In that case a molecule in the excited state might be formed. This molecule can go to the ground state with emission of a photon of smaller energy. After molecule dissociation energy difference transforms to the kinetic energy that is higher than potential well. For avoiding this effect the presence of the resonance radiation in the trap must be strongly suppressed.

The third leakage way is collision of an atom with background gas. High vacuum level is required. In addition to various methods of lowering residual pressure in the trap in case of cesium there is another one: four linear tube conductors may be cooled with internal liquid nitrogen fluid so the pressure of the Cs saturated vapor must be much lower than without cooling. Also it gives a possibility to use higher current and to get deeper magnetic trap.

Additional advantage of this type of the trap is relatively simple increase of its length without constructive changes.

One of the first ways of getting cooled alkali atomic beam is slowing and cooling conventional effusion atomic beam, which is formed by a hot source, diaphragms and oncoming laser beam [4, 5]. Because a Doppler width is about10^2 times greater than the natural width, and the laser linewidth is usually narrower than natural width atoms go off resonance rapidly due to the Doppler shift and stop interacting with the light. Two methods were proposed to eliminate this detuning. In [27, Wat86] the laser frequency changes periodically following the Doppler-shifted frequency of the cooled atoms, which produces bunches of cooled and slowed atoms and a strong background of hot atoms. This method is not effective for many applications including our task. In another method the resonance frequency of the atom is changed by the magnetic field varying along the atom trajectory [8, Phil82]. The disadvantage is a complicated organization of the strong magnetic field with a given space variation. Strong magnetic field of the Zeeman slower may penetrate to the pure magnetic trap. Nevertheless, the method is still used: recently in [20] the flux of the cooled atoms was $2.6 \cdot 10^{10}$ s^{-1} at brightness of the atomic beam $7 \cdot 10^{23}$ $s^{-1}m^{-2}sr^{-1}$, but relatively high speed (35-120 m/s) of atoms.

Among all the versions of atomic beams with hot source and post cooling the most attractive is a method of cooling and slowing by oncoming beam with big number of equidistant spectral components [18]. The interval between them must be smaller than (or about the same as) the natural linewidth of the atomic transition. This so-called "white light" cooling of the thermal beam provides simultaneous slowing of all atoms in the beam without longitudinal velocity dependence giving continuous monoenergetic cooled atomic beam. However, it was shown

[33] that this technique works only with the support by an additional oncoming monochromatic beam. Find detailed discussion of hot sources in the "Work results" chapter.

General disadvantage of the hot sources is a more strict vacuum system requirement, because the atomic beam and the oven poison the setup with resonance atoms and other gas atoms. Especially it is significant in the case of ^{133}Cs, because its saturated vapor pressure at room temperature is 10^{-6} Torr.

There is a fundamentally different way of forming the atomic beam, where the sequence of operations with atoms is changed. Instead of first forming the beam followed by cooling, atoms are first cooled and then build up the beam. The cooling occurs in the magneto-optical trap (MOT). It can be either 3D or 2D. In any case there is a shadow in one of the beams, provided by the aperture in the mirror (fig. 2, table1, [15]). There is no oncoming force acting on the atoms in the shadow, so atoms leave the trap, forming the atomic beam. Note that in the case of 2D cooling on fig. 2 [15] atoms in the shadow are not deliberately cooled in the longitudinal direction. Nevertheless, aperture in the mirror acts like a filter - it doesn't pass most of the atoms with high longitude velocity, because the atoms that have not spent enough time in the trap have both high longitudinal and high transverse velocities, hence the space deflection from the axis is bigger than the mirror aperture. These fast atoms are blocked by the mirror and returned back to the trap by the field (recycling effect), which increases the efficiency of the cold atoms trapping. Changing 3D MOT (anti-Helmholz coils) to the 2D MOT configuration allows decreasing the efficiency of the laser power keeping the same atomic flux. In [32] the 10^{10} atoms/s flux was achieved as in the 3D MOT configuration with hollow beam but using 10 times smaller power of laser. The described source of cold atoms gives an additional possibility to narrow longitudinal velocity distribution and to control its mean value. This can be made by using the laser fields with shifted frequencies, propagating along the trap axis, where the magnetic field value is small. Frequency shifts are set to realize a molasses in one direction for atoms with specific velocity. A molasses provides lower longitudinal temperature. Remarkable, in [12] only four beams in non-orthogonal geometry (fig. 3 in Table 1.) have been used for 2D-trapping and moving molasses, so-called MM-MOT. Another modification of this method, admitted to our project, is described in the "results" chapter.

Compact source of the bright atomic beam is described in the [13]. The speed of atoms is variable from 2 m/s to 15 m/s, the flux being $8 \cdot 10^9$ atoms/sec. This source is simpler but the flux and the brightness are not upgradeable.
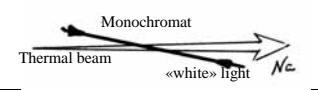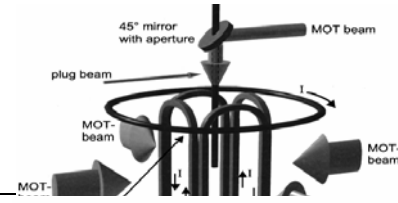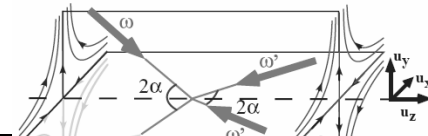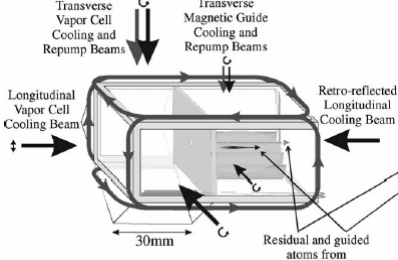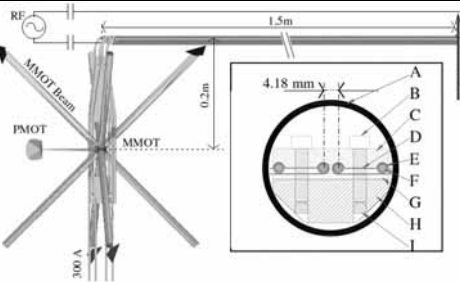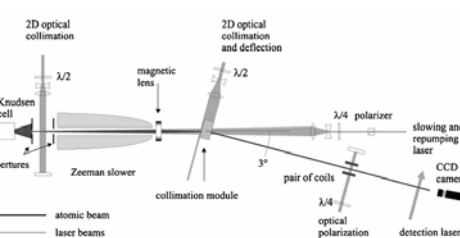
In [25] it is reported about forming a cold atomic beam with longitudinal velocity of 1m/s, which might be used in atomic interferometry. Technique of continuous injection of the cold atomic beam of ^{87}Rb to the extended magnetic trap with transversal magnetic field gradient 2.7 kG/cm is described. A sequence of two modified magneto-optical traps (Pyramidal MOT, Moving MOT) is used for continuous injection. The cold atomic beam collected with evaporative cooling in PMOT was led out through the top of the pyramidal mirror and moved to the second MMOT. The atomic beam was injected then to the four-line extended magnetic trap. It was combined from vertical part (0.2 m) for injection, gravitational compression, slowing and horizontal part (1.5 m) with AC current in the rf-range with fixed frequency, which allows to reject atoms with high transversal velocity from the beam. Stationary measurements of temperature and leakage were developed. The atomic beam in the area with high magnetic field had transversal temperature of 400μK±60μK, the longitudinal temperature of 1mK, the mean velocity of 1 m/s, and the $4 \cdot 10^7$ s^{-1} atomic flux at the laser power of 100 mW. Authors expect to increase flux by two orders with the Zeeman slower scheme.

In [20] authors report about getting a beam of cold Cs atoms with modified Zeeman slower with high magnetic field gradient at the end of the slower provided by permanent magnets. Careful search of the optimum parameters for finishing the stopping process in the slower gave the narrow distribution of the longitude velocity and high brightness. Slow atomic beam was transversally compressed, collimated and deflected from the origin axis using magnetic lens and tilted section of 2D-MOT. Atomic beam had average velocity in 35-120 m/s range and the flux greater than $2 \cdot 10^{10}$ cold atoms per second. The numerical calculations of the slowing process fit the result.

Schemes of the discussed methods and basic properties are shown in the Table 1. It shows that the flux doesn't exceed 10^{10} atom/s in the discussed works and there is no strong correlation between the flux and used laser power. The table does not show an important property of the atomic beam – the divergence, which also determines the brightness of the beam (the requirement to the divergence in our case is not very strict: if the atoms' lifetime in the trap is significantly greater that the transversal oscillation relaxation time, just trapping the atoms is enough, otherwise the high divergence increases the transversal size of the beam in the trap).The efficiency of laser power utilization might be very different. The greatest efficiency is achieved in [15] (maximum flux of 9 x 10^9 at minimum final speed of 8 m/s and minimum laser power of 34 mW). At much higher power, like 500 mW (as in [21]), the 10^{11} s^{-1} flux is expected. It is significant, that at speeds greater than 1m/s there might be the time-of-flight limit for the life time of atoms in the trap. Thus, using the effective method is as important as the increase of the power.
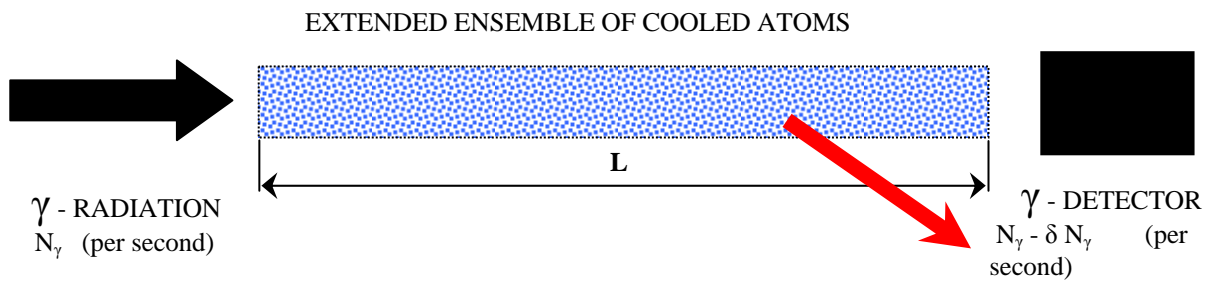
Paragraph 2.2 describes the selecting of linear magnetic trap scheme and estimation of the necessary laser and vacuum system parameters.

Table 1.

Link	Figure	$V_{m.p.}$, m/s	ΔV, m/s	Φ, atom/s	P, mW
[33]		335	0.75	9.5×10^8	105
[21]		26	6.3	5×10^9	500
[15]		8	3.3	9×10^9	34
[12]		0.3 – 3	0.03– 0.3	2.2×10^9	30
[13]		15	3	8×10^9	~100
[25]		1	0.4	4×10^7	~100
[20]		35-120	0.5-5	2×10^{10}	~100

2. RESULTS

2.1 Selection of the isotope

EXTENDED ENSEMBLE OF COOLED ATOMS

γ - RADIATION
N_γ (per second)

L

γ - DETECTOR
$N_\gamma - \delta N_\gamma$ (per second)

A is the area of the cross section
N is the total number of atoms in the trap
Fig. 3

The scheme of probing the extended ensemble of cooled atoms (to put it more precisely - nucleus) by gamma radiation is shown on Fig. 3. The frequency of gamma-radiation is tuned to the nucleus transition (with the recoil effect taken into account). σ_γ is the resonant cross-section of the gamma-transition at the maximum of the absorption line.

The absorption coefficient is

$$\alpha_\gamma = n\,\sigma_\gamma L\beta, \qquad (2.3)$$
$$\beta = \Gamma_\gamma / \Gamma_{D.res}, \qquad (2.4)$$

where $n = N/AL$ is the concentration of atoms, Γ_γ is the natural linewidth of the gamma-transition, $\Gamma_{D.res}$ is the residual Doppler linewidth of the gamma-transition It is assumed that $\Gamma_{D.res}$ is greater than $\Gamma_{\gamma.}$.

The linewidth of the probing gamma-radiation is supposed to be narrower or of the same order as $\Gamma_{D.res}$. By taking into account that $\Gamma_{D.res} = \nu_\gamma V_\parallel/c = V_\parallel/\lambda_\gamma$, $V_\parallel = (2k_B T_\parallel/M)^{1/2}$, the absorption coefficient is

$$\alpha_\gamma = N\,\sigma_\gamma \beta/A = (1/2k_B)^{1/2}\sigma_\gamma\,\Gamma_\gamma\,\lambda_\gamma(M)^{1/2}\,(N/A)T_\parallel^{-1/2} \qquad (2.5)$$

where ν_γ, λ_γ are frequency and wavelength of the gamma-radiation respectively, $V_\parallel$ is the most probable velocity of the cooled ensemble of atoms. Aqua colored factor is determined by the nucleus selection, yellow colored factor is limited by the performance of the experimental setup.

In collaboration with the MIREA team, we worked on the selection of a few most suitable nuclides and on the classification of the relevant information. The parameters of interest were divided in four groups describing: i) gamma transition (energy, lifetime, resonant cross section), ii) atomic transition (wavelength, linewidth, resonant cross section, hyperfine structure and the possibility of deep, sub Doppler cooling), iii) temperature dependence of the saturated vapour density, the abundance and price of the isotope, iv) the parameters and the accessibility of lasers providing the relevant wavelength.

The last column of the Table 2 shows the parameter, which determines the absorption of the gamma-radiation. According to this data ^{40}K ^{133}Ba ^{161}Dy, ^{162}Dy ^{153}Eu are the most attractive isotopes, ^{133}Cs is the least attractive one.

Table 2.

isotope	abs. cross-section		energy	Freq.	Wave-length	line width	abund-ance	Con version	
	σ_γ	$T_{1/2}$	E_γ	ν_γ	λ_γ	Γ_γ	c	α_T	$\sigma_\gamma\cdot\Gamma_\gamma\cdot\lambda_\gamma\cdot M^{1/2}$
	10^{-20} cm^2	ns	keV	10^{18} Hz	10^{-2} nm	MHz	%		AU
^{40}K	163,1	4,25	29,56	7,12	4,21	25,9	0,012	0,35	458,42
^{57}Fe	255,8	97,8	14,41	3,47	8,65	1,12	2,14	8,21	76,3
^{73}Ge	22,88	1,86	68,75	16,57	1,81	59,1	7,76	0,8	85,2
^{85}Kr	107,5	147	9,40	2,27	13,22	0,75	11,55	19,6	40,1
^{127}I	20,57	1,95	57,60	13,88	2,16	56,4	100	3,78	57,4
^{129}Xe	23,48	1,01	39,58	9,54	3,14	108,9	26,44	12,3	371,7
^{133}Cs	10,28	6,31	81,00	19,52	1,54	17,4	100	1,72	12,9
^{133}Ba	29,18	8,10	12,29	2,96	10,14	13,6	0	-	189,1
^{151}Eu	23,77	9,7	21,53	5,19	5,78	11,34	47,82	28,6	78,0
^{153}Eu	17,97	0,21	97,43	23,48	1,28	523,8	52,18	0,42	607,4
^{161}Dy	31,92	0,78	43,83	10,56	2,84	141,0	18,88	4,32	661,0
^{162}Dy	121,3	2,27	80,65	19,44	1,54	48,5	25,53	-	470,0

The Table 3 (presented by MIREA group) contains the information about the optical resonance absorption of some selected atoms. The column "Critical temp of nuclear ensemble" contains the critical temperature of the atoms. At this temperature the residual Doppler broadening equals the natural linewidth. As it was mentioned, there are still no sources of the monochromatic gamma-radiation with the linewidth lower than 1 meV. Thus, cooling down to these temperatures is not expedient.

Table 3.

Nuclear data					Atomic data				
Iso tope	Transition energy [keV]	Ground state half life [y]	First excited state half life [ns]	Electron conv. coeff.	Wave length [nm]	Trans. probab. $[10^8 s^{-1}]$	Photo absorpt. cross section 10^{-7} см^2	Critical temp of nuclear ensemble [μK]	Threshold spectral photon flux density at T=10 μK $[10^{35}$ ph/(cm^2 s keV)]
$^{40}_{19}K$	29.830	$1.3 \cdot 10^9$	4.24	0.357	766.4	0.387	$2.04 \cdot 10^{-2}$	$1.03 \cdot 10^{-3}$	$4.12 \cdot 10^{-2}$
$^{183}_{74}W$	46.483	$1.1 \cdot 10^{17}$	0.188	8.63	400.9	0.163	0.197	0.98	1.49
$^{81}_{36}Kr$	49.56	$2.3 \cdot 10^5$	3.9	1.3	877.7	0.27	$6.01 \cdot 10^{-2}$	$8.89 \cdot 10^{-4}$	1.78
$^{119}_{50}Sn$	23.870	stable	18.03	5.22	284.0	1.7	0.241	$2.63 \cdot 10^{-4}$	3.22
$^{161}_{66}Dy$	25.652	stable	29.1	2.35	421.2	2.08	0.627	$1.18 \cdot 10^{-4}$	9.67
$^{133}_{56}Ba$	12.327	10.51	7.0	70.3	706.0	0.71	2.38	$7.32 \cdot 10^{-3}$	56.35
$^{227}_{89}Ac$	27.36	21.77	38.3	4.5	418.0	-	1.74	$8.48 \cdot 10^{-5}$	62.86
$^{151}_{63}Eu$	21.542	stable	9.6	28	459.4	1.4	0.837	$1.45 \cdot 10^{-3}$	103.02
$^{54}_{25}Mn$	54.40	312.3d	0.049	0.2116	403.1	0.17	$1.04 \cdot 10^{-2}$	3.11	$3.68 \cdot 10^{-3}$
$^{131}_{54}Xe$	80.185	stable	0.480	1.57	823.2	-	$7.28 \cdot 10^{-2}$	$3.63 \cdot 10^{-2}$	7.21
$^{159}_{66}Dy$	56.626	144.4d	0.21	13.19	421.2	2.08	0.382	0.46	26.81
$^{153}_{63}Eu$	83.367	stable	0.790	3.82	459.4	1.4	0.116	$1.45 \cdot 10^{-2}$	28.03
$^{133}_{55}Cs$	80.997	stable	6.28	1.72	852.1	0.328	$7.59 \cdot 10^{-2}$	$2.11 \cdot 10^{-4}$	43.11

Most of the isotopes have short wavelength resonant lines; therefore they require expensive lasers or second harmonic generation. Some isotopes, like **tungsten** and **dysprosium**, are not usable because the temperature, which gives enough pressure of the saturated vapor, is too high. **Noble gas atoms** have ultraviolet lines. In the table 3 the lines of these atoms correspond to a metastable (not the ground) initial state. For excitation of such transitions, a discharge must be used, but the much greater number of the atoms in the ground state kills the possibility of using them. **Barium** line is not initial-ground-state transition either, so it cannot be used for direct cooling. Suitable resonance transition has the wavelength equals to 553,5 nm. Deep cooling of barium must be two-step process: pre-cooling on the 553.5 nm wavelength, post-cooling on the intercombination transition with the 711 nm wavelength. The nucleus properties of the manganese (^{54}Mn) isotope make it the most attractive one. However, the half-decay time of 312 days would sophisticate the experiment. Also getting sufficient laser power at manganese resonance wavelength 403 nm is difficult (but solvable) problem. The temperature for reaching required saturated vapor pressure is not too high (10^{-6} Torr at 600 °C). The most important advantage of this isotope is relatively wide homogeneous linewidth of the gamma-transition. It means, while the sources are being improved and the gamma-radiation linewidth is getting narrower, the ^{54}Mn will be the first isotope that will provide the homogeneous absorption linewidth of the cooled ensemble comparable to the linewidth of the pumping gamma-radiation. Large linewidth of the excited state of the nucleus also leads to the relatively high and obtainable critical temperature (Table 3). Practically, matching of the pumping radiation linewidth to the linewidth of the homogeneous absorption gives the basic possibility to narrow the gamma-radiation linewidth of the ensemble of free nuclei due to regenerative effect in amplification. Inhomogeneous broadened lines do not give such opportunity, thus it is impossible to narrow the linewidth with the effective use of energy.

On account of the cooling experiments experience in general and particularly in our laboratory, taking into consideration the availability of the sufficiently powerful lasers, and the temperature, that provides enough saturated vapor pressure, the atoms of alkali metals are the most suitable ones, especially cesium, rubidium, potassium. Resonant lines of these atoms overlap with the radiation of laser diodes, which are being used in the laboratory for a long time (exception – a dye laser is required for sodium atoms). Unfortunately, there are no proper rubidium isotopes with the gamma-transition of the nucleus. However, some preliminary atomic cooling experiments were

done with the rubidium isotopes. The obtained experience was very valuable in the designing of the experimental setup. Thus, the final choice is **[133]Cs or [40]K.**

The implicit advantages of the [40]K isotope are smaller (much more accessible, than in the case of Cs) energy of the nucleus transition, significantly greater cross-section of the gamma-radiation absorption, smaller (by the order of two) pressure of the saturated vapor pressure at room temperature. The last factor simplifies the obtaining of high vacuum level. There are some disadvantages: narrow structure and reversed order of the excited states in the D_2 line of the isotope, lower power of the diode lasers in this range (767 nm). These disadvantages do not hamper the cooling of the [40]K atoms [17]. But the significant disadvantage of the [40]K (at least in this project) is extremely low abundance in the natural mixture and very high cost. Thus, cesium was selected.

Table 4

NUCLEUS		[133]Cs	[40]K
Abundance	%	100	0.0117
PSV @295K	Torr	10^{-6}	10^{-8}
Vm.pr.	m/s	192	349
M	g	$2.2 \cdot 10^{-22}$	$6.65 \cdot 10^{-23}$

OPTICAL TRANSITION			
λ	nm	852.112	766.49
ν	Hz	$3.521 \cdot 10^{14}$	$3.914 \cdot 10^{14}$
τ	ns	30	25
Γ	MHz	5.3	6.2
Vrec	cm/s	0.35	1.34
NpMIN		$9 \cdot 10^4$	$4.7 \cdot 10^4$

$\tilde{\gamma}$TRANSITION			
E	keV	81	29.4
ν	Hz	$1.96 \cdot 10^{19}$	$7.14 \cdot 10^{18}$
λ_γ	Å	0.15	0.42
Vrec	cm/s	$1.97 \cdot 10^4$	$2.37 \cdot 10^4$
σ_γ	cm^2	$1.064 \cdot 10^{-19}$	$1.631 \cdot 10^{-18}$
Γ_γ	MHz	25	41
$\sqrt{M}\lambda_\gamma\Gamma_\gamma\sigma_\gamma$	AU	1	38
$\sigma_\gamma/(1+\alpha_\gamma)$	AU	1	30.9

2.2 The estimation of required setup parameters.

We worked on choosing the scheme of the linear trap and on the evaluation of needed lasers parameters, degree of vacuum. We analysed the limiting values for the concentration, temperature, and dimensions of the ensemble of atoms for realistic parameters of the laser radiation. Most of the estimates are based on three simple relationships:

1) The geometry of the ensemble of cooled atoms, their density, and their longitudinal velocity distribution should provide the detectable absorption of a resonant gamma radiation. Both a direct (by measuring the absorption of a gamma quanta) and an indirect (by detecting scattered gamma photons) techniques have been considered. This condition gives the estimate of the temperature of cooled atoms, and of their total number (for a given geometry of a cooled ensemble).
2) The total number of cooled atoms divided by their lifetime in the linear trap should be equal to the rate at which atoms are loaded into the trap. The lifetime is sensitive to the degree of vacuum in the trap. The set-up should provide high vacuum in any case. By the order of magnitude the lifetime caused by collisions with residual gas atoms is $P/10^{-8}$ s, where P is a pressure in Torr [22]. It's not reasonable to get a vacuum better then 10^{-10}, because the other factors are going to limit the lifetime, particularly the transit time, or the final longitudinal velocity. The choice of this velocity is a compromise. Small velocity results in the higher time of flight through the magnetic trap, but it makes more difficult to transport the atoms from the first trap to the second one, because of a higher beam divergence.

3) The flux of the atoms to be launched into the trap and the number of photons per atom required for the cooling give a conservation-of-energy (and very optimistic) estimate of the needed laser power.

The number of absorbed resonant gamma quanta (δN_γ) in the pulse of N_γ quanta after propagation through a linear trap with a cross section A and length L filled with N atoms cooled to the temperature T equals:

$$\delta N_\gamma = N_\gamma \, N \, \sigma_\gamma \, \beta/A, \qquad (2.6)$$

provided that the divergence of gamma radiation corresponds to the geometry of the trap. β is the ratio of the natural width of the gamma transition to its residual Doppler width. In what follows we consider the involved factors separately.

The total flux of cooled atoms Φ to be launched into the linear magnetic trap (LMT) can't exceed the value of $P/(h\nu N_c)$ where P is the laser power absorbed by atoms, $h\nu$ is the energy of the resonant optical photon, and N_c is the number of photons needed to diminish the speed of atom from the most probable value at room temperature (or that of the beam source) to almost zero. For 1 W laser power and Cs atom it gives the flux of $4\cdot10^{13}$ atoms per second. This is a very optimistic estimate. However, the requirement to work at a saturation intensity in the whole region of interaction, losses of the laser power that accompany proper tailoring of the laser beams and theirs polarization and losses on optical isolators decrease this flux at least down to 10^{12} atoms per second. In the case of trapping atoms in the MOT from a wing of the velocity distribution for room temperature (accepted version of the set-up)), the initial velocity (trapping velocity) for Cs is $V_c = \Gamma\lambda = 4.4 \cdot 10^2$ cm/s, where the light intensity is equal to the saturation intensity. Nevertheless, is doesn't give an essential decrease of the number of photons needed for slowing down one atom, because the atomic density outside the center of the trap is small and the part of the light that is absorbed is also small. More accurate estimation will be done during the experiment.

The total number of collected cooled atoms is limited by

$$N_\gamma = \Phi\tau_{trap} \,, \qquad (2.7)$$

with τ_{trap} being the lifetime of atoms in the traps. The large τ_{trap} of 10 …100s are achieved in a pure magnetic trap. In such a trap the total number of atoms can reach $10^{13} \ldots 10^{14}$ provided that such a simple estimation still works at a given large numbers of atoms. The pressure of the background gas should be 10^{-9}-10^{-10} Torr to provide the needed lifetime. However for the length of the trap equal to 1m the lifetime of 100 s means that velocity of atoms should be about 1cm/s Assuming that $\tau_{trap} =10s….100s$, $\Phi = 10^{12}$ s^{-1} and using (2.7) we get the value of $10^{13}….10^{14}$ for the total number of atoms in the trap. With dimensions of the trapped cloud of atoms being 1000 mm x 1mm^2 the concentrations can reach the value of $10^{13} ….10^{14}$ cm^{-3} and the number of atoms per unit of area in the cross section of the trap becomes $10^{15} ….10^{16}$ cm^{-2}. It should be noted that the flux of cooled atoms taken in this estimate is 50 times greater than maximum value obtained in the experiment.

The longitudinal temperature of an ensemble of atoms extended in one dimension is expected to be of the order of or less than the Doppler limit ($T_D =\hbar\gamma/2k_B = 124.4$ μK with most probable velocity V_D being 8.8 cm/s) but not less than the recoil temperature ($T_R =\hbar^2\gamma^2/Mk_B = .0194$ μK with V_R being 0.352 cm/s). The well known techniques of sub recoil cooling are not applicable for large ensembles that are of interest in this project. Especially this applies to the evaporating cooling technique, where lower temperatures are achieved at the cost of loosing a large number of atoms (the final amount of atoms is a very tiny part of the initial trapped ones).

Assuming the recoil limit for the longitudinal temperature it is easy to estimate β factor: $\beta= \gamma_\gamma (V_r\nu_\gamma/c)^{-1} = \gamma_\gamma/\gamma_D = 17.5$ MHz/228MHz=0.075. That is, even at such low temperature the natural linewidth of gamma transition is still smaller than its residual Doppler width. For higher temperatures β decreases as $(T)^{-1/2}$. Note that the spectral width of probing synchrotron radiation Γ_{probe} will be most likely greater than γ_γ and even than γ_D. In such a case β becomes less important and relative absorption will decrease on increasing the Γ_{probe}. The width of probing spectrum should be made as small as possible. Also it does not make sense to make γ_D much less than Γ_{probe}. At the big width Γ_{probe} the velocity range from 10 cm/s ($\approx V_D$) to 100 cm/s (T = 16 mK) is interesting. For a typical longitudinal trap dimension (about 1 m) the lifetime in the trap decreases at the big residual velocities. So the spectral width of the probing light should be minimized.

Thus for a given conditions and the most optimistic combination of parameters the relative number of absorbed gamma quanta will be

$$\delta N_\gamma/ N_\gamma = \Phi\tau_{trap}\sigma_\gamma \gamma_\gamma/ \gamma_D A= (10^{-3}…10^{-4}). \qquad (2.8)$$

The result for potassium could be thirty times greater.

The direct detection of such a variation of the flux of gamma quanta is not simple and alternative ways of detection of the events of gamma absorption should be inspected. An interesting possibility is to detect the burst of Cs atoms escaping the trap after getting the recoil of gamma photon. The most promising is the detection of scattered gamma photons. It should be noted that the combination of the best known parameters previously obtained in experiments was used for the estimation (2.8). It is a very complicated task to obtain simultaneously the maximum atomic flux, the lowest possible temperature and the longest lifetime of atoms in the trap.

2.3 The scheme for making a cold atomic ensemble.

At the choosing of the particular setup scheme it was clear that it should consist of two main parts: a source of atoms and a collecting trap. But there are few different types of sources and traps. Initially the parameter $nL/\sqrt{T_{\parallel}}$ was chosen as a criterion. It determines the absorption of a gamma radiation (n – concentration of atoms,

L – the ensemble length, $T_\parallel$ – temperature describing the longitudinal velocity distribution). But the estimations made afore showed that at this point the increasing of the number of trapped atoms is more important than the achieving of low temperatures cause of wide probe radiation spectrum. The laser light power should be about 1 W, and the vacuum level should be better than 10^{-8}, hopefully 10^{-9} Torr.

Two types of a setup were considered. They differ by 1) a source of cold atoms, 2) an additional longitudinal temperature decreasing technique. The system will consist of the following main parts:

i) Two-D quadrupole linear magnetic trap that will transversally confine the extended ensemble of cooled atoms. It has a possibility for a longitudinal probing with a resonance or quasi resonance optical field.

ii) The source of a cold atomic beam.

iii) The compression and injection system that should increase a brightness of the beam and efficiently transfer it into the pure magnetic trap with minimum loss of atoms and with blocking resonant optical photons from penetration into the main body of the trap. Will consider two possible basic schemes for making a cold atomic beam:
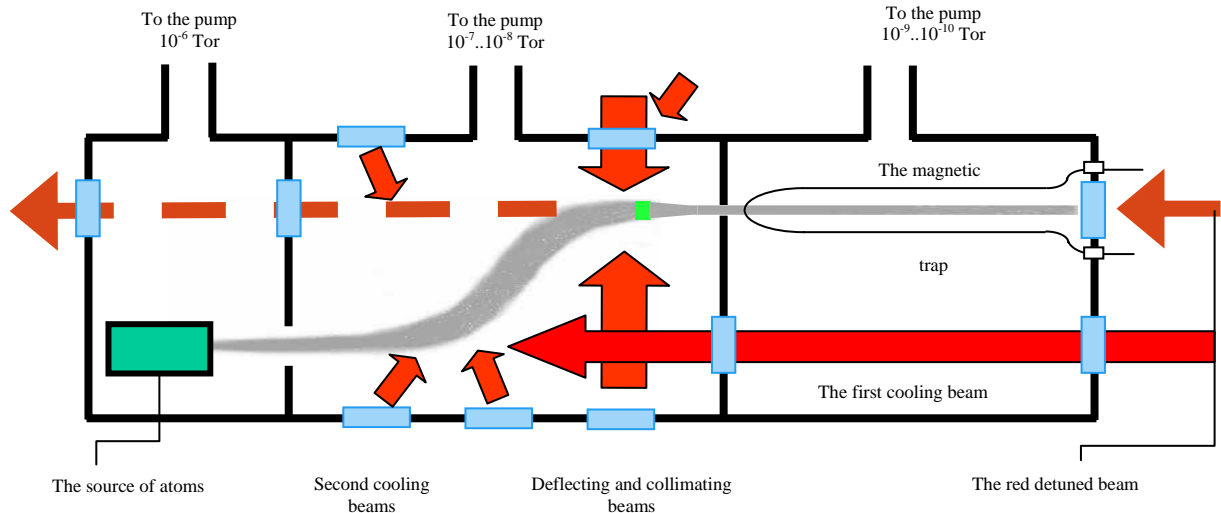
Fig. 4. The scheme of the setup.

A. Multi-channel aperture in the heater with Cs has to be a source of an effusion atomic beam. The main decelerating wave coming from the opposite direction is focused on this source. A circular polarization of the radiation and low longitudinal magnetic field provide cycling interaction between atoms and light. The light radiation has wide spectrum consisting of about 200 lines separated by 2-3 MHz intervals. The full power of the laser radiation in the vacuum system should be more then 0.5 W for providing saturation in each spectral component and in each corresponding group of atoms in the beam with the corresponding longitudinal velocity. The additional monochromatic co-propagating beam [18] will be directed along the atomic beam for providing deceleration and cooling. Using such a "relay" method or the "white light" method instead of Zeeman tuning technique removes strong dispersed magnetic fields and opens access for deceleration optical beams in transverse direction. It enables to improve the collimation of the atomic beam and decreases an influence of the transverse heating. The atoms will be decelerated down to the velocity of the order of several m/s and cooling down to values close to the Doppler limit. The diameter of the collimated atomic beam will be 10-15 mm.

The axis of the initial atomic beam and the pure magnetic trap axis are parallel for a possibility of a direct longitudinal probe of atoms in the magnetic trap with a help of gamma rays or far detuned form the resonance optical radiation and for decreasing a probability of the resonant light penetration in the magnetic trap. The main decelerated and the oncoming additional laser beams don't go through the magnetic trap. Formed on the first stage the atomic beam is deflected with a help of two tilted laser beam coming from the opposite direction. The atomic beam is cooled by two longitudinal oncoming laser beams in a molasses regime and the atomic velocity decreases down to 10-30 cm/s. At the end of this part the atomic beam goes in the transverse direction molasses region and compressed by transverse magnetic trap. Further it is focused on the iris that separates the injection section from the pure magnetic trap. We have refused the scheme A, because a heating source generates a large number of background atoms (it is especially undesirable for a cesium because of great pressure of a saturated vapor at room temperature 10^{-6} Torr). Available amplifiers with a linear inclined active area provide essentially smaller power: 120 mW. The second reason we've leaved scheme A is a degradation of the amplifiers with an expanding output end (see "Laser system"). We had no possibility to slow down a worm beam with a "white" light that requires a total power to be not lower than 0.5 W. Amplifiers that we have give essentially lower power: 120 mW.

B. An alternative source of an atomic beam can be made from a magneto optical trap of atoms (MOT) with a special design of a leakage in the atomic confinement force. One way to do it is to plug the central part of one of

the six beams forming the trap. Atoms are ejected along this shadow by unbalanced force of radiation pressure due to the action of the opposite (not shadowed) laser beam. In a more efficient modification of this technique the central parts of the two counter propagating beams are blocked and filled with laser radiation that is shifted in frequency.

The scheme of the vacuum glass part of the trap is depicted on Fig. 5a, b. It consists of three parts: 1) two dimensional magnetic trap that cools atoms and localize them in the narrow long part of the system; 2) buffer part, where the beam is focused and tilted; 3) pure magnetic two dimensional trap. Further they are described separately.
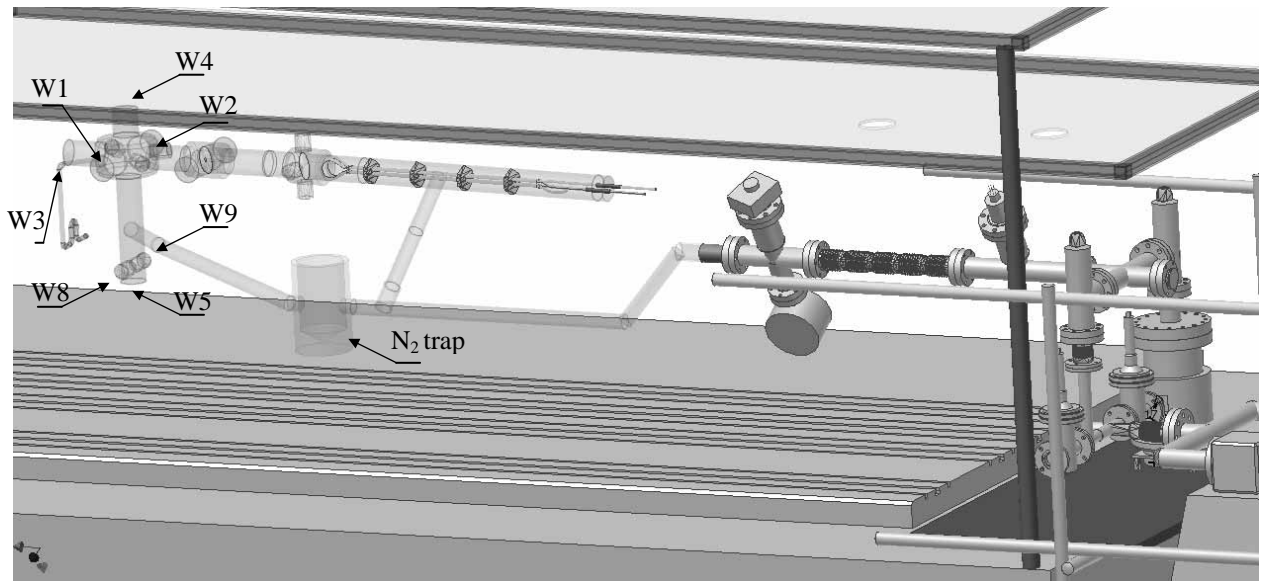
Fig. 5a. The pump system and the glass trap body.
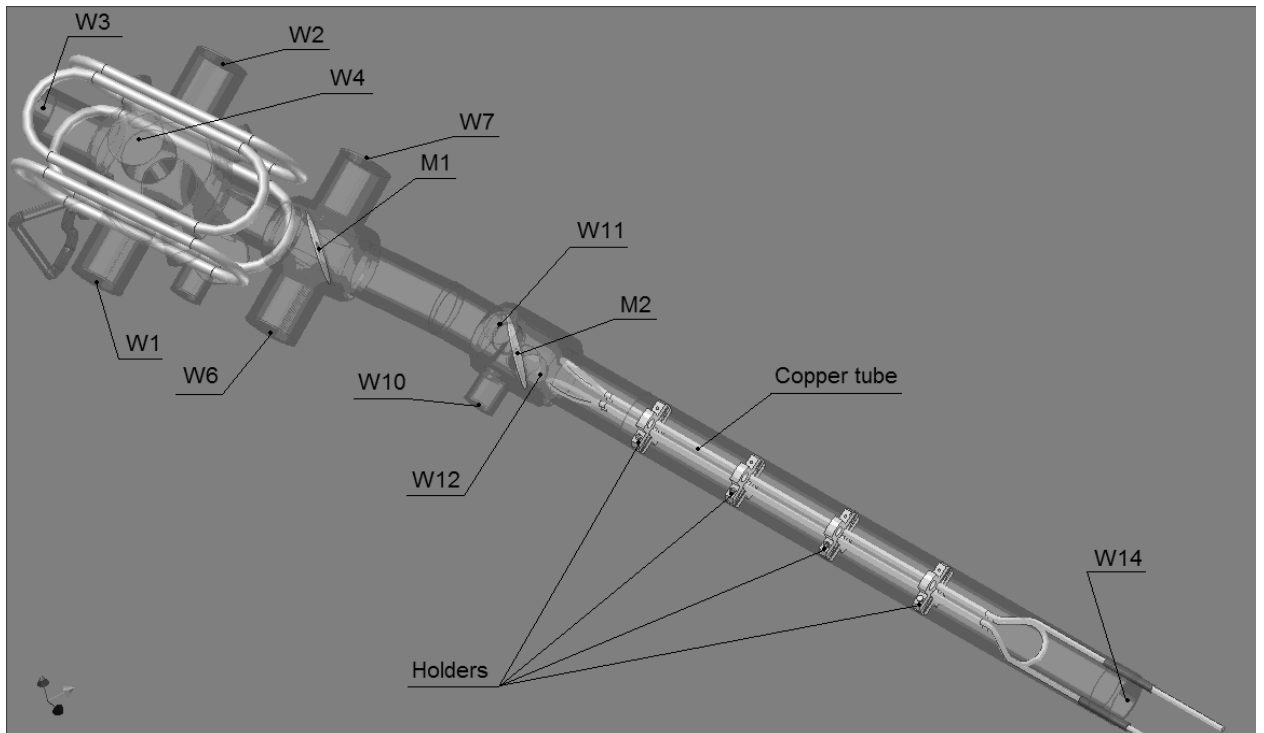
Fig. 5b. The vacuum part of the setup.

There are eight laser beams with three different frequencies in the first part of the vacuum setup. Four wide beams with the frequency ν_m go perpendicularly to the axis of the two dimensional trap though windows W1, W2, W4, W5. These beams have a circular polarization and a nearly elliptical cross section. The major ellipse semiaxis is parallel to the trap axis and about 5 cm long. The window the upward beam is going through (W5) is shifted from an atom localization place by 30 cm for the purpose of using the time-of-flight method for estimation of an atomic ensemble temperature. There are windows W8 and W9 for a probing a fluorescence of falling atoms. Two counter propagating hollow beams move in a longitudinal direction making a molasses (there is no magnetic field gradient in this direction). One of them goes through the shifted window W6 and then it is directed along the trap axis by

mirror M1 with a hole. The narrow laser beam with a detuned frequency goes through this hole. This beam comes in through the window W10 and directed to the first part by mirror M2. A combined laser beam going from left to right and entering through the window W3 is formed by the same way (but outside the vacuum system). Central parts of these beams (diameters are equal 6 mm) are filled with a radiation with shifted frequencies. There are two counter propagating waves (from left to right and reverse) with frequencies $\nu_m + \delta$ and $\nu_m - \delta$. Frequency shifts of these waves are equal by magnitude and opposite by sign (one dimensional molasses configuration). We talk about frequency shifts $\nu_m \pm \delta$ relatively to a molasses making frequency ν_m in a lab reference frame. The frequency ν_m is shifted from a resonance atomic frequency ν_0 corresponding to the cycle transition $6S_{1/2} \rightarrow 6P_{3/2}$. This shift is about natural width of the $6P_{3/2}$ state. It is possible to increase the magnitude of this shift increasing the light intensity. Atoms are launched rightwards through the mirror hole with a speed $c(\delta/\nu)$, which is changed by adjusting the detuning δ. The moving molasses case gives a larger atomic flux and a lower longitudinal temperature.

To return atoms from the F=3 sublevel of the ground state, where they are collected due to optical pumping, all beams are mixed with an additional laser radiation that resonant with a $6S_{1/2}$ (F=3) $\rightarrow 6P_{3/2}$(F=4) transition.

The second central part is confined by mirrors M1 and M2 with holes. The left one (M1) with a 6 mm diameter hole separates this part from the two dimensional magneto-optical trap (i.e. from a first part). The right one (M2) with a 1.6 mm diameter hole is the entrance to the pure magnetic trap. Also this mirror directs the narrow beam to the MOT. The axis of the pure magnetic trap is turned by small angle relatively to the MOT axis to eliminate ingress of the moving from the left central beam to the pure magnetic trap. It's necessary to eliminate one of the mentioned afore cold atoms leakage paths. At the central section the cold atomic beam is deflected by small angle and focused on the second tilted mirror hole. After this mirror the pure magnetic trap begins.

The third part is the pure magnetic trap. There is a for wires current line inside a 50 mm glass tube to create a desirable magnetic field configuration. Conductors are made from a single cooper tube with an external and internal diameters equal 5 and 3 mm correspondingly. Axes of four linear conductors go through apexes of a square with a 9 mm side. To establish these conductors four metallic mounts is used. They made from an oxygen-free cooper. For an electrical insulation of the current line a kapton film is used, because it maintains its insulation features in a wide temperature range (from a liquid nitrogen temperature to a baking temperature, which is about 400°C). The kapton film was bought from the "Dr. D. D. Müller GmbH". The current carrying line was chosen in a form of a tube because it had to be cooled. A trapping force in the transverse direction and the transverse atomic ensemble size are determined by magnetic field gradient and directly proportional to the current value. It will be 100 A. At this point we should avoid heating of the current line and cool it with a nitrogen vapor to the temperatures about -50° C, when a temperature of a Cs saturated vapor is lower then 10^{-10} Tor. At room temperature this pressure is 10^{-6} Tor. Cesium atoms on walls of the third magnetic trap and high background concentration of hot cesium atoms rapidly reduce the atoms lifetime in the trap and therefore total number of atoms in the trap. Cooper conductors go to the vacuum section through kovar enters on the right end of the glass part of the setup. Central part of this end has an optical quality and used for a probe beam injection. The narrow probe beam should go along the magnetic trap and go out through the hole in the mirror M2. Further it should be reflected by mirror M1 and go out through the window W7. The small angle between the pure magnetic and the magneto-optical trap axes give a possibility for such a probing technique.

2.4   The pump system.
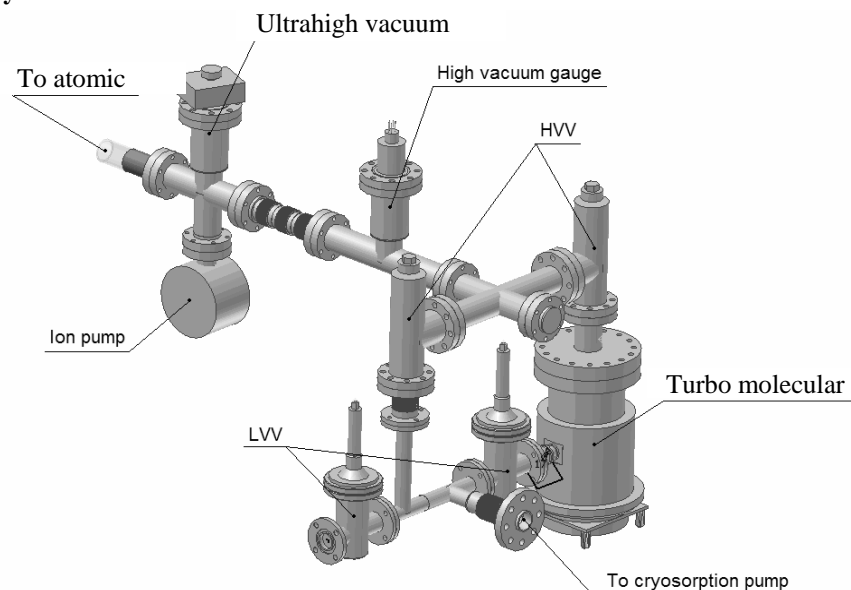
Fig. 6a. The scheme of the pump system.

The vacuum system should give a $10^{-7} \ldots 10^{-8}$ Torr at the sections with laser fields and atomic source (Fig. 3) and $10^{-8} \ldots 10^{-10}$ Torr at the magnetic trap section. The pumping system is shown on the Fig. 6a, X+1, X+2. On the Fig. X the two dimensional principle scheme is shown, on the Fig. X+1 – three dimensional elements location. The picture of the pumping system is shown on the Fig. X+2. Mechanical forepump pumps the cryosorption pump through the nitrogen trap (are not shown on figures). The forepump is separated from the system during the pumping. Valves LVV are low vacuum, HVV – high vacuum. A bypass for a prior pumping consists of the left LVV and the HVV valves. Further the turbo-molecular pump (150 h/p) is used for pumping. The ion pump and the ultrahigh vacuum gauge go after. All connections in the high vacuum section are made with a help of cooper gaskets that gives a possibility to bake the system. The connection to the glass body of the system is made using the kovar crossing.
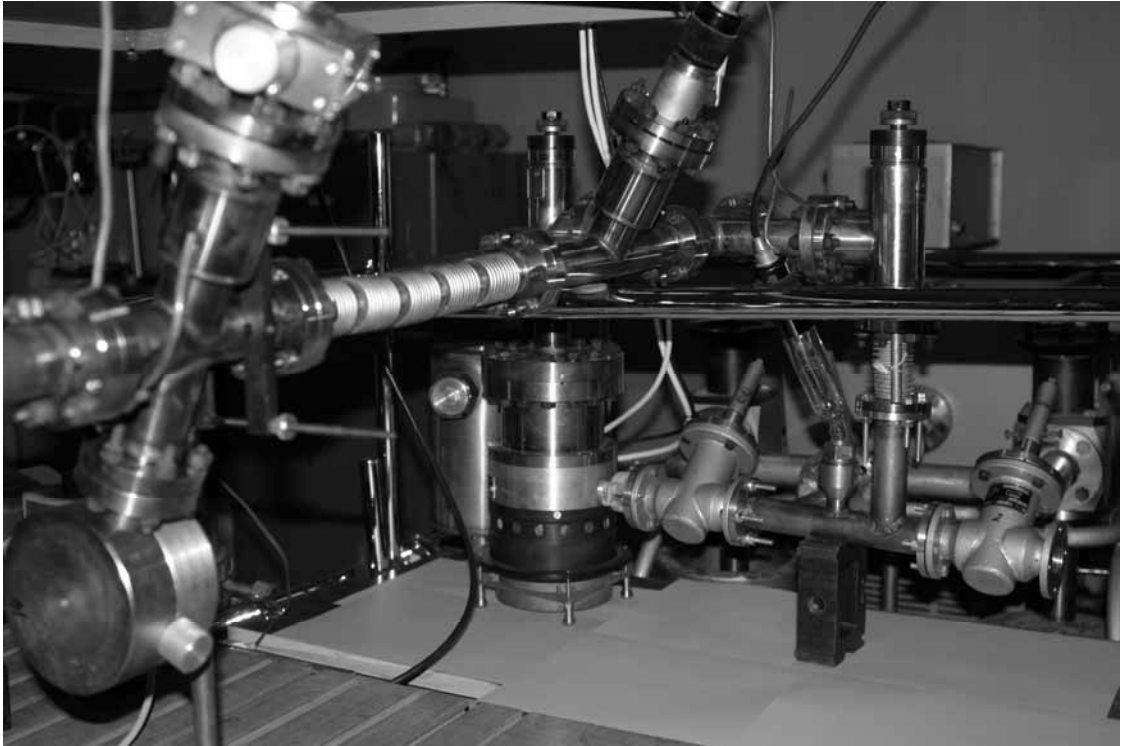
Fig. 6b. The pump system.

There is a turbo-molecular pump at the center of the pumping system picture (Fig. 6b). It's mounted on the individual base, which is separated from an optical table. There are two tilted low vacuum valves on the right from it.

2.5   The laser system.
2.5.1   The scheme providing desirable laser frequencies.
Four laser beams with a frequency $\nu_m \approx \nu_0 - \xi\Gamma$, two longitudinal beams with the same frequency and two narrow beams with a frequency $\nu_m \pm \delta$ are needed to make the two dimensional magneto-optical trap. ξ is in the range 1-5 at achievable saturation parameters and is determined by the intensity; δ depends on the desired velocity of atoms in a cold beam. For the launching speed $V_{out} = 2$ m/s the detuning is $\delta = (V_{out}/c) \cdot \nu_0 = 3$ MHz. Deflection and focusing of the beam in the buffer setup section of the setup is made by using the same frequency ν_m radiation.

The hyperfine splitting of the ground state is 20 times greater than Doppler width of hot atoms. Hence, if they are pumped into the $6S_{1/2}$ (F=3) state they stop to interact with the ν_m frequency radiation and escape the trap. For eliminating an optical pumping to the $6S_{1/2}$ (F=3) state the radiation resonant with open transitions $6S_{1/2}$ (F=3) $\rightarrow 6P_{3/2}$(F'=3,4) (D$_2$-line) or $6S_{1/2}$ (F=3)$\rightarrow 6P_{1/2}$(F'=3,4) (D$_1$-line) is needed. Also a tunable laser (the tuning range is about 10 GHz) is required for longitudinal probing of the ensemble of cold atoms (i.e. measuring the main feature – the number of atoms per unit of the cross section the extended ensemble).

The master laser generates the frequency ν_m, which is stabilized using a sub Doppler resonance that is shifted by magnetic field (see section 2.5). The beam of this laser (5mW) passes through an optical isolator, is injected into the slave laser, and locks its frequency. The slave laser beam (power is about 30 mW) goes through the second optical isolator and is then divided into three beams that are injected into traveling wave amplifiers. Two of the beams with a power of 100-120 mW are split in six beams and directed to the trap. The four transverse beams pass through quarter-wave plates and telescopes for expansion right before the trap and then go inside through windows W1, W2, W3, W4, W5 (Fig. 5a, b). Two other beams go through telescopes and are directed along the trap axis. These beams enter through windows W3 and W6 and the mirror M1 is used for changing a direction of propagation. Central parts of these beams are blocked.
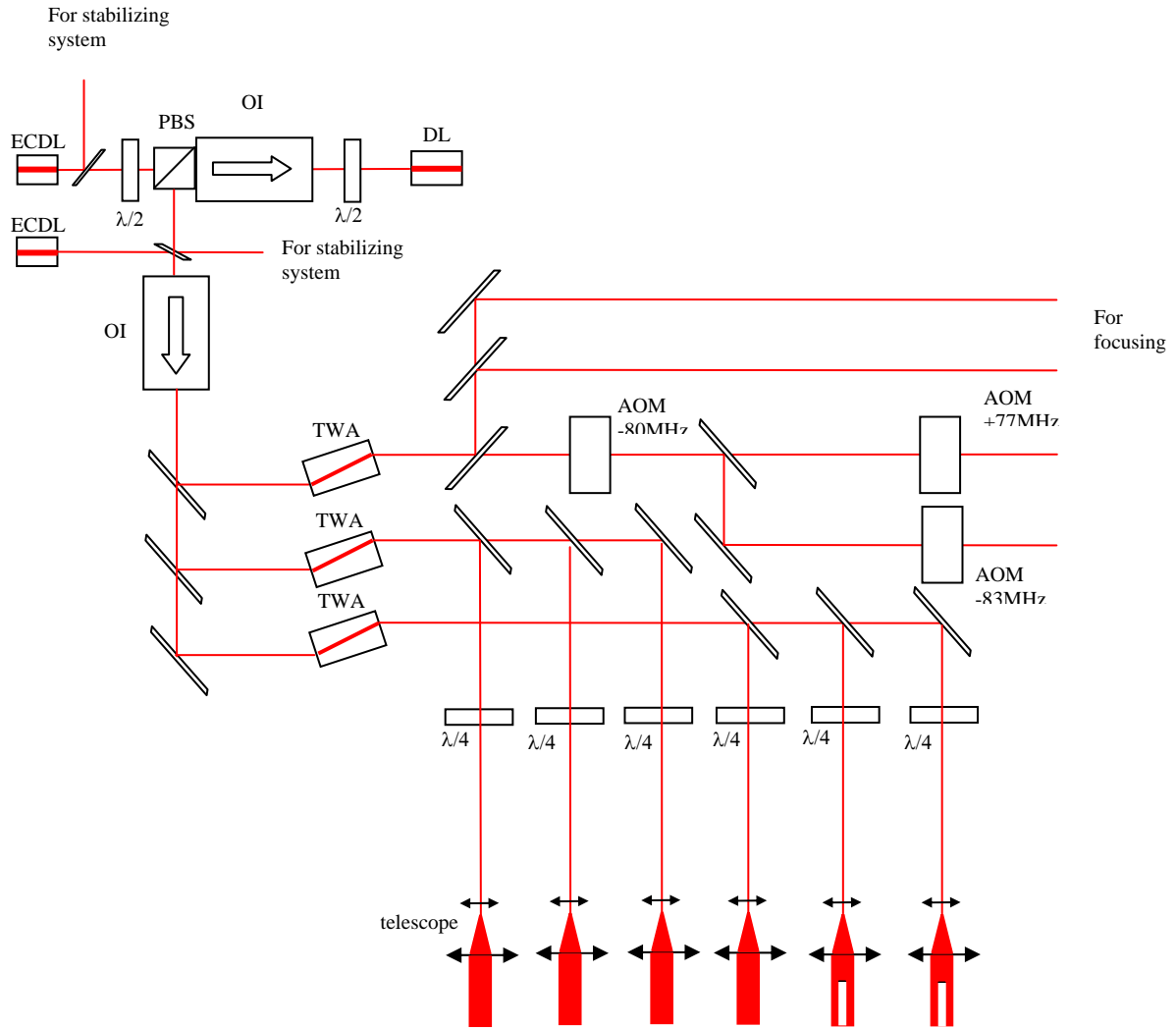
Fig. 7. The scheme of the laser system.

A part of radiation of the third traveling wave amplifier radiation is directed into the second vacuum system section to focus and to inject the atomic beam into the magnetic trap. The rest part of the light goes through an acousto-optic modulator (AOM) that decreases frequency by 80 MHz. After the AOM the beam is divided into two equal parts. Each of them passes through its own AOM. One of AOMs increases frequency by $80 + \delta$, the other – by $80 - \delta$ MHz (e.g. for the average launching speed 2 m/s: by 83 MHz and 77MHz). These two narrow beams go along the trap axis inside the holes (the blocked parts) in wide beams.

The second master laser is used to get the beam that eliminates optical pumping. Its radiation is mixed with the first master laser radiation on the beam splitter between the slave laser and the second optical isolator. Thus, all the beams have the part of radiation from the second master laser, and its intensity is thirty times smaller than the total intensity.

2.5.2 Master lasers and their parameters.

Three laser controllers have been made for master lasers. Each of them includes a stabilized current source (the maximal current is 150 mA) and a controller for the extended cavity. Additional controllers have been made for traveling wave amplifiers with maximum current of 1.5 A. The master laser construction is shown on Fig. 8.

The laser body is made from a solid piece of duralumin. It plays a role of a heatsink for thermo-stabilization of a diode laser and of a base-plate for all mechanical parts. Its temperature is stabilized with an independent feedback loop. It stabilizes the extended cavity length, position of diffraction grating, and the feedback level. In this way it provides the long term stability of the single-mode regime and its frequency. The laser body in turn is (and should be) mounted on a massive metallic base-plate for heat transfer. The time constant for the body thermo-stabilization is much greater then the time constant for the diode laser thermo-stabilization. It provides stability for their combined work. The laser outlook is shown on Fig. 9.
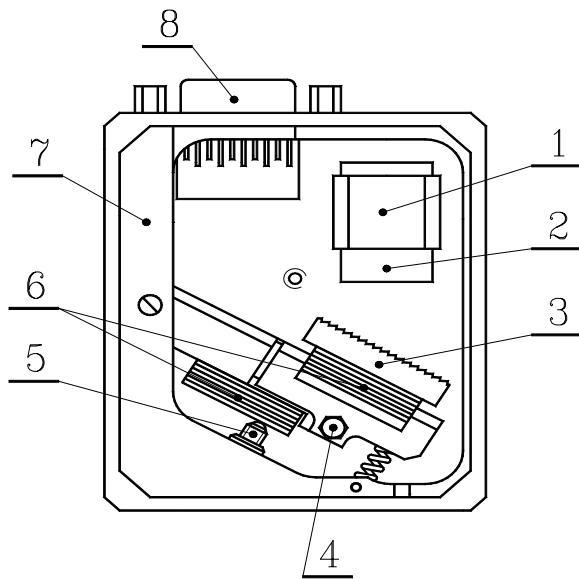
1. Laser diode and objective.
2. Peltier module.
3. Grating.
4. Clamping screw.
5. Screw pair.
6. PZT.
7. Body.
8. Connector.
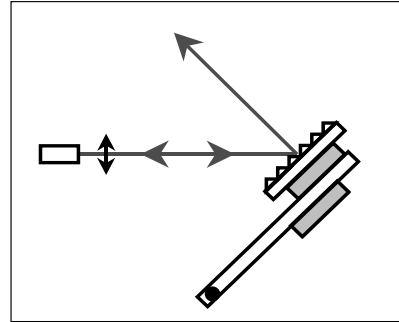
Fig. 8. The master laser construction. The optical scheme is shown in the inset.

Fig. 9. The master laser (extended cavity diode laser).
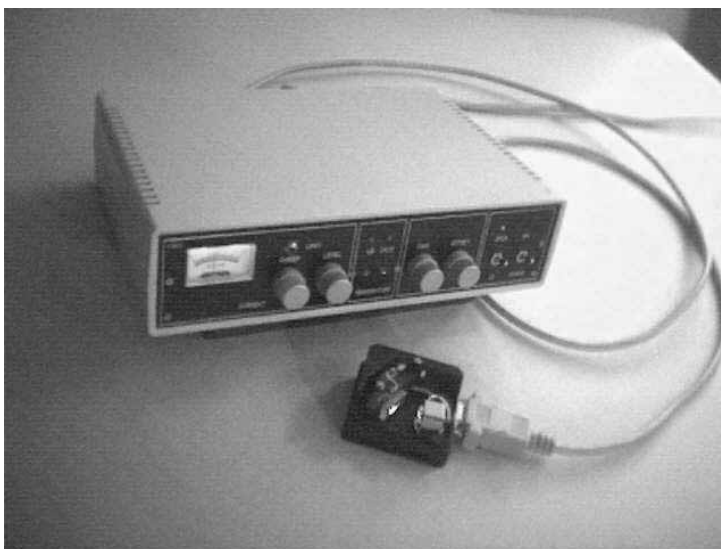
Fig. 10. The laser (and amplifier) controller.

The experience shows that using common laser current sources leads to degradation of laser diodes due to several reasons. Therefore special laser controllers were developed (Fig. 10). They provide following features: the current range 0-180 mA (0-1.5A for amplifiers); the current set-on accuracy 0.1 mA (1 mA for amplifiers); mean-square current fluctuations in the 1 MHz band do not exceed 2 µA; current fluctuations at the line frequency are less than 5 µA; the frequency range for the current modulation is 0-50 kHz with the 10 kΩ input resistance and with the 15 mA/V gain coefficient. There are an adjustable current limit and a protection from current spikes during the external voltage instabilities, not-planned power switching off etc.

The laser operation is based on a traditional Littrow scheme, where the radiation goes out through a zero order of the grating. Loosing the clamping screw enables rough tuning of the laser frequency. Two PZT's change both the cavity length and the grating angle at the same time which gives a continuous tuning range of about 10 GHz. With simultaneous scanning of the laser current this range increases up to 30-40 GHz.
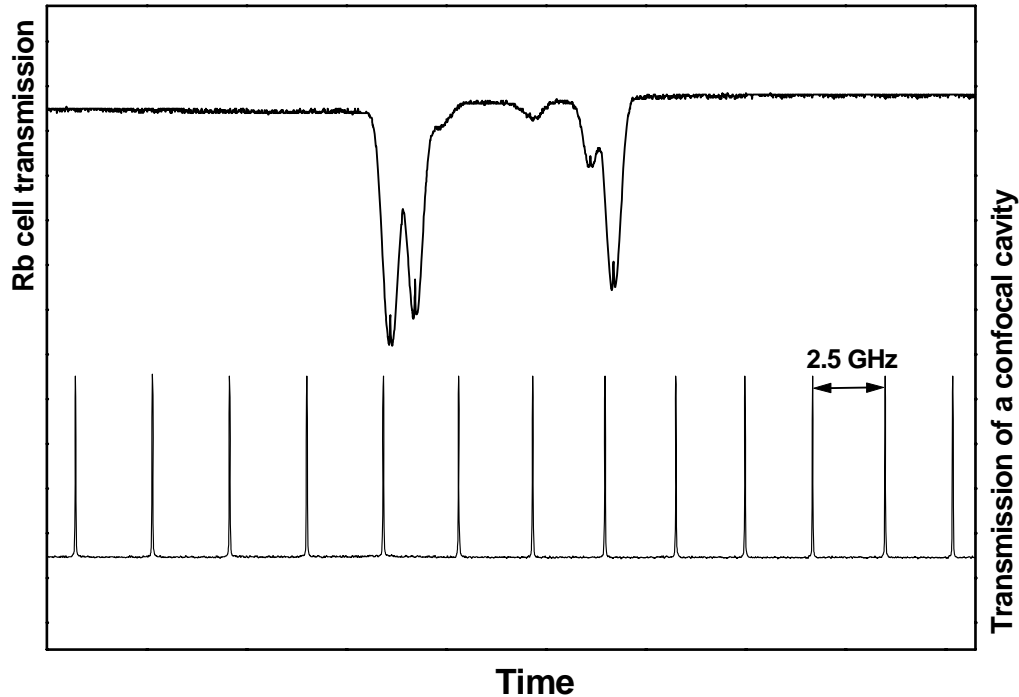
Fig. 11. The upper curve is rubidium-cell transmission spectrum. The lower curve is transmission of the interferometer (FSR = 2.5 GHz).

Master lasers for Rb. ECDLs for D_1- and D_2-lines of the Rb were made first. They showed better frequency stability and more reliable single-mode operation in comparison with ECDLs on a pyroceram base plate that were used in the laboratory before. An estimation of the passive frequency stability was made using a lambda-meter and subdoppler resonances in Rb vapor. An estimation of the laser line width was made using a heterodyne technique.

The transmission spectrum of a cell containing ^{85}Rb and ^{87}Rb (enriched with ^{87}Rb) is shown on the Fig. 11. Four Doppler broadened lines on of the spectrum correspond to all hyperfine transitions of rubidium D_1-line: $5S_{1/2}$ (F=1,2)→$5P_{1/2}$(F'=1,2) (there are Doppler-free resonances at the center of each contour). Two lines between them are the lines $5S_{1/2}$(F=2)→$5P_{1/2}$(F'=2,3) and $5S_{1/2}$ (F=3)→$5P_{1/2}$(F'=2,3) of ^{85}Rb. The P sublevels are within the Doppler width.

A beat note of two identical ECDLs is shown on Fig. 12a, b. The Lorentz approximation is given in Fig. 12a. The width of the Lorentz curve provides a simple estimation of the laser line width. It is less than 60 kHz. There is an additional broadening at the center of the curve that is caused by technical fluctuations. It is fitted with a 700 kHz Gaussian (Fig. 12b). A part of these fluctuations is caused by periodic voltage fluctuations of the PZT with an amplitude 2 mV, which corresponds to the 400 kHz contribution to the width (the tuning coefficient is 100 kHz/mV).

A systematic temperature drift results eventually in the mode-hopping even in the case of active frequency stabilization. The mode-hopping is caused by sufficient thermal cavity expansion that can not be compensated with maximum translation of PZT. The traditional way to improve a passive stability is to use materials with a small thermal-expansion coefficient for a laser base-plate (e.g. pyroceram and invar). But the temperature drift of other mechanical parts that are made from usual materials (the copper heat sink, metallic clip and alignment screws etc.) leads to undesirable change of the feedback level. This decreases laser power, increases the amplitude and frequency noise, and can result in mode switching. A common way to solve this problem is the thermo-stabilization of the whole body of the extended cavity. It can be a complicated technical task in the case of large dimensions, complicate configuration and low thermo-conductivity of some parts. A simple and compact construction of a laser

makes this task simpler. The laser wavelength drift measured with the lambda-meter (it was bought in this project) is shown on the Fig. 13. The drift was being measured during seven hours of CW operation. During the last three hours the frequency shift was smaller than 100 MHz/h.
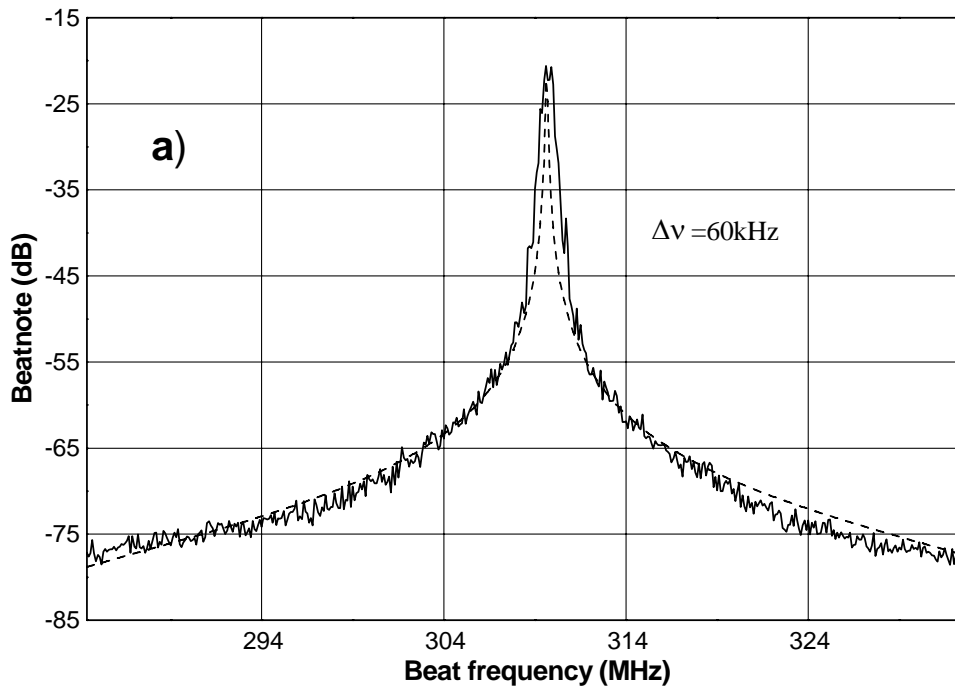
Fig. 12 a).
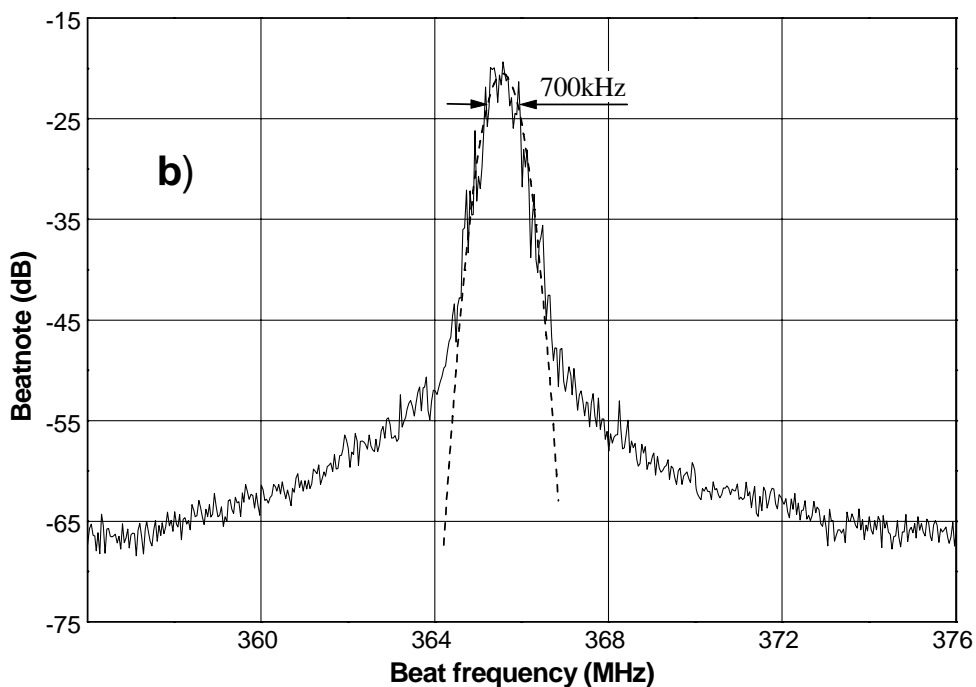
Fig. 12b).

This corresponds to the relative frequency fluctuations of about 10^{-7}. It is remarkable, because the temperature in the laboratory is not stabilized and its fluctuations during the day are about 5 °C. The high frequency noise on the curve is not the laser noise but the noise of the analog –to- digital converter of the lambda-meter.

Two ECDLs (working on D_1- and D_2-lines of Rb) work reliably in the magneto-optical rubidium trap during the day without and additional cavity alignment (see section 2.7).

Master lasers for Cs. Two master lasers working on cesium D_2-line were assembled and tested after first experiments with Rb lasers. Threshold currents are lower than 30 mA. Lasers work in a single mode regime and their wavelengths correspond to the cesium line 852.1 nm at operating currents 43 and 75 mA. Output powers are

equal 5 and 12.3 mW respectively. The continuous tuning range is more than 10 GHz and covers both hyperfine components of the cesium D_2-line. These features for both lasers are shown in Table 5.

740 MHz
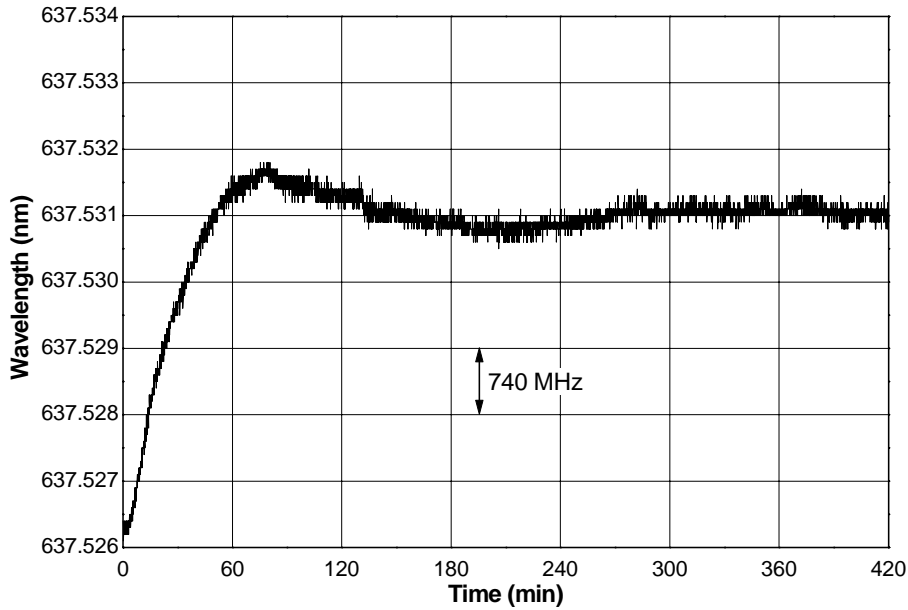
Fig. 13.
Table 5.

Laser	Threshold current I_{th}, mA	Operating current I_{op}, mA	Temperature t, ^{o}C	Power P, mW
1	26	43 48	25.0	5 6.5
2	28	48 53	26.1	6.5 7.6

The table gives two operating current values and two power values for both lasers that correspond to the tuning on different hyperfine components. Linewidths of both lasers were measured in free operating mode (without active frequency stabilization). Measurements were made in two ways: 1) by the beat note spectrum of two lasers; 2) by observation of the coherent population trapping resonance in cesium vapor. The experimental setup for the beat note spectrum observation is shown on Fig. 14. The beat note spectrum is shown on Fig. 15.

Спектр биения двух полупроводниковых
лазеров с внешним резонатором.
Ширина лоренцовского контура Δν = 1 МГц
Полоса анализатора 300 кГц
Время записи 50 мс
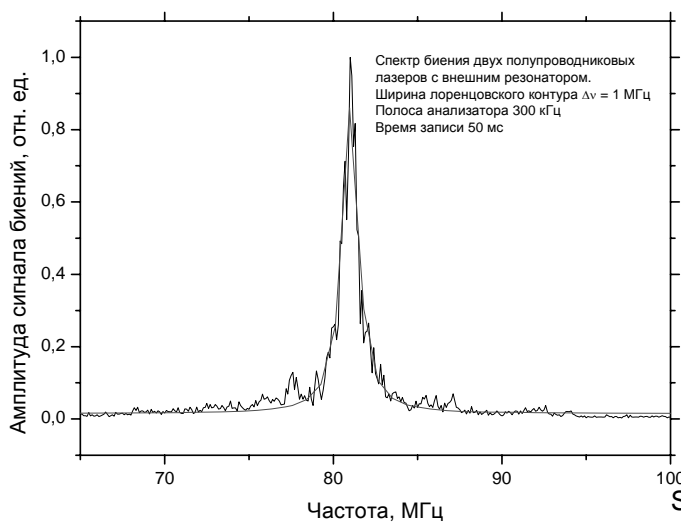
Fig. 15 Master lasers beat note spectrum.
The spectrum width is lower than 1.5 MHz.
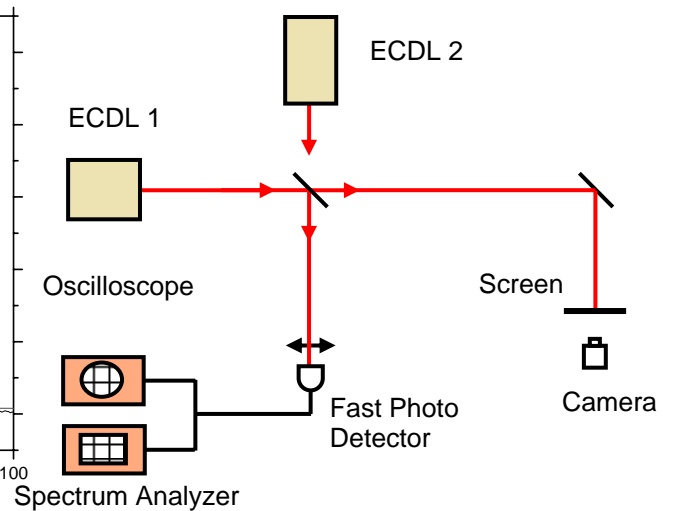
Fig. 14. The experimental setup for the beat note observation.

The coherent population trapping resonance (lambda resonance) excitation scheme is demonstrated on Fig. 16. Because the Doppler broadening is greater than hyperfine splitting of the excited state ($6P_{3/2}$ F'=3, 4), both sublevels (F'=3, 4) are involved in the lambda resonance. Other two sublevels ($6P_{3/2}$ F'=2, 5) give no contribution to the resonance, because each of them is dipole-coupled only to   one of the hyperfine sublevels of the ground state (cycling transitions).

The experimental setup for observation of coherent population trapping resonance is shown on Fig. 17. Co-propagating laser beams go through the cesium vapor cell. One laser was tuned to the F=4→F'=4 transition, the other one was scanned around the F=3→F'=4 transition. The transmission of both beams was measured. The lambda resonance is shown on Fig. 18. Both of described methods provide the linewidth value of about 0.5-1 MHz. Such a temporal coherence is enough for the deep laser cooling. A third assembled master laser was built for cesium D_1-line. It is used for an optical pumping compensation. Except the wavelength (895 mn) all properties are close to those given in Table 5.

Cesium D_2-line lasers have passed passive wavelength stability test. They are used as master lasers in the laser system described above.
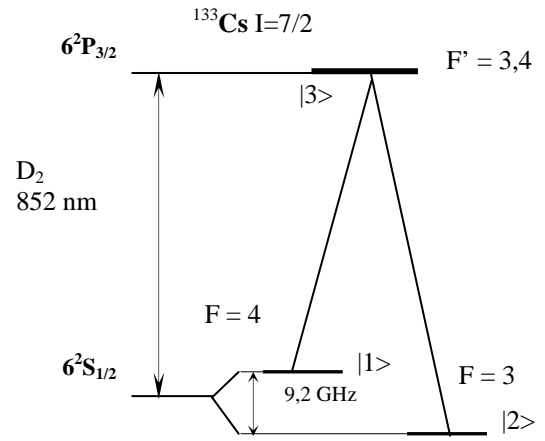
Fig. 16. The lambda scheme.
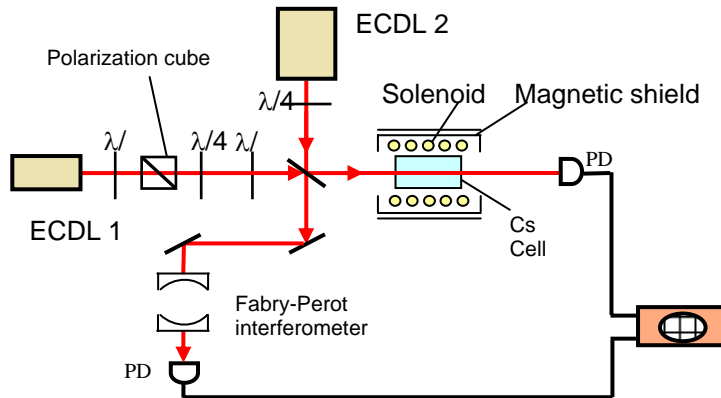
Fig. 17 The experimental setup for observation of coherent population trapping resonance
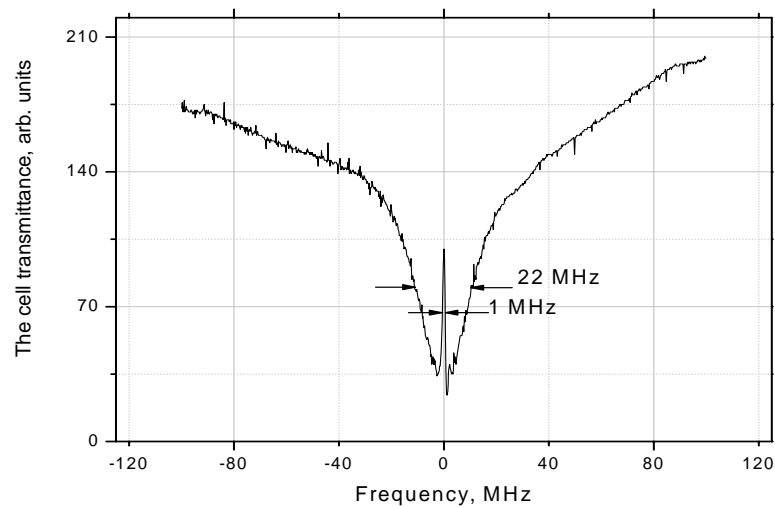
Fig. 18. The coherent population trapping resonance, or the lambda resonance.

2.6.   Frequency stabilization.
2.6.1   Frequency stabilization of master laser
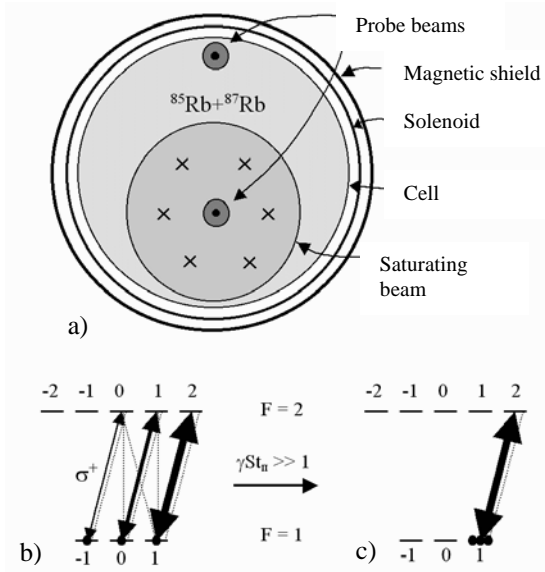
Fig.19. Mutual arrangement of the saturating and probe beams in an atomic cell (a); the relative transition probabilities in the system of magnetic sublevels of the ground state of rubidium in a circularly polarized field resonant with the cyclic $5S_{1=2}$ (F ̂ 3) À $5P_{3=2}$ (F н ̂ 4) transition ($_{85}$ Rb) (b); the transfer of atoms on the extreme sublevel due to repeated absorption-emission cycles (c). The solid and dotted arrows are stimulated and spontaneous transitions, respectively.
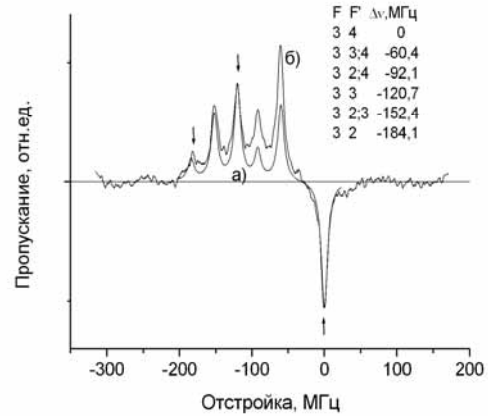
Fig. 20. Comparison of the theoretical and experimental saturated absorption spectra at the D2 line of $_{85}$ Rb in the zero magnetic field. Three of the six resonances indicated by arrows correspond to the hyperfine-structure transitions F= 3 -> F` = 2, 3, 4. The rest of the transitions are crossovers. For all the resonances, except F= 3 -> F` = 4 (zero detuning), the redistribution of atoms among the ground-state sublevels and the transition to the excited state reduce absorption.

Many applications, in particular, laser cooling of atoms require simultaneously the high frequency stability and the possibility of precision frequency detuning from the atomic resonance (+40…-150 MHz).

The stabilization scheme is based on the Zeeman shift of levels in a homogeneous magnetic field. A sub-Doppler resonance is produced as the difference between the intensities of two probe beams of a small diameter transmitted through an atomic cell. A saturating beam of a large diameter propagates towards one of the probe beams. All the three beams have the same circular polarization (Fig. 19). This method provides the compensation for the Doppler broadened response of the system to a change in the magnetic field, which is independent of the saturating field. In particular, the modulation of the width and amplitude of the Doppler profile of the line caused by a change in the distance between magnetic sublevels is suppressed in the difference signal. The scheme of the resonance formation, in which atoms are accumulated in one magnetic sublevel, allows the variation in the resonance frequency by a magnetic field without the resonance broadening. The stabilization scheme is close to that considered in [Din92, Ike89].

Upon frequency stabilization, a transmission minimum at the line centre is useful for minimization of shot noise in the detection scheme. The sub-Doppler absorption peak is separated from the rest of resonances in the D2 line (Fig. 20).

Figure 21 shows the stabilization scheme including the three-beam scheme to shape the reference signal in one cell and the two-beam scheme to observe the reference polarization resonance in the second cell. The rotation of the polarization plane of probe beams in two successive quarter wave plates provides the separation of the probe and saturating beams with the help of a polarization beamsplitter cube. A combined use of a screen at the central part of the saturating beam and a blocking aperture not only eliminates a competing mechanism of two-level nonlinearity (see section 5) but also suppresses a parasitic optical feed- back in the laser.

The shift of the resonance at the extreme magnetic sublevel is proportional to a constant magnetic field of a solenoid in which the reference cell is placed. A modulating signal at the frequency 15 kHz, which produces the error signal, is fed to this solenoid. Therefore, the laser frequency is not modulated and the laser line is not broadened. The frequency shift of the reference resonance in the magnetic field equal to 1.4 MHz/G coincides with its theoretical value. The instability of the current source of a coil is 10 mA, corresponding to the instability of the magnetic field in the cell equal to 150 mG. The background longitudinal magnetic field in the reference cell is screened down to ~2 mG.
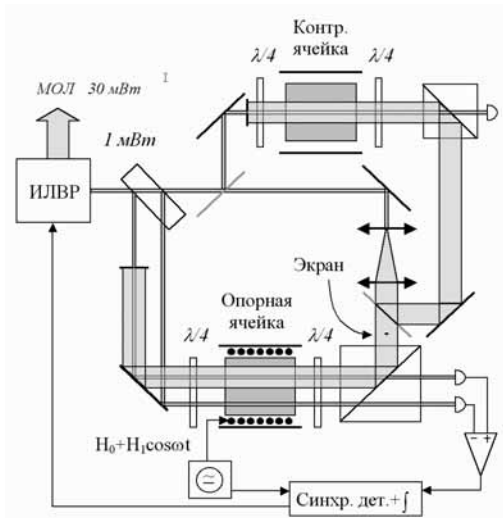
Fig. 21. Scheme for frequency stabilisation of an diode laser with an external resonator (DLER) by the sub-Doppler absorption resonance in an atomic cell.
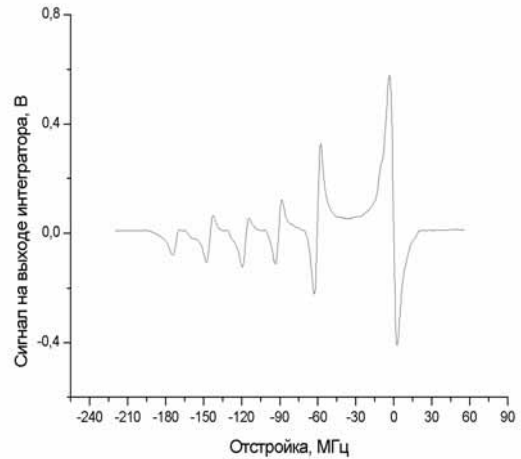

Fig.22. Discrimination curve for resonances at the $5S_{1/2}$ (F =3)->$P_{3/2}$ (F` = 2, 3, 4) transition obtained by modulating the longitudinal magnetic field in the reference cell with 85 Rb and detecting synchronously the difference absorption signal of two probe beams. The saturating beam intensity is 0.1 mW cm^{-2} and the recording time is 120s.

The error signal of the AFC system was fed, after synchronous detection, integration, and amplification (Fig. 22), to a piezoelectric element controlling the resonator length. The feedback band of the system at the -3dB level was 2 kHz. The frequency detuning in the capture regime was determined by using the nonlinear absorption resonance in the control atomic cell formed by two counterpropagating beams with the same circular polarization. The beam diameters and intensities were as those in the reference cell (Fig. 21). The background longitudinal magnetic field in the control cell was screened down to ~ 20 mG. Figure 23 shows the transient characteristic of the stabilization system observed upon a fast change in the current in the solenoid of the reference cell. The time constant of the integrator in the stabilization system was 1 ms and the duration of the aperiodic transfer process was a few milliseconds. Right part of Figure 23 shows the scheme of frequency calibration using the resonance slope in the control cell.

The width of the noise path during the frequency tuning to the resonance slope in the reference cell (laser frequency fluctuations) was 300 kHz in the 15-kHz bandwidth of the detector. In the white noise approximation, this corresponds to 2.5 kHz in the 1-Hz bandwidth. Therefore, the instability of the laser frequency was $7 \cdot 10^{-12}$ Hz$^{1/2}$.

The study of the dissipative light pressure force of a new type assumes laser frequency stabilization in the region of detuning close to zero. In the stabilization system described above, this corresponds to the absence of a magnetic field in the reference cell. In the absence of an appreciable longitudinal component of the magnetic field, the transverse background component can change the selection rules in the interaction with a circularly polarized field; therefore, the laboratory field should be screened. The residual magnetic field splits Zeeman sublevels; thereby restricting the minimum intensity of a saturating field, i.e., the rate of optical pumping in the ground state should exceed this splitting.

A slight deviation of polarization of a light field from purely circular polarization, i.e., the presence of a linearly polarized component in it, in the region of a zero magnetic field leads to formation of coherent
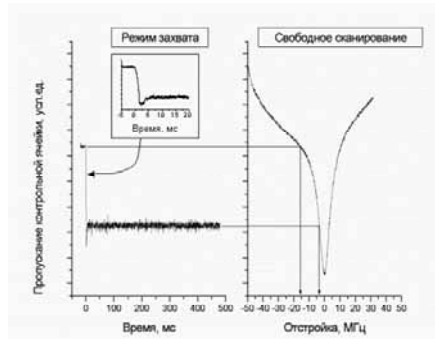
Fig. 23. Transmission in the reference cell during a `step' variation of the magnetic field in the reference cell in the regimes of stabilization and free scan of the laser. Figure 5b shows the method for determining the frequency detuning. The inset at the left top shows the initial stage of frequency switching.
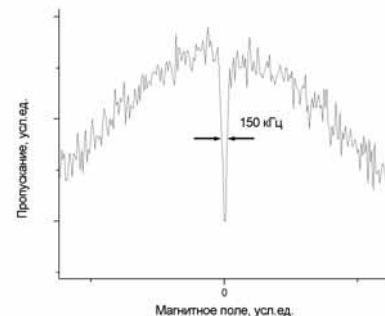
Fig.24. Typical shape of the photoinduced absorption resonance in the reference cell in the case of incomplete elimination of the linearly polarized component in a saturating field.

53

superposition states with increased or decreased absorption. The presence of such states violates the operation of the stabilization system. These effects are known in the literature as electromagnetically induced absorption (EIA) [Aku98, Lez96] and electromagnetically induced transmission (EIT) [Ari96]. In the system for frequency stabilization and tuning based on the Zeeman effect, EIA leads to the distortion and even discontinuity in a linear dependence of the laser frequency on the longitudinal magnetic field (with increasing the deviation of polarization from the circular one and in the presence of the transverse component of the field).

On the other hand, the polarization state can be accurately adjusted and the transverse component of the field can be suppressed by the minimum of the EIA resonance. In addition, the resonance allows us to calibrate the zero of the longitudinal component of the magnetic field. Figure 6 illustrates the dependence of a saturated absorption signal in the reference cell on the magnetic field near the line centre. The narrow photoinduced absorption resonance at the line centre at the cyclic transition has the width of ~150 kHz and appears due to a slight deviation of polarization of the saturating beam from a purely circular polarization.

2.6.2   Contrast of polarization resonance.

In the scheme of counterpropagating beams (Fig. 19a), two nonlinear mechanisms act simultaneously: a decrease in absorption due to transfer of a part of atoms to the excited state ($5P_{3/2}$, F`= 4) and an increase in absorption due to optical pumping to the extreme magnetic sublevel of the ground state (($5S_{1/2}$, F=3, m=3)) (Figs 19 b, c). We will call them the two-level and polarization saturation mechanisms, respectively.

The relaxation time of polarization in the ground state is determined by the time of flight of an atom through a light beam $t_\text{п}$. It is much longer than the excited-state lifetime γ^{-1}. To pump atoms efficiently to the extreme magnetic sublevel, a great number of absorption-emission events are required, which are described by the dimensionless parameter $\gamma S t_\text{п}$ of polarization saturation in the ground state, where S is the saturation parameter in a two-level system.

An increase in absorption upon pumping atoms to the extreme magnetic sublevel is caused by the fact that the absorption probability in the cyclic F->F+1 transition from the extreme magnetic sublevel in a circularly polarized field is higher than on average over the multiple (Fig. 19b). Because of the competition

Fig. 25. Transmission spectra for the D2 line of 85 Rb for different intensities of the saturating beam in a zero magnetic field.

between the two above mechanisms, the shape and sign of the nonlinear resonance are determined by the intensity and diameter of the saturating beam. When the beam diameter is small and its intensity is high, a hole dominates in the absorption signal. As the beam diameter increases and its intensity decreases, the hole is replaced by a peak. In the case of intermediate values of these parameters, a broad polarization peak contains a narrow two-level hole (Fig. 25). The different width of the peaks is caused by the difference of the saturation parameters S and $\gamma S t_\text{п}$. Note that both nonlinear mechanisms reduce absorption at other transitions of the D$_2$ line.

Let us estimate optimal conditions for the observation of polarization resonance. The maximum contrast of nonlinear absorption with respect to linear absorption is realized when total absorption in an optically thin cell is weak. In the case of an infinitely broad low-intensity saturating beam ($S \ll 1$, but $\gamma S t_\text{п} \gg 1$), optical pumping leads to an ultimate polarisation of the ground state, which is homogeneous within the volume where probe radiation propagates. Let α_L and $\alpha_\text{н}$ –be the absorption coefficients at the line centre in the absence and presence of the saturating field, respectively. The contrast $c_\text{H} = (\alpha_\text{H} - \alpha_\text{Л})/\alpha_\text{Л}$ of the nonlinear absorption peak can in principle exceed unity. In the limit $\gamma S t_\text{п} \gg 1$, we have :

$$\alpha_{\text{H max}} \propto \left(C^{F+1,F+1}_{F,F;1,1} \right)^2 = 1$$

$$\alpha_{\text{Л max}} \propto \frac{1}{2F+1} \sum_m \left(C^{F+1,m+1}_{F,m;1,1} \right)^2 = \frac{2F+3}{3(2F+1)}$$

$$c_{\text{H max}} = \frac{4F}{2F+3}$$

(2.9)

where F is the total angular momentum of the ground state For rubidium isotopes, the maximum contrasts are $c_\text{H max}$(^{87}Rb) = 8/7 (114%) и $c_\text{H max}$(^{85}Rb) = 4/3 (133%). Figure 26 shows the calculated dependences of the contrast of the nonlinear resonance on the intensity and flight time in an optically thin cell in the case of simultaneous action of the two above-mentioned mechanisms (the lower curves in each pair of curves). However, if linear absorption is too small, the linear component is also small. When absorption increases (due to an increase in the concentration of atoms or the cell length), the intensity of the saturating field and polarization of the medium become spatially
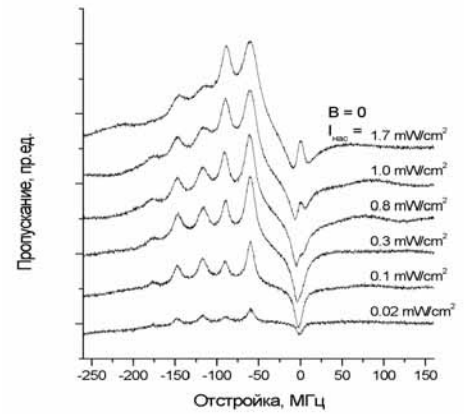
inhomogeneous and the contrast of the nonlinear resonance decreases although the number of probe photons absorbed at the line centre increases.

In this case, the coefficients $\alpha_\text{л}$ and $\alpha_\text{н}$ describe local absorption, and we will denote the fraction of the absorbed total power by $A_\text{л}$ and $A_\text{н}$ for linear and nonlinear cases, respectively. In the case of strong linear absorption ($A_\text{л} \sim 100\%$), the nonlinear addition is negligibly small. We can roughly estimate the total absorption in the cell, in which the nonlinear component is maximal, assuming that absorption is homogeneous in the central region of the saturating beam over the entire length L of the cell, the ground-state polarization has the ultimate value and relations (1) are valid. Linear absorption in a homogeneous medium is $A_\text{л} = 1 - t$, where $t = \exp(-\alpha_\text{л} L)$ is the transmission in the cell, and a change in transmission at the line centre caused by the saturating field is

$$A_\text{н} - A_\text{л} = t - t^\beta, \qquad \beta = \alpha_{\text{нmax}} / \alpha_{\text{л max}} \quad (2.10)$$

Fig. 26. Theoretical dependences of the nonlinear contrast c_nl ($= (a_\text{nl} \text{ À } a_\text{lin})=a_\text{nl}$ at the cyclic transitions from the F ˆ 2 level of the ground state of 87 Rb on the saturation parameter S. The upper curve in each pair of curves for the same value of gt_b corresponds to the scheme with the screening of the central part of the saturating beam. The horizontal dashed curve is the ultimate contrast (114 %) discussed in the text.

The nonlinear addition (2) is maximal for $t = \beta^{-1/(\beta-1)} \approx 50\%$:

$$\left(A_\text{н} - A_\text{л}\right)_\text{опт} = \beta^{-\beta/(\beta-1)}(\beta - 1), \qquad\qquad (2.11)$$

which comprises 30 % of the radiation power incident on the cell and 60 % of linear absorption. Therefore, the contrast of nonlinear resonance in a `thick' cell under optimal observation conditions is approximately half the ultimate contrast (2.9). The exact values of the contrast for isotopes are slightly different, however, there is no point in refining estimates within the framework of our model.

Figure 20 shows the experimental and theoretical [Aku89] signals of saturated absorption for identically oriented circular polarizations of the probe and saturating beams at the D2 line of 85 Rb. The expression obtained in [Aku89] describes the absorption probability at all hyperfine-structure transitions for $\gamma t_\text{п} \gg 1$, $\gamma S t_\text{п} < 1$ and takes into account scalar, magnetic dipole, and quadrupole scattering, which are of the same order of magnitude. Good agreement is observed between the theory and experiment for intrinsic resonances (indicated by arrows).

We proposed the method for eliminating a competition between two nonlinearity mechanisms, which uses a partial screening of the saturating in the region of propagation of the probe beam of a lower diameter. Figure 27 shows the example of nonlinear resonance absorption with the nonlinear contrast $c_\text{н} = 38\%$ ($t = 5\%$) for the saturating beam intensity close to the intensity of two-level saturation. The central part of the beam was screened. The dependence of the nonlinear contrast on the intensity in this situation is shown in Fig. 26 (the upper curves in each pair of curves).

As $\gamma S t_\text{п}$ increases, the contrast of the polarization resonance tends to the maximum value (2.11), however, the width of the resonance also begins to increase. A similar scheme is used for stabilizing the frequency of the laser resonant with the cycling transition.

2.5.5 Amplification of master-laser power .

The natural limit of the number of trapped atoms is determined by the available cooling laser power (see 2.1). Master lasers use extended cavity and provide the required wavelength, the coherence of the radiation, stability and reproducibility of a single-mode regime and frequency of the radiation. But the power is usually limited by 30-50% of the nominal power of the origin solitary laser, that is by the value of about 15-30 mW. The master lasers, which have been assembled in this project, have output power 6-7 mW. Power limit of the diode lasers is a result of a
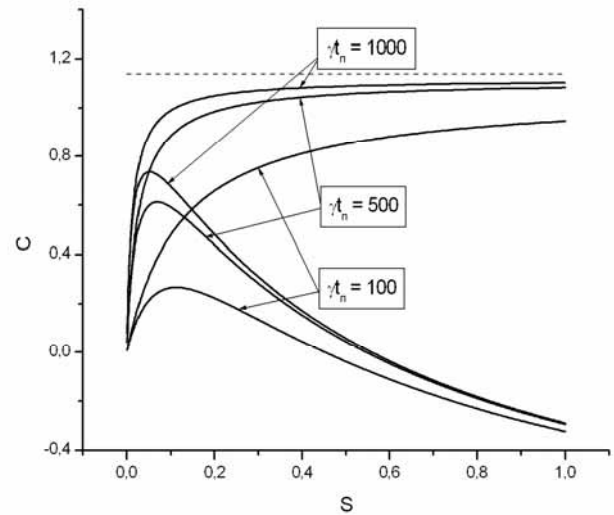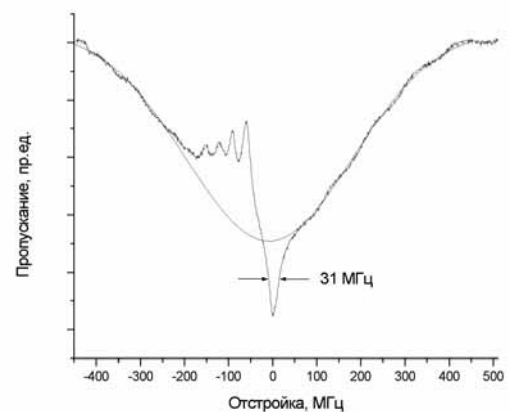

Fig.27. Nonlinear resonance at the $5S_{1=2}$ (F ˆ 3) À $5P_{3=2}$ (F $_\text{H}$ ˆ 4) transition in 85 Rb with the 38 % contrast obtained for the saturating beam intensity I_s ˆ 1:7 mW cm À2 and diameter 14 mm. At the central part of the beam, a screen of diameter 2.5 mm was placed, in whose shadow the probe beam of diameter 2 mm with the intensity of 0.1 mW cm À2 propagated. The smooth curve is the Gaussian approximation of the linear absorption line, which was plotted by the absorption data at the line wings.

small cross section of the active region generating the light (several μm^2).

Several well-known techniques for increasing the laser power are described below.

1) The first one is increasing the cross-section of the active region. Size variations in the current direction are constrained by the condition of single transverse mode and technology. Increasing another, so-called, "lateral", transversal dimension is practically realizable, but in addition to the multi-mode problem, there are problems connected with the instability of the generation due to the self-focusing effect and formation of independent channels of generation. It leads to enhanced noise of laser radiation and actually provides independent work of several lasers within their common active region. Nevertheless, in the case of wide and sufficiently homogeneous active region (broad contact) it is possible to force single mode operation via external feedback or via injection of an external signal from the master laser or by using the combination of both [31]. Unfortunately, we haven't success in the realization of this technique in the domestic lasers with wide contact.

2) Injection locking of the slave diode laser, which works in above-threshold regime, by the external coherent signal, was realized. However, it has the same fundamental limits of the maximum power; the gain of the laser power was only several times.

3) Amplification of the power with a resonant amplifier is another modification of the above-mentioned method. In that case, the amplifier functions a laser in the below-threshold mode, which results in significant restrictions of amplification. Beside, this regime is very sensitive to the temperature and the pumping current of the amplifier, because parameters of the amplification are dependent on the relative position of the frequency of the input signal and the frequency of the mode of the amplifier.

4) Application of the traveling wave amplifier (TWA) is especially effective method. Commercially available TWA are known to provide >0.5 W of the amplified laser power. However, the cost ($10000-$12000 with additional expenses in the case of purchasing in Russia) and the risk of the irreversible degradation (there are more than 1000 ways to kill a diode laser [Wie91]) did not allow to use this method.

5) Using several amplifiers after dividing a single input beam into several beams is another possibility.

6) Various combinations of the listed methods are possible. One of them is used in our experiment because of the limited maximum power of the traveling wave amplifiers, which are available. Radiation of the master laser provides injection locking of a more powerful slave laser. The beam of the slave laser is divided then into three parts and is amplified by three TWAs. This method requires more power supplies and optical isolators. We notice that the optical isolators are needed in all above-mentioned techniques for suppressing the feedback from the amplifier and the slave laser to the master laser.

Grant co-workers (MIREA) manufactured a semiconductor wafer with a double heterostructure providing maximum of amplification at 850 nm wavelength. This wafer was used to make the traveling wave amplifiers with stripe contacts, which are tilted respectively to the crystal facets (fig. 28). Accordingly, the mirror facets were tilted with respect to the optical axis of the amplifying waveguide. The combination of this geometry and the anti-reflection coating allow to suppress the resonant properties of a DL cavity and to transform it into an amplifier. The width of the stripe contact and of the active region was 4 μm.
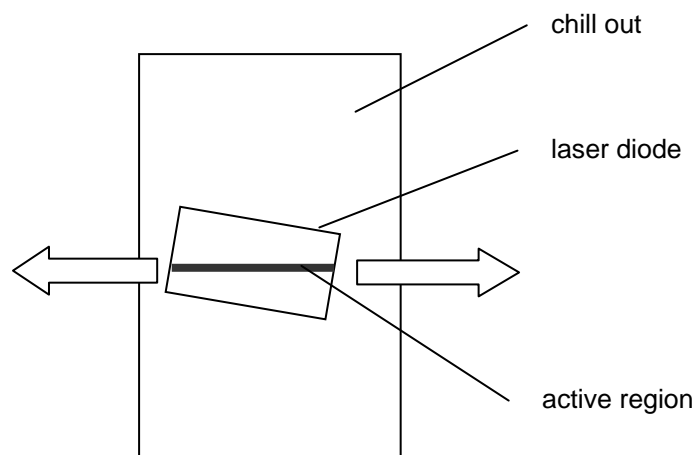

Fig.28 *Amplifying element with the tilted stripe structure*

Two series of samples with tilted stripe structure of the active region have been tested by using an experimental setup shown on Fig.28. For the first 8 samples (with 4 μm contact width and 1.4 mm length) the threshold of the fatal degradation was higher than or about 120 mW. One of them delivered 130 mW power of radiation tuned to the D_2 line of Cs. It is important that some amplifiers from this group revealed no long-term degradation at the 120 mW output power level. The output power of the other amplifiers decreased by an order of value in 30 hours.

In the eighth quarter the dependence of the power on current was taken for 12 new amplifiers with the active region having constant width of 4 μm and the length of 1.8 mm. The quality of the anti-reflection coatings

and long active region provided the enhanced threshold of the fatal degradation, increased output power up to 200 mW in CW mode at 525 mA pumping current and at 5 mW input laser power. However, these TWAs also revealed the long term degradation/ Such TWA start working as super luminescence diodes at 100 mA current only. The differential efficiency of their intrinsic radiation in the 100-200, 200-300 and 300-400 mA ranges was 0.22, 0.25 and 0.23 mW/mA respectively. The differential efficiency in the presence of the input laser radiation (~5 mW before the amplifier) was 0.5 mW/mA in the 100-200 mA range, 0.47 mW/mA, 0.43 mW/mA in the 300-400 mA range, and 0.35 mW/mA in the 400-500 mA range. The data show, that the differential efficiency in the amplification mode exceeds the value in the super luminescence mode by a factor of 2. It is connected with the suppression of the counter propagating wave due to saturation. In contrast to the TWA with a tapered active region (see below), the field distribution in the plane of the p-n transition had only one maximum, i.e. the field was homogeneous in this direction for all samples. Preliminary investigation showed, that the radiation of the amplifier with the constant width of the active region could be injected into the fiber with the bigger efficiency than in the case of the TWA with the tapered active region.

In the fourth quarter, masks for photolithography of special TWA structures have been ordered. These masks were used to fabricate the TWA with the tapered active region. (see the insertion on the Fig. 29). These amplifiers have two areas of the amplifying active medium. The first area is an input part. It is a stripe having a 400 μm length, and 4 μm width. The length of the second part is 1mm. The width of the active region increases along the length of the second section up to 40 μm. The optical axis is tilted relatively to the facets at 7°. These amplifiers were fabricated from the same wafer as the TWA with the constant width, thus the power was expected to be at least 0.5 W. Further we call this system as "tapered traveling wave amplifier" (TTWA). 18 TTWA samples were manufactured in collaboration with the MIREA group and were tested at 25 °C temperature and 350 mA current. 11 samples didn't pass the test (the output power dropped fast during the first hour).

Only 7 samples have successfully passed the 48-hour test and were tested as amplifiers. The dependence of the output power on the amplifier current at the 6.4 mW input master laser power is given on the Fig. 30.
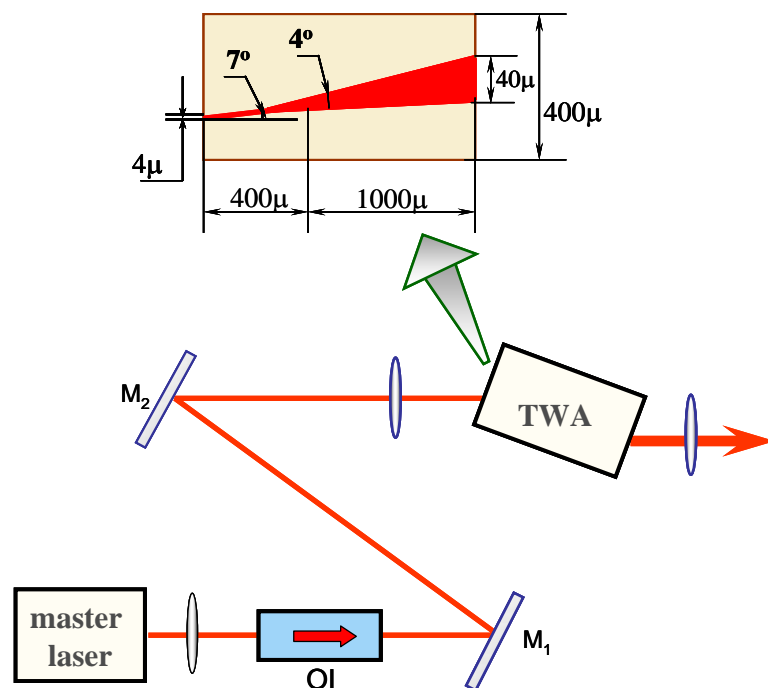
Fig. 29. The optical scheme of the amplifier test. OI – optical isolator.

The amplification saturates at the >2 mW input laser power and the pumping current exceeding 0.5A. The output power achieved 220 mW power level at the 800 mA TTWA current (measured without collimation optics). The properties of the amplifiers are close to each other. One of the amplifiers had catastrophic degradation at the 850 mA current. The others were operated with the 800 mA current limit.
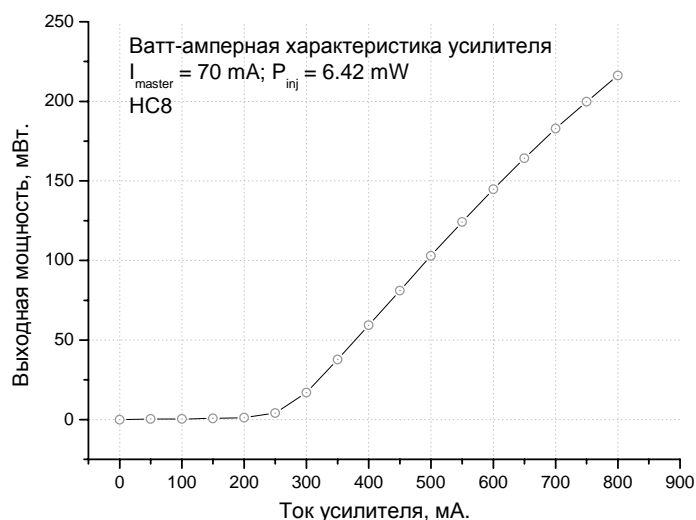
Fig. 30. The dependence of the output laser power upon the injected current at the 6.4 mW input laser power.

Totally, the degradation and the operational properties of the 42 amplifiers (including the above-mentioned) have been investigated. Out of them 28 samples were rejected during the preliminary training at the 350 mA current because of the degradation. The other 14 samples were checked with the current 800 mA, and only 2 samples were tested at the 850 mA current. The amplifiers begin working as a super-luminescent diodes at the 280 mA currents. The differential efficiency of the output radiation (without the laser input signal) was 0.15 mW/mA in the 300-400 mA range, 0.13 mW/mA in the 400-500 mA. The differential efficiency in the case of input laser power (9 mW before the coupling objective) was 0.5 mW/mA in the 300-400 mA, 0.46 mW/mA in the 400-500 mA, 0.44 mW/mA in the 700-800 mA. It is 10-20% higher than in the case of the linear amplifiers and decreases slower, when the current is getting higher.

The repeatability of the power properties of the amplifiers was nice, but the amplifiers differed from the previous group by the degradation and the far field. Only 2 from 14 samples had homogeneous far field in the lateral direction, the others had a number of stripes in this direction. Some of the samples with the inhomogeneous direction pattern degraded at the pumping current <800 mA. The degradation always leads to the destruction of the homogeneous directional diagram. One of the possible reasons for variations in the far field can be the filamentation of radiation in active region which in turn can be initiated by local inhomogeneity or interference and supported by selffocusing. The intensity threshold of selffocusing is relatively small since the refractive index in semiconductor depends strongly on inversion (that is on electron concentration).

The maximum power in the amplifying regime was 260 mW at the ~5 mW input master laser power. The wavelength of the input radiation was tuned to the D_2 line of Cs.
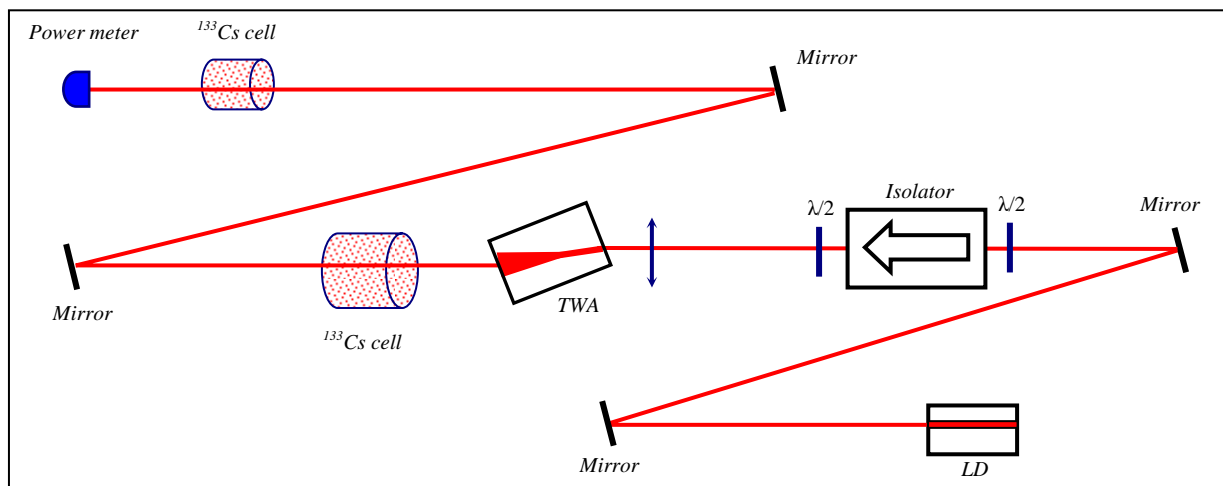
Fig 31. The experimental setup for measuring off-resonance background in the TWA radiation. The master laser is tuned to the resonant D_2 line of Cs.

Spectral characteristics of the amplifiers. The experimental setup built to estimate the fraction of the background (spontaneous) radiation in the output signal is shown in Fig. 31.

The light from the amplifier passed two Cs cells. A cell located near the amplifier was heated for increasing the concentration of the Cs atoms and was used for the absorption of the coherent resonant electromagnetic field. A second cell checked whether the first one has suppressed the resonant radiation in the first cell totally. The spectrum of radiation before the cells consists of two parts: a wide background (~30 nm) due to amplified intrinsic spontaneous radiation of the amplifier and a narrow peak, the amplified master laser radiation. The central narrow peak was reduced with the first cell practically down zero, which was controlled by disappearing fluorescence in the second cell. The power difference before and after the first cell gives the total background power. The level of the amplified spontaneous noise was 9% of the total power at the 8.5 mW (before the coupling lens) input laser power and at 500 mA pumping current. This value increased to 12% with the 800 mA current. Thus, the result power is 220 mW, which has proper spectral characteristics and can be used in the trap.

However, there are still problems with the increasing the laser power. The percentage of the working TTWA (described in the 6 quarter report) was too small. Only 26 from 80 samples passed training (fast degradation at low power test), 12 of them passed high power test. Only 2 from 12 had homogeneous lateral field. One of them degraded after 1 week at the 200 mW power level. In addition, we investigated the tunability and the contrast (the ratio of the amplified master laser radiation with the same spectral and polarization characteristics to the amplified spontaneous noise of the amplifier) of the amplifier.

The described above experiment for measuring the spontaneous noise background used the heated Cs cell, which worked as a 1 GHz filter. In the eleventh quarter, another experiment has been carried out, which gave more information about the amplified radiation, because both the frequency and the linewidth of the output signal could be controlled.
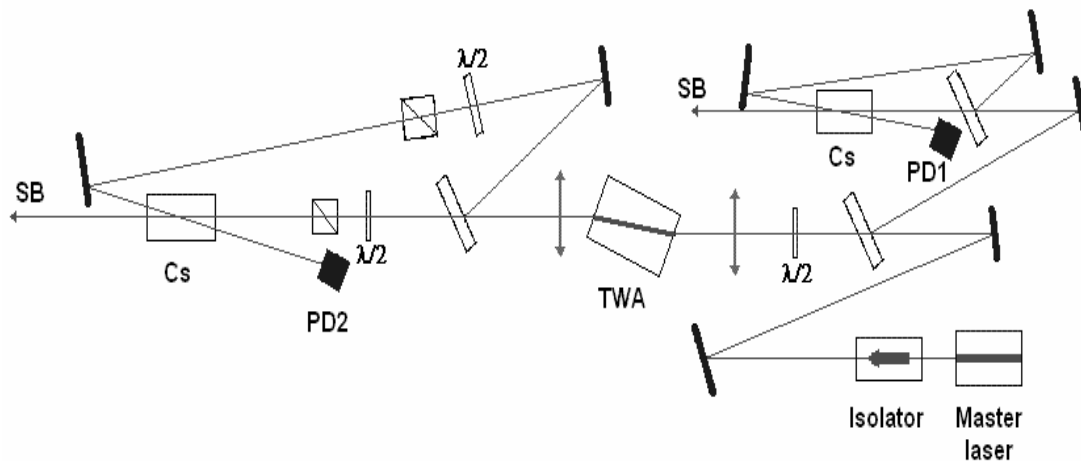
Fig.32. The experimental setup for recording the sub-Doppler spectra with the master laser and the amplifier. SB – saturating beams. Cs – cesium cells, PD – photodiodes.

In order to realize it the two identical and independent sub-Doppler spectroscopy setups have been built (Fig. 32). The first monitored the properties of the master laser; the second tested the characteristics of amplified radiation. The sub-Doppler spectra are very sensitive to the linewidth and the power of the pumping and probing beams. The half-wave plates and the polarizers provided similar conditions in the two schemes. The dimensions of the two probing beams differed a bit. Typical spectra obtained in the experiment are shown on the Fig.33.

The close similarity of the spectra shows, that a) the frequency of the amplified radiation follows the frequency of the master laser; b) the highly coherent part of radiation has at least 90% of power and doesn't change with the frequency tuning (it was estimated by the attenuation of the amplifier's beam); c) the linewidth of the amplified radiation is <10MHz in the whole tuning range of the master laser frequency.

We demonstrated also a possibility to use the linear strip amplifier as a laser, when optical feedback was provided on each side of the amplifier. The feedback on the left side in Fig.34 was made selective with a grating having 1800 grooves/mm. The efficiency of the grating depends strongly on the polarization of radiation, therefore we used a half-wave plate, which rotated the polarization plane by 90 degrees. A semitransparent mirror on the right side served both for external feedback and for the output. The output power was 10-15 mW at the pumping level 50% above the threshold. All the samples were successfully tuned to the D_2 line of the Cs atoms, so they give additional resource for master lasers.

Thus, we couldn't build the 0.5 W traveling wave amplifiers in this project. Most likely the main reason is the presence of some defects in the active region, which is connected with production process (technology). The probability of getting them in active region increases with its area, hence this degradation is more likely to occur in the amplifiers with broad area, that is in TTWA. The second reason may be connected with a mismatch of the diffraction divergence inside the tapered part and its spread angle. The reflections from the boundaries of tapered

structure may interfere and form maximums of the local field, and trigger the filamentation of radiation. The last effect deteriorates the far field, increases the divergence in the lateral direction and accelerates the degradation.

Since the linear TWA are more reliable, but deliver power no greater than 120 mW, three such amplifiers are used in parallel in our laser system.
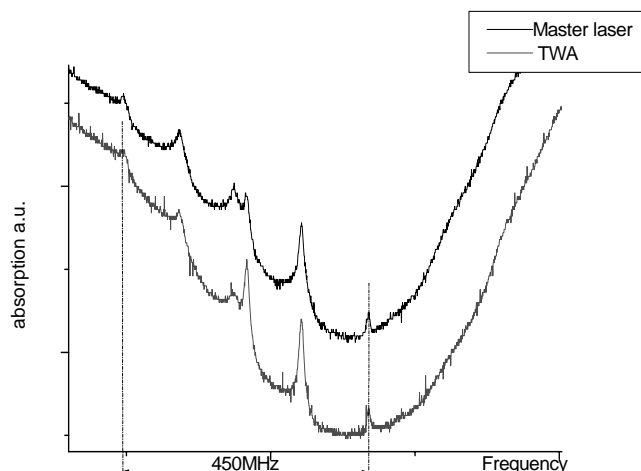

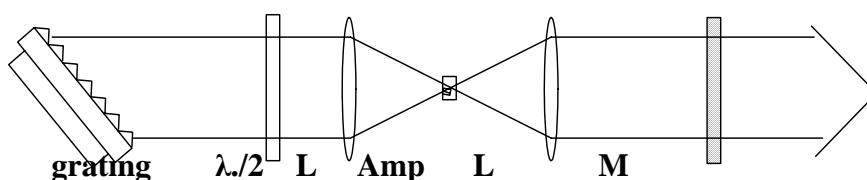**Fig.33.** Sub-Doppler spectra taken with master laser (black curve), and with amplified radiation.

Fig .34. *Injection diode laser with two-sided optical feedback. λ./2 - half-wave plate, L- aspheric lens ,Amp –amplifying element,* M – output mirror.

2.8 The magnetic field configuration.

Inhomogeneous magnetic field with axial symmetry is needed for the pure magnetic trap and for the magneto-optical trap, where the cold atomic beam is formed. In both cases it is produced by four-line current loop. The arrangement scheme for conductors was developed. It consists of two contours: the first is placed inside the vacuum part in the section of pure magnetic trap; the second is mounted outside the vacuum part and goes along the first and the second section. The two contours overlap partially in the direction of axis for the purpose of reduction of the boundary effects (at the ends of the current loop, where the linear parts of the conductors are connected) that influence the magnetic field configuration.

The length of conductors is 40 cm while their cross section is a tube with a 5 mm inner diameter and a 3 mm outer diameter. The axes of the conductors are placed in the corners of a square with a side of 9mm. The stabilized current source provides 100 A current.

The transverse magnetic field magnitude (the magnetic field vector belongs to the XY plane) on the axes X and X' are described by the following formulas:

$$B(\xi) = \frac{B_4 \xi}{1 - \xi^4} \ , \quad \text{где} \quad \xi = \frac{x}{a}, \quad (|x| \le a - r), \quad B_4(\Gamma c) = \frac{8I(A)}{a(\text{мм})} = \frac{8 \cdot 100}{6,4} = 125,7(\Gamma c)$$

$$B(\xi') = \frac{B_4 \xi'}{1 + \xi'^4} \ , \quad \text{где} \quad \xi' = \frac{x'}{a}.$$

Graphs of these quantities are depicted on Fig. 36a.
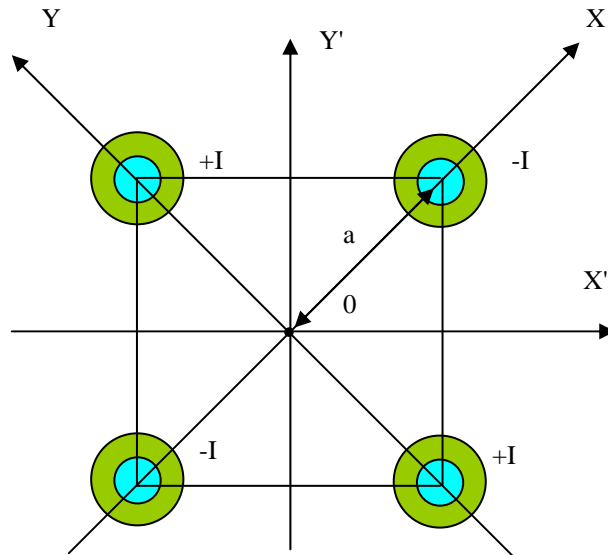
Fig. 35. Cross-section of the current carrying line. Square side – 9 мм. a – half-diagonal of the square. I – current (100A). Conductor radius – r (2,5 мм). The Z axis is perpendicular to the figure plane.
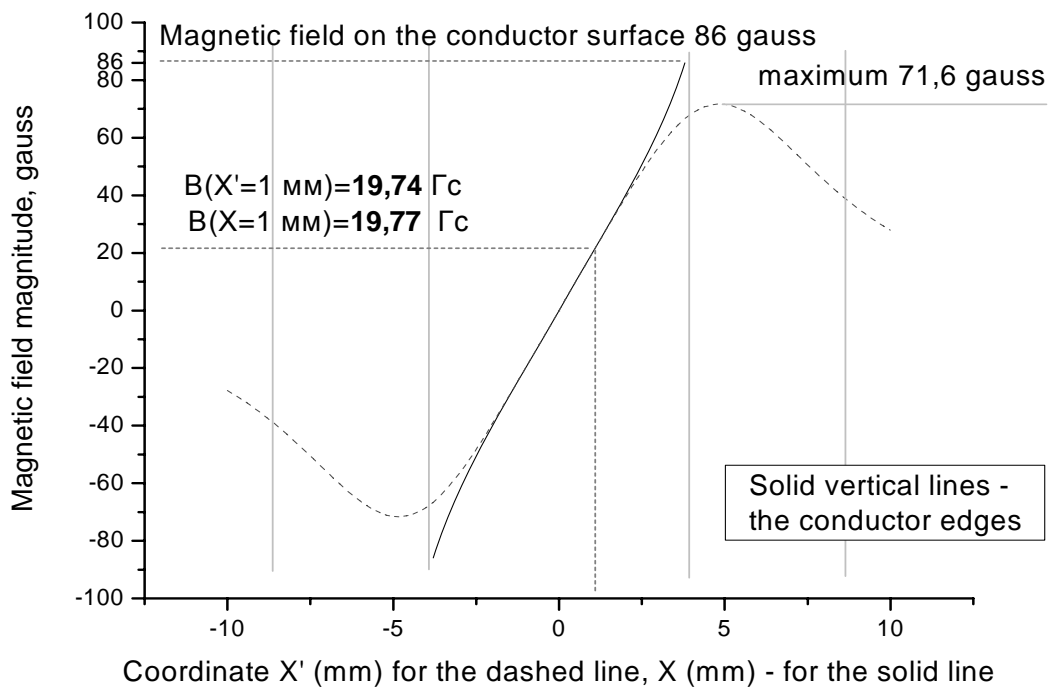
Fig. 36a. The magnetic field variations along X- and X'- axis.

The maximal and minimal magnetic field magnitudes are ±86 gauss. They are achieved at the ends of the conductors. The minimum transverse atom velocity that atom need to escape the trap is 85 cm/s. It is determined by the field extremum along the X' axis (71.6 gauss, Fig. 36). Actually it is a saddle point. The magnetic field distribution is shown on the Fig. 36b.
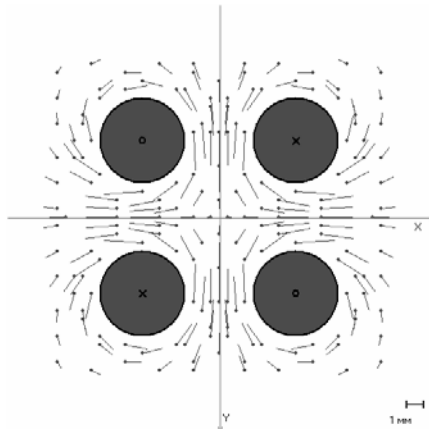
Fig. 36b. The transverse magnetic field of the four-wire line.

If the external longitudinal magnetic field is zero and side-effects are negligible, then magnetic field in such a configuration is parallel to the axis and equals zero at the axis. The absolute value of the magnitude of the field increases with the distance to the axis and it changes the sign on the axis. If the projection of the magnetic moment of an atom corresponds to the increase of atom energy with the field magnitude and direction of its projection on magnetic field doesn't change during the atom motion, then potential energy of the atom has a minimum on the axis and increases with the displacement from the axis.
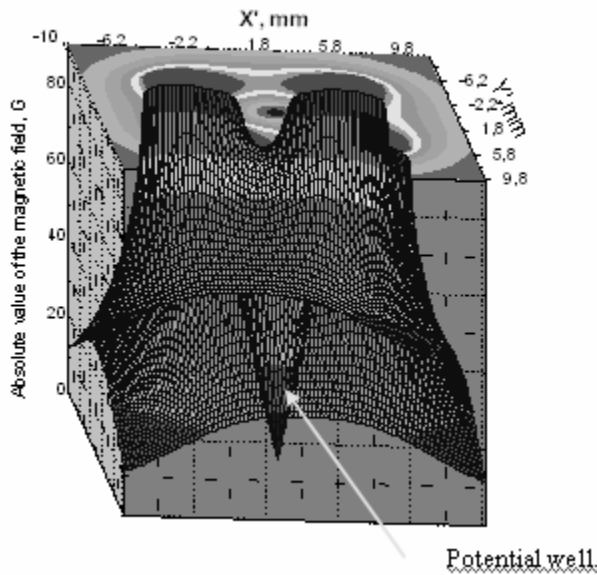
Fig. 36c. Spatial magnetic field configuration. The magnetic field magnitude multiplied by magnetic momentum of the atom is equal to the potential energy.

It's seen from the Fig. 36a,b that atoms will leak mostly along the ±X' and ±Y' directions. And the leakage through the ±X and ±Y directions will be 20% smaller. Fig. 36d shows also a cylindrical isotropy of the potential well at the distances up to ~2.5 mm that makes possible existence of the circular trajectories of atoms in the trap. At further distances it transforms into a C4 (square) symmetry.
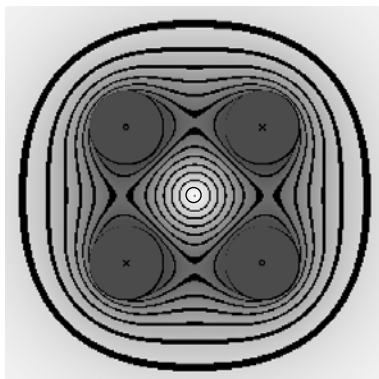
Fig. 36d. Black lines – equipotential lines in the magnetic trap. The intensity of red color is proportional to the magnetic field magnitude.
Width of the black line is inversely proportional to the magnetic field gradient (it doesn't change practically in the central part).

As atoms travel across the trap axis with a high speed the field direction changes very quickly so that the change of the projection of magnetic momentum onto the field may occur. In such a case the second condition of the existence of the potential-energy minimum is violated. It leads to the rejection of atoms from the trap. This leaking way was shortly described in section 1.3. To exclude this effect it is enough to add a longitudinal component of magnetic field. Five external coils mounted across the trap axis are used for this purpose. But longitudinal magnetic field decreases also the trapping force and the potential well depth. Assuming that the adiabatic condition is satisfied the potential energy of an atom in the magnetic trap is given by:

$$\Delta E = \mu[\sqrt{B_z^2 + B_\perp^2} - B_z] \qquad , \qquad B_\perp \quad \text{- magnetic field in the XY plane.}$$
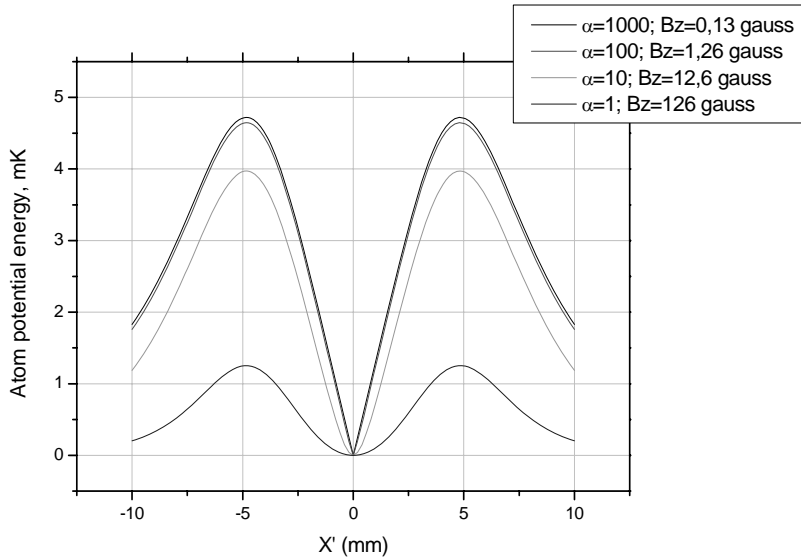
Fig. 37. The atom potential energy vs. the displacement along X' axis
for several longitudinal magnetic field values.

The dependencies of potential energy of an atom on the coordinate X' are shown on the Fig. 36 for different values of the longitudinal magnetic field component B_z. It's obvious that the longitudinal magnetic field component decreases the potential well depth.

The longitudinal field is produced by five external coils (they aren't shown on the Fig. 5a, b). Two of them are placed on the sides (as in the Ioffe trap) and the other three are placed between them. The increasing of the longitudinal component magnitude during the moving to the end of the trap could increase the atoms life-time, because it results in deceleration of atoms.

If the magnetic field increases from 1 to 11 gauss and the input atoms velocity is less or equal to 35 cm/s, than the life-time of the atoms increases four times because of reflection and returning processes. And at the same time the transverse atomic ensemble size at the input of the trap is $\sqrt{2}$ times greater than at the end of the trap. On the other hand the longitudinal component increases the width of the longitudinal velocity distribution. Optimization of the longitudinal field magnitude and its space dependence will be done experimentally.

The dependence of the potential energy of atoms in the F = 4, m = -4 state on the longitudinal magnetic field is shown on the Fig. 37 (for atoms moving at 1 and 4.5 mm distances from the axis). It's seen that 10 gauss longitudinal field decreases the potential energy two times down to 0.75 mK (for the 1 mm distance). Thus, atoms having transverse velocity smaller than 30 cm/s are trapped inside the one millimeter radius cylinder.

It's essential that trapping by inhomogeneous magnetic field is possible only for the atoms with the negative projection (m = -1, -2, -3, -4) of the magnetic momentum onto the magnetic field direction. The atoms with the projection m = 0 are not trapped. And the atoms with the projections m = 1, 2, 3, 4 are rejected from the trap. Thus, for the F = 4 state and for the uniform distribution of the atoms among magnetic sublevels only 4/9 part of them could be trapped. For the F = 3 state this part is 3/7. Hence, the potential well depth and the amount of atoms that are localized near the axis depend on the absolute value of the magnetic momentum projection onto the magnetic field direction. The m = -4 state is the best choice. The internal mirrors in the second section of the trap provide a possibility of pumping atoms in this state. However the optical pumping right before the trap is undesirable, because the light scattered by the atoms could penetrate into the magnetic trap.
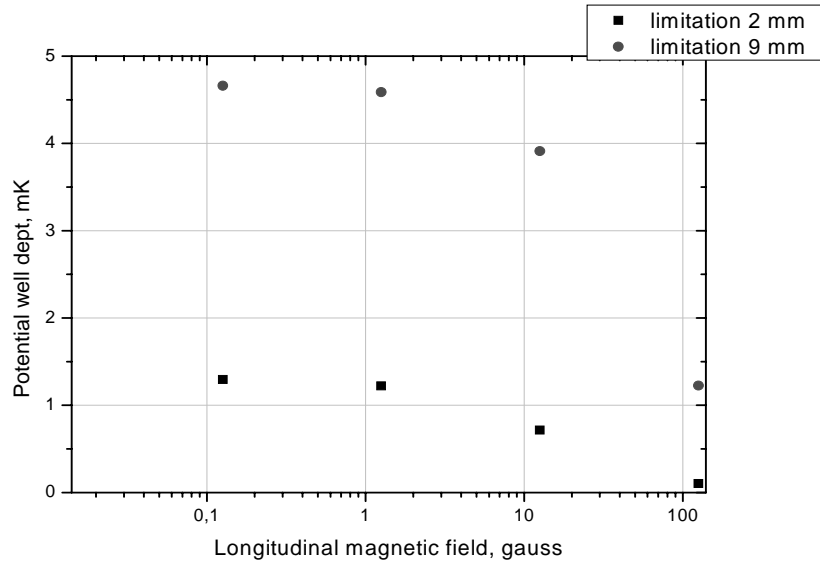
Fig. 38. Potential well depth vs. longitudinal magnetic field.

The atoms in the F = 4, m = -4 state with transversal velocity lover than 30 cm/s are trapped in the 1 mm radius cylinder in the desired magnetic field configuration with B_z = 1.3 gauss. If atoms enter at 5 mm distance form the axis, then their admissible velocity is $(2)^{1/2}$ times smaller and equals 21 cm/s. Thus the beam of cesium atoms in the F = 4, m = -4 state has to be focused into a hole of 1 mm diameter. Then the atoms with transverse velocities smaller than 20 cm/s will be localized inside a cylinder of 1 mm radius.
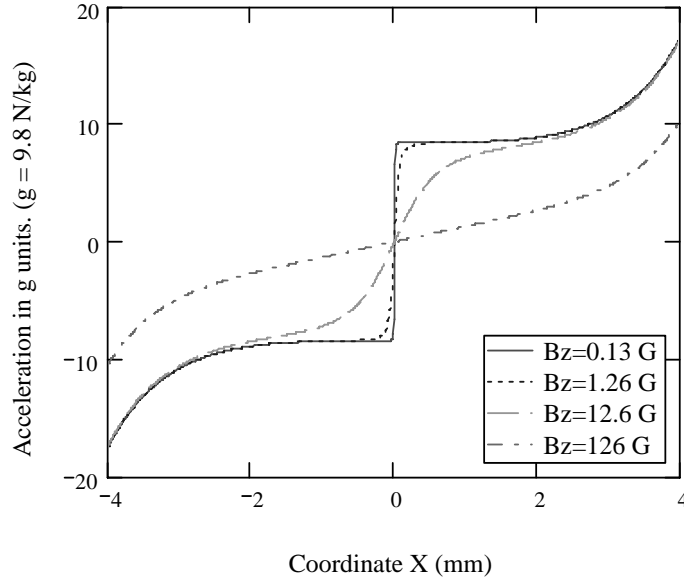
Coordinate X (mm)

Fig. 39. Atom acceleration vs. coordinate for different longitudinal magnetic field values.

In conclusion, the dependence of the cesium atom acceleration in the trap on the transversal coordinate is shown below:

$$a_4 = \frac{a_{c4} \cdot \alpha \cdot \xi (1 + 3\xi^4)}{(1-\xi^4)^3 \cdot \sqrt{1 + [\frac{\alpha \cdot \xi}{(1-\xi^4)}]}} \quad , \qquad \alpha = \frac{B_4}{B_z}, \quad B_z \quad \text{- longitudinal magnetic field}$$

$$a_{c4} = \frac{\mu \cdot B_4}{a \cdot m_{Cs}} = \frac{1,4(\frac{M\Gamma\text{ц}}{\Gamma c}) \cdot 6,6 \cdot 10^{-34}(\frac{\text{Дж}}{\Gamma\text{ц}}) \cdot 126(\Gamma c)}{6,4 \cdot 10^{-3}(\text{м}) \cdot 2,2 \cdot 10^{-25}(\text{кг})} = 8,47g, \quad (g = 9,8\frac{\text{м}}{c^2}).$$

The Fig. 39 represents the dependences of the atom acceleration on the transversal coordinate for the different longitudinal magnetic field magnitudes.

In the case of small longitudinal magnetic field (in comparison with the transverse magnetic field) the acceleration is a constant that has different signs at the different sides from the center. With the increase of longitudinal magnetic field the acceleration tends to zero and the potential well disappears. This causes the beam expanding in case of atoms deceleration in the gradient magnetic field. The best value of longitudinal field will be found experimentally. The ratio of the total number of atoms to the cross-section area of the ensemble should be chosen as a criterion.

2.9 The rubidium magneto-optical trap.

At the beginning of the project experiments with the rubidium magneto-optical trap have been carried out, because diode lasers with anti-reflection coating were available in the laboratory for making the master lasers for the rubidium absorption lines. In addition the Dutch scientists, professors E.R. Elien and J.P.Woerdman, pleasantly gifted us a vacuum part of this trap with an ion pump (our collaborator V.A. Sautenkov delivered it from Holland in operational condition), and it was very important to get some experience in laser cooling and measuring characteristics of a cold atomic ensemble.

The main features of the rubidium magneto-optical trap are described below. Pressure in a metallic chamber with windows with an anti-reflection coating that is joined to a magneto-discharge pump is 10^{-8} Torr. Rubidium atoms penetrate in the trap from a glass branch piece of the chamber that is temperature controlled. The background pressure of other gases determines the atoms accumulation time in the trap which is equal to 0.7 – 1 s. The lifetime of atoms in the trap equals to the accumulation time. Six cooling beams with intensity of 3 mW/cm^2 and diameters of 10 mm penetrate in the chamber through the windows. There is a quarterwave plate in a rotatable mount for each beam to control their polarization. Four repumping laser beams with a 1 - 2 mW total power go inside the chamber along one vertical and one horizontal direction. A magnetic field gradient at the chamber center (around the point with a zero magnetic field) could achieve 6 gauss/cm. It's limited by heating of coils. The ratio of the magnetic field gradient along the coils axis to the gradient along the transverse direction is 1.9/1. When features of the trap are optimized, $1.5 \cdot 10^7$ atoms could be trapped. The characteristic size of the atomic cloud is 0.4 mm and the ensemble temperature is 20 – 50 mK. The fluorescence signal dynamics is measured by using an imaging system and a PMT mounted after an iris diaphragm. The ensemble image is also displayed with help of television system consisting of a CCD matrix and a display. A mixture of both rubidium isotopes (^{85}Rb and ^{87}Rb) is loaded into the trap, however most of results was achieved for the ^{85}Rb isotope.
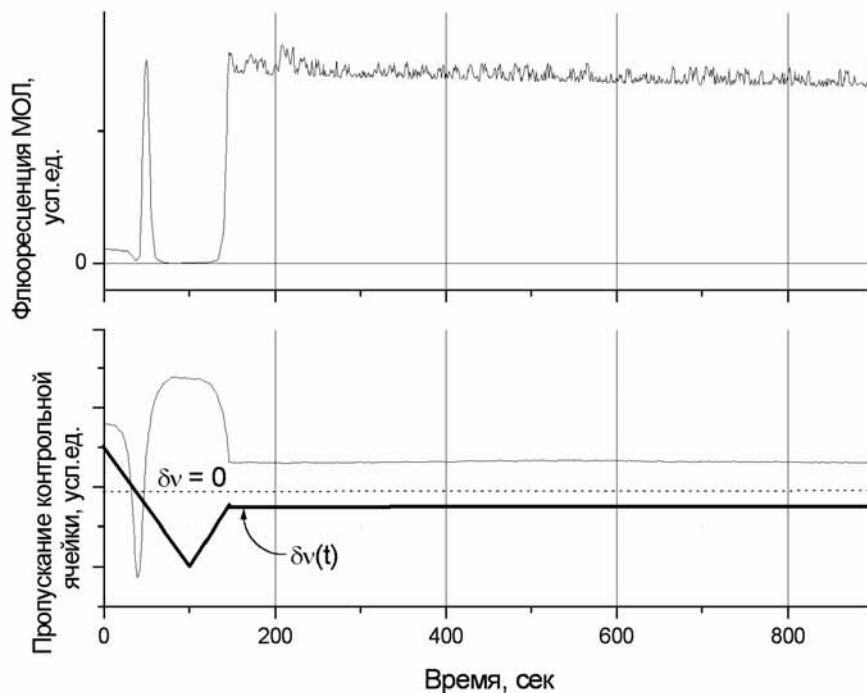

Fig. 40.The fluorescence signal of cold ^{85}Rb atoms and the reference cell transmission signal during the slow frequency scanning of laser around the resonance frequency.

The fluorescence signal of cold ^{85}Rb atoms and the reference cell transmission signal during the slow frequency scanning of laser around the resonance frequency are shown on the Fig. 40. During first 100 s the stabilized laser frequency was decreasing linearly in the vicinity of the cooling transition, next 50 s it was increasing, and eventually it was locked with a 10 MHz offset.

Low drift speed of the signal on the edge of the frequency discriminator (lower curve) provides long term stability for the cooling laser stabilization system.

The fluorescence signal from the trap (upper curve) has a local minimum precisely at the resonance that is caused by the transition saturation in the background rubidium vapor in powerful counter propagating waves.

For this setup the frequency stabilization technique based on saturation spectroscopy of the cycling transition was developed. It's very convenient for magneto-optical traps. Major features of this technique are: absence of a laser frequency modulation; possibility to detune the laser frequency by several natural widths. Experience with the rubidium trap was very important for the cesium trap construction and it afforded an opportunity to determine requirements for magnetic field homogeneity, homogeneity of laser beams, quality of windows antireflection coating, a magneto-optical part configuration, and windows for probing a cold atomic ensemble features.

3. CONCLUSION.

During the work on this project the following results were obtained:

1. The published papers on traps and cold atomic beams have been analyzed and reviewed. It was shown that not only available laser power determines the flux and brightness of cold atoms in a beam but also the right choice of an effective technique corresponding to a desired task plays an important role. The mentioned review was very helpful in developing the scheme of the setup.

2. In collaboration with MIREA team the isotope of Cs has been chosen. Physical characteristics of nuclear and optical transitions were compared (isotope availability, temperature at which a required pressure of an element vapor is achieved). Required laser wavelengths, powers, and costs were also taken into account. From the physical point of view ^{54}Mn isotope is most attractive. With increasing of monochromaticity of gamma-radiation sources ^{54}Mn will become the first isotope that will have a pumping-spectrum width equal to a homogeneous line-width of absorption line of a cold atomic ensemble. For applications the equality of the width of the pumping radiation line to the homogeneous line width of nuclear absorption means a possibility to narrow the gamma radiation line of an ensemble of cold atoms due to regenerative effect in amplification. Lines with inhomogeneous broadening do not give such a possibility. Unfortunately, ^{54}Mn is radioactive with a half-life about 312 days which makes it impossible to work with it in our laboratory. The next best isotope is ^{40}K. It has a homogeneous line-width which is 100 times smaller than that of ^{54}Mn's, but the energy of a gamma-transition is smaller (a synchrotron exploring is easier), lasers are more available (including diode lasers), operating temperatures are lower. The main disadvantage of ^{40}K is a very low abundance in natural mixture and, consequently, high price. So, the ^{133}Cs isotope has been chosen. The nuclear transition features of cesium are worse than potassium's ones (the natural linewidth is two times smaller, the energy is three times higher, and the cross-section is 10 times smaller). The main advantages of cesium are its availability, stability, and existence of high power diode lasers working at D_2 resonance line of cesium.

3. The estimation of required parameters was made taking into account status of modern pumping sources of gamma radiation. A laser power should not be lower than 0.5 - 1 W. If laser power is used effectively (like in the [15], 10^{10} atoms per 35 mW), then we can get atomic flux of about $3 \cdot 10^{11}$. Further increase of power makes sense only together with the increase of the trap windows diameter, which is difficult for a glass construction. A laser linewidth should be smaller than 1 MHz. The expected longitudinal speed of atoms is 1 m/s with a dispersion of 10 cm/s, which is close to the Doppler limit. Lower velocity makes it difficult to transfer atoms from the magneto-optical trap into the pure magnetic trap. Estimations showed that presently increasing the number of atoms is more important than achieving lower temperatures because of a wide spectrum of available sources of probing gamma-radiation. With the achievable monochromaticity of synchrotron radiation the absorption wouldn't change even if the atoms are turned back by the magnetic field gradient along the trap axis (which increases the life-time of atoms). It should be noted that the longitudinal component of magnetic field is limited by the requirement of suppression of spin-flip transitions and by its influence on transversal dimensions of the atomic ensemble in the trap (see section 7).

The pressure of residual gases shouldn't exceed 10^{-9} Torr, so that collisions won't reduce the life-time of atoms. For this purpose an effective removal of hot cesium atoms should be used. The vacuum part of the setup is assembled. It consists of a source of cold atoms, a collimation and focusing system, and a pure magnetic trap. The construction has seven windows with 50 mm diameter for powerful laser beams, and a few additional 30 mm windows for probing, internal mirrors to manipulate the longitudinal atomic velocity, and internal four-wire current loop forming the magnetic field. These conductors are made from copper tubes. The cooling of these tubes provides catching of the hot background atoms of Cs^{133}.

4. The extended cavity diode laser has been designed, which has good passive stability of the frequency and operation regime. Two series of master lasers based on this design were assembled. The lasers from the first series were tuned to the D_2 line of Rb. Important characteristics of these lasers were investigated. The spectrum line of the laser radiation was analyzed from the beatnote signal of two identical ECDL, and the linewidth

was shown to be smaller than 1 MHz. Tuning properties were obtained by using the absorption spectrum in Rb gas. The tuning range (without mode-hopping) covers all hyperfine structure of stable Rb isotopes. The passive stability was estimated with the wavelength meter. These lasers have been utilized in the Rb trap without any power amplifiers. The second series of master lasers was tuned to the D_2 line Cs. The spectrum characteristics of these lasers were analyzed by means of the beat-note signal of the two identical ECDL and the resonance of electromagnetically induced transparency (EIT). The laser linewidth (lower than 1 MHz) and the tunability range (about 30 GHz) are good enough for the laser cooling of atoms, but the power (5-7 mW) is by about two orders of value lower than is required for manipulating large numbers of atoms needed in the project.

5. High stability and precise detuning from the atomic resonance are required for the laser cooling. In order to fit these requirements a system for active stabilization of laser frequency was designed and studied. It is based on the sub-Doppler resonance, which is formed with circular polarized light resonant to the cycling transition of Rb or Cs. Zeeman modulation of the reference resonance gives an error signal and an additional constant magnetic field shifts the resonance. This combination gives possibility to stabilize the laser frequency in the +40…-150 MHz range with respect to resonance. The short-term stability (2.5 kHz in the 1 Hz bandwidth) was estimated by the transmission signal of the independent reference resonance in an independent cell. A method of enhancing the resonance contrast up to 50% was proposed and realized. It was done by blocking central part of a large saturating beam and sending the counter propagating probe beam along the shadowed part. The contrast of the resonance has been compared with theory. An explanation of the anomalous behavior of the stabilization system on tuning through zero magnetic field in the reference cell was proposed and a method of suppressing it was realized. The effect is connected with phenomena of electromagnetically induced transparency and electromagnetically induced absorption (EIT-EIA). High quality circular polarization (no ellipticity) and an effective screening of the transverse laboratory magnetic field are needed to eliminate discontinuity of discrimination curve of the feedback loop induced by these effects.

6. Several techniques of amplification the power of master lasers have been investigated: **a)** an injection locking of the narrow-stripe slave laser by the master laser radiation. **b)** injection locking of a laser with a broad contact **c)** using traveling wave amplifiers based of a tilted active regions with constant width of the stripe **d)** using tapered amplifiers. Available diode lasers give about 50 mW power in the "**a**" method (more powerful lasers may be purchased). The "**b**" technique did not give positive results. We couldn't get homogeneous far field in the lateral direction, lock the full width of the active region in samples with 100 μm width. In principle, this method may give 1 W output power. The **"c"** method allows increasing the power up to 120-130 mW and will be used in the experimental setup. A lot of attempts were made for building tapered amplifiers (**"d"**). The production engineers expected the amplified power to reach about 0.5 W, but after the test of a number of such amplifiers the maximum power was found to be 260 mW (that was a record obtained at 800-850 mA injection current, with a wavelength tuned to Cs D_2 line, and fraction of spontaneous emission in amplifier spectrum <10%). The higher pumping level led to fatal degradation. Unfortunately, at lower powers the degradation still remained, much slower but inconvenient for spectroscopic application due to the systematic drift of parameters. We noted two other disadvantages of such amplifiers. The first is a crescent-like shape of the far field; the second one is the existence of several maximums in the far field in the lateral direction. Because of these problems this technique was rejected. The combination of "a" and "c" methods is used in the experimental setup. The injection locking of a slave laser is a preliminary amplification cascade that provides 50 mW of power. This radiation is divided into three parts and amplified by three TWAs giving 340 mW. The saturation of the amplifier occurs at 5 mW of the input laser radiation, so two additional amplifiers can be used to reach 500-600 mW power level.

7. The gradient of magnetic field in the transverse direction and the transverse velocity of the atoms entering the magnetic trap determine the level of localization of the atoms around the trap axis. The greater is the magnetic field gradient, the narrower is the extended ensemble of cooled atoms and the greater is the ratio of the total number of the atoms to the cross-section of the ensemble (the parameter of main interest). Real limit of the current (100A) that produces magnetic field is defined by the available stabilized current source. Internal quadruple system of conductors line is built, which is supposed to trap the F=4, m=-4 state atoms with the transverse velocity < 20 cm/s in the pure magnetic trap if the input beam is focused to 1 mm diameter spot at the entrance of the trap. Such atoms will be confined in a cylinder with 2 mm diameter.

The longitude component of the magnetic field is used to decrease the longitude velocity of the atoms, to increase the life time of atoms and to keep constant the projection of the atom's magnetic moment on the magnetic field direction. The relationship between the longitude component of the magnetic field and typical transversal size of the beam is found.

8. In the beginning of the project the experiments were carried out with Rb trap, because the vacuum part of the trap was available in the laboratory. This gave an opportunity to gain an experience in laser cooling and measuring the characteristics of the atomic ensemble since the very beginning of the project. Master lasers have been tested using the Rb trap and a convenient frequency stabilization technique based on the locking to the sub-Doppler resonance on the cycling transition has been developed. The main advantages of this technique are the following. The laser frequency is free from the modulation and can be off-tuned up to several natural linewidths of the reference atomic transition from exact resonance. The experience gained with the Rb trap was important during the designing of the Cs trap. It helped to determine the requirements to the magnetic field homogeneity, laser beams homogeneity, windows antireflection level, configuration of the magneto-optical part and extra windows for probing

cooled atomic ensemble.

9. A part of experiment is not complete, because of the delays in the building the vacuum system and the pumping system. Originally it was planned to assemble it using mostly imported components. But real prices for Russia turned to be too large both for laboratory funds and grant possibilities. After that the pumping system was ordered in the Kirov's factory (Saint-Petersburg), the same place where the turbo molecular pump was purchased. After long consultations and detailing the drafts the new price was set too high with another additional condition (no electro polishing). On the next step the order was placed in the Kurchatov's institute (Moscow) where it was fabricated only by the July 2006. Currently the pumping system is being prepared for baking. The other parts of the setup are ready and have passed the trials. The experiment will be continued without additional finance support.

10. The results of the work were published in the articles [1-3]. In [1] the high coherent extended cavity diode laser with high stability of the regime and frequency is described in details. The developed lasers are used as master lasers and their radiation after amplification will cool and trap atoms in the magneto-optical trap, form an atomic beam and direct it to the pure magnetic trap. In [2] the application of such lasers in the Rb trap is given; effective method of stabilizing the laser frequency by the sub-Doppler cycling resonance in the Rb D_2 line is proposed and investigated. In [3] the influence of the ellipticity of the bichromatic radiation on the generation of dark superposition states has been studied. Pumping of the atoms to such states would lead to its losses from the trap. Since the bichromatic radiation is used almost everywhere in the trap and the ellipticity may occur because of the stress in the windows these states may be created. The results of [3] allow avoiding such a possibility and suppressing additional leakage channels.

The extended linear cooled atomic ensemble may be applied in many other physical problems like investigations of very weak atomic lines by probing with an optical radiation in longitude direction, studying collisions of cold atoms, generating cooled ensembles of Rydberg atoms, getting and studying Bose-Einstein condensates, building a laser without inversion with increasing the frequency, "slow" light experiments, light storage, quantum information storage, etc.

REFERENCES

[1]. C.S.Adams, E.Riis "Laser cooling and trapping of neutral atoms" Prog.Quant.Electr. **21** (1997) 1-79.
[2]. L. Allen, et al., Phys. Rev. A **45**, 8185, 1992.
[3]. V.I. Balykin, et al., Rep. Prog. Phys. **63**, 1429-1510, 2000.
[4]. Balykin V.I., Letokhov V.S. and Mishin V.I. 1979 1979 JETP Lett. **29** 560.
[5]. Balykin V.I., Letokhov V.S. and Mishin V.I. 1980 JETP **51** 692.
[6]. V. Balykin, et al., JETP Lett. **45**, 353-356, 1987.
[7]. V. Balykin, et al., Phys. Rev. Lett. **60**, 2137, 1988.
[8]. T.E. Barrett, et al., Phys. Rev. Lett. **67**, 3483-3487, 1991.
[9]. M. Beijersbergen, et al., Opt. Commun. **96**, 123, 1993.
[10]. T. Bergeman, et al., Phys. Rev A **35**, 1535, 1987.
[11]. S. Chu, et al., Phys. Rev. Lett. **57**, 314, 1986.
[12]. P. Cren, et al., Eur. Phys. J. D **20**, 107, 2002.
[13]. R.S.Conroy, Y. Xiao, M. Vengalattore, W. Rooijakkers, M. Prentiss. Opt. Commun. **226** (2003) 259-266.
[14]. Davis K.B. et all, Phys. Rev. Lett. **75** (1995) 3969, N. Davidson, et al., Phys. Rev. Lett. **74**, 1311, 1995.
[15]. K. Dieckmann, et al., Phys. Rev. A **58**, 3891, 1998.
[16]. J.P. Dowling, et al., Adv. Atom. Mol. Opt. Phys. **37**, 1-94, 1996.
[17]. J. Goldwin et al, Phys.Rev. A, 65, 021402 (2002)
[18]. J.Hoffnagle. Proposal for continuous white-light cooling of an atomic beam. Opt.Lett.**13,** 102 (1998).
[19]. M.A. Kasevich, et al., Opt. Lett. **15**, 607-609, 1990.
[20]. F. Lison, et al., Phys. Rev. A **61**, 013405.
[21]. Z.T. Lu, et al., Phys. Rev. Lett. **77**, 3331, 1996.
[22]. Harold J.Metcalf, Peter van der Straten, "Laser cooling and trapping", Springer, 1999
[23]. A. Migdall, et al., Phys. Rev. Lett. **54**, 2569, 1985.
[24]. J.D. Miller, et al., Phys. Rev. A **47**, R4567-R4570, 1993.
[25]. Spencer E. Olson, et al., Phys. Rev. A **73**, 033622, 2006.
[26]. Yu.B. Ovchinnikov, et al., Phys. Rev. Lett. **79**, 2225, 1997.
[27]. J. Prodan, et al., Prog. Quant. Elect. **8**,231, 1984.
[28]. L.A.Rivlin - *(invited paper),* Quantum Electronics (Moscow) **29**, 467, 1999.
[29]. L.A.Rivlin - Soviet Inventor's Certificate # 621265 of Jan. 10, 1961. (Sov. Bull. of Inventions # 23, 220, 1979 - in Russian).
[30]. G. Turnbull, et al., Opt. Commun. **127**, 183, 1996.
[31]. V.V.Vassiliev, et al , Electron.Lett., 33(14) (1997) 1222-1223.
[32]. Vuletic V. et all, Phys.Rev.Lett. **81** (1998) 5768.
[33]. M. Zhu, C.W. Oates, and J.L. Hall, Phys.Rev.Lett. **67,** 46-49 (1991)

TASK 3, 5. LOW-ENERGY NUCLEAR LEVELS EXCITATION IN LASER PRODUCED PLASMA

INTRODUCTION

Coherent gamma radiation may be generated by a gamma-ray lasing (GRL) process which makes use of excited nuclei as an amplifying medium. It is well known that to obtain a sufficiently high gamma-photon gain, care should be taken to increase two crucial factors of a nuclear medium: the linewidth ratio (e. g., the ratio of natural radiative linewidth of the lasing transition to the total linewidth caused by all possible broadening factors, including inhomogeneous broadening), and the degree of population inversion or, in more correct terms, the positive difference between the densities of the excited and unexcited nuclei. The Mossbauer effect, as a method for increasing the linewidth ratio, came to the attention of the authors of the very first Soviet and American proposals of a nuclear gamma-ray laser (Refs. [1-3]). Regrettably, this approach encounters the so-called (and insoluble) *GRL dilemma* (Ref. [4]). This expresses the impossibility of reconciling the requirements of a very intensive pump flux of any kind with maintaining the delicate Mossbauer conditions and has not furnished positive results even at the conceptual level during the past 40 years.

An alternative approach of recoil-assisted GRL in ensembles of free nuclei (Refs. [5]) appears today to be much more promising. The use of nuclear recoil opens up, contrary to the standard scheme of optical lasers, entirely new possibilities possessed exclusively by radiative processes with sufficiently hard photons. Among these are:

the possibility to establish a *hidden inversion* of state populations in an ensemble of free nuclei, which appears without excess of the number of excited nucleus over the number of unexcited ones;

the possibility to achieve incoherent x-ray pumping of a nuclear ensemble in the so-called *two-level* scheme (which is similar to the well-known three-level scheme of optical lasers, but does not resort to a third, auxiliary level), as well as in an anti-Stokes scheme that uses for lasing the intranuclear energy of long-lived isomers. The latter process has already been studied experimentally [6, 7]

the possibility of anisotropic quantum amplification of a unidirectional gamma-photon flux without any reflecting mirrors; and many other possibilities.

A salient feature of radiative processes in free nuclei is their recoil as a consequence of the laws of energy and momentum conservation in the emission or absorption of a gamma photon with a relatively large momentum. Thus, in any radiative transition a nucleus acquires a recoil kinetic energy equal approximately to 1 meV. In an emission process, this kinetic energy is drawn from the energy of a nuclear state and, in absorption, from the photon energy. This signifies that the absorption and emission spectral lines are shifted by the recoil energy relative to the transition energy and by twice the recoil energy relative to each other. This phenomenon and its more complex forms can conventionally be termed the kinematic shift and line splitting. An important conclusion is drawn from this kinematic shift: if the specified shift is comparable with the total linewidth, there arise prerequisite conditions for the formation of a so-called hidden inversion, because emitted photons have no possibility to be absorbed by unexcited nuclei. Thus, a total inversion is not required, i.e. the total number of excited nuclei need not be greater than the number of unexcited ones and consequently, in principle, the gain coefficient is positive for any finite population of upper state which is provided by sufficient incoherent x-ray pumping.

The above-listed and other remarkable features reveal themselves only in a laser with free nuclei. But this simultaneously creates a need for a radical reduction in the inhomogeneous Doppler broadening of the emission line to attain an acceptable linewidth ratio and gain coefficient for the photon flux. This very important task is to be accomplished by present-day techniques of deep cooling of atomic ensembles by the light pressure of optical lasers.

The technique of laser cooling allowed for the 10^{-8} decrease of the temperature during the last twenty years [21,22]. It gives 10^4 increase of ratio of the homogeneous (radiative) linewidth to the inhomogeneous (Doppler) linewidth.. Nevertheless even for he record concentration of cooled atoms 10^{13}-10^{14} cm^{-3}, [23,24] the resonant γ-absorption of about 10^{-2}-10^{-3} requires at least one meter length of ensemble. It is clear that the simultaneous providing of maximum concentration, minimum ("longitudinal") temperature and large dimension is a challenging problem. The practical goal of the proposed research is to look for maximum available parameter $nL\big/\sqrt{T_{\parallel}}$ (n is the concentration of atoms nuclei, L is the length cooled ensemble, $T_{\parallel}$ is the "longitudinal" temperature) and it's dependence on intensities, polarizations and diameters of all laser beams involved, the vacuum level, geometry of magnetic fields and their gradients etc.

To detect a γ-resonance in nuclei absorption in atomic gas or to pump nuclear transition one need the relevant source of γ-radiation. Solid-state Mossbauer sources of γ-quanta and synchrotron might be distinguished as possible candidates. The first type has an advantage of the narrow spectrum. But it has the following disadvantages: the angular distribution of the radiation is isotropic which means that a narrow beam can be produced only by a passive apperturing, so that the narrower is the beam the smaller becomes the efficiency of the source; to compensate the recoil shift the precise relative motion of atoms and γ-radiation source is needed. A small resonant cross-section and limited concentrations of cooled atoms attainable in the traps imply the need to utilize long (thread-like) configurations of the free-atoms target. The isotropic angular distribution of γ-radiation does not fit the large longitudinal dimension of the target.

The main advantages of synchrotron radiation are a small divergence and a big brightness. A disadvantage is a relatively large spectral width. However, crystal monochromator have sufficiently suppressed the width down to

the value of about 1 meV. A possibility to produce high-power short pulses of γ-radiation needed for pumping and inversion at γ-transition is another advantage of synchrotron radiation. The experiments on observation of γ-resonance in a gas of free atoms seems to be much more feasible with this γ-quanta source and we'll build-up the ensemble of cooled atoms by taking into account it's available characteristics. The parameters of the ensemble and γ-probe radiation should be compatible. E.g., there is no sense to make the Doppler width of the γ-absorption line much smaller than the available width of the synchrotron radiation.

The hot, dense plasma created at interaction of a high intensity short laser pulse with a solid is a bright source of energetic electrons, photons and other elementary particles. Especially the production of the hot electrons can be very efficient as reported recently [25,26]. Due to the high kinetic energy of these particles, ranging from few keV at laser intensity $I \sim 10^{16} W/cm^2$ to a few MeV at $I \sim 10^{19} W/cm^2$, different nuclear processes can be initiated in the plasma and surrounding media: fusion, fission, excitation and nuclear reactions, etc [27]. Among these phenomena excitation of nuclear levels with energy below 20 keV can find a wide set of application ranging from nuclear spectroscopy, population inversion and gamma-lasing to isotope separation. From general point of view femtosecond-plasma-based electron and hard x-ray sources could play important or even basic role in the newly establishing field of Quantum Nucleonics (see, for example, materials from LPHYS 2000 Conference [28]).

By now only a few sources are capable to excite nuclear levels within 0-20 keV range either directly (synchrotrons [29], high voltage x-ray tubes [30]) or indirectly (ion and electron accelerators [31]). The very idea to use laser plasma for this purpose dated back to the beginning of 70-s [32, 33], but experimental attempts failed due low plasma density and long time duration of laser pulses used [34,35]. In our paper [36] we proposed to use hot dense femtosecond plasma to enhance excitation efficiency. Following this idea we did observe gamma-decay of 6.238 keV Ta-181 isomeric level with the lifetime of 6 mcs excited in plasma produced by 200 fs, 600 nm and 1 ps, 1053 nm laser pulses at intensity $2*10^{16}$ W/cm^2 [37]. In so doing we counted for single gamma-quantum with the help of NaI scintillator detector, having 250 ns temporal response and 50% energy resolution, or making use of ns-gated MCP detector equipped special with x-ray filters. Those experiments mostly backed the very idea of feasibility to detect low energy nuclear excitation in femtosecond plasma, but experimental techniques used can not be treated as very useful for possible applications: one needs better resolution both in time and quantum energy. Some theoretical attempts were made as well in our papers to describe qualitatively basic mechanisms of low energy nuclear excitation and decay channels [37,38], but experiment to theory comparison shows a few orders of magnitude discrepancy.

One of the main problem for the gamma ray laser development is the inverse population creation at the isomeric levels of nuclei. The hot and dense plasma can serve for this purpose. Such plasma can provide a lot of excited isomeric nuclei for a short time.

We are going to investigate the interaction of plasma's photons and electrons with atomic nuclei in the frame work of perturbation theory for the quantum electrodynamics (QED). In this scheme the different interaction processes are systematised via the number of the Feynman diagram vertexes. One needs to calculate a cross sections and the excited nuclei quantity for all these processes, and to find the range of plasma parameters, where some specific processes are dominated.

The purpose of this task is estimation of the hot dense plasma possibilities to be a source of the isomeric nuclei for the gamma ray laser and optimization for laser pulse parameters. So, one needs to know the half-lifes of the isomeric nuclei in the plasma, and their decay channels.

The main decay channel of the nucleus isomeric levels in a neutral atoms is the electronic conversion. Atom is ionized in the hot dense plasma. That is why other decay channels became possible. This task is devoted to the consideration of such channels. The internal conversion probability is decreasing if atomic shell ionization is increasing. As a result, the relative probability of the gamma emission will increase. However, the new decay channel as electron bridge became possible for the same reason. The electron bridge is the third order process, which is unobservable practically under the ordinary conditions. The energy of nuclear excitation is transformed into the atomic shell excitation, and x-ray are emitted in the process of atomic shell relaxation.

The relative probabilities of the gamma emission process, internal conversion and electron bridge depend on the plasma ionization state.

Expected Results

- Designing of complex of methods and algorithms for thorough characterization of electrons, ions and x-rays from femtosecond laser plasma at intensities 10^{16} - 10^{17} W/cm^2.
- Determining of the laser pulse parameters optimal for excitation of nuclear level with a given energy through the given excitation channel.
- Designing methods and techniques for detection of nuclear level excitation and decay in plasma.
- Development of the theory of nuclear level excitation and decay in femtosecond laser plasma and making experiment to theory comparison.
- And finally backing low energy nuclear level excitation in femtosecond plasma as a new tool for nuclear spectroscopy.

- Develop laser system at SRC RF TRINITI with the following parameters: energy per pulse ~10mJ, pulse duration less than 5ps, focusing spot size less 10mkm, intensity on the surface of the target more than 10^{16} W/cm^2 for experiments with nuclear levels excitation in laser plasma experiments.

TECHNICAL APPROACH

Task 3.

This task starts with adopting and improving available and developing new x-ray, electronic and ionic plasma diagnostics. We are going to make rigorous proving of the double method of hot electron temperature assessing, and develop new MCP based detector to make temporal gamma ray measurements. Besides we are going to apply Si cooled x-ray detector for spectrally resolved x-ray and gamma-ray diagnostics. We are going to develop numerical algorithms to extract information on plasma thermal and hot electron temperature and concentration from ionic time-of-flight measurements basing on two energy beam steady state approximation. We will also design electronic spectrometer using flat field geometry to obtain 10% energy resolution in 100 eV –10 keV electron energy range.

On the next step we will apply all this methods for plasma characterization. At first we will use 200 fs, 0.5 mJ, 600 nm, 0.1 Hz laser system at ILC. The upper intensity available now is $4*10^{16}$ W/cm^2. On the 2-nd year of the project we will use the same diagnostics in SRC RF TRINITI with 5 ps, 10 mJ, 10 Hz laser system which will be upgraded from the current 100 ps, 50 mJ system during the first year of the project. All this enables us to determine optimal experimental parameters to achieve desired plasma conditions.

The key part of the project will be devoted to various diagnostics of nuclear level excitation in plasma. Experiments will run in the both institutions. We will start from measuring gamma-decay of Ta-181 6.2 keV level with the help of NaI, MCP and Si cooled detector. The first one is the most simple in use, the next has higher temporal resolution of 1 ns, while the last possesses 100-200 eV spectral resolution. To measure IEC processes we will apply electronic spectrometer with temporal resolution of 10 ns, and spectral resolution of 10%. The latter value is the most suitable taking into account wide spreading of IEC electrons energies. We will start again from Ta-181 nucleus, and than move to Fe-57 isotope with 14.41 keV 98 ns nuclear level. In this case we have also unique possibility to measure 14 keV gammas and 7 keV K-alpha quanta thus estimating IEC coefficient. This experiment demands good statistics acquiring that will be possible making use of SRC RF TRINITI laser system.

Task 4.

In accordance with the main goal of the task we are going to develop general approaches describing peculiarities of low energy nuclear levels excitation and decay in plasma created by ultrashort laser pulse and make numerical modelling. To accomplish this one needs describing a set of different processes, those gathering together yields in full description of the processes under interest. At first this is description of plasma formation and cooling by the ultrashort laser pulse. We are going to use existing in the MSU code, but it demands certain improvements: account for viscosity of plasma hydrodynamic flow, phenomenological description of hot electrons production, improved description of x-ray production in plasma and some others. This enables us to use it up to intensities of 10^{17} W/cm^2 and also to calculate plasma dynamics correctly. Results of these calculations will be compared with experimental data. Hence it enables us to check the model and than to use it while optimizing plasma parameters. Secondly it is developing of the set of equations describing low energy nuclear level excitation in plasma with given parameters tacking into account different excitation channels: photoexcitation, inverse internal electronic conversion and inelastic scattering. For this we will calculate in the frame of QED cross-sections of different excitation channels including second and third order processes, those might be important in highly ionised plasma. After that we will develop the theory of low energy nuclear level excitation in plasma tacking into account different channels of excitation, real electron spectrum and x-ray spectrum, nuclear level broadening in plasma, and also temporal and spatial dynamics of plasma parameters. We will develop schemes of x-ray focusing by distorted crystals to study the nucleus photoexcitation by monochromatic x-rays outside the plasma volume. We will treat low energy nuclear decay in plasma starting from existing code for internal conversion calculation in a single ion. We will improve this model for the case of plasma and its dynamics. For a set of applications, such as isotope separation, gamma-lasing, it is essential to prolongate nuclear level decay we will consider different methods of preserving plasma ionisation state, hence this can lead to internal conversion blocking and increase in life time. Here it is important accounting for such high order processes as electronic bridge, etc.

Task 5.

We will develop laser system with the following parameters: energy per pulse ~ 10 mJ, pulse duration less than 5 ps, focusing spot size less 10 mkm, intensity on the surface of the target more than 10^{16} W/cm^2 for experiments with nuclear levels excitation in laser plasma experiments. To upgrade the existing laser system up to these parameters the pulse compression technique under Stimulated Scattering Processes will be used. To avoid well known shortcuts the single mode single frequency stable master oscillator was developed. In addition, it was paid special attention to obtain the clean Gaussian cross-section distribution of the pumping beam intensity (noise energy less than 10^{-4}). For this purpose phase conjugation mirror and compensation of the depolarization and additional space filtering of the output beam were used. To obtain the output beam with closed to the diffraction limit divergence of the radiation the special geometry pulse compression scheme was proposed.

EXPERIMENTS
3.1. Laser systems

3.1.1. Ti:Sa laser system

New Ti:Sa system has been launched during the project. The layout of TiSa laser system is presented in Fig.3.1.1.1. Master oscillator, pumped by 5 W continuous radiation of "Verdi" laser, generates 30 fs pulses at 800 nm central wavelength and with repetition rate of 77 MHz. Fig 3.1.1.2 demonstrates temporal and spectral parameters of Mira-seed output radiation. The scheme of autocorrelator is present in Fig. . Spectrum was measured by fiber spectrometer. After passing through all-reflecting optics stretcher the duration of laser pulse increased up to the level of about 200 fs. Stretcher consists of one 1400 lines/mm grating, one concave mirror (R) with focal length of about 914 mm , and two retoreflectors (RR1, RR2). The angle of incidence on the stretcher is about of 43 degrees Stretched radiation is amplified in regen amplifier from the energy of about 1 nJ up to the level of about 8-9 mJ. Regen amplifier consist of two concave mirrors (R1, R2), Pockels Cell (PC), TiSa crystal and polarizer (P). After beam diameter expansion this radiation is sent to 4-passess amplifier there its energy is increased to the level of about 60 mJ. Both regen and multi-pass amplifiers are pumped by the second harmonic (532 nm) of output radiation of Surelite III YAG laser. Its total energy is 340 mJ and about 80 mJ of it are used for the pump of regen amplifier. The residual pump (240 mJ) is sent to the multi-pass amplifier.

The amplified radiation comes to the compressor consisting of two 1440 lines/mm gratings (G1, G2) and one retro-reflector RR3. After compression the energy of output radiation is of 35 mJ. The cross correlation function (CCF) of compressed femtosecond pulse, along with its spectra is presented in Fig. 3.1.1.3. The 100 fs CCF duration corresponds to about 70 fs pulse duration, if $sech^2$ pulse shape is assumed. The FWHM diameter of output radiation is about 10 mm.

The spatial quality and focusability of output radiation were examined by measurements of M^2 quantity. The scheme of experimental set-up for M^2 measurement is in Fig 3.1.1.4. FWHM diameter d of the laser beam measured at the focus of 4000 mm lens Fig. 3.1.1.5 is compared with the theoretical value determined by the formula: $d=0.44*\lambda*(F/D)$ gives M^2 value of 1.7. Here F=4000 mm is the focal length of the lens , λ=800nm is the central wavelength of femtosecond pulse, and D=10 mm is beam diameter at the lens.

In order to deliver 0.5 TW radiation without spatial and temporal distortion to the target surface, it is necessary to place optical elements of compressor into the vacuum. For that purpose we constructed huge vacuum chamber with volume of about 294524 cm^3. As placing of compressor into the chamber prevents one from direct access to the optical elements, we mounted gratings assembles at translation and rotation stages (Fig. 3.1.1.6), controllable remotely by computer. To reach maximally tight focusing of femtosecond radiation at the target by Al coated parabolic mirror with diameter of 50 mm it is necessary to increase beam diameter. So apart from pulse compressor we placed into the chamber the telescope made from convex mirror with focal length of -1000 mm and concave mirror with f=2000 mm. This telescope allowed twofold increase in beam diameter.
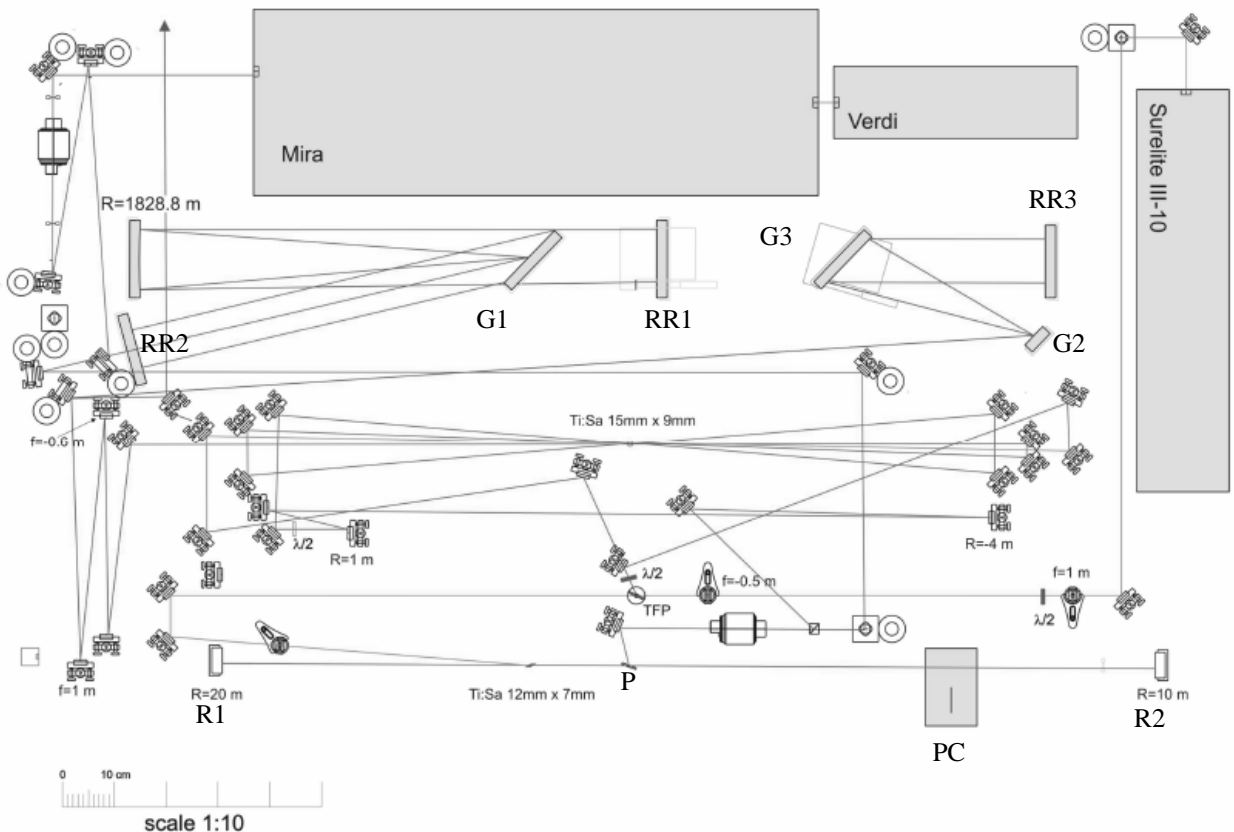

Fig. 3.1.1.1 Layout of Sub TW Ti:Saphire laser system.

Lens with focal length of F=4000 mm focuses the collimated beam with diameter of D=10 mm on the CCD array. M^2 quantity is determined as a ratio of experimentally measured FWHM beam diameter at the waist to the theoretically predicted one. If Gaussian spatial distribution of the beam is assumed, the theoretical value of beam diameter is given by the formula: $d=0.44*\lambda*(F/D)$. For radiation with wavelength of 800 nm it is 130 um. So $M^2 \approx 1.7$.
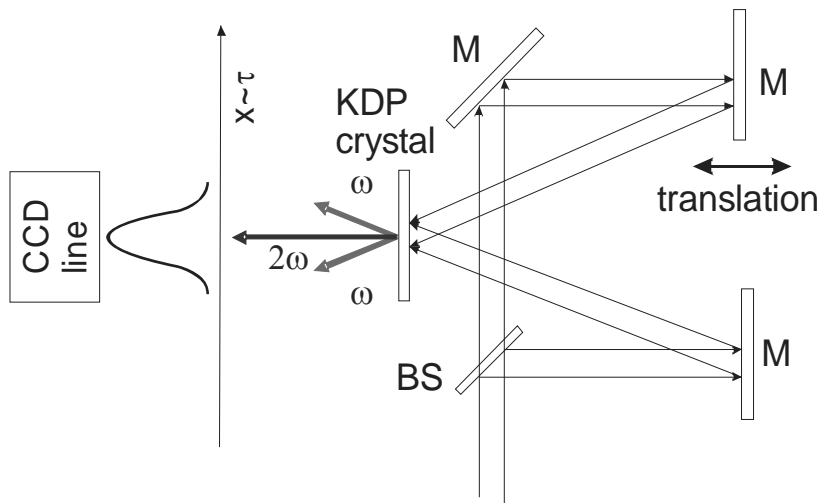

Fig. 3.1.1.2 The scheme of single-shot autocorrelator. Laser pulse is splitted by beam splitter into two equal parts, which afterwards intersect at the surface of nonlinear crystal and generate non-collinear second harmonic (SH). The delay between pulses is proportional to coordinate x in the direction along crystal surface. Energy distribution of SH signal against x coordinate gives autocorrelation function of the pulse under examine.
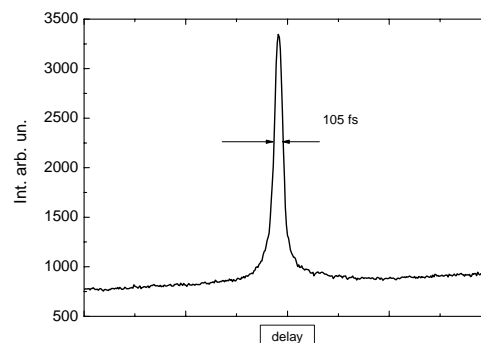
Fig. 3.1.1.3 The autocorrelation function (ACF) of the output pulse of Ti:Saphire laser system. The duration of ACF of 105 fs corresponds to the about 70 fs duration of femtosecond pulse if $sech^2$ shape of the pulse is assumed.
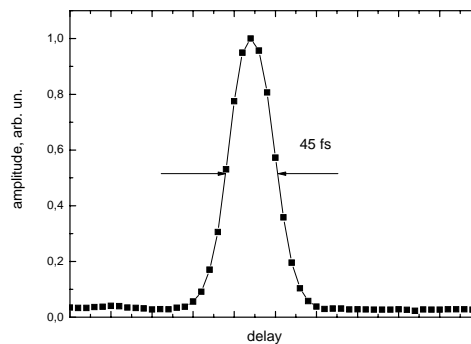
Fig. 3.1.1.4 Autocorrelation function of radiation of Mira Seed oscillator. The duration of ACF of 45 fs corresponds to the about 30 fs duration of femtosecond pulse if $sech^2$ shape of the pulse is assumed.
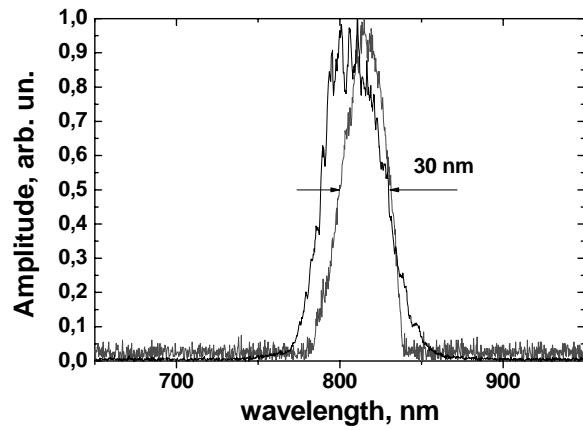
Fig. 3.1.1.5 Spectra of the Mira Seed radiation (black line) and output radiation of the TW system (red line).
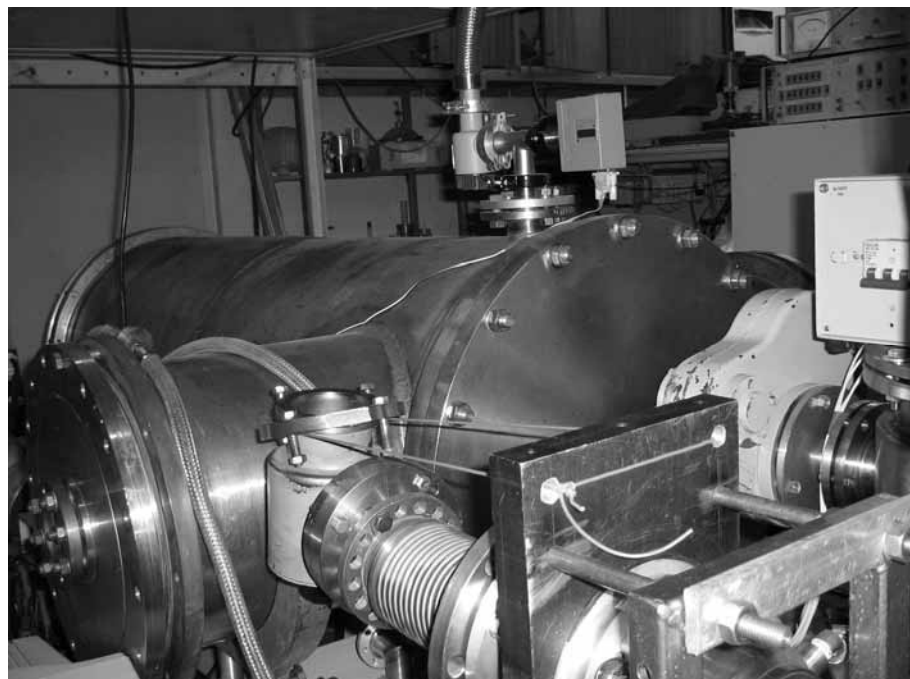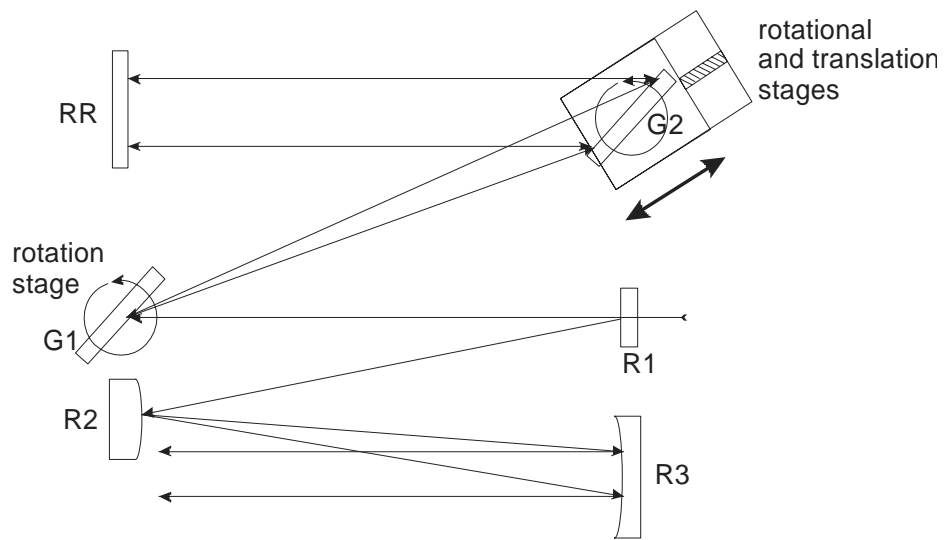
Fig. 3.1.1.6 Vacuum compressor. A) layout G1 and G2 – gratings with 1400 lines/mm, RR- retroreflector, R1 – flat mirror, R2 – convex mirror with focal length F=-1000mm, R3 – concave mirror with focal length F=2000mm. b) view.

The contrast ratio of output radiation over nanosecond time scale was measured by fast photodiode. The measurements showed that over this time scale contrast is mainly determined by the ratio of the energy of the main pulse to the energy of the pulse presiding the main one by the time of radiation roundtrip in regenerative amplifier (~12 ns). This pre-pulse leaves regen amplifier due to the leakage of the optical switcher. The contrast ratio is 300-500.

3.1.2. Cr:F laser system

We've used typical technique of chirped-pulse amplification, based on regenerative and multipass amplifiers. The Cr:forsterite femtosecond laser system set-up is shown in Fig. 3.1.2.1. Measurements of the amplified pulse energy at the laser system output has been conducted with thermocouple power meter *Gentek* taking into account average power (in the repetition rate regime) and using piroelectric (in the single-shot regime). The output laser pulse energy was about 400 μJ at the RegAmp and MPA pump energy level 4 mJ and 18 mJ respectively. The femtosecond pulse duration has been measured by single-short autocorrelator. Principal scheme of the autocorrelator processing is shown in Fig. 3.1.2.2. Autocorrelation function is depicted in Fig. 3.1.2.3, that gives the compressed laser pulse duration $\tau=115\pm5$ fs.

The beam spatial quality was controlled by CCD-camera. The arrangement for measuring of the beam diameter at the lens focus is represented in Fig. 3.1.2.4. The magnified beam image (a) and it's X-axis profile & Gaussian fit (b) at the non-aberration objective focus (F=6 cm) is shown in Fig. 3.1.2.5. The beam waist diameter (F/D=5.5) is about $D_F\sim4$ μm, corresponding with M^2-factor near 1.3. So, the output laser pulse parameters (E~400 μJ, $\tau\sim115$ fs, D~4 μm) allow us to achieve intensity $I >10^{16}$ W/cm². This is enough to create hot dense plasma and to make experiments on low energy nuclear level excitation.
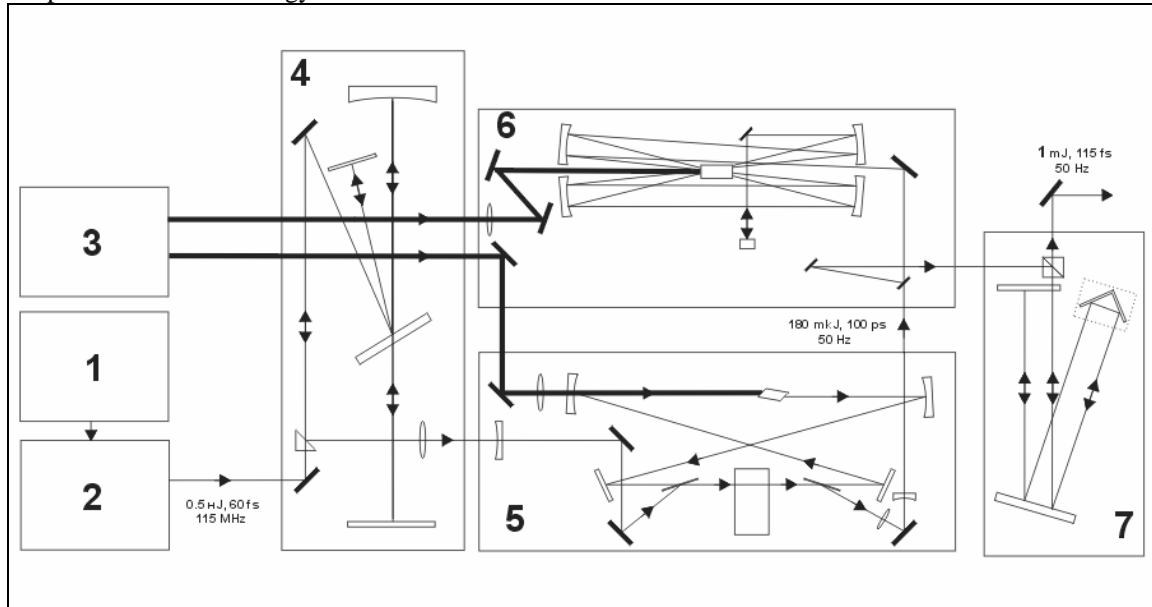

Fig. 3.1.2.1 Set-up of Cr:forsterite femtosecond laser system. 1 – ytterbium pump laser, 2 – Cr:F femtosecond master oscillator, 3 - two-channel YAG:Nd RegAmp and MPA pump laser, 4 – stretcher, 5 – regenerative amplifier, 6 – multipass amplifier, 7 – compressor.
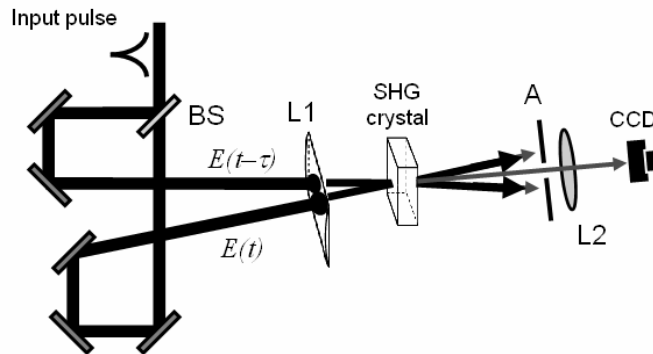

Fig. 3.1.2.2 Scheme of the single-short autocorrelator processing. BS – beam splitter, L1 – cylinder lens, A – aperture, CCD – CCD-camera, L2 – lens for imaging on the CCD-camera.
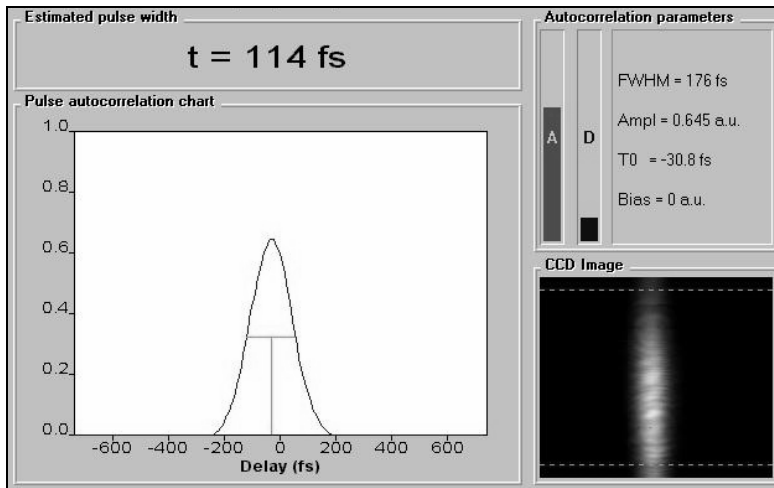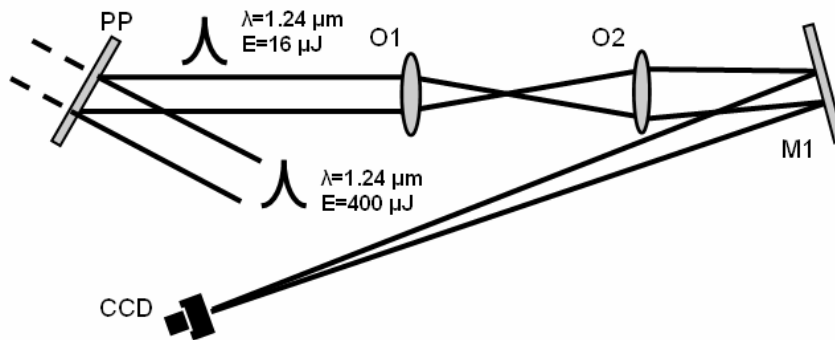
Fig. 3.1.2.3 Normalized autocorrelation function.

Fig. 3.1.2.4. The arrangement for the measuring of the beam diameter at the lens focus. O1 – non-aberration objective (F= 6 см), O2 – imaging objective, PP –plate, M1 – plain mirror, CCD – CCD-camera.
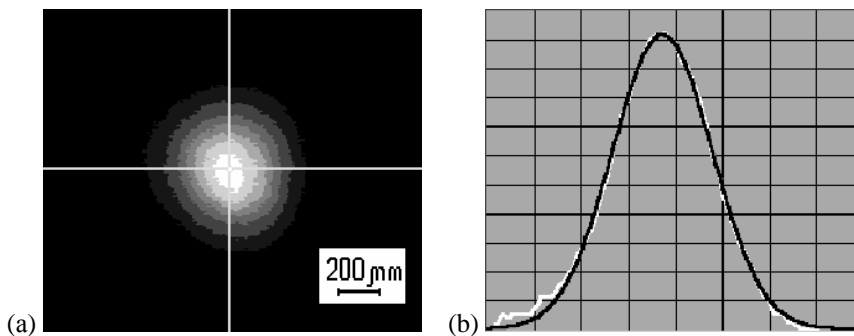

(a)   (b)

Fig. 3.1.2.5 Beam image at the lens focus with F/D=8 (a) and it's X-axis profile & Gaussian fit (b). Magnification factor M=47, λ=1240 nm.

3.1.3 Raman-laser.

For carrying out of experiments on excitation of nuclear levels in laser plasma in SRC RF TRINITI the creation of a laser system with the following parameters was planned: energy ~10mJ in a pulse duration less than 5psec, an opportunity of focusing in a spot size less than 10 microns, with density of power on a target over 10^{16} W/cm^2. The laser with the mentioned above parameters was supposed to be received from an available laser complex with use of a pulse compression of light pulses during SBS and SRS scattering.

The important feature of the technical approach in the given project the choice of the circuit of the laser with a compression of light pulses was during the SBS and the SRS as against the traditional circuit of direct amplification which is more complex and unreliable architecture.

Transformations of laser pulses by a method of a light compression during SBS in a nanosecond range now are well investigated and frequently applied in laser techniques. Features of a light compression of pulses in picoseconds a range during SRS are investigated less in details and in practical applications are used less often. A principal cause to this is instability of output parameters of the laser pulses received as a result of a compression. Thus such parameters of a laser pulse as its energy and duration, from flash to flash can differ on tens percent. Other

undesirable effect is increase of divergence of output radiation at short duration of pulses. In traditional circuits of a compression geometrical factors in these conditions do not allow to generate a beam of radiation with divergence of diffraction quality.
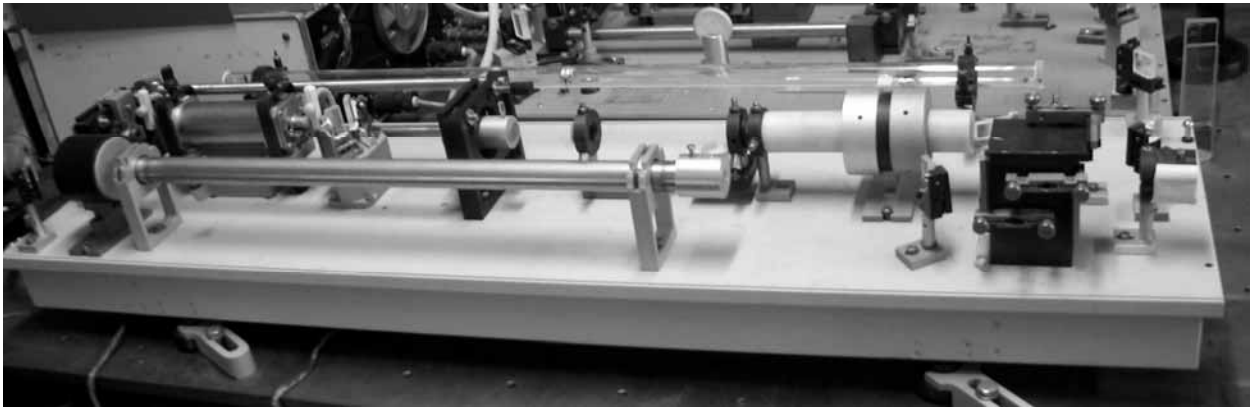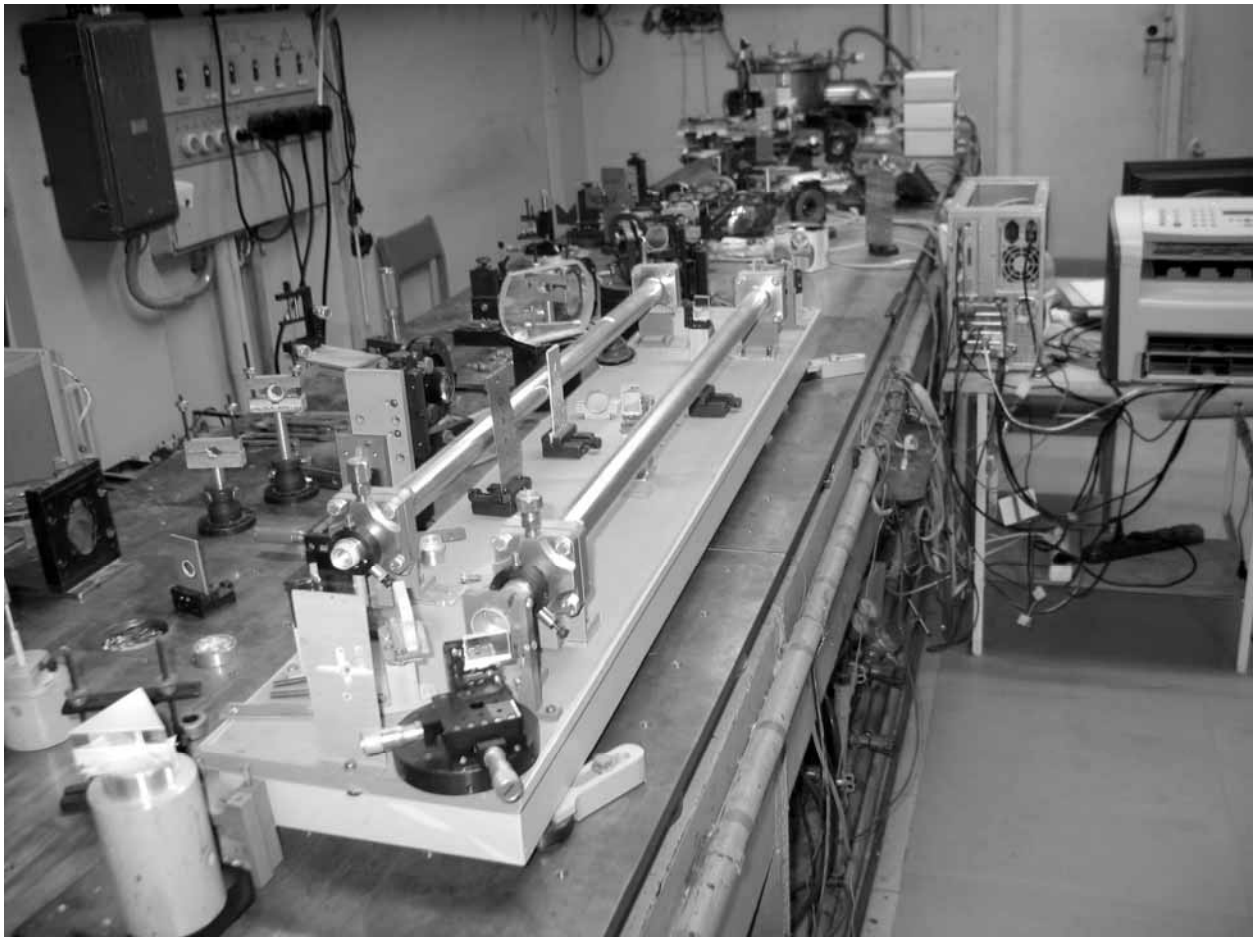

Fig. 3.1.3.1 Raman – Laser.

Fig. 3.1.3.2 Raman amplifiers.

The carried out researches have shown, that instability of output parameters is caused by instability of a frequency spectrum and presence of «hot points » in cross-section distribution of intensity in a pumping beam. For elimination of sources of instability of output parameters of laser system the special steadily working on one longitudinal mode oscillator has been developed. Also the special attention was given reception of an output beam for pulse compressors with pure Gaussian cross-section distribution of intensity (a share of energy in noise less than 10^{-4}). For this purpose in the laser the mode of the of wave front conjugation in a combination with a depolarization compensation was exposed and additional spatial filtration was used. For reception of output radiation with divergence close to diffraction quality the pumping circuit has been offered to special geometry.

The optical circuit of laser system has been developed in view of the requirements showed to output parameters of the SRS - LASER, working in a reprate mode with the divergence close to diffraction quality and practical prepulse absence. Also the estimation of amount of works on updating the existing laser for achievement of the above-stated parameters has been carried out.

On the basis of the developed optical circuit the following works have been lead. Changes are brought in a design of the specifying generator of the Nd:YAG-laser. Namely, the design of the resonator is advanced with the purpose of increase in its rigidity and stability, and also adjustment convenience. Resonant rear mirror in the specifying generator has been replaced with pair resonant mirrors for increase in good quality of the resonator. For the further improvement of quality of output radiation in a design of the amplifier the telescope with a spatial filtration of an angular spectrum of an amplified beam has been changed.

Also with the purpose of modernization of the laser and improvement of its output parameters such components of the laser, as active Nd:YAG-rods, the complete set 45˚ mirrors with factor of reflection for S and P polarizations more than 99 % and the complete set of nonlinear crystals BBO for up conversion of output radiation of the laser to the high harmonics have been got and replaced.

Optimization of the first cascade of the pulse compressor was carried out on such parameters, as power efficiency of a compression that is the relation of energy of an output beam to energy of a pumping beam, and also on stability of the spatial and time form of output pulses. Optimization the geometry of a pumping beam and the active SRS gases varied. As the SBS - ACTIVE gases of the compressor such gases, as Xenon, argon, six-fluoric sulfur and nitrogen were used. Pressure of gases varied from units up to tens atmospheres.

For obtaining of extremely short SRS - pulses are necessary to use architecture of SRS - lasers with amplification in the focused pumping beams.

Carrying out researches of modes of amplification of SRS - pulses in the focused pumping beams and dependences of Stokes pulse duration, and also its power dependence from of character of distribution of intensity in a pumping beam were studied.

In experiments on studying modes of amplification of the SRS of pulses in the counter focused pumping beams the basic attention was given a presence of the conditions providing reception of pulses with stable time and power characteristics, and also with preservation of angular divergence amplified beams at the greatest possible factor of amplification.

Dependences of a mode of amplification Stokes pulses from a convergence value of a pumping beam have been investigated. Optimization of a value of a corner of a convergence of a pumping beam was carried out in view of parameters of amplified Stokes pulses and characteristics of the used SRS - gases. By such optimization the time delay between an amplified pulse and a pumping pulse also varied. The time delay also provided suppression of an oscillation operation of the SRS - amplifier.

In the carried out experiments strong influence of non homogeneity of intensity in an amplified beam and in a pumping beam on time and power stability of amplified pulses was revealed. Therefore the special attention at carrying out of researches was given maintenance of homogeneous cross-section distribution of intensity, both in amplified Stokes beam, and in a pumping beam.

As a result of the executed researches modes of amplification of SRS - pulses in the counter focused pumping beams with factors of amplification~50 have been found. Thus output Stokes pulses with duration~160psec and energy~50mJ had divergence close to diffraction quality, and also possessed stable time and power characteristics.

Researches of processes and the mechanisms influencing extremely possible duration of SRS - pulses have been lead. The special attention was given operating modes of the SRS - laser with stable parameters as instability of output parameters is one of essential lacks of SRS - lasers that basically explains their rather rare application in practice. Besides such important parameter of the SRS - laser, as angular divergence of an output beam was studied.

For reduction of influence by stability of output parameters of accompanying nonlinear processes such as optical breakdown and ionization of the SRS of gas, working gas got out with the big energy of ionization and electro negativity, for example methane CH4 or six-fluoric sulfur SF6.

Earlier in experiments it has been shown, that presence of two or more centers of formation of the SRS radiation results as interference in increase in duration Stokes pulse, to reduction of energy in the reflected pulse and the big instability of output pulses.

In the further research it was used pumping beam with smooth distribution of intensity, namely, with Gaussian and hyper Gaussian distribution of intensity. For experiments with Gaussian distribution of intensity the spatial filtration initial pumping beam was carried out. For reception hyper Gaussian distributions of intensity after a spatial filtration formation of a beam with the help of a diaphragm was carried out.

With help of streak-camera it was shown, that at Gaussian distribution of intensity in pumping beam, there is a formation of a nonlinear mirror in central, more intensive part of a beam earlier, and Stokes pulse in the center of a beam is pulled out forward. From the analysis of results of these experiments follows, that optimum distribution of intensity in cross-section of a pumping beam for a pulse compression of light pulses during the SBS or SRS processes is the hyper Gaussian distribution with a constant intensity on all section.

Comparative experiments with Gaussian and hyper Gaussian pumping beam SRS - compressors have shown, that at hyper Gaussian pumping beam Stokes pulses have smaller duration, the big energy and the big

stability of output parameters, that is, on all parameters of output radiation the usage of pumping beam with hyper Gaussian distribution of intensity is preferable.

Thus, as a result of the carried out research it has been shown, that at performance of some conditions it is possible to obtain stable parameters of output radiation at the SRS - compression. So in a stable mode with divergence close to diffraction quality pulses by duration less 10psec with energy 8 mJ±15 % at repetition rate 5Hz have been received. For such compression the pumping pulses with duration 160psec and with energy 55мДж, received in the preliminary SBS - compressor were used. For pumping of preliminary SBS – compressor the radiation of the second harmonic of the Nd:YAG-laser with hyper Gaussian distribution of intensity in cross-section of a beam was used. The cascade of the SBS - compressor has been constructed under the architecture an oscillator – an amplifier.

The carried out experiments on studying a multistage SRS - compression of light pulses in the compressed gases have revealed the following processes limiting duration Stokes pulses at the SRS - compression. One of the basic processes limiting duration of output Stokes pulses, optical breakdown of working SRS - gas is.

With other important process influencing duration Stokes pulses, smooth heterogeneity of intensity is connected, for example at Gaussian distribution. It results in various growth rate of amplitude of the SRS - signal in cross-section distribution of Stokes beam. Duration of output pulse is delayed due to a bend of front of equal intensity that was experimentally observed with the help of the streak camera under pulse compression in argon. In this case it is possible to reduce duration of Stokes pulse, with help of diaphragm. Thus peripheral areas of a beam with the low intensity are cut out.

In restriction of duration of output pulses also results the presence in cross-section of a beam the heterogeneity of intensity as «hot points». In that case formation Stokes radiations occurs from several areas of focal spot, and seeding SRS - signals start to compete among themselves during amplification, that essentially increases duration of output pulses.

As a result of the carried out research it has been shown, that by the principal causes limiting duration of SRS - pulses, optical breakdown of the SRS - active gas, self-modulation of a parameter of refraction of the SRS - active gas and the geometrical factor of the SRS - laser are.

Together with group MLTS of the Moscow State University besides measurements of duration of output radiation with the help of streak camera, the system of measurement of duration of pulses with the help of nonlinear optical correlator has been established and adjusted.

The quartz focusing lens in the SRS - compressor has been replaced with sapphire lens with antireflection coating more durable to laser radiation.

For increase of stability of work of the SRS - compressor and elimination of influence of optical breakdown of a pumping beam in the SRS gas on process of a pulse compression, in its design has been built - in deionizer of working gas.

Fig. 3.1.3.3 Vacuum chamber.

For increase of output energy of radiation from the second cascade of the compressor the distribution of intensity in cross-section of a beam from the specifying laser on an input in the first cascade of the compressor was transformed in hyper Gaussian. Thus simultaneously with increase in output energy of radiation from the second cascade of the compressor there was an increase in stability of output pulses on energy and duration of pulses.

Together with Moscow State University team it have been carried out works on testing output radiation of the laser after an upgrade of laser system and preparation of the vacuum chamber for the planned experiments.

During works it has been shown, that time stability of such output parameters of the laser as duration of pulses and energy of pulses has essentially increased. At repetition rate of the laser 5Hz the output energy 8mJ ± 15 %, duration of pulses less 10psec ± 20 %.

3.2. Preparatory work
3.2.1. Laser beam quality measurement

Under carrying out the experiments on the nuclear excitation in plasma it is necessary to have the laser intensity on the target surface more than 10^{16} W/cm^2. At the fixed power of laser system the intensity is defined by the focus spot diameter, which depends on the input laser beam quality. So, in order to obtain a required intensity on a target surface, it is necessary to control the beam quality.

We have developed the block of the laser beam quality measuring (by the example of Cr:F laser system (λ=1,25 mkm)). There are different methods of the laser beam quality estimation. One of them is the estimation of the measured beam profile closeness to the Gaussian beam profile. For that the M^2-factor, which equals to the ratio of the beam waist diameter D (at FW1/eM of the electric field) to the Gaussian beam waist diameter D_G.

The measuring of the beam quality factor M^2 involves 1) measuring of the beam diameter D (at FW1/eM of the intensity) within three Rayleigh lengths (L_R= b/2, where b – is the waist length) on either side of the beam waist z, 2) hyperbolic fit of the obtained data $\sqrt{A + Bz + Cz^2}$ and 3) calculation the M^2-factor by using the A, B, C

coefficients and formula $M^2 = \dfrac{\pi}{4\lambda}\sqrt{A \cdot C - \dfrac{B^2}{4}}$. Note that we have to fit the beam diameter at FW1/eM of the

electric field, so the measured beam diameter at FW1/eM of the intensity is multiplied by $\sqrt{2}$.

Under development of the M^2-factor measure system the calculation of the following parameters has been carried out: the laser beam diameter (at FW1/eM of the intensity) D, waist length b depending on the lens focus length F and the input beam diameter D_0 (at FW1/eM of the intensity). The major criterion of the focusing system optimal parameters was the minimum size of the laser radiation spot at the CCD-camera surface. The reliable measuring of the beam diameter is possible under beam registration by more than 15 pixels of CCD-camera. Moreover, three waist lengths must be less than the full transition length of the positioner (L~15 см), and the cross section maximum square at the distance 1,5b must be at least 10 times less than the sensitive region square of the CCD.

We suppose that the input beam is collimated. Then, the beam diameter (at FW1/eM of the intensity) at the lens focus D_f is:

$$D_f = \frac{2}{\pi}\lambda\frac{F}{D_0} \sim 0,6\lambda\frac{F}{D_0} \tag{1}$$

The waist length b is:

$$b = \frac{4}{\pi}\lambda\left(\frac{F}{D_0}\right)^2 \sim 1.3\lambda\left(\frac{F}{D_0}\right)^2 \tag{2}$$

The beam diameter at the distance z concerning the beam waist is:

$$D(z) = D_f \cdot \sqrt{1 + \frac{z^2}{(b/2)^2}} \tag{3}$$

where point of origin z is positioned on centre of beam waist. *Table 1.3.2.1.1 shows t*he calculation results.

Table 3.2.1.1. *The beam waist diameter D_f and the waist length b depending on the input beam diameter D_0 and the lens focus length F. The laser radiation wavelength - λ=1.25 mkm, b/2 – the Rayleigh length, N – the pixel number (pixel size - 7.5×7.5 mkm^2)*

F=60 cm	D_f, mkm / N	b, mm	D(b/2), mkm / N	D(3b/2), mkm / N	D(5 cm), mkm
D_0= 3 mm	159 / 20	64	225 / 30	356 / 66	296
D_0= 4 mm	119 / 16	35	169 / 22	377 / 50	354
D_0= 5 mm	95 / 12	23	135 / 18	302 / 40	427

F=50 cm	D_f, mkm / N	b, mm	N	D(b/2), mkm / N	D(3b/2), mkm / N	D(5 cm), mkm
D_0= 3 mm	133 / 17	4	4	188 / 25	419 / 55	328
D_0= 4 mm	99 / 13	2	5	141 / 18	315 / 41	412
D_0= 5 mm	80 / 10	1	6	113 / 15	252 / 33	506
F=40 cm	D_f, mkm / N	b, mm	N	D(b/2), mkm / N	D(3b/2), mkm / N	D(5 cm), mkm
D_0= 3 mm	106 / 14	2	8	150 / 20	336 / 44	390
D_0= 4 mm	80 / 10	1	6	113 / 15	252 / 33	506
D_0= 5 mm	64 / 8	1	0	90 / 11	201 / 26	628

As follow from the *Table 3.2.1.1*, for the M^2-factor measuring it is necessary to have the lens with the focal length F=50 cm, and the input beam diameter must to be about 3 mm, i.e. $F/D_0 \sim 170$.

Figure 3.2.1.1 shows the scheme of the M^2-factor measuring block The Cr:F laser system radiation 1 falls on focusing lens (F=50 cm) 2 and passes through attenuator system. Then it falls into CCD camera. CCD camera signal digitized by computer system of image input and processing. Figure 1.3.2.1.2 shows the example of laser beam profile measurements. Figure 3.2.1.3 shows results of measurements of laser beam diameter in dependence on longitudinal coordinate z and data fit. The measured M^2 value is *1.3±0.2*. Thus, the output radiation of Cr:F laser system is close to Gaussian, that permit us to obtain focal spot diameter close to ideal (see formula (1)) and control laser pulse intensity at a target.
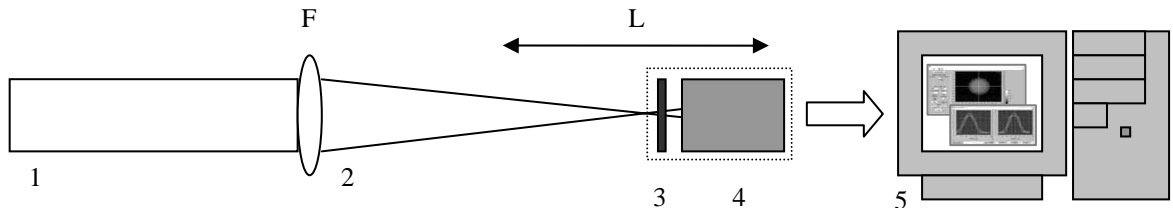

Fig. 3.2.1.1. Scheme of laser beam profile measurements for Cr:F laser system: 1-laser radiation, 2 – focusing lens (F=50 cm), 3 – system of optical filters, 4 – CCD camera, 5 – the image input and processing computer system.
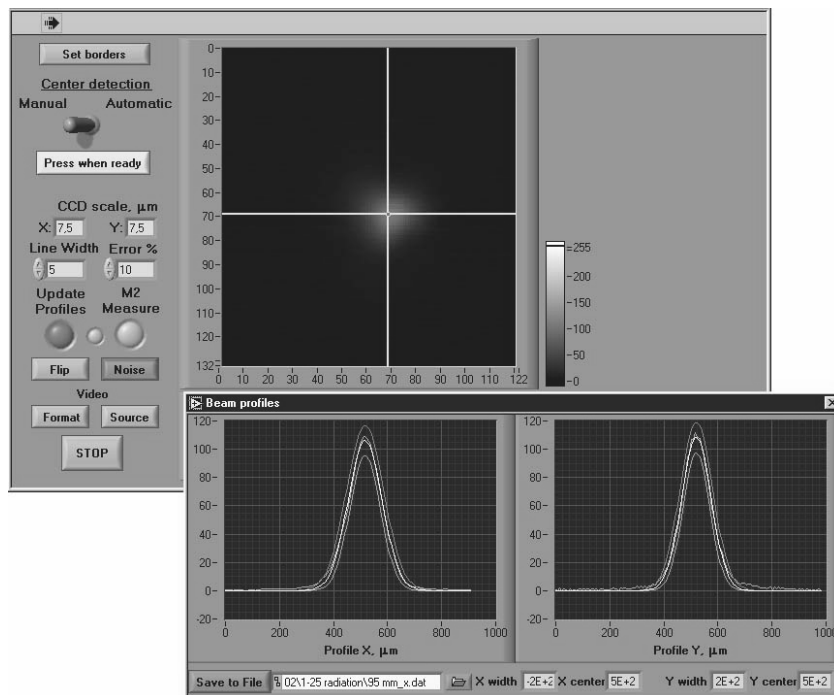

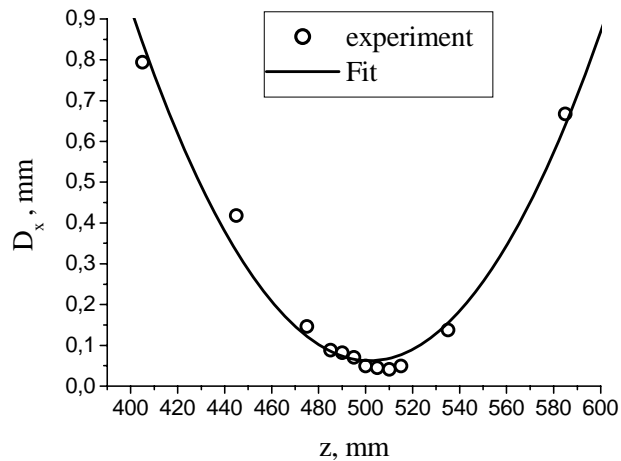Fig. 3.2.1.2. Profiles of the beam from the Cr:F laser system at focus.

Fig. 3.2.1.3. Dependence of the laser beam diameter D on the longitudinal coordinate z and its hyperbolic fit.

3.2.2. Vacuum set up

The new vacuum system (VS) for pump of interaction chamber was made. Parameters of VS:

Pressure of residual gas in vacuum chamber is no less than 10^{-6} torr.

Pump rate under residual gas pressure ~10^{-6} torr is no less than 150 liters per second (for nitrogen).

Power supply of VS is alternating three-phase current with 380 V voltage and 50 Hz frequency. The maximum power consumption is 500 W. The VS has an air-cooling system. So water-cooling is not required. Size of VS is (length x width x height, mm) 350x600x1300. Weight is 90 kg.

Figure 3.2.2.1 shows whole view of vacuum system and figure 3.2.2.2 – flow-block. Vacuum system is assembled on hard frame with four wheels. In order to fix the frame you can use step-bearings. VS connects with experimental chamber by means of two connection mains (№1, №2). The №1 connection main is flexible branch pipe with stainless steel flanges. To prevention of branch pipe deformation under connecting of VS with experimental chamber possibility of vertical shift of vacuum cock №5 coupled with molecular turbo pump is provided. The maximum height of lifting is 120 mm.
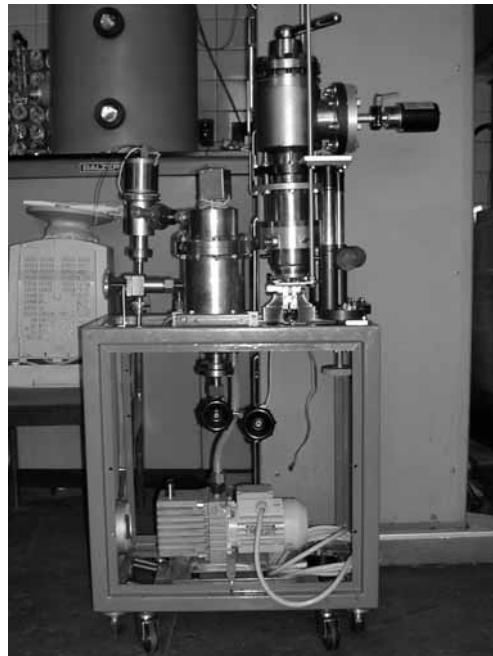

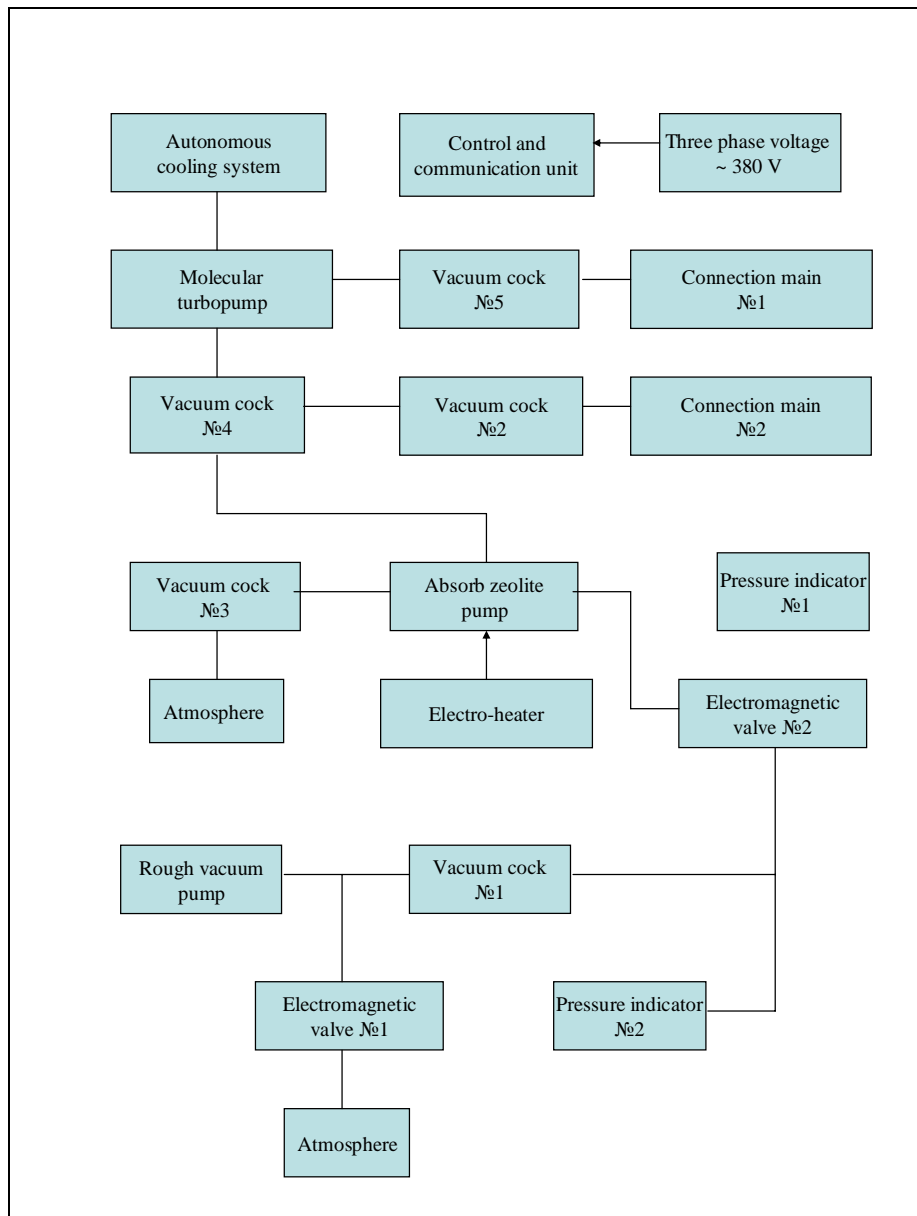Fig. 3.2.2.1. The whole view of vacuum system.

Autonomous cooling system

Control and communication unit

Three phase voltage ~ 380 V

Molecular turbopump

Vacuum cock №5

Connection main №1

Vacuum cock №4

Vacuum cock №2

Connection main №2

Vacuum cock №3

Absorb zeolite pump

Pressure indicator №1

Atmosphere

Electro-heater

Electromagnetic valve №2

Rough vacuum pump

Vacuum cock №1

Electromagnetic valve №1

Pressure indicator №2

Atmosphere

Fig. 3.2.2.2. Flow block of vacuum system.

The new interaction chamber for making experiments on the superstrong laser fields interaction with matter under focusing by off-axes parabola has been done (Fig. 3.2.2.3). The mounting arrangement of the major chamber blocks – flanges for the laser radiation injection, for docking with the vacuum pump system, for electric connectors and for the plasma parameters detection system - has been developed.

Optical scheme of adjustment of the off-axes parabolic mirror has been made and tested. The scheme is based on transference of focus imaging of parabolic mirror to CCD, to allow adjust the mirror only by observing increasing image of focus.

In fig 3.2.2.4 we can see the scheme. 1 – He-Ne laser, 2 – telescope, 3 and 5 – mirrors, 4 – input window of vacuum chamber, 6 – off-axes parabolic mirror (f=5cm), 7 – reflected target, situated on the plate (8) with 3-dimensions micrometric movements, 9 – plane glass plate to deflect the radiation, reflected from target to the CCD, 10 – lens (f=4m), 11 – mirror, 12 – CCD.

Fig 3.2.2.5 shows the beam profile, taken by CCD. The measured diameter (HWFM) of the input beam D_0 was (7.0±0.5) mm (Fig. 1.3.2.2.4). So, the theoretical value of the beam waist equals to $D_F^{theory} \approx \frac{1}{2} \frac{\lambda \cdot F}{D_0} = \frac{1}{2} \frac{0.61 \cdot 5}{0.7} \cong 2.1$ μm. The measured beam diameter at the focal length of the parabolic mirror D_F^{exp} was (3.5±0.5) μm. The discrepancy between experimental and theoretical (3.9 μm) values of the waist seems to be associated with the input beam quality.
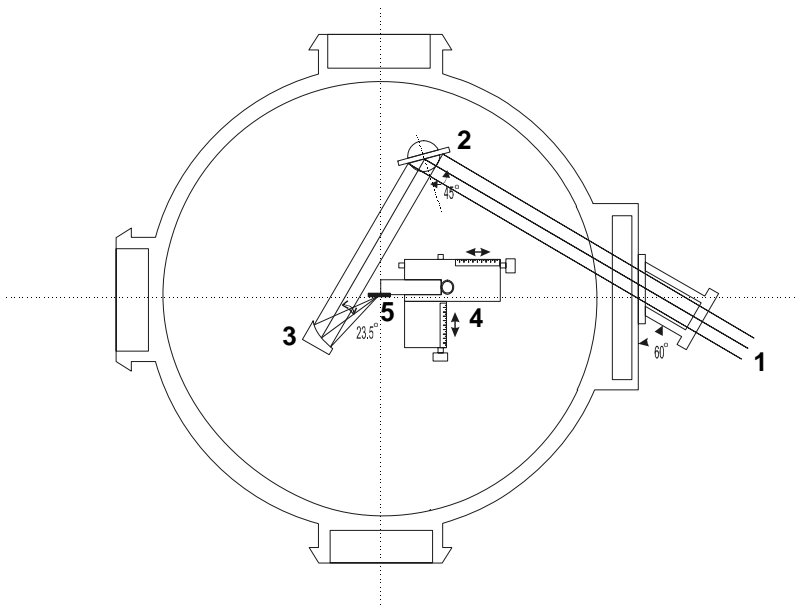
Fig. 3.2.2.3. Scheme of opto-mechanical elements arrangement inside the vacuum chamber: 1- laser beam (D~2 cm); 2 – flat mirror; 3 – off-axis parabolic mirror; 4 – system of 3D target position; 5 – target.
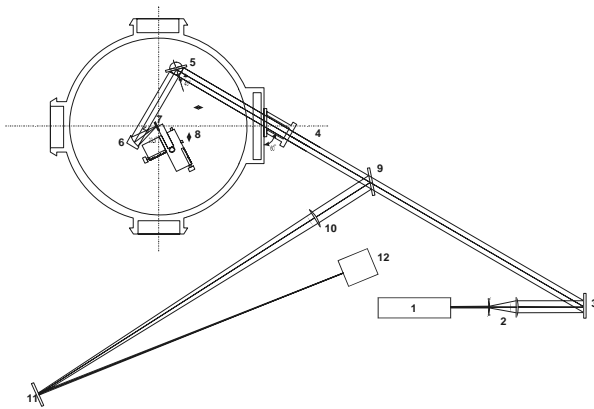

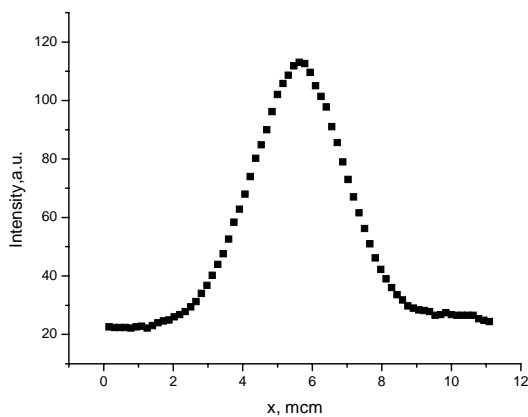Fig. 3.2.2.4 Optical scheme for off-axes mirror adjustment.

Fig. 3.2.2.5 Beam profile as focused by the off-axes parabolic mirror

3.3. X-ray plasma diagnostics

3.3.1. X-ray methods development and implementation

The possibility of usage of silicon avalanche photodiodes (APD) (Advanced Photonix, USA) with thickness of sensitive layer ~80 μm as detectors of X-ray and gamma-radiation and for estimations of average energy of hot electrons of laser produced plasma was investigated. The calibration experiments have shown that APDs have

efficiency above 50% in the range of photon energy from 2 to 15 keV, energy resolution ~20%, and signal/noise ratio ~10. The obtained parameters are several times better then characteristics of detectors based on photo-multiplying tube (FEU-119) with scintillator NaI(Tl).

The new x-ray detectors based on photodiode Hamamatsu S8559 and charge amplifier РШ2731Э were tested in real experiment with femtosecond laser plasma. The usage of new detectors should permit us to register hard x-ray yield from plasma formed by laser pulses with intensity more then 10^{18} W/cm^2. In experiment we measured x-ray yield in spectral band more then 2.5 keV from plasma created by laser pulse delivered by Ti:Sa laser system (τ=70 fs, E~ 2 mJ, λ=800 nm, I~10^{17} W/cm^2) onto the tungsten target surface. The x-ray yield was measured simultaneously by two different detectors. First one was old and based on PMT-119 with scintillator NaI(Tl) and the second one was new. The comparative experimental data are shown in figure 3.3.1.1. The dispersion of ratio of x-ray signals from both detectors does not exceed 25%. At the same time the precision of old detector based on PMT is about 30%. This points out that a good correlation between values measured by different detectors is observed. Thus, we can exploit the new detectors for hard x-ray yield measuring.
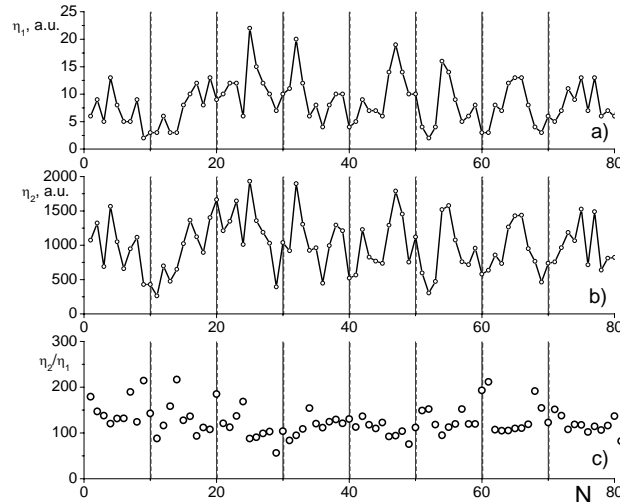

Fig. 3.3.1.1 The x-ray yield in spectral band more then 2.5 keV as a function of laser shot number (a – the measurements are carried out by detector based on photodiode Hamamatsu S8555, b – the measurements are carried out by detector based on PMT-119). The ratio of x-ray signals registered by both detectors as a function of laser shot number (c).

The accuracy of method of multiple absorption foils for determination of the average energy of hot electrons in laser-produced plasma is investigated. The method of estimation of the average energy of hot electrons in every laser shot with accuracy ~25-30% is developed for wide range of laser pulse intensities and X-ray detectors (APD or PMT+scintillator) with different spectral sensitivities. It is shown that accuracy of estimations of the average energy of hot electrons is determined by accuracy of X-ray yield measurements by detectors in the case when low-energy boundaries of transmission of foils used in experiment have difference higher then average energy of hot electrons of plasma. For example, in the case of laser pulse intensities I~10^{16}-10^{17} W/cm^2 the average energy of hot electrons is of the order of 3-5 keV and one needs to use a pair of aluminum foils with thickness 100 μm and 500-700 μm in front of two X-ray detectors. Also it is obtained that the region of spectral sensitivity of X-ray detectors determines accuracy and range of estimations of the average energy of hot electrons. So silicon APD with thickness of sensitive layer ~80 μm have maximal spectral sensitivity in the energy range of X-ray quanta 2-20 keV and could be used for measurements of the average energy of hot electrons ~5-15 keV. At the same time detectors based on PMT (FEU-119) and scintillator NaI(Tl) with thickness ~5 mm are sensitive in the range 2-100 keV and could be used for measurements of the average energy of hot electrons upto 50-70 keV. But the usage of APDs provides the better accuracy of estimations due to better accuracy of X-ray yield measurements in the spectral range corresponding to maximal sensitivity.

Using silicon APD detectors and detectors based PMT (FEU-119) and scintillator NaI(Tl) the value of the average energy of hot electrons in the laser produced (I~5·10^{15}-2·10^{16} W/cm^2) tungsten plasma was determined. The obtained values are in good agreement with theoretical predictions and equal to $<E_h>_{APD}$=5.1±1.4 keV and $<E_h>_{PMT}$=5.7±1.9 keV (Fig. 3.3.1.2).
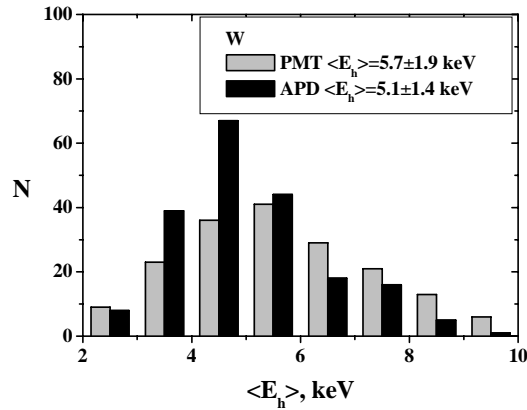
Fig. 3.3.1.2. The histogram of laser shots realization with appointed mean energy of hot electrons (tungsten target, I~5·10^{15}-2·10^{16} W/cm^2). The mean energy of hot electrons was estimated by double channel hard X-rays yield measurements with detectors based on silicon avalanche photo diode (APD) and photo multiplier tube (PMT) with scintillator NaI(Tl).

3.3.2. Plasma X-ray measurements

Figure 3.3.2.1 shows the results of estimation of hot electron mean energy by means of different methods (ionic time-of-flight measurements, x-ray measurements and direct measurements of electronic spectra). Analysis of results shows good coincidence of all estimations.
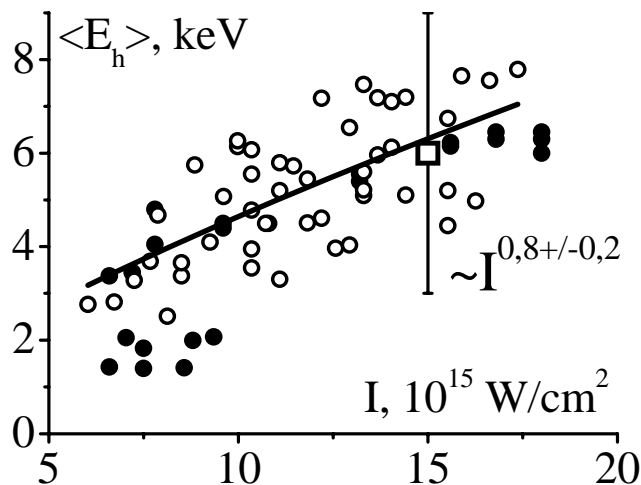

Fig. 3.3.2.1. Dependence of mean energy of hot electrons on laser pulse intensity estimated by double channel hard X-rays yield (o) and ionic time-of-flight spectra measurements (•).

Mark □ denotes result from the direct electronic spectrum study.

A series of experiments was carried out in order to investigate hot electron generation and hard x-ray production in pyramidal cavities on Si wafer. The cavities were obtained by means of electrochemical etching of flat Si sample through two-dimensional metal grating with 8x8μm orifices. The cavities have a shape of regular rectangular pyramids with base angle of 57.8°. A method for precise focusing of intense laser pulse into pyramidal cavity was developed. It was found out that when pyramidal cavities were irradiated by laser pulse with intensity ~10^{16}W/cm^2 the X-rays output from plasma increases 5-10 times in comparison to flat Si target. For electrochemically modified sample mean hot electron temperature is (5.8±1.5) keV, in the case of flat Si target this value is (3.7±0.7) keV under the same pulse intensity of ~10^{16}W/cm^2. So pyramidal craters creation allows to increase hot electron temperature and thus may lead to more efficient Kα generation.

The typical experimental set-up is shown in Fig. 3.3.2.2. The Cr:forsterite laser system radiation (E~380 μJ, τ~115 fs) was focused with the non-aberration objective onto BaF$_2$-target. The beam diameter at the surface was D~4 μm, that gives intensity 2·10^{16} W/cm^2. The target was placed inside the vacuum chamber with pressure near 5·10^{-2} torr. To measure hard X-ray yield we used detectors, based on photomultiplier tube and scintillator NaI(Tl),

with different set of band-pass filters - Be(200 μm)+Al(300 μm), Be(200 μm)+Al(1 mm), Be(200 μm)+Ta(26 mm), Be(200 μm)+Cu(1 mm). It allowed us measuring X-ray yield to the different spectral ranges: E>8 keV, E>12 keV, E>15 keV and E>60 keV respectively. The signal from the detectors passed through charge sensitive amplifier and measured by analog-to-digital converter (ADC). ADC starting was realized by the laser system strobe and was synchronized with the moment laser pulse arrived the target surface. Measured X-ray yield to different spectral regions is depicted in Fig. 3.3.2.3. Double channel hard X-ray detection technique was used to estimate plasma temperature. Mean hot electron temperature for BaF$_2$-target at the laser radiation intensity I=(2±0.2)·10^{16} W/cm^2 is T$_e^{hot}$=(7±1) keV. Hence Cr:F laser system can be efficiently used in experiments on low energy nuclear level excitation in hot dense plasma.
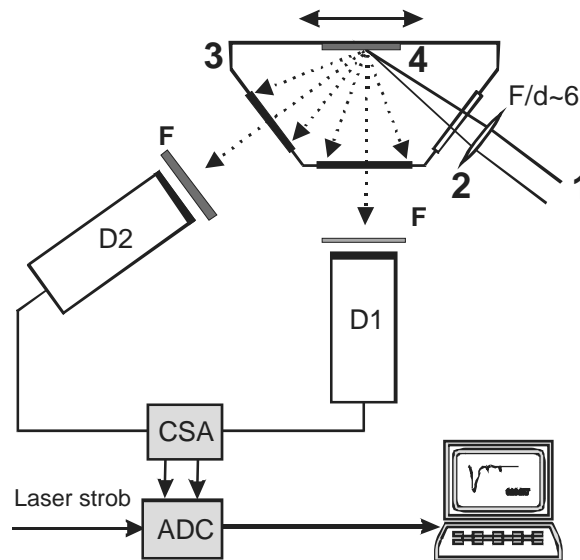

Fig. 3.3.2.2 Experiment set-up. 1- laser radiation; 2- non-aberration objective; 3- vacuum chamber; 4-target; F – band-pass filters; CSA – charge sensitive amplifier; ADC – analog-to-digital converter; D1,D2 - hard X-ray detectors.
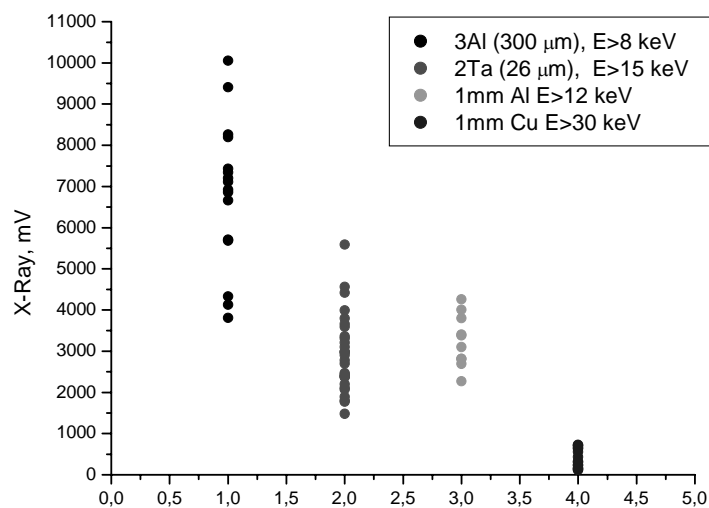

Fig. 3.3.2.3. X-ray yield to different spectral regions.

3.3.3. Time of flight ionic diagnostics

In a given time the method of hot electron mean energy estimation was proposed and developed. The method is based on approximation of proton signal in time-of-flight ionic current by analytical curve. The analytical dependence corresponds to 1D adiabatic model of plasma expansion. We also take into account that ion detector has non-linear response with respect to ions with different energy and charge. The model of adiabatic plasma expansion possesses several advantages by compare with self-similar solution of hydrodynamic plasma expansion task, which is usually used at plasma expansion description. In the model kinetic equations for electrons and ion are solved and it permits to consider finite number of particles and electron cooling during ion acceleration.

Analyzing experimentally registered time-of-flight ionic signal one can find that ionic current front and its minimum correspond only protons. (see fig. 3.3.3.1). Moreover from energy spectra consideration it is known that such protons are accelerated by hot electrons.
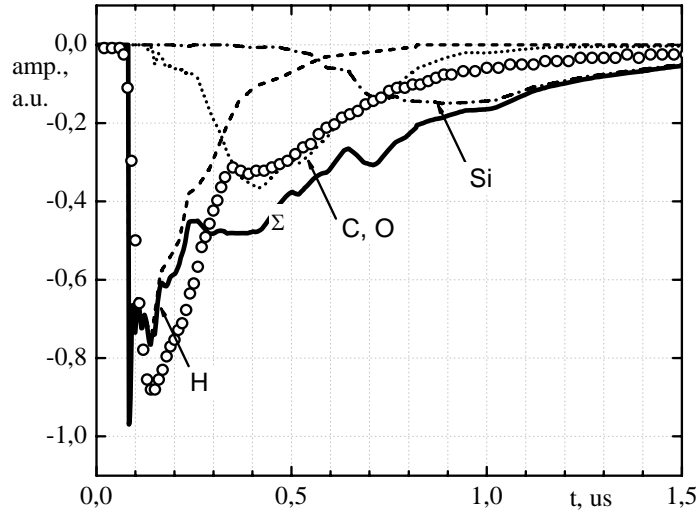

Fig. 3.3.3.1 Time-of-flight ionic current from silicon plasma. Cycles – the signal registered in experiment, curves – signals restored from ion energy spectra.

Besides, if we analytically consider expansion of plasma having one ion type and bi-maxwellian electrons we can find out that independence of thermal electrons presence and independence the ratio between hot an thermal electrons temperatures and concentrations the minimum in ionic current does not change its shape and its position in time scale. So, for experimental signal approximation one can exploit the solution corresponding to expansion of plasma with protons and hot electrons.

Adiabatic model of plasma expansion allow us to construct ionic distribution function at any time and space point:

$$f^i(x,v,t) = \frac{n_{i_0}}{\sqrt{2\pi}V_{T_i}} exp\left\{-\frac{U^2}{2V_{T_i}^2} - \frac{\left(1+\Omega^2 t^2\right)}{V_{T_i}^2}\left(\frac{(v-u)^2}{2} + \frac{Ze\Phi}{M}\right)\right\}. \tag{1}$$

Here n_{i0}-ionic concentration, $V_{T_i} = \sqrt{\frac{T_{i_0}}{M}}$ - thermal velocity of ions, $U = \frac{\Omega x}{\sqrt{1+\Omega^2 t^2}}$ - plasma

characteristic velocity, $u = \frac{xt\Omega^2}{1+\Omega^2 t^2}$ - plasma local velocity, $\Omega = C_s/L_0$ - the ratio of characteristic velocity of

ions to initial scale of plasma heterogeneity, $C_s = \frac{ZT_{e_0} + T_{i_0}}{mZ + M}$ - ionic sound speed,

$\Phi(x,t) = \frac{\Omega^2 x^2}{2e\left(1+\Omega^2 t^2\right)^2}\frac{mT_i - MT_e}{T_i + ZT_e}$ - electrostatic field potential, T_{e_0} и T_{i_0} -temperatures of electrons and

ions, m,e – mass and charge of electron, M – ion mass.

To construct ionic current we should consider ion flow through single square and single time unit

$$S(x,t) = \int\limits_{-\infty}^{+\infty} dv \cdot v \cdot f^i(x,v,t):$$

under $\Omega t \to \infty$ $S(x,t) = \frac{n_{i_0} x}{\Omega t^2} exp\left\{-\frac{x^2}{2C_s^2 t^2}\right\}. \tag{2}$

At ionic current approximation one should also take into account the fact that ion detector has a non-linear response to ions with different charge and energy. To register ions in experiment we used chevron micro-channel plate (MCP) VEU-7. As a result the expression (2) was multiplied by power function $a \cdot v_{ion}^{\alpha}$, which describes the dependence of current amplification on ion velocity. Figure 3.3.3.2 shows the example of experimental curve approximation by analytical curve with MCP nonlinearity.
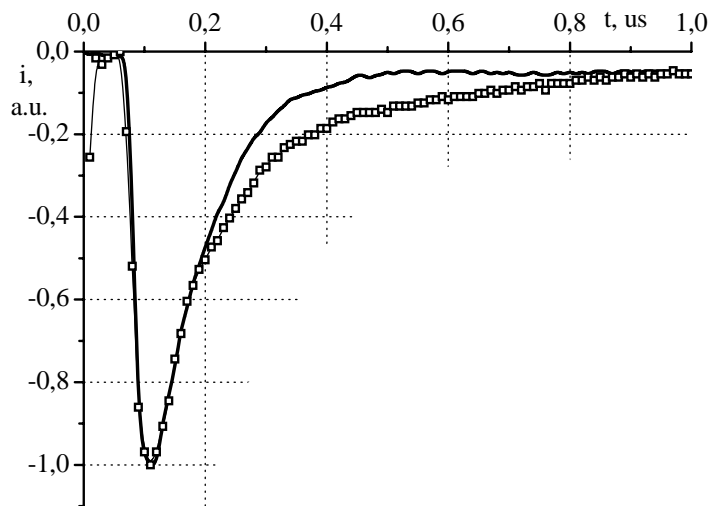
Fig. 3.3.3.2 Time-of flight ionic current from plasma at vacuum oil VM-1. Solid curve –analytical dependence, ☐ – experimental data.

To test our method of hot electron mean energy estimation we carried out the experiment with simultaneous measurements of hard x-ray yield in two different spectral bands and ionic time-of-flight measurements from plasma created by laser pulse (τ=200 fs, E=300 uJ, λ=616 nm, I~$2 \cdot 10^{16}$ W/cm^2) at free surface of vacuum oil (VM-1). It gave us a possibility to estimate mean energy of hot electrons by means of two different independent methods. Figure 3.3.3.3 shows the comparative data.
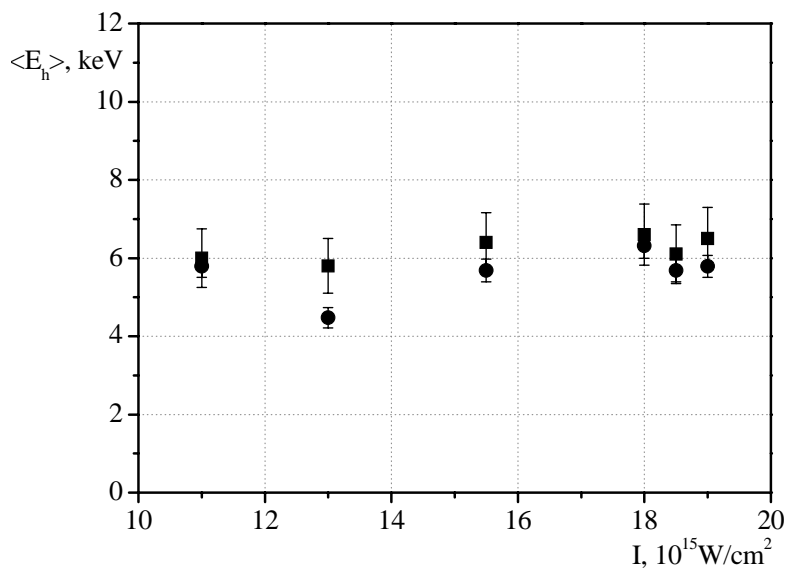

Fig. 3.3.3.3 Mean energy of hot electrons in plasma as a function of laser pulse intensity. ■ - estimation corresponding to x-ray method, ●- estimation corresponding to ionic method.

So, it was shown that estimates for hot electrons mean energy obtained by means of ionic method well agreed with estimates obtained by means of early developed x-ray method. And we can exploit the new method in our experiments.

3.3.4. Energy resolved ionic diagnostics and data

The experiments on measurements of time-of-flight and energetic ionic spectra from plasma formed by femtosecond laser pulse at clean solid target surface were carried out. It is known that in air and in atmosphere of residual gas in chamber at target surface the contamination layer is formed. This layer contains molecules of hydrogen, carbon and oxygen. Thickness of layer is about 10 nm, this value is comparable with plasma thickness. So plasma formed at unclean surface of target is substantively multi-component. The presence of protons leads to quicker cooling of plasma and complicates the conversion electrons registration. To remove contamination layer we used pulse heating of target surface by means of CO_2 and XeCl laser radiation. Femtosecond laser pulse interacted with target in some delay after cleaning pulse. By the contrast to the instantaneous resistive heating the pulsed laser cleaning provides higher heating temperatures and can be used for any solid targets in the thermal and plasma regimes. We obtained in experiment that after influence of cleaning laser pulse part of ions H, C and O in plasma is reduced in 10-20 times (see fig. 3.3.4.1). It was determined the optimal parameters for efficient laser cleaning. These parameters are: energy

fluence (~ 3-10 J/cm^2), temporal delay between cleaning pulse and plasma forming pulse (~ 1 us – 1 ms). The optimal parameters provide with removing of 90-95 % of contaminants.
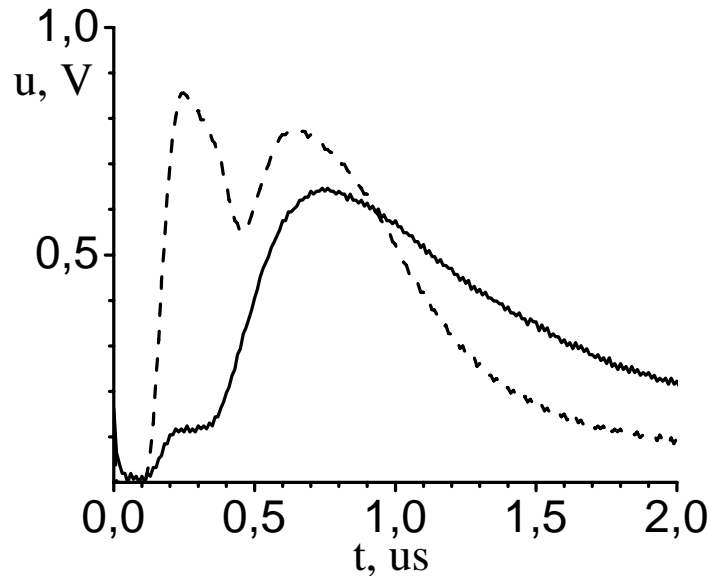

Fig. 3.3.4.1. Time-of-flight ionic current without preliminary cleaning of target surface (dashed line) and after cleaning by CO$_2$ laser radiation (solid line) (time delay between laser pulses is t=100us, target Si).

This effect could play a major role in the further experiments on registration of conversion electrons. As soon as the reducing light contaminants leads to reducing of their negative ions amount. Exactly the negative ions of light materials interfered with conversion electrons on TOF spectra, obtained in mass-spectrometer measurements.

Laser plasma emits ions, having charge state in the order of 10$^+$ for heavy elements, and reach kinetic energy higher than 100 keV. Their angular distribution is narrow and directed along the normal to the target surface. So placing a collector on the path of ablating ions one can implant them into the bulk of the substrate. Implanted ions depth profile gives information about ion energy. In laser-plasma experiments the ion implantation into substrate can be used as an effective and simple method of diagnostics of both energy and angular distribution of ablating ions. The diagnostics can be utilized in experiments with large number of laser shots, for example, in experiments on thermonuclear neutron production on solid targets, when ion energy distribution averaged by large number of shots is only needed. The method of ion implantation may be especially useful at high pulse repetition rates of more then 1 kHz, when other ways of ion diagnostics are significantly complicated.

For our laser pulse parameters (τ=200fs, I=10^{16}W/cm^2), ion dose on collector placed at a distance of 1,5 cm from the target in the direction of target normal was estimated as 1,5*10^{11} ions/cm^2 per laser shot. So 2*10^4 laser pulses are needed for integral dose achievement of 3*10^{14} ions/cm^2, when solid density surface layer of implanted atoms is formed. The SRIM-2003 code program was employed to simulate the effects of the Ti ion energy loss and projected ranges in Si substrate. Considering a particular initial Ti ion distribution, obtained by means of mass-spectrometer, an expected density profile of implanted ions was calculated. It was obtained that density of implanted ions can reach the value of 10^{18} at/cm^3 at depth of 50nm. The value can lightly be measured by SIMS technique. An experiment was carried out with pulse intensity of ~10^{15}W/cm^2 and 1.5*10^3 shots applied to Ge target, flat Si wafer serves as a collector. Implanted Si was examined by SIMS method. Data processing of SIMS data has allowed to receive a concentration profile of implanted Ge atoms in a silicon substrate.

Figure 3.3.4.2 shows the concentration profile of Ge atoms in silicon substrate after 1500 laser shots, received by means of SIMS technique. Calibration of an ionic signal on depth was carried out by measurement of depth of the crater left by an ion bunch, and on concentration by comparison of an ionic signal from implanted sample SiGe with a known concentration profile.

There is maximum of Ge atom concentration on ~100 angstroms depth. For processing of a spectrum SRIM-2003 code was used. The concentration profile of implanted atoms allows us to receive some characteristics of an ion energy spectrum. In a Fig. 3.3.4.3 the calculated concentration profile of atoms Ge in the silicon matrix is represented, implanted atoms had energy 8 keV. One can see that maxima of curves coincide. It specifies that in an ion spectrum of plasma prevailed ions with energy 8 keV. Measured in experiment with the help of a two-detector technique the temperature of hot electron components of plasma was 0,7-2 keV. At a plasma degree of ionization of Z~5-8 energy of hot ions can be in limits from 3,5 up to 16 keV. Average energy of ions calculated with the help of the concentration profile (8 keV) coincides by the order of magnitude to an estimation received by measurement of electronic temperature. Ion free path of 400 nanometers corresponds to energy of ions in 300-400 keV. This circumstance specifies that at plasma there are ions and with energy up to 400 keV, but their relative quantity does not exceed 10^{-3} from quantity of ions with energy 8 keV.

As a result of the experiments the following conclusions can be made:

The method of estimation of energy characteristics of ion component of laser plasma with the help of direct laser-induced ion implantation was developed. The method of direct ion implantation allows us to receive some energy characteristics of laser plasma, in particular the maximal energy of ions of plasma and average energy of ions.

Implantation of Ge ions in silicon substrate was made with the help of a laser pulse with duration 200 fs at intensity of laser radiation ~ $(0.5\text{-}3.5)\cdot10^{15}$ W/cm^2. By position of a maximum of concentration profile of implanted atoms average energy of ions in plasma was obtained, it makes up 8 keV.

On the maximal penetration depth of Ge ions in a silicon collector the maximal energy of ions in laser plasma was calculated. The maximal energy is 400 keV.
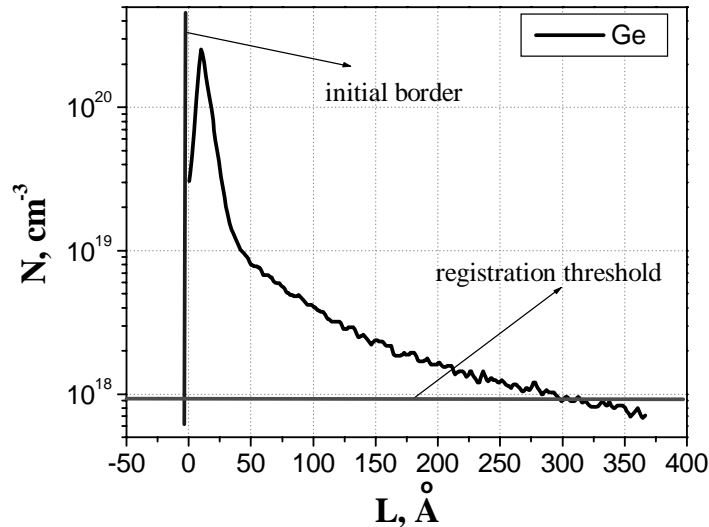
Fig. 3.3.4.2. Profile of Ge atoms concentration in a silicon matrix.
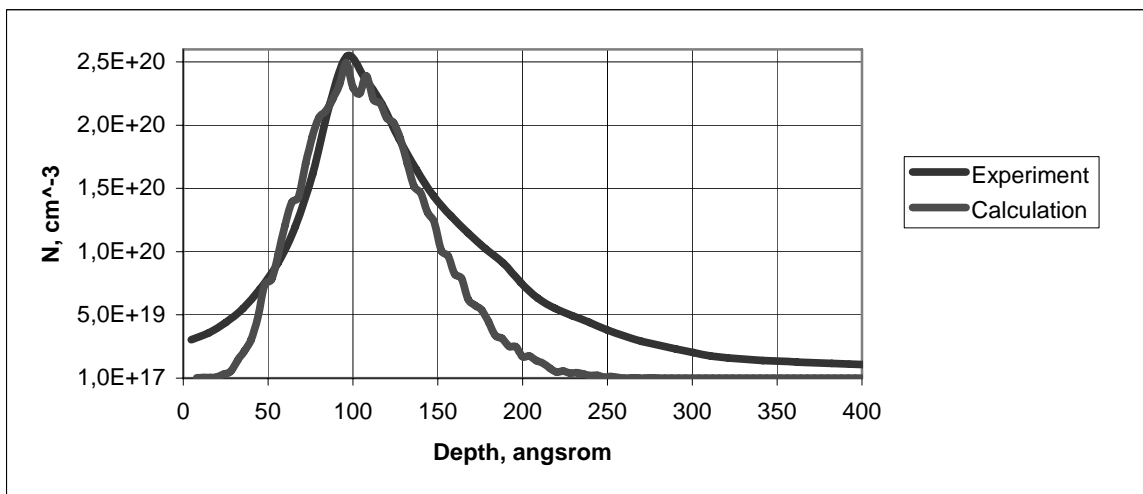
Fig. 3.3.4.3 An experimental concentration profile of Ge ions in a silicon collector and a calculated one for a monochromatic ion beam with energy 8 keV.

3.3.5 Pulsed laser cleaning and data

The experimental setup is shown schematically in Fig. 3.3.5.1 The plasma was formed by a laser pulse generated by a femtosecond dye laser system. This system makes it possible to obtain a laser pulse at a wavelength of 616 nm with a duration of 200 fs and an energy up to 500 µJ. Focusing this pulse to the target surface with the help of an aberration-free objective lens made it possible to attain an intensity of about 2.5×10^{16} W/cm^2. The spontaneous luminescence energy density did not exceed 0.3 J/cm^2 (the spontaneous luminescence pulse duration was 40 ps, the energy was approximately 100 nJ, the area of the focusing spot was 150−200 µm^2, and the intensity was about 10^{10} W/cm^2). Such a value of energy density is lower than the known values for the tungsten breakdown threshold. For a laser pulse of duration 100 fs, the breakdown threshold constitutes 0.25 J/cm^2; this value slowly increases as the laser pulse duration increases from 100 fs to 10 ps. Radiation was incident on the target at an angle

of 45° and was *p*-polarized. The target in the form of a tungsten wafer was in a vacuum chamber evacuated to a pressure of 10^{-5} Torr with the help of a turbomolecular pump. After each laser shot, the target was displaced by 100 µm to ensure fresh surface.
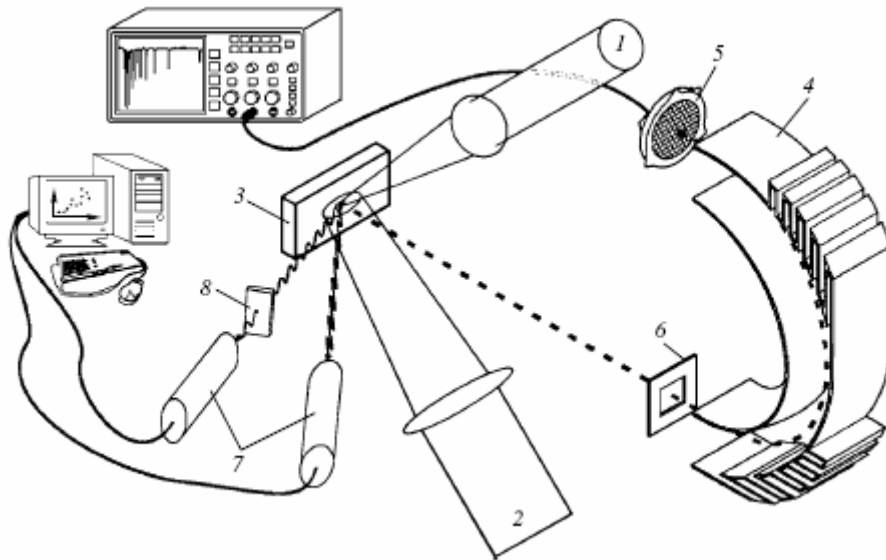

Fig. 3.3.5.1. Block diagram of the experiment: 1—femtosecond laser pulse; 2—cleaning nanosecond laser pulse; 3—tungsten target; 4—electrostatic mass spectrometer; 5—microchannel plate; 6—diaphragm; 7—X-ray detectors based on NaI(Tl) scintillator and FEU-119 photomultiplier; 8—band-pass X-ray filters (Al, Be).

To remove the contaminating surfaces layer, the target was exposed to a pulse from a XeCl excimer laser before each shot. The duration of a cleaning laser pulse was 30 ns, its energy being 10 mJ at a wavelength of 308 nm; the pulse propagating against the femtosecond laser pulse hit the target at an angle of 45°. Radiation was focused by a quartz lens to a spot 500 µm in diameter so that the region of action of the femtosecond pulse was covered completely. The delay time between the cleaning and femtosecond pulses was chosen on the basis of previous experiments and was equal to 100 µs. The delay time should not be too short for the target to have time to be cooled after the action of the cleaning pulse. On the other hand, this time cannot be too long since the contaminating surface layer is restored after some time as a result of adsorption of residual gas atoms in the chamber and atomic diffusion from the bulk of the target. The energy density in the that, for this value of energy density, a layer of the target about 100 nm in thickness is heated to a temperature of the order of 10^5 K, and the plasma cleaning mode is realized. In such a regime, not only water and oil vapors, but also the oxide layer is effectively removed from the target surface. It should be noted that the 03 6 912 action of a cleaning pulse did not noticeable change the topology of the target surface. The photographs of the surface obtained with the help of a scanning field electron microscope in the normal (2 kV) and topographic modes show that only small stochastic irregularities with a characteristic longitudinal size on the order of tens of micrometers remain after the action of a cleaning pulse; the height of such irregularities does not exceed 0.1 µm.
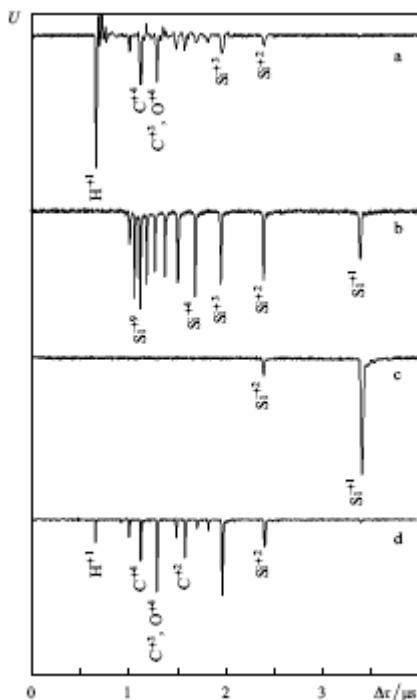
The ionic currents were measured with the help of an electrostatic spectrometer. This spectrometer makes it possible to detect ions with their separation in energy and in the ion charge-to-mass ratio. Since the charge-to-mass ratio is a unique number for most ions, which is not repeated for another ion, ions can be separated with respect to charge as well as mass.

Figure 3.3.5.2. Time-of-flight signal of the plasma ions recorded with a mass spectrometer in the cases when the plasma is produced by a pulse with a high energy contrast ratio with an unpurified target (a), with a clean target for At = 100 us (b) and 400 ns (c) as well as by a laser pulse with a low energy contrast (d) (the energy of all ions shown is ~ 5 keV per unit charge).

The results of X-ray diagnostics of the plasma formed in the experiments also show that the plasma parameters of the cleaned target do not differ from the plasma parameters of the initial target. The conversion of the laser pulse energy to X-ray quanta with an energy exceeding 6 keV and the mean energy of hot electrons amounted in this case to 10^{-3} % and 6.6 ± 1.5 keV, respectively.

Figure 3.3.5.2 shows the typical profiles of time-of-flight signals recorded with an electrostatic mass spectrometer. The analysing voltage in the spectrometer was set equal to ~ 1.3 kV, which ensured detecting ions with the same energy per unit ion charge (~5 keV). In Fig. 3.3.5.2a, which corresponds to the ion signal from the plasma produced by the high-contrast femtosecond radiation on an unpurified target surface, the first, and the most intense peak arises from the detection of hydrogen ions (protons) from the plasma. The remaining peaks arise from oxygen, carbon, and silicon (the parent target material) ions of different multiplicity. For a target prepurified by a nanosecond laser pulse (Figs 3.3.5.2b and 3.3.5.2c), the peaks corresponding to the detection of impurity ions vanish. A comparison of Figs 3.3.5.2b and 3.3.5.2c suggests that the length of time delay AT has a significant effect on the charge-state composition of the plasma of the parent target material. Figure 3.3.5.2d, which corresponds to the case when the laser plasma was produced by low-contrast femtosecond radiation, also shows some decreasing of the proton peak, which is attributable to the removal of a part of hydrocarbons by the prepulse.

To obtain the mass, charge, and energy spectra of the plasma ion current, we measured the time-of-flight mass spectrometric signals, which are analogous to those presented in Fig. 3.3.5.2, in the ion energy range between 400 eV and 35 keV per unit charge. An analysis of mass spectra (Fig. 3.3.5.3) shows that the pulsed laser cleaning of the target results in a substantial suppression of the current of all impurity ions. In particular, the total fraction of hydrogen, carbon, and oxygen ions in the ion current lowers by more than an order of magnitude both for AT equal to 100 |a.s and to 400 ns (see Fig. 3.3.5.3). Making the delay AT longer than the 'optimal' value (100 us) has the effect that the efficiency of laser treatment of the target becomes lower due to a partial recovery of the impurity layer
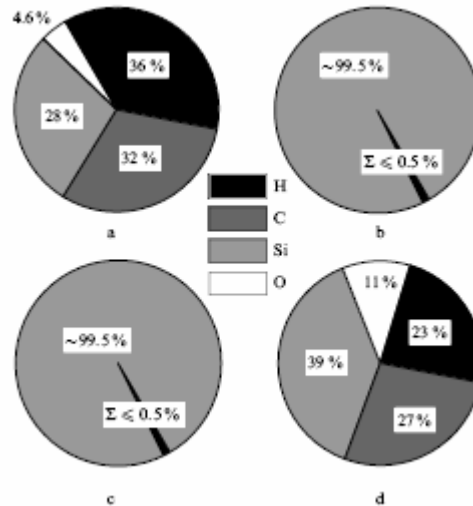
Figure 3.3.5.3. Mass spectra of the plasma ion current without application of laser treatment (a), with the use of laser cleaning for a delay AT = 100 us (b) and 400 ns (c) as well as for the radiation with a low energy contrast ratio (d).

When the target was exposed to the femtosecond radiation with a low-contrast ratio, we observed a lowering of the percentage of hydrogen and carbon ions and a growth of the content of oxygen and silicon ions. This is indication that the prepulse partly cleans the hydrocarbons from the target surface, while the oxygen, which is primarily contained in the form of silicon oxide, is not removed.

Significant changes take place also in the charge spectrum of silicon ions (Fig. 3.3.5.4). Removing the impurity layer from the target surface in the laser treatment with a lead time AT = 100 mcs gives rise to fast silicon ions with charges up to 12^{+} (Fig. 3.3.5.4a). This effect is attributable to the fact that the plasma front in the case of a treated surface is formed by silicon atoms, which are ionized by thermal electrons, accelerated due to hot electrons, and do not undergo recombination in their flight to the detector. Silicon atoms located at a depth in the target cannot be accelerated by hot electrons and undergo substantial recombination.

With lengthening lead time AT, the average charge of silicon ions lowers from 4^{+} to 3^{+}. At the same time, the peak charge of detectable silicon ions lowers from 12^{+} to 5^{+} - a value characteristic of the initial unpurified target. Shortening the lead time AT to ~400 ns (Fig. 3.3.5.4b) has the effect that the average silicon ion charge falls to 1^{+} for a peak ion charge of 4^{+}.

Figure 3.3.5.4. Charge spectra of silicon ions. White columns in all diagrams correspond to the charge-state distribution of Si ions in the plasma pro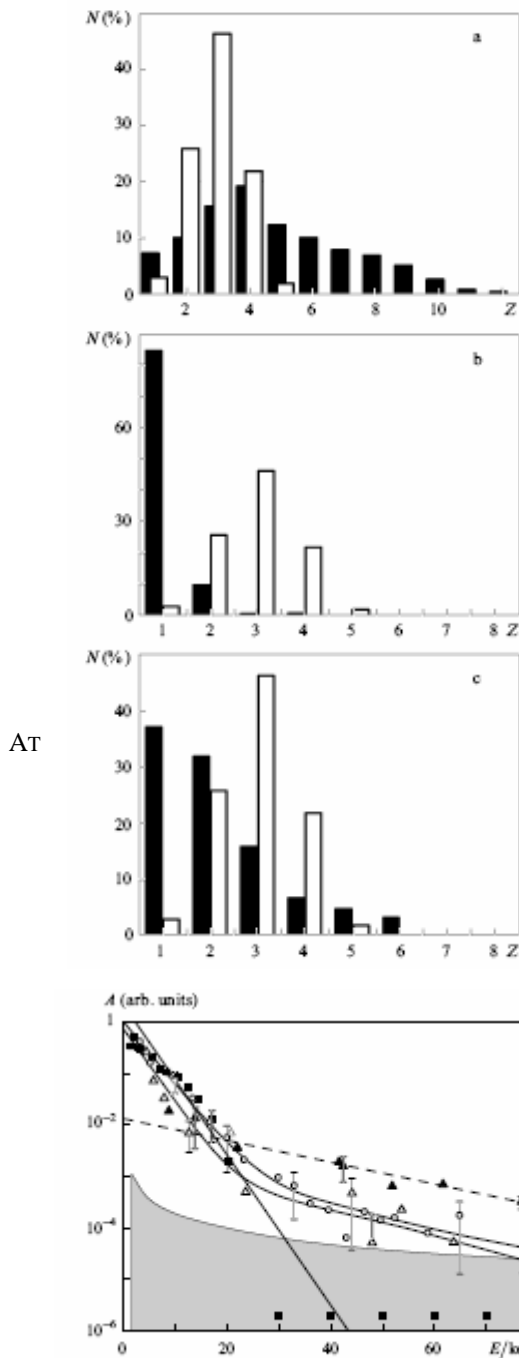duced by a pulse with a high energy contrast with an unpurified target. The columns shown in black represent the charge-state distribution of Si ions for a laser cleaning with At = 100 us (a) and 400 ns (b) as well as for a plasma produced by the radiation with a low energy contrast (c).

The average charge also decreases significantly when low-contrast femtosecond laser radiation is used (Fig. 3.3.5.4c), which can also be explained by the existence of the extended electron density gradient. The differences between the spectra in Figs 3.3.5.4b and 3.3.5.4c may arise from the difference in spatial gradient scales: about 300 mcm in the case of Fig. 3.3.5.4b and less than 1 mcm in the case of Fig. 3.3.5.4c.

The changes in silicon ion energy spectra are most amply illustrated by the example of the silicon ion with the 2$^+$ charge. Figure 3.3.5.5 shows the spectra obtained using a cleaned target (At = 100mcs.s and 400 ns) and an unpurified target, as well as the energy spectrum of the plasma ions produced by the radiation with a low energy contrast. The energy spectra for an unpurified target and a target cleaned for = 100 mcs coincide in the ion energy region $E\backslash < 20$ keV. This suggests that the ionisation and acceleration processes for the silicon ions residing at some depth in the plasma, which take place due to thermal electrons, do not undergo appreciable changes. Note that the increase in the lead time to 1 s results, as would be expected, in the disappearance of the high-energy ion component of the parent material due to the recovery of the impurity layer.

Figure 3.3.5.5. Energy spectra A of the silicon ions with a charge 2 + ; ■ — uncleaned target, o — cleaning mode with a delay At = 100 us, a — cleaning mode with a delay At = 400 ns, a — femtosecond laser radiation with a low energy contrast. The dashed line represents an exponential decay for 22 keV, the grey area corresponds to the noise level.

For a short lead time (At = 400 ns), we observed a significant decrease in the fraction of slow silicon ions (see Fig. 3.3.5.5). This behavior may be due both to a decrease of the total ion current from the plasma in this regime and to a rapid recombination of silicon ions in the extended low-density plasma. somewhat larger than At = 100 mcs. At the same time, an approximation of the energy spectrum of the 2$^+$ silicon ion by an exponentially decaying exponential function. in the 20-70 keV ion energy range yields the same value 22 ± 6 keV irrespective of At. This result correlates also with X-ray diagnostic data: they suggest that the average energy of hot electrons, which determine the fast ion acceleration, remains constant (see above). The ion spectrum of the plasma produced by the radiation with a low energy contrast also contains the high-energy component.

We made a comparative analysis of the energy spectra of all ion types observed, including those for an unpurified silicon surface. The spectra of every ion were also approximated by an exponentially decaying function. For a part of the spectra of carbon (3$^+$-6$^+$) and silicon ions (3$^+$ and higher), a satisfactory result was achieved only by approximation with a sum of two exponential functions. The results shown in Fig. 3.3.5.6 suggest that two ion groups are present: the ions of the first group cluster near the straight line $E = 2Z$ keV and the ions of the second group near the straight line $E = 12Z$ keV. The first group corresponds to slow ions and the second to the fast ones. It is pertinent to note that an important part for the slow ions is played by recombination. That is why the ion charge recorded by the spectrometer is significantly different from the charge of this ion at the instant of its acceleration in the plasma. Moreover, the recombination rate also depends strongly on the ion charge. First of all, this implies that the slope (2 keV) of the straight line obtained from Fig. 3.3.5.6 cannot be associated with the energy

94

of thermal electrons in the plasma. For fast ions, recombination can be neglected, and the slope of the straight line (a = 12 keV) can be correlated with the average energy of the hot electrons as $a = 2E$.
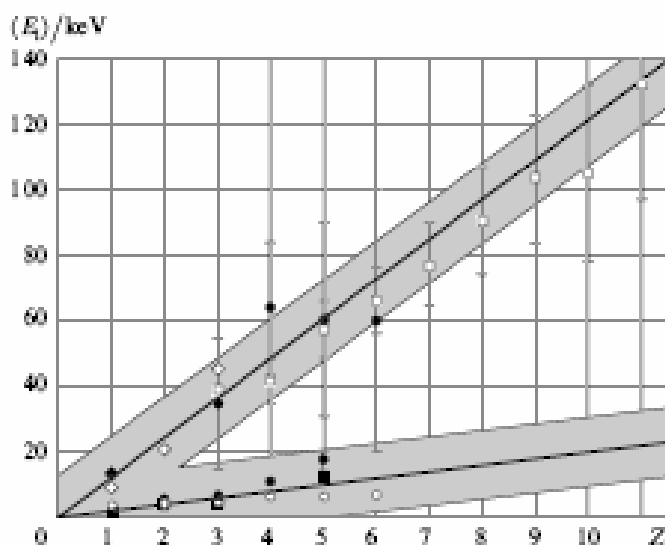

Figure 3.3.5.6. Average ion energies {£;) as functions of Z for an unpurified target (♦ — protons, • — C, a — O, ■ — Si) and a target cleaning with delays At = 100 us (d — high-energy Si component, o — low-energy Si component) and At = 400 ns (o — Si).

The existence of two ion components both for clean and initial targets is most clearly demonstrated in Fig. 3.3.5.6; in this case, the fast-ion acceleration is related to hot electrons and the slow-ion acceleration to the thermal ones. The division of the ions into two components is primarily determined by their initial position relative to the target surface. The atoms

In the ion energy range above 20 keV for an unpurified target, the signal becomes lower than the noise level, which is conventionally shown in Fig. 3.3.5.5. The target cleaning gives rise to fast ions with energies up to 70 keV (the highest energy which the spectrometer in use can detect for ions with the charge 2 $^+$). Their number for A_T = 400 ns is somewhat larger than A_T = 10 mcs. At the same time, an approximation of the energy spectrum of the 2 $^+$ silicon ion by an exponentially decaying function of the form exp(-£'$_i$/(£'$_i$)) (here, (is^1;) is the average ion energy) in the 20-70 keV ion energy range yields the same value 22 ± 6 keV irrespective of A_T. This result correlates also with X-ray diagnostic data: they suggest that the average energy of hot electrons, which determine the fast ion acceleration, remains constant (see above). The ion spectrum of the plasma produced by the radiation with a low energy contrast also contains the high-energy component.

Therefore, the impurity layer exerts a significant effect on the formation of energy, elemental, and charge spectra of the ion current from the plasma of a solid target irradiated by ultrahigh-intensity femtosecond laser radiation. For the most part, the effect of impurity layer reduces to the electric screening of the ions of the parent target material from the accelerating field of hot plasma electrons. As a result, the highest energy per unit charge is acquired by the impurity ions, while the ions of the parent target material gain substantially lower velocities. The preferential acceleration of protons compared to carbon ions is evidently related to the lower Z/M ratio for carbon *(M is the ion mass)*: $Z/M = 1$ for hydrogen and no greater than 0.5 for carbon.

Not only does the pulsed laser cleaning of a surface afford the production of an ion beam consisting primarily of the ions of a parent target material, but it also enables controlling the parameters of this ion beam - its energy and charge spectrum. In particular, when the cleaning pulse arrives 100 mcs prior to the femtosecond one, we observed a large number of fast silicon ions with an energy of about 12 keV per unit charge and multiplicities up to 12$^+$. Shortening the lead time to 400 ns lowers the charge of silicon ions to 1$^+$ -2$^+$ for the same energy per unit charge.

The contrast ratio of femtosecond laser radiation also exerts a significant effect on the charge and energy of accelerated ions. To obtain high-multiplicity ions requires employing femtosecond radiation with a large contrast ratio to ensure the ionization and the ion acceleration at the sharp plasma-vacuum interface. In particular, the existence of a 40-ps prepulse with an energy density of about 30 J/cm^2 lowers the average charge of the ions detected.
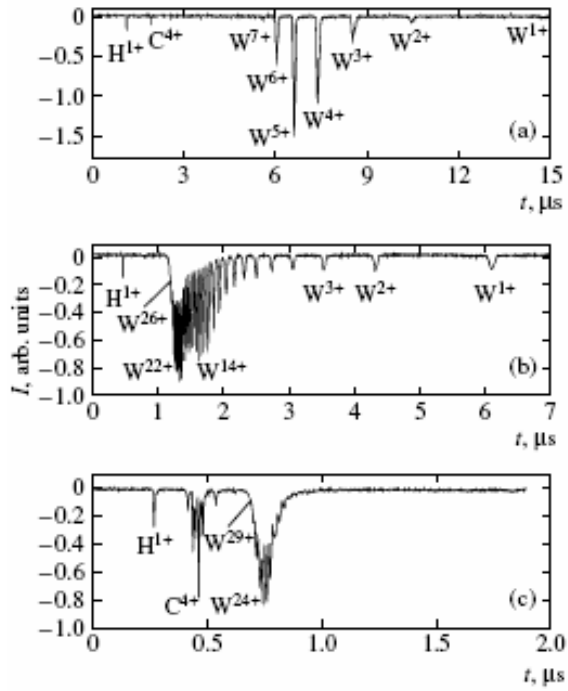
Fig. 3.3.5.7. Ionic currents from the tungsten plasma, recorded for different values of the ion energy per unit charge: 1.8 (a), 10.1 (b), 28.0 keV (c).
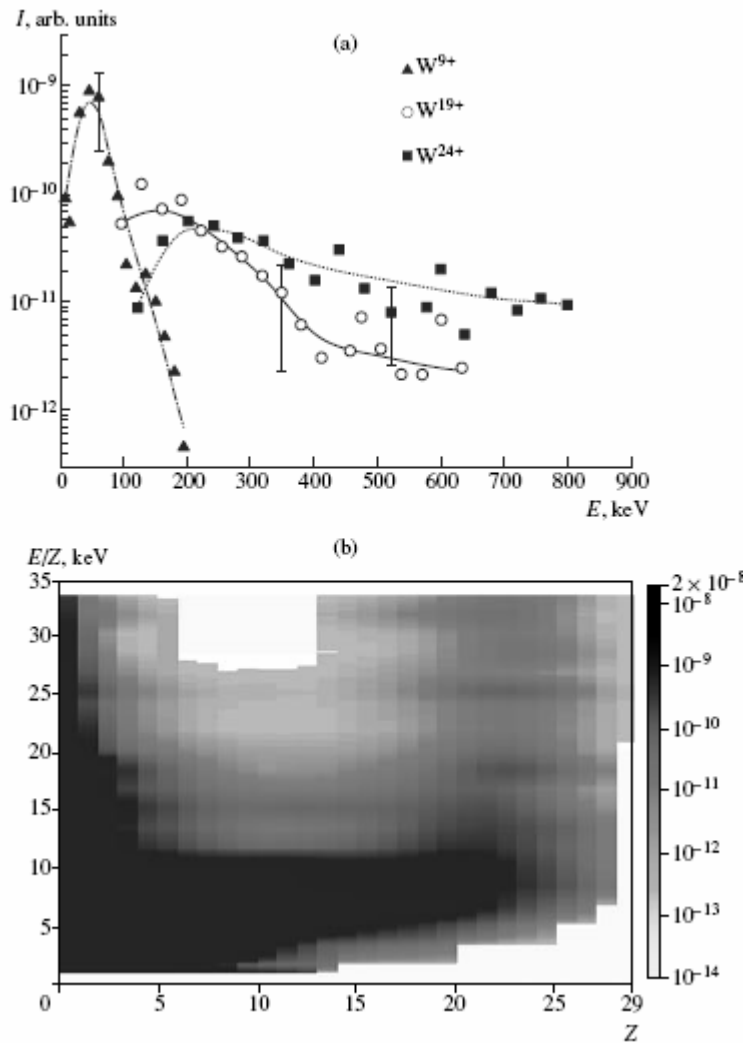

Fig. 3.3.5.8. (a) Energy spectra of tungsten ions (the curves are plotted for better visualization); (b) diagram of energy spectra of ions.

When the energy of the ions being detected in the plasma on the cleaned target increases still further, tungsten ions with a charge up to 29+ and an energy up to 960 keV are observed (see Fig. 3.3.5.7c). The detection of ions with higher energies was limited by the potentialities of the spectrometer. Along with the tungsten ions, the plasma contains fully ionized oxygen and carbon ions. It should be noted that the highest energy of the tungsten ion on the "dirty" target for the same laser pulse parameters does not exceed 150 keV. Highly ionized oxygen ions are not observed either.

To analyze the experimental data, we carried out numerical simulation of the space-time dynamics of the plasma both at the instant of plasma formation and during its subsequent spread. For this purpose, we used two numerical codes. The first code makes it possible to analyze the dynamics of interaction of a high-intensity short laser pulse with a solid target . The code takes into account the absorption of a laser pulse at the moving plasma-vacuum interface, the kinetics of ionization and recombination, the Spitzer and ballistic heat conduction, and hydrodynamic expansion of the plasma and makes it possible to trace the plasma dynamics up to times of the order of a picosecond. The input parameters of the code are the pulse intensity and duration, polarization, wavelength of the laser pulse, angle of incidence of radiation on the target, and the atomic number of the substance of the target. All calculations presented below were performed for the input parameters of the code, which correspond to our experimental conditions.

For simulating the recombination of ions in the course of subsequent spread of the plasma, we used the second code modified to take into account the geometry of the plasma torch, which was chosen on the basis of analysis of available data in the form of a cone with an angle of the order of 30°. This code makes it possible to analyze hydrodynamic expansion of the plasma to vacuum or to a neutral gas on time scales from a few picoseconds to several microseconds. In this case, the kinetics of ionization and recombination as well as heat conduction and electron-ion heat exchange is taken into account. The peculiar feature of the code is the inclusion of excited states of an ion in the calculation of ionization rates. The recombination rate was calculated taking into account three-particle and dielectronic recombination as well as photorecombination. It was shown in , however, that the effect of dielectronic recombination and photorecombination on the total recombination rate is small. For the input parameters of this code, we used the space-time profiles of the ion concentration, ion charge, and the temperature of electrons and ions obtained with the help of the first code. Both numerical codes disregard the presence of hot electrons in the plasma; however, such an approximation does not strongly distort the results of simulation since the contribution of hot electrons to the energy spectrum of the plasma does not exceed 1% for our experimental conditions.
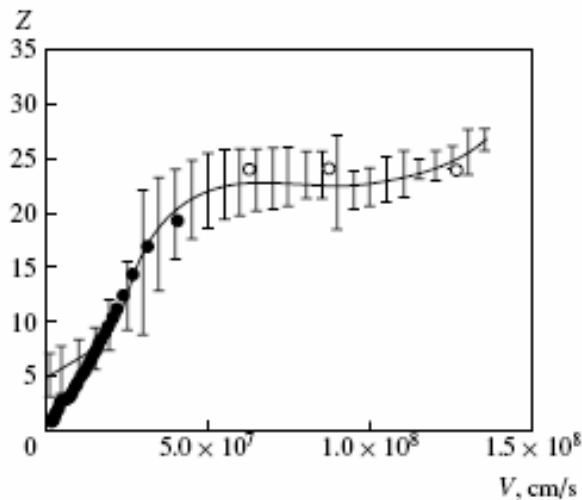
Fig. 3.3.5.9. Dependence of the average charge of tungsten ions on their velocity (the curve corresponds to experimental data; dark and white circles are the results of calculations for thermal and fast ions, respectively).

Figure 3.3.5.10 shows the spatial profiles of the number density of ions, electron temperature, the average charge of ions, and the electromagnetic field amplitude at the instants corresponding the beginning of a laser pulse ($t = -200$ fs), the peak of the laser pulse ($t = 0$), and the end of the laser pulse ($t = 2000$ fs). Calculations were performed for a laser pulse intensity of 2.5×10^{16} W/cm^2.
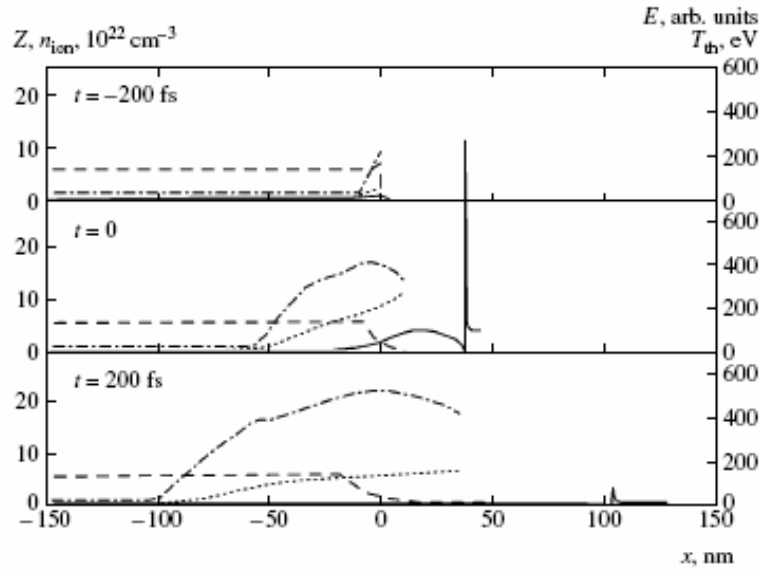
Fig. 3.3.5.10. Spatial profiles of the ions concentration (dashed lines), electron temperature (dotted curves), ion charge (dot-and-dash curves), and electromagnetic field amplitude (solid curve) in the plasma at different instants.
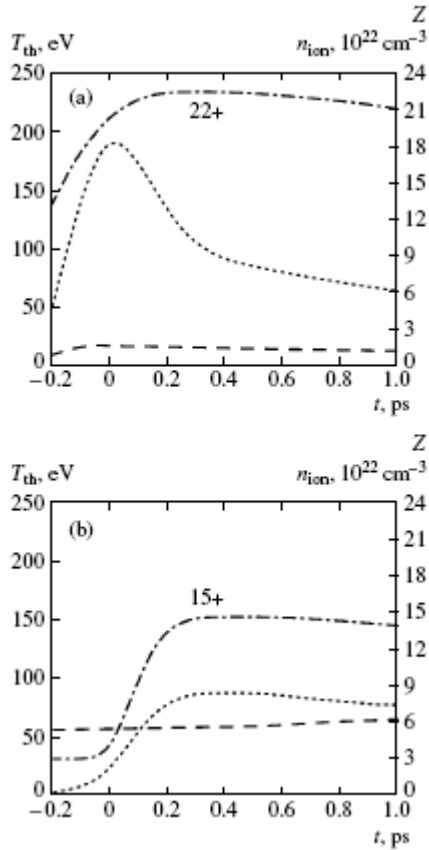
Fig. 3.3.5.11. Temporal profiles of the ion concentration (dashed curves), electron temperature (dotted curves), and ion charge (dot-and-dash curves) (a) in the surface layer of the plasma (x = 0) and (b) in the bulk of the target (x = -50 nm).

It can be seen that the peak values of the ion charge are attained in the surface region of the target (in the vicinity of x-coordinate zero). In the same region of the plasma, hot electrons are effectively generated above the surface of the target . Indeed, irrespective of the mechanism of generation, hot electrons are accelerated in the region of the peak of the electromagnetic field, i.e., in the region of the critical plasma density (the critical plasma density $n_{cr} = 3 \times 10^{21}$ cm^{-3} for a laser pulse wavelength of 616 nm). Thus, the ions located in the surface region of the target are the first to be accelerated by hot electrons. Conversely, the ions from deeper layers of the target are less sensitive to the field of hot electrons and are mainly accelerated by thermal electrons. To analyze the charge distribution of ions accelerated by thermal and hot electrons, let us consider the time dynamics of n_{ion}, T_{th}, and Z (Fig. 3.3.5.11) in the bulk of the target ($x = -50$ nm) (Fig. 3.3.5.11b) and on its surface ($x = 0$) (Fig. 3.3.5.11a). At the surface of the target ($x = 0$), the temperature of thermal electrons over the length of a laser pulse attains 200 eV, the average charge of ions becomes 22+, and the number density of ions becomes $.3 \times 10^{22}$ cm^{-3} ~ $n_{sol}/4$ almost immediately and subsequently changes only slightly. The plasma formed in the bulk of the target differs from the plasma at the surface. In this region ($x = -50$ nm), the ion concentration corresponds to the solid-state concentration ($n_{sol} = 5.4 \times 10^{22}$ cm^{-3}), the electron temperature attains only 90 eV, and the ion charge is 15+. At the same time, analysis of the ionization kinetics shows that the average charge by the end of a laser pulse is close to the equilibrium value in both spatial regions under investigation. For this reason, we used the Saha equations for calculating the charge distribution at this instant. To estimate the charge distribution of ions in the surface layer of the plasma, we used the value of ion concentration equal to $n_{sol}/4$; the electron temperature was taken equal to the value averaged over the time profile of the temperature ($T_e = 140$ eV for $I = 2.5 \times 10^{16}$ W/cm^2). In addition, the average charge of fast ions estimated by the Saha formulas was compared to the average charge of ions in the surface layer of the plasma, which was obtained as a result of numerical simulation. The calculated charge distribution of fast ions is compared with the experimentally recorded charge distribution. The calculated charge distribution is noticeably narrower than the experimental

98

distribution. The large width of the experimental distribution in the region of lower charges (on the left of the peak) can be attributed to recombination of ions, while the broadening on the side of higher charges (on the right of the peak) cannot be explained unambiguously. Possible reasons for the increase in the ion charge will be considered in the next section.

During plasma spread, the charge of the ions may substantially decrease as a result of their collisions with electrons, ions, and atoms of the residual gas. In the numerical model for analyzing the plasma spread, we assumed that the tungsten plasma spreads into molecular nitrogen with a pressure of 10^{-5} Torr. The gas pressure was chosen in accordance with our experimental conditions. Figure 3.3.5.12 shows the time dependences of the average charge of the ions accelerated by thermal electrons at the front of spreading plasma at the point corresponding approximately to the center of the plasma cloud and at the point on the trailing edge of the plasma. After the termination of a laser pulse, the charge continues to increase at the plasma front. This effect can easily be explained. In accordance with the Saha distribution, the average charge increases upon a decrease in the plasma concentration at a fixed temperature. At the plasma front, the ion concentration rapidly decreases, while the electron temperature has no time to change appreciably; for this reason, the ion charge continues to increase. The stage of charge growth at the plasma front changes into rapid recombination. This is due to the fact that plasma cools from 150 to 20 eV over a time on the order of 0.1 ns. Over longer time periods, the plasma attains a stationary charge state at the front. This is the well-known effect of freezing of the ion composition, which can be explained by a decrease in the plasma concentration and electron temperature to such an extent that the recombination rate becomes close to zero. Over time intervals on the order of 1–10 µs, the effect of charge exchange of ions at neutral atoms of the residual gas comes into play. On the average, a fast ion covering the time-of-flight base (70 cm) over a time of the order of 1 µs manages to participate in the charge-exchange process four times. In denser regions of the plasma, the recombination is slow. Freezing of the ion composition occurs at later stages.
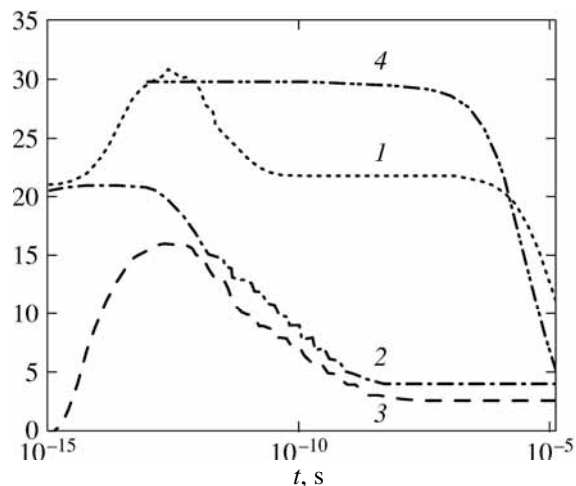
Fig. 3.3.5.12. Dependence of the average charge of ions accelerated by thermal electrons at the front of the spreading plasma (curve *1*), at the point corresponding approximately to the center of the plasma cloud (curve *2*), and at the point at the trailing edge of the plasma (curve *3*). Curve *4* describes the dependence of the average charge of ions flying at the plasma front and accelerated by hot electrons.

The dependence of the average charge of slow ions on their velocity, which is calculated in the framework of our models, is in good agreement with the analogous experimental dependence (see Fig. 3.3.5.9). Thus, calculations show that the temperature of thermal electrons in the bulk of the plasma does not exceed 200 eV, which is substantially lower than the estimate of 700 eV obtained above from the experimental data without taking recombination into account. To analyze the recombination of fast ions, we supplemented the model with several Lagrangian cells with parameters corresponding to fast ions (ion concentration 5×10^{19} cm^{-3}; initial average charge of ions $Z = 30$; initial velocities of cells 5×10^{7}, 9×10^{7}, and 1.3×10^{8} cm/s). Figure 3.3.5.12 illustrates the temporal dynamics of the average charge of ions accelerated by hot electrons. Fast ions lose their charge only as a result of collisions with residual gas molecules in the vacuum chamber. The numerically obtained value for the average charge of fast ions after their passage through the time-of-flight base is in good agreement with the experimentally detected average charge. Thus, it is shown that the average charge of ions obtained in experiments can be attained as a result of successive effects of impact ionization, three-particle recombination in the plasma, and recombination at residual gas molecules. However, such an approach predicts a lower value for the maximum charge of the ions as compared to the experimentally detected value.

To obtain a more comprehensive pattern, we additionally measured the charge spectra of ions for three lower values of the laser pulse intensity (1×10^{16}, 7×10^{15}, and 4×10^{15} W/cm^2). It was obtained that a decrease in the laser pulse intensity leads to a decrease in the maximum charge of ions. It should be noted in addition that the relative

number of ions with a low charge (1+, 2+, etc.) increases upon a decrease in the laser pulse intensity. This is due to the fact that, for low intensities, ions have lower velocities and recombine more intensely during the plasma spread. In addition, the charge distribution of fast ions obtained analogously to that described above is plotted on all histograms. The electron temperatures were set as follows: 100 eV for $I = 1 \times 10^{16}$ W/cm^2, 80 eV for $I = 7 \times 10^{15}$ W/cm^2, and 60 eV for $I = 4 \times 10^{15}$ W/cm^2. It was noted above that the ions with the highest charge and energy are formed in the surface layer of the target and are accelerated by fast electrons. It can be seen from the histograms that the maximum charge predicted by the Saha equation is lower than the experimentally detected charge for all intensities.

Thus, the discrepancy between the calculated and experimental charge spectra of fast ions is also preserved for lower intensities of the laser pulse. To explain the experimentally observed charge composition of fast ions, we must consider in greater detail possible additional mechanisms of ionization of the ions at the plasma-vacuum interface.

Figure 13 shows the dependences of the maximum charge of tungsten ions on the laser radiation intensity, which were obtained taking into account the effect of various mechanisms of ionization. In the given case, we consider the charge of the ions reaching the detector (i.e., ionization, recombination in the plasma, and recombination in the residual gas in the interaction chamber are taken into consideration). Thus, impact ionization in the plasma cannot ensure the experimentally observed values of the maximum charge of ions. In the given case, we must take into account additional ionization mechanisms emerging at the sharp plasma-vacuum boundary due to the presence of a strong ambipolar field. The most significant mechanism is impact ionization of the ions possessing low ionization potentials due to their location in the electrostatic ambipolar field. At low temperatures of the plasma, a significant fast ions production.
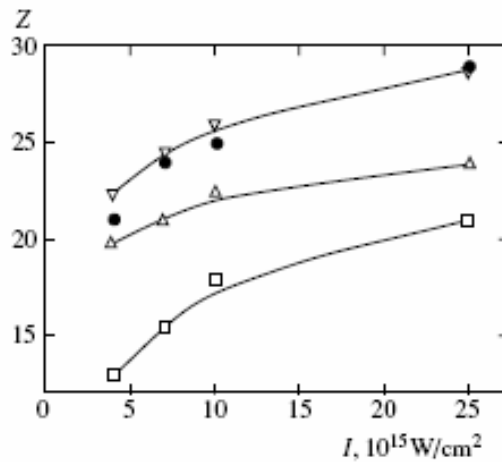
Fig. 3.3.5.13. Dependence of the maximum charge of ions on the laser pulse intensity: experimental data (•); calculations taking into account the effect of above-threshold ionization by the ambipolar field (A); calculations taking into account the effect of impact ionization in the presence of the ambipolar field (V), and dependence of the average charge of ions on the laser pulse intensity, calculated taking into account impact ionization in the plasma (□).

A noticeable increase in the charge and energy of ions accelerated from a solid tungsten target irradiated by a femtosecond laser pulse with the intensity higher than 10^{16} W/cm^2 has been found when the target surface is previously cleaned by a nanosecond laser pulse with an energy density of 3 J/cm^3. Tungsten ions with the charge up to +29 and energies up to 1 MeV were detected in this case, while the charge and energy of tungsten ions from a target with the uncleaned surface are not exceed +3 and 12 keV, respectively.

In the absence of pulsed laser cleaning, ion current comprises predominantly hydrogen, carbon, and oxygen ions. The maximum ion charge reaches +6 for carbon (fully ionized atom, the ionization potential of the last K-shell electron is equal to 490 eV), +6 for oxygen (helium-like ion, the ionization potential of the lithium-like ion is equal to 138 eV), and only +3 for tungsten (ionization potential is 24 eV), where the total number of electrons is 74. The observed ion charge distribution is undoubtedly determined not only by ionization in the dense plasma, but also by recombination during plasma expansion and flight of ions to the detector. The latter process depends strongly on ion velocity: as the velocity increases, the recombination rate decreases because the electron density of the plasma though which the ion moves decreases. Thus, the initial tungsten ion charge immediately after the impact of a femtosecond laser pulse is considerably higher than the detected charge.
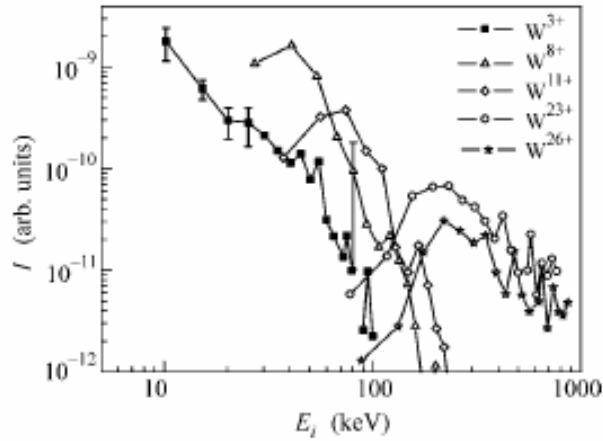
Fig. 3.3.5.14. Energy spectra of tungsten ions from the cleaned target.

In the case of the uncleaned target, tungsten ions with a wide charge spectrum from +1 to +7 (ionization potential of W^{+7} is about 60 eV) dominate in the ion current. A weak signal corresponding to protons and carbon ions is also present. The ion current from the uncleaned initial target consists mainly of hydrogen, carbon, and oxygen ions, and tungsten ions have charges +1 and +2. When the energy per unit charge of detected ions increases to 10 keV, tungsten ions with charges from +1 to +3, as well as protons and carbon ions, were observed from the initial target, while mainly tungsten ions with a wide charge spectrum from +1 to +26 were detected for the cleaned target.

A further increase in the energy of detected ions did not result in noticeable change in the parameters of the ion current from the uncleaned target, while high energy tungsten ions with an average charge of +22 were detected from the cleaned target. The maximum charge of tungsten ions in our experiments reached +29 (the ionization potential of the W^{+28} ion is higher than 700 eV) for the maximum ion energy 980 keV. Moreover, oxygen ions with a charge of +8 (ionization potential is 870 eV) were also observed. The energy spectra of some tungsten ions from the cleaned target are shown in Fig. 3.3.5.14. Analysis shows that the energy spectrum of tungsten ions with the charge $Z > 18$ is well approximated by an exponential function of the form $e^{-\alpha \varepsilon_i}$, where α is independent of the ion charge Z and $\alpha^{-1} \approx 11.2 \pm 2$ keV. The independence of α from the ion charge shows that recombination of fast tungsten ions during their flight to the detector is negligible and the recorded charge spectrum depicts the charge spectrum of tungsten ions at the very moment of their acceleration in the hot dense plasma.
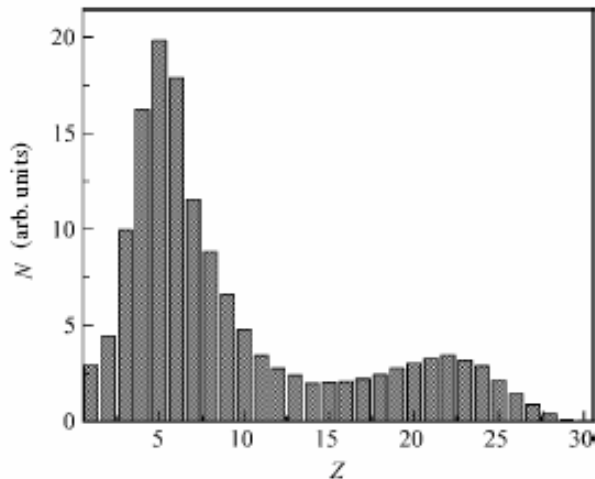
Fig. 3.3.5.15. Charge distribution of tungsten ions from the cleaned target.

The charge spectrum of tungsten ions from the cleaned target is shown in Fig. 3.3.5.15. Two groups of ions with average charges +5 and +22 are clearly visible. The presence of the two groups of ions is attributed to efficient generation of hot electrons, and, therefore, to a non-Maxwellian character of the electron energy distribution in the plasma. The estimate obtained for the parameter α agrees well with the energy of hot electrons that is estimated above using the hard x-ray yield from the plasma (see above): the mean energy of a three-dimensional electron distribution E_e relates to the average energy of one-dimensional ion motion as $E_e \approx 0.5\alpha$. It should be noted that the charge and energy spectra of tungsten ions from the initial target are determined only by the equilibrium thermal

part of the electron energy distribution, while hot electrons accelerate hydrogen, carbon, and oxygen ions from the target surface layer.

Thus, cleaning of the target surface leads to an increase in the energy of the ions of the dominant target material due to, first, the efficient acceleration of these ions by the hot electron component and, second, an increase in the ionization degree. The latter effect may be attributed to the inhomogeneity of the spatial temperature distribution of plasma thermal electrons during a femtosecond laser pulse. The 1D hydrodynamic simulations of the interaction of the femtosecond laser pulse with a plasma show that the temperature at the plasma–vacuum interface in the maximum of the heating 200-fs pulse with the intensity 10^{16} W/cm^2 is twice as high as the temperature at a depth of 40 nm and reaches 200 eV for an electron density of 10^{23} cm^{-3}. The average ionization degree in the surface layer, where the ion concentration is 1/5 of the solid-state value, reaches 20–22 at the laser pulse maximum. Note that the effect of hot electrons on the plasma charge distribution is not significant due to their high average energy and low concentration. Since hot electrons accelerate ions near the interface, some ions of the main target material are ionized to high charge values only on the cleaned target surface and then are efficiently accelerated by hot electrons.

Our experiments revealed strong dependence of ionic current from laser-produced femtosecond plasma on the presence of contamination (or oxide) layer at the top of the target. With relation to internal conversion decay of low energy nuclear levels excited in plasma such a dependence could be crucial at various aspects. From one hand by surface cleaning one can achieve more bulk ions (possessing low energy nuclear state) in hot plasma region thus enhancing excited nuclei yield. Moreover, as it follows from our experiments, at cleaned surface the interaction of hot electrons with bulk ions becomes more efficient – more bulk ions are located in the same plasma volume as hot electrons are. This also should lead to an increase in the number of excited nuclei.

From another hand fast light ions, which come mostly from contamination layer have time-of-flight that is comparable to the low energy nuclear level life-time. Thus elimination of contaminant layer greatly decreases the "noise" signal from negative ions. It is this signal mostly preventing IC electrons detection by electrostatic time-of-light separator in the case of ^{57}Fe or ^{181}Ta isomeric levels. Finally the observed increase in the charge multiplicity of fast bulk ions could enhance IC blocking giving rise to gamma decay events. The appropriate candidate to observe this phenomenon could be ^{201}Hg isomeric state.

3.4 Gamma experiments
3.4.1. Gated APD detector

We were aimed at experiments on registration of gamma-decay of ^{181}Ta$_{73}$ (6.238 keV, 6.05 μs) excited in femtosecond laser plasma. We carried out the test experiments on registration with APD with preamplifier of gamma-radiation of Co-57 (6.4 keV, 14.4 keV) together with X-ray emission of tungsten W$_{74}$ plasma produced by laser pulses with intensity (5-20)·10^{15} W/cm^2.

The experiments with modified detector shown that registration efficiency of gamma-quanta with described above energies had not changed with modification of detector and is in agreement with previous estimations ~70-80 % for 6 keV quanta. Besides as mentioned above the effective registration of gamma-quanta became possible after 2-3 μs after the laser shot.

The purpose definition of amplitudes of the signals arising at registration single γ-quantum by the silicon avalanche photo diode (APD), were spent calibrating experiments with use of a radioactive source γ-radiation ^{57}Co. The characteristic of the given source show in table 3.4.1.1.

Table 3.4.1.1 The basic lines of radiation 57Co.

Energy of quantum, keV	Intensity, rel. units
6,4	0,5
7,1	0,07
14,4	0,0915
6,5*	0,57

* since resolution of the avalanche photo diode has enough to resolve lines with energy 6,4 keV and 7,1 keV, will consider, that they bring the collective contribution with energy 6,5 keV and relative intensity 0,57.

In figure 3.4.1.1a the characteristic signal received at registration single γ-quantum from a radioactive source ^{57}Co is presented. In figure 3.4.1.1b the histogram of distribution of the measured impulses on the amplitude, received in the same series of calibrating experiments is represented.

From results of the lead measurements follows, that:
- duration of the signals recorded by means of APD makes size of the order of 40-50 ns;
- average amplitude of the impulses corresponding registration of γ-quantum with energy 6,5 keV for APD 19 mV.

Besides for check of working capacity of the detector in conditions of real experiment, registration single γ-quantum of a source ^{57}Co in the scheme with gating measured signal has been lead. In figure 3.4.1.2 the signal received during given measurement is presented.
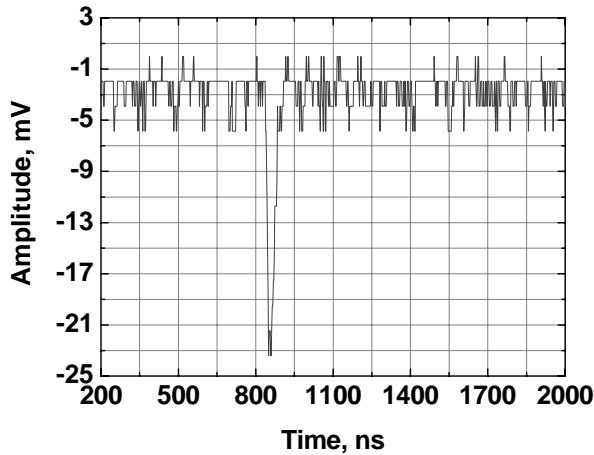
Fig. 3.4.1.1a The signal received at registration single γ-quantum from a radioactive source [57]Co
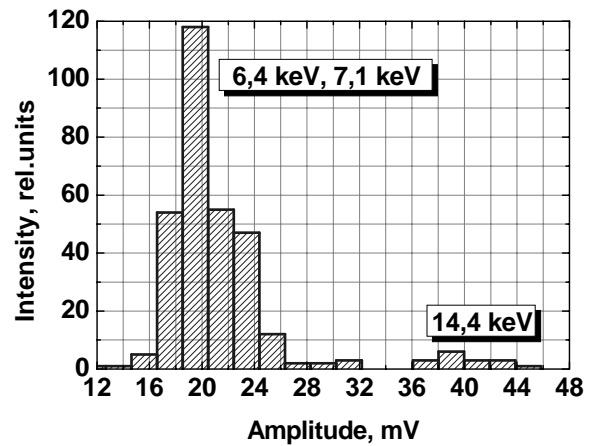
Fig. 3.4.1.1b Histogram of distribution of the measured impulses on amplitude
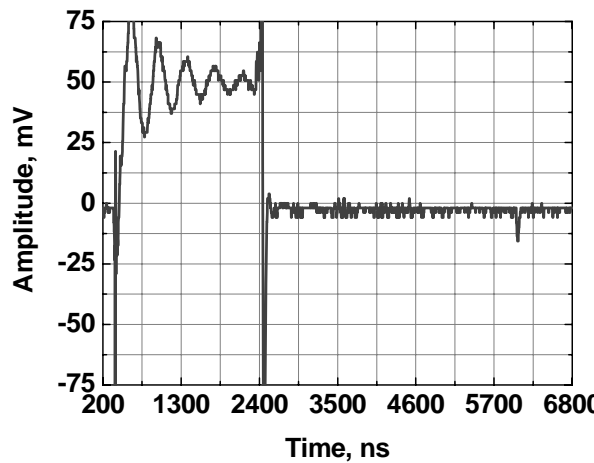
Fig. 3.4.1.2a Signal from APD with strobing, received at registration single γ-quantum from a source [57]Co
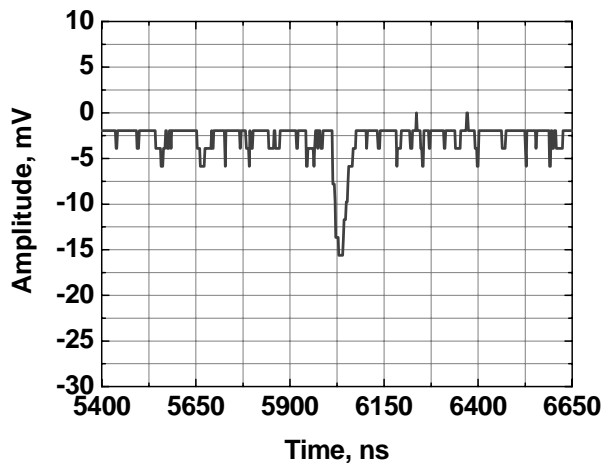
Fig. 3.4.1.2b Kind of single γ-quantum, received from APD in the scheme with strobing

Thus, as a result of calibration of the detector by means of a source [57]Co in the scheme with strobing in a mode of registration single γ-quantum with energy ~ 6.5 keV it has been received, that:

- the amplitude of the fixed pulses makes size 14 mV;
- duration of impulses makes size of ~ 50 ns.

Hence, in experiments with a tantalum target detection of such signals also will testify to registration scale-disintegration of the kernels excited in laser plasma of femtosecond laser pulse.

3.4.2. Experiments on tantalum-181 (6.238 keV, 6.05 mks), excited in femtosecond laser plasma.

Thus, on the basis of the data received as a result of calibrations of the detector in experiments with a source [57]Co in the scheme with gating in a mode of registration single γ-quantum the following technique of carrying out of experiments on supervision scale-disintegration of nuclei of tantalum-181 (6.238 keV, 6.05 mks), excited in laser plasma of femtosecond laser pulse has been developed.

In the lead experiment the laser system on crystal Ti:Sa with energy of a laser impulse 1 mJ and duration 70 fs was used, allowing to achieve intensity on a surface of a target ~10^{17} W/sm^2 at rigid focusing aberration free objective with a focal length 6 sm. Interaction of laser radiation with a solid-state target of tantalum was carried out in the vacuum chamber at residual pressure 10^{-2} Torr.

As a result of the lead experiment 2174 samples have been received and processed. Glitch with the parameters set above it was revealed not.

Including, that in a solid angle of registration of the used detector one scale-quantum gets, we shall estimate the minimal number the γ-quantum, formed in plasma for one laser shot. We shall consider also, that efficiency of registration the γ-quantum with energy 6.238 keV and the specified amplitude of signals for APD makes 80 %. We receive as a result the minimal number radiated γ-quantum in laser plasma of femtosecond laser pulse, necessary for registration single γ-quantum on APD ~ 10^3.

Let's calculate now, what probability to not register any γ-quantum in experiment, depending on number of laser impulses, and also from quantity formed γ-quantum in laser plasma. We shall consider, that probability of registration one γ-quantum, arisen in laser plasma, with use APD it is equal $p = \Omega/(4 \cdot \pi)$, where Ω - a solid angle of registration of the device. Then, according to binomial distribution, probability to not register any γ-quantum in one laser shot, is equal , where $N_\gamma = N_{am} \cdot \eta$ - number γ-quantum in laser plasma, N_{am} - number of atoms of a target in volume of plasma, - efficiency of excitation of kernels in plasma. Hence, in N laser shots with probability $P_N(0) = \left(P_{N\gamma}(0)\right)^N = \left(1 - p\right)^{N\gamma \cdot N}$ any γ-quantum also will not be possible to register. In figure 3.4.2.3a the probability to register even one γ-quantum in N laser shots depending on their number is presented at the fixed number γ-quantum, arise in laser plasma in each shot. In figure 3.4.2.3b the probability to register even one γ-quantum in N laser shots depending on number γ-quantum, arise in laser plasma in each laser shot is resulted at number of laser shots equal $N = 2174$.
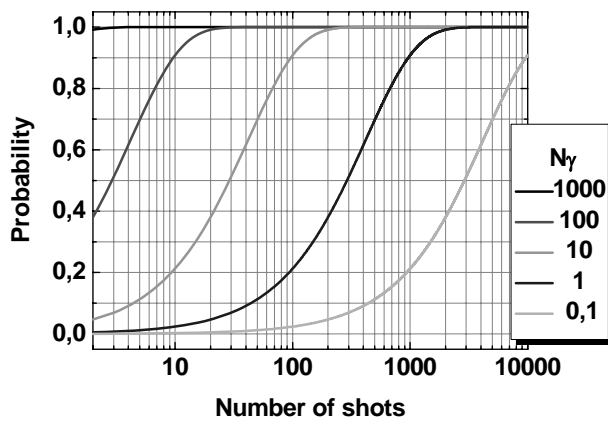
Fig. 3.4.2.3a Probability to register even one γ-quantum in N laser shots depending on their number at the fixed number γ-quantum, arise in laser plasma in each shot.
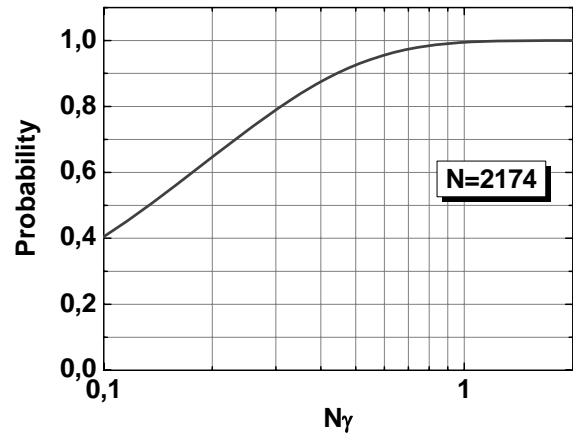
Fig. 3.4.2.3b Probability to register even one γ-quantum in N laser shots depending on number γ-quantum, arise in laser plasma in each laser shot at number of laser shots equal $N = 2174$.

Thus, on the basis of the lead calculations, it is possible to approve, that with probability of 50 % arising the γ-quantum does not exceed quantity 0,2 in each laser shot.

3.4.3. Comparison with previous data

Let's lead comparison of conditions and results of the given experiment with earlier lead experiments (table 3.4.3.2).

Table 3.4.3.2 Comparison with the previous experiments.

Parameter	1999	2003	2005
Amplitude of registered signals	> 3 mV	~ 10 mV	~ 14 mV
Duration of signals	~ 255 ns	~ 40-50 ns	~ 40-50 ns
The attitude a signal/noise	~ 1	~ 4	~ 4
Efficiency of registration γ-quantum with energy 6.238 keV and the specified amplitude of signals on a background of radiation of plasma	~ 50%	~ 80%	~ 80%
The initial moment of registration γ-quantum after a laser shot	3 mks	~ 2-3 mks	~ 2-3 mks
Solid angle of registration	0.07 ster	0.03 ster	0.03 ster
The temperature of hot electrons in plasmas	~ 4 keV	~ 4 keV	~ 10 keV
Quantity of the fixed disintegrations (on 1 laser shot)	~ 0.5	~ 0	~ 0
Quantity of the excited kernels for a shot (on 1 laser shot)	~ 10^3-10^4	<<1	<<1

3.5. IEC experiments
3.5.1. Negative plasma particle detection

We also made experiments on registration of internal conversion of nuclei excited in laser produced plasma the experiments. Measurements of energy spectra of charged particles of laser plasma with time-of-flight electrostatic mass-spectrometer were carried out. During experiments on interaction of femtosecond laser pulses ($I \sim 5 \cdot 10^{15}$-$2 \cdot 10^{16}$ W/cm^2) with silicon target the intense flows of negative ions of hydrogen, carbon, oxygen and silicon with energies $\sim$ 10 keV were registered . It is significant that presence of negative ions is negative factor for conversion decay registration. The analysis shows that presence in registered signal of components corresponding to the flow of negative ions at times ~ 0.1–10 μsec after the laser shot could sufficiently embarrass the detection of conversion electrons.

The measurements of the energy, charge, and mass spectra of laser plasma ions were performed using a time-of-flight electrostatic ion analyzer employing the irradiation of silicon, iron, titanium, and KDP crystal targets by high-intensity (I $\sim 10^{16}$ W/cm^2) laser pulses (E = 0.5 mJ, λ = 616 nm, τ = 200 fs). We measured the ion currents in plasma at angles of 0° and 16° relative to the normal to the target at a distance of 75 cm from its surface for a gas pressure of 10^{-5}-10^{-4} torr inside the interaction chamber. Our setup makes it possible to measure the energy and mass spectra of both negative and positive plasma ions of various degrees of ionization. The analysis of the time-of-flight spectra of the negatively charged particles measured at various settings of the spectrometer makes it possible to obtain mass spectra (Fig. 3.5.1.1) that qualitatively describe the relative content of the negative ions of various substances in the expanding plasma. Note that, in addition to the peaks corresponding to the ions of the target material, we always detect hydrogen, carbon, and oxygen ions, the amount of which exceeds the amount of ions of the target material. We suppose that presence of H, C, and O ions is related to the impurity layer at the target surface emerging owing to the adsorption of residual gas molecules from the environment of the target.
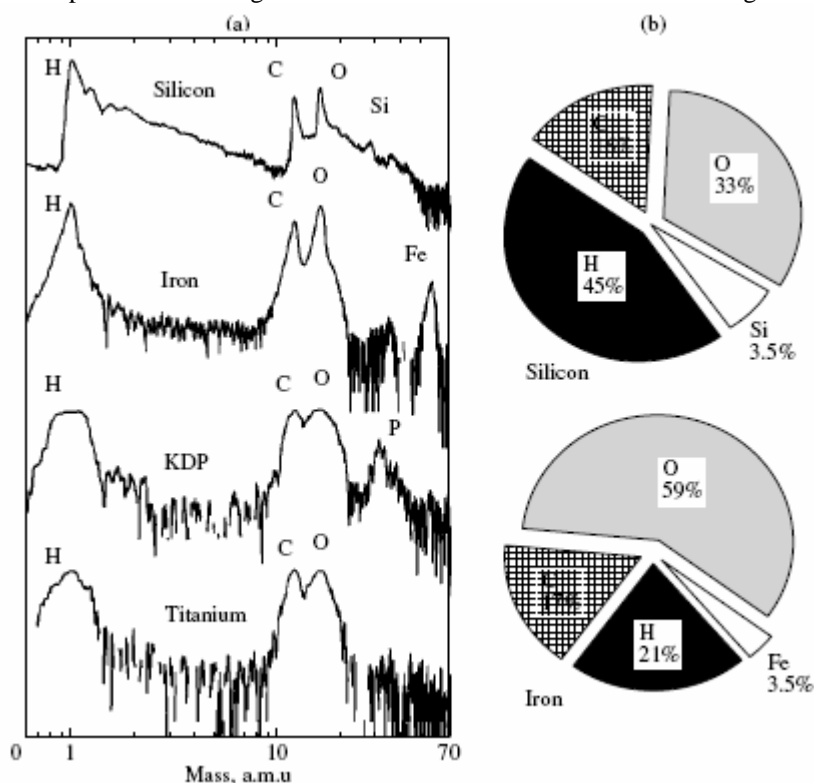
Fig. 3.5.1.1. (a) Qualitative mass spectra of the negative ions and (b) the relative contents of the negative ions in the laser plasma. The measurements are performed along the normals to the surfaces of the silicon, iron, titanium, and KDP targets.

The results of experiments show a high degree of correlation between the energy spectra of the singly charged positive and negative ions (Fig. 3.5.1.2b). Note that the yield of negative H, C, O, Si, P, and Fe ions with energies up to a few tens of kiloelectronvolts amounts to a few percent of the yield of the positively charged particles. Note also that in the experiments with iron targets, we performed the ion current measurements at angles of 0° and 16° relative to the target normal. This makes it possible to study the angular distribution of the energy spectra of the negative and positive plasma ions and the charge composition of the plasma.
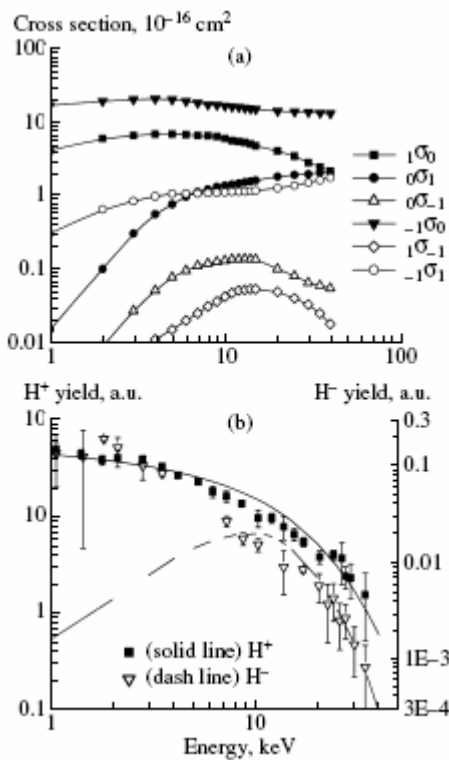
Fig. 3.5.1.2. (a) Cross sections $\sigma Z1$, $Z2$ of the hydrogen ion charge exchange at N2 molecules. (b) Energy spectra of the positive and negative hydrogen ions for the 75-cm-long ion path in a nitrogen atmosphere at a pressure of 10^{-4} torr measured along the normal to the silicon target surface and obtained using the solution of the system of equations (1) and (2).

The formation of negative ions in low-temperature laser plasma has been studied both experimentally and theoretically predominantly upon target irradiation using low-intensity ($I < 10^{10}$ W/cm2) nanosecond laser pulses. Under such conditions, the density of the laser plasma is less than critical, and it is in the near-equilibrium state at the electron temperature $T_e \sim 1$ eV. At such plasma temperatures, the formation of the negative ions becomes thermodynamically efficient and the amount of such ions depends on the relationship between the temperature T_e and the electron affinity E_a The formation of negative ions in low-temperature laser plasma has been studied both experimentally and theoretically predominantly upon target irradiation using low-intensity ($I < 10^{10}$ W/cm^2) nanosecond laser pulses. Under such conditions, the density of the laser plasma is less than critical, and it is in the near-equilibrium state at the electron temperature $T_e \sim 1$ eV. At such plasma temperatures, the formation of the negative ions becomes thermodynamically efficient and the amount of such ions depends on the relationship between the temperature T_e and the electron affinity E_a.

However, the kinetic energy of the negative ions is no greater than a few electronvolts owing to the low plasma temperature. The increase in the laser pulse intensity leads to an increase in the kinetic energy of the negative plasma ions with a simultaneous decrease in the efficiency of formation of negative ions. The maximum velocity of the negative ions measured in such experiments is about 10^5 cm/s .
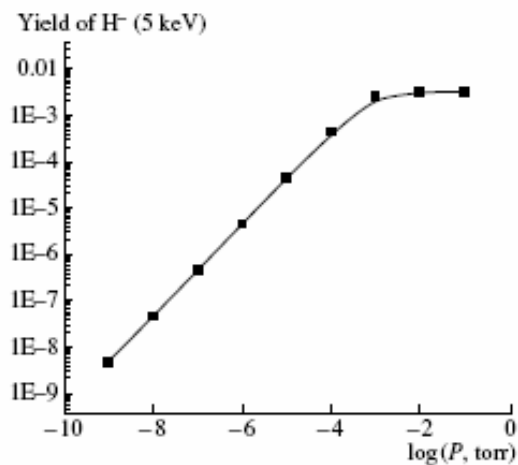
Fig. 3.5.1.3. Plot of the yield of negative hydrogen ions with an energy of 5 keV versus the nitrogen N2 vapor pressure for the 75-cm-long proton path in the gas.

A distinctive feature of the results obtained in our experiments is the observation of substantial flows of high-energy (10–40 keV) negative ions resulting from the interaction of the high-intensity ($I \sim 10^{16}$ W/cm^2) femtosecond laser radiation with solid targets (Figs. 3.5.1.1, 3.5.1.4, 3.5.1.5). However, the appearance of the negative ions in the hot laser plasma formed at the target surface in experiments with such high intensities cannot be interpreted in the framework of the above approach. To account for this, recall that at laser intensities of no less than 10^{16} W/cm^2, the temperature of the plasma electrons is about 100 eV, which leads, in turn, to a high degree of plasma ionization $Z \sim$ 10. Thus, the formation of the negative ions in a hot solid-state laser plasma in the vicinity of the target surface becomes impossible owing to both the low efficiency of formation of the particles at high temperatures and the low (virtually zero) content of neutral atoms in the plasma. The assumption regarding the formation of negative ions in plasma at the stage of its expansion into vacuum at the moment when the electron temperature decreases to about 1 eV appears to be also inconsistent, since a significant decrease in the plasma density ($n_e \sim 10^{19}$ cm^{-3}) leads to suppression of the electron capture in collisions. In addition, the effect of ionization freezing in expanding laser plasma prevents the increase in the content of neutral atoms needed for the formation of negative ions. The above analysis shows that, by taking into account only the formation of the negative ions related to the capture of free

106

electrons in the hot laser plasma, we are unable to interpret the experimentally measured yields and the characteristic energy spectra of the negative ions. Thus, it is needed to search for an alternative mechanism for the formation of negative ions in an expanding laser plasma.
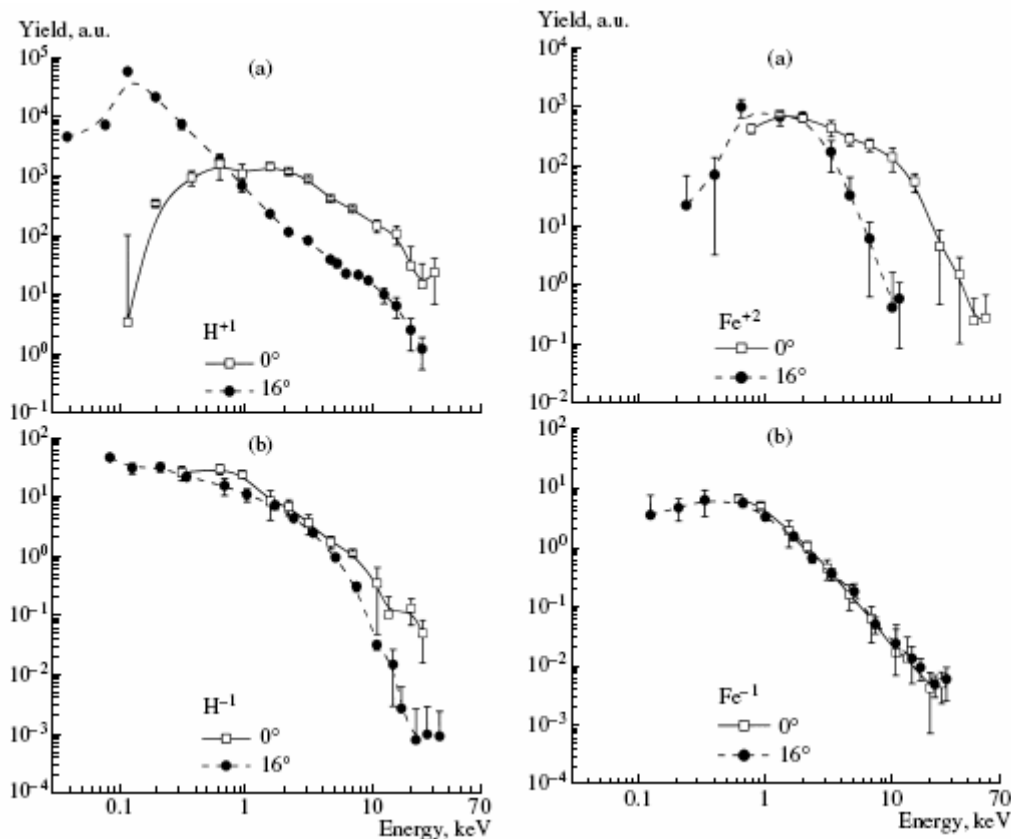
Fig. 3.5.1.4. Energy spectra of (a) the positive H^{+1} and (b) negative H^{-1} hydrogen ions measured at angles of $0°$ and $16°$ relative to the normal to the iron target surface.

Fig. 3.5.1.5. Energy spectra of (a) the positive Fe^{+2} and (b) negative Fe^{-1} iron ions measured at angles of $0°$ and $16°$ relative to the normal to the iron target surface.

It is known that the observations of ions with a high degree of ionization in experiments on laser-matter interaction necessitate high vacuum in the entire system, from the target to the detector. The reason for this is a relatively fast recombination of the expanding laser plasma related to the charge exchange at the molecules of the residual gas inside the chamber. It is known that the observations of, for example, $Al^{11}+$ ions in a chamber about 1 m in size are possible if the vacuum is better than 10^{-7} torr. Therefore, it can be concluded that the experimentally observed charge composition of the plasma (Fig. 3.5.1.6) does not correspond to the distribution of ions with respect to the degree of ionization in the vicinity of the target and depends on the ion charge exchange during the flight from the target to the mass spectrometer. In our experiments, the residual gas pressure inside the chamber was about 10^{-5}-10^{-4} torr, which should lead to a significant decrease in the mean charge of the laser plasma on the path from the target to the detector. It can also be stated that the negative ions detected in the experiments are, most probably, formed owing to the charge exchange of the positive ions and neutral atoms of the plasma at the molecules of the residual gas inside the chamber: A + P -A − A + P+.

Fig. 3.5.1.6. Ion distributions with respect to the atomic composition and degree of ionization measured (a) along the normal to the target and (b) at an angle of $16°$ to the normal in experiments with the iron target.
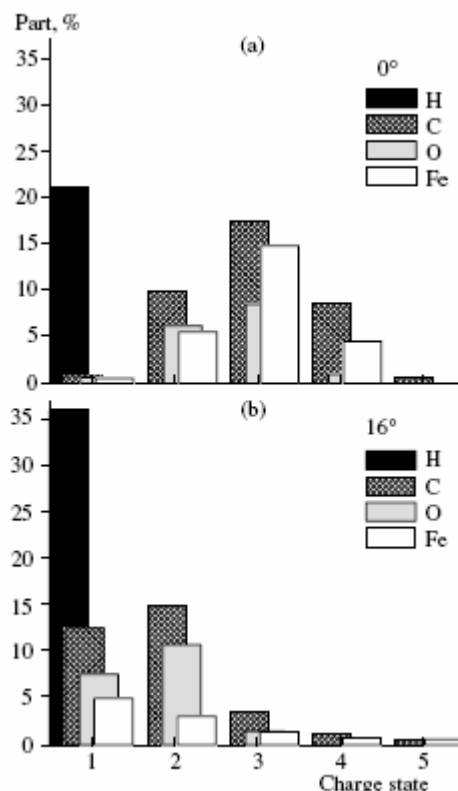
To verify the above assumption, we performed model calculations of the formation of a negative hydrogen ion H^{-1} at a path length of 75 cm (the distance from the target surface to the ion analyzer) in a nitrogen atmosphere at a pressure of 10^{-4} torr corresponding to the mean (with respect to the ion path length) pressure of the residual gas inside the chamber. In this case, the system of kinetic equations describing the charge exchange of various hydrogen ions with the residual gas molecules is written as

$$\begin{cases} \dfrac{dn_1}{dx} = [-(\sigma_{10}+\sigma_{1-1})n_1 + \sigma_{01}n_0 + \sigma_{-11}n_{-1}]N_{gas}, \\[2mm] \dfrac{dn_0}{dx} = [\sigma_{10}n_1 - (\sigma_{01}+\sigma_{0-1})n_0 + \sigma_{-11}n_{-1}]N_{gas}, \\[2mm] \dfrac{dn_{-1}}{dx} = [\sigma_{1-1}n_1 + \sigma_{0-1}n_0 - (\sigma_{-10}+\sigma_{-11})n_{-1}]N_{gas}, \\[2mm] n_1 + n_0 + n_{-1} = 1, \end{cases} \quad (1)$$

where nZ is the content of hydrogen ions with a degree of ionization Z = (-1, 0, +1) in the expanding plasma and σZ1, Z2 corresponds to the cross section of the charge exchange of hydrogen ions with a degree of ionization Z1 with their transformation into ions with a degree of ionization Z2 with the residual gas molecules with concentration Ngas. The original conditions (at x = 0) for the system under consideration imply ionization of all the hydrogen atoms in the plasma:

$$\begin{cases} n_1 = 1 \\ n_0 = n_{-1} = 0, \end{cases} \quad \text{at} \quad x = 0. \quad (2)$$

In calculations, we assume that the initial energy distribution of the hydrogen ions has exponential shape with a temperature of about 9 keV corresponding to the parameters of the hydrogen ion energy spectrum measured in experiments with the silicon target (Fig. 3.5.1.2b). Note that, in general, the shape of the energy spectrum of the negative plasma ions measured by the detector depends not only on the spectrum of the positive ions but also on the cross sections σZ1, Z2 as functions of the energy of colliding particles (Fig. 3.5.1.2a).

Figure 2b demonstrates the calculated kinetics of formation of the negative hydrogen ions for a proton path length of 75 cm in a nitrogen atmosphere at a pressure of 10^{-4} torr. Comparative analysis of the results of calculations and the experimental data shows relatively good agreement for particle energies exceeding 8 keV. In both cases, the increase in the energy of the particles in the above range leads to a faster decrease in the curve corresponding to the spectrum of the negative ions in comparison to the curve corresponding to the positively charged protons. In the framework of the model under consideration, this fact is related to the decrease in the cross sections a0_t and σ1,–1 at energies exceeding 10-20 keV (Fig. 3.5.1.2a). Note also the significant difference between the model and experimental data at ion energies less than 5 keV. For this energy range, the shapes of the experimentally measured spectra of the positive and negative hydrogen ions coincide, whereas the results of calculations predict a substantial difference between these spectra related to the decrease in cross sections a0 _t and σ1,–1 at energies less than 10 keV (Fig. 3.5.1.2a). To account for this discrepancy, note that the model calculations employ the assumption that the residual gas inside the chamber is air (predominantly nitrogen N2). Under real experimental conditions, the composition of the residual gas, most likely, would depend on the presence of vacuum oil vapors. Additional supporting evidence is provided by the presence of the large amount of hydrocarbon impurities adsorbed at the target surface detected by mass spectrometer. Thus, we can conclude that the charge exchange of the plasma ions involves large hydrocarbon molecules contained in the vacuum oil rather than the molecules of air. Hence, the results of calculations shown in Fig. 3.5.1.2b can only be used for qualitative interpretation of the experimental results.

Analysis shows that the charge exchange of hydrogen ions with the complex hydrocarbons has the following features.

(i) The charge exchange cross section peaks at energies of the colliding particles that are less than the energies for the case of charge exchange with the nitrogen molecules.

(ii) The relative width of the energy range of the incident particle corresponding to the maximum charge exchange cross section for the hydrocarbons is greater than that for the nitrogen molecules.

(iii) The cross section of the charge exchange with the complex hydrocarbons must be greater than the cross section of the charge exchange with the nitrogen molecules.

For example, for the charge exchange of the positive hydrogen ion H+ with N2 molecules with the formation of a neutral atom, the maximum cross section (σ1, 0(max) ~ 7×10^{-16} cm^2) corresponds to an energy of about 5 keV. In the case of charge exchange at C3H8 molecules, the maximum cross section (σ1, 0(max) ~ 3×10^{-15}cm^2) corresponds to an energy of the colliding particles of about 1 keV. Similar relationships appear to be valid for the cross sections a0_t and out. The above features are primarily related to the abundance of channels of the charge exchange accompanied by the excitation and dissociation of the complex molecule and its relatively low ionization potential. In general, with allowance for the aforesaid facts, the spectrum of the negative hydrogen ions becomes

more smooth than in the case of the model calculations with nitrogen, which makes it possible to interpret the experimental results (Fig. 3.5.1.2b).

In addition, note that the above model for the formation of negative ions on the particle path in the gas surrounding the target makes it possible to adequately interpret the values of the negative hydrogen ion yield relative to the experimental values of the proton yield. The measured signal from the negative hydrogen ions is two to three orders of magnitude weaker than the signal from the positive protons, which is in agreement with the results of calculations presented in Fig. 3.5.1.2b. Figure 3.5.1.3 demonstrates the dependence of the negative hydrogen ion yield for an ion energy of 5 keV on the nitrogen N_2 vapor pressure for a 75-cm-long proton path in the gas. It is seen that, at a gas pressure of about 10 3 torr, the negative hydrogen ion yield reaches saturation and is equal to about 0.5% of the total number of hydrogen particles.

Note also that the relationship between the yields of various negative ions (Fig. 3.5.1.1) can also be interpreted in the framework of the model proposed. In accordance with the experimental results, the cross section of the charge exchange of particles accompanied by the formation of negative ions increases with the electron affinity E_a. The table shows the affinities for the atoms detected in experiments. It follows from the data presented that the maximum (minimum) yield of negative ions should be observed for C and O (Ti) atoms, which is in agreement with the experimental data (Fig. 3.5.1.1). Apparently, we must take into account the dependence of the ion yield on the ion content in the target.

The values of affinity for the elements detected in experiments

	H_1	C_{12}	O_{16}	Si_{28}	P_{31}	K_{39}	Ti_{48}	Fe_{56}
E_a, eV	0.7542	1.2629	1.462	1.385	0.7464	0.5015	0.080	0.164

We also performed an experimental study of the angular distribution, charge composition, and energy spectra of ions in the expanding laser plasma. Figures 43.5.1. and 3.5.1.5 show the energy spectra of H^{+1}, H^{-1}, Fe^{+2}, and Fe^{-1} ions measured at angles of 0° and 16° relative to the normal to the surface of the iron target. The distinctive feature of the results obtained lies in the fact that the mean energy of all positive ions (including C and O ions not shown in the figure) moving at an angle of 16° is less than the energy of ions moving along the normal to the target surface. At energies less than 1 keV, for all ions with charge $Z \geq 2$, we observe coincidence of the energy spectra of the particles moving at angles of 0° and 16°. Thus, the low-energy ions move in a relatively wide solid angle, while the high-energy (energy greater than 5 keV) ions with a high degree of ionization exhibit a narrow angle diagram with an angle of less than 16° relative to the target normal. The reason for this is the fact that the high-energy ions are formed owing to the ambipolar accelerating potential of hot electrons acting upon the ions with a large charge in the direction perpendicular to the target surface. Indirect supporting evidence can be found in the experimental results on the angular distribution of the laser plasma charge composition (Fig. 3.5.1.6), which demonstrate the shift of the mean charge from Z ~ 3-4 (measurements along the normal to the target surface) to Z ~ 1-2 (measurements at an angle of 16° relative to the normal). Thus, the results obtained show that, in comparison to the low-energy ions, the high-energy ions exhibit a higher degree of ionization and a narrower angular distribution.

Finally, note that we observed a complete coincidence of the energy spectra and the yields of the negative plasma Fe, C, and O ions measured at angles of 0° and 16° relative to the normal to the target surface (Fig. 3.5.1.5). This fact needs to be further analyzed in detail. A possible reason for this is the wide diagram of the neutral plasma particles. For the negative hydrogen ions, we do not observe such a correlation: the mean energy of ions moving at an angle of 16° is less than the energy of the ions moving along the normal to the target surface.

3.5.2. IC electrons detection

The mass-spectrometer, which was designed, was successfully used for registration of charged particles with energies up to 40 keV from plasma previously. In particular the electrons from plasma with energies up to 40 keV were measured. Hence, this mass-spectrometer could be used in further experiments on registration of conversion electrons as well (in case of their energies are in the same range).

Unfortunately, the previously observed negative ions, formed during of the plasma expansion into vacuum, make the serious obstacles for the conversional electrons observations. Normally, the signal of plasma electrons and plasma ions could be easily distinguished from each other. This takes place die to variety of velocities between ions and electrons, while both ions and electrons have the same kinetic energy after the transmission through the mass-spectrometer.

It could be concluded, that the conversion electrons would be delayed on a time, comparable with the nuclear level lifetime, and hence, the time of their arrival to the detector and arrival of negative ions could be contemporize to each other. So, it should be taken into account, that a part of conversion electrons within a fixed delay range could not be detected by means of mentioned electrostatic mass-spectrometer.

The most preferable cases, to our knowledge, are as follow: the nuclear lifetime is greatly exceeds the arrival time of the heaviest ions, or nuclear lifetime less than time of hydrogen ions appearance. At the same time, the nuclear lifetime should greatly exceed 10 ns – the typical response time of MCP electronic circuit (otherwise, the conversion electrons and electrons from plasma could not be resolved).

Several isotopes have been investigated as the potential objects for the laser-matter interaction experiments on low-lying nuclear levels excitation. The estimations of the conversion electrons yield, which are able to be

detected by means of mentioned mass-spectrometer were performed for each of them. The follow parameters were took into account during the calculations: the nuclear lifetime, the temporal positions of negative ions peaks (which were calculated from the energy of nuclear level with the deduction of atomic bonding energy), the whole quantity of excited nuclei during one laser shot, solid angle and energy resolution of the mass-spectrometer and the share of isotope in natural sample.

All calculations were performed for the existing experimental setup which based on mass-spectroscopy measurements of particles from plasma and which was used previously.

Both theoretical calculations and experimental data (obtained in previous experiments on registrations of gamma decay of Ta 181 nuclear level (6.2 keV)), were used for these estimations. Theoretical calculation takes into account the distinctions between the isotopes in efficiency of excitations by the incoherent hard x-rays radiation from plasma, which is a function of: nuclear level energy, hard x-rays spectra of the bremsstrahlung irradiations of plasma, radiation nuclear level lifetime (nuclear level width).

Mostly due to short lifetime, exactly Fe 57 was evaluated as the most preferable among a number of nuclei with low-lying nuclear levels. Short lifetime (98ns) leads to:

The gain of the nuclear level energy width. This leads to increasing of gamma quanta, which are able to excite the nuclear, and hence, leads to increasing efficiency.

The conditions, where the intersection of the exponential decay tail (envelope of conversion electrons signal) and the signal from negative ions does not exceed 1% of the whole yield of conversion electrons. In particular, the hydrogen ions with the energy of 7-8 keV (which corresponds to the energy of conversion electrons escaped from the K-shell; nuclear level energy – 14.1 keV) situated at the 400 – 500 ns after the plasma formation stage for the length-of-flight distance of 62-67 cm. As could be seem this time is higher enough than the nuclear lifetime of Fe 57 (98ns).

At the other hand, this time is greatly exceeds to the typical time response of the MCP. So, exactly Fe 57 was chosen as the object for further experiments on excitation of low-lying nuclear levels and their observation through the internal electronic conversion.

The experiments on electronic conversion decay of excited nuclei (*Fe, E=14 keV, t=98 ns*) were carried out. Excitation was created by radiation of plasma, which provided by femtosecond laser radiation ($W=2 \ mJ, \tau = 60 \ fs$, $S_{foc} =12 \mu m^2$, $I=10^{17} \ W/cm^2$).

The known value of IEC coefficient is $\alpha \approx 8.5$, thus conversion decay is the dominant process of nuclei relaxation. To evaluate the spectra of conversion electrons we have to estimate the partial coefficients of IEC for different atomic shells.
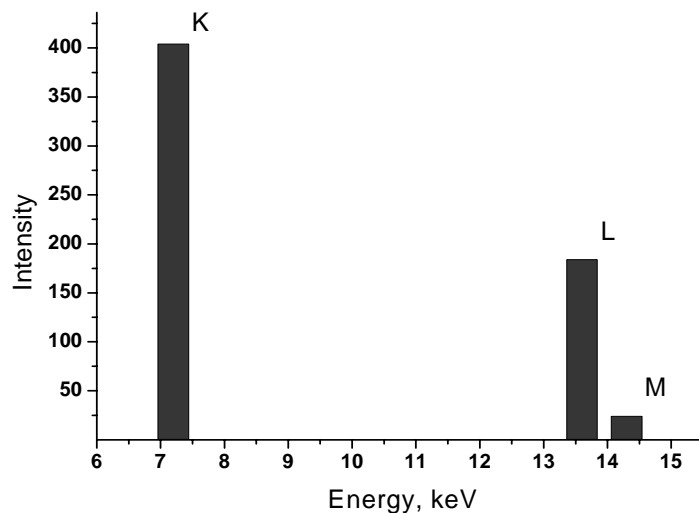
Fig. 3.5.2.1. The spectra of conversion electrons

So, the main decay products of excited nuclear level (*Fe, E=14 keV*) are conversion electrons with energy *E=7,2 keV*. The concept of experiment for decay registration of excited nuclear level *Fe* in this case is simple: we should measure the electron current from the plasma and pick out the conversion component, delayed from the main plasma current.

Experimental setup is shown at Fig. 3.5.2.2. Experimental setup consists of 2 chambers. In interaction chamber there is a target which we can move in vertical plane by means of 2 translators. Laser beam comes to this chamber though the focusing lens and defense window. Electron current passes through connecting tube into measurement chamber on electrostatic-field mass spectrometer. Micro channel plate register the electronic current.

Spectrometer is the cylindrical condenser, voltage on its plates control traceable particles according to relation of its energies and charges. Resolution of spectrometer by energy $E/\Delta E = 10$.
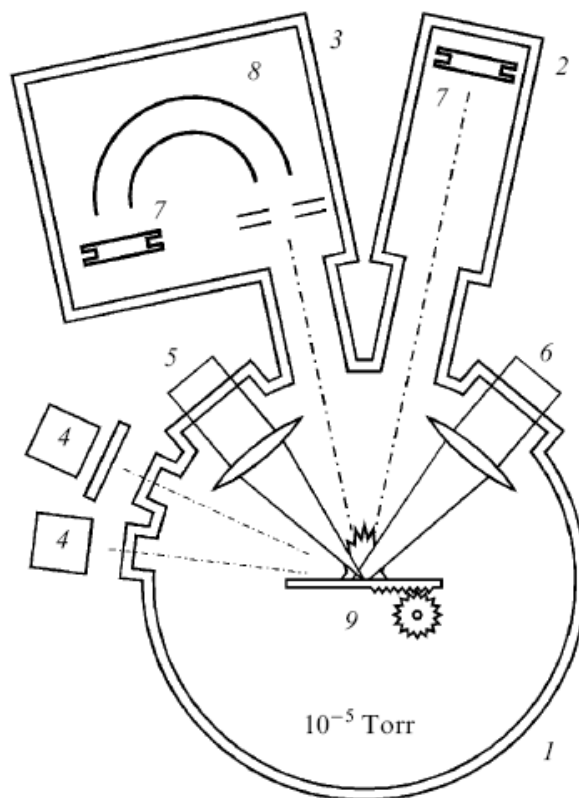
Fig. 3.5.2.2. Experimental setup: (1) interaction chamber; (2) time-of-flight measurement chamber; (3) mass-spectrometry measurement chamber; (4) X-ray detectors (NaI) with filters; (5) plasma-generating femtosecond pulse radiation; (7) VEU-7 detectors; (8) electrostatic-field mass spectrometer; (9) movable target

Electronic current from plasma was measured in 30 series with different energy of registered particles.
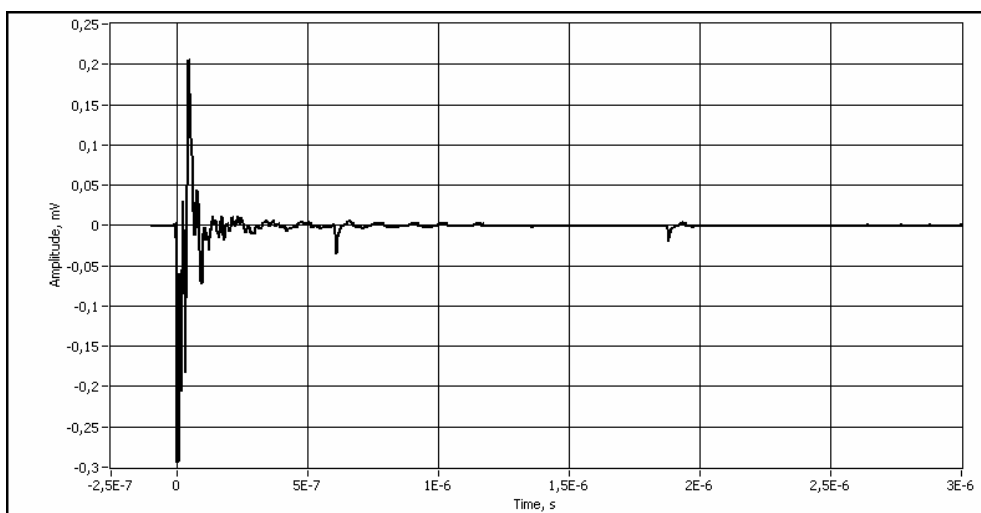
Fig. 3.5.2.3. Signal from micro channel plate from electronic current with energy of particles $7.2 \pm 0.3 \, keV$

The sharp minimum at the beginning of signal specified by "hot" electrons from plasma. The peaks follows after the unavoidable oscillation. The calibrating experiments with electronic gun showed that peaks with amplitude of 30-40 mV correspond to registration of single electron. It can be both conversion electron and noise.

We realized 30 series of experiment for different energies of registered particles. In each series there were about 10000 laser shots. We estimated the quantity of registered peaks in each series in identical period of time (400-1000 ns). The quantity of noisy electrons doesn't depend on energy of registered particles. That we can expect increasing the quantity of registered electrons with energy $E=7,2 \, keV$ owing to conversion constituent.
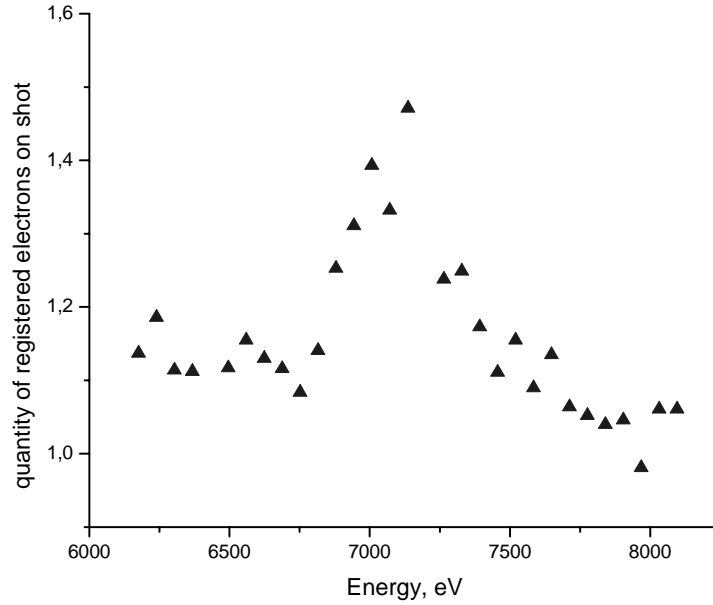
Fig. 2.5.2.4. Dependency of registered electrons quantity on its energies

The experimental results are plotted at figure 2.5.2.4. Measured electronic distribution on energy has a maximum at energy of 7.2 keV. This value is in a good agreement with theoretical energy of internal conversion electrons (estimated value is 7.2 keV). Width of distribution peak corresponds to energy resolution of our spectrometer ~10% (0.7 keV).

4. THEORY
4.1. Low energy nuclear level excitation in stationary plasma

Hot dense plasma generated at the surface of the sample by a high-intensity laser pulse can serve as a source of excited nuclei. Note the promising character of such study for various branches of physics and technology. Examples are plasma diagnostics using the number of excited nuclei, the creation of population inversion in a system of nuclear levels, and the study of the lowest nuclear states.

To obtain positive experimental results, one must choose the nucleus appropriately. Thus, it is expedient to consider all of the most important processes leading to nuclear excitation and to estimate the efficiency of the excitation processes as a function of the energy and multipolarity of the nuclear transition and the plasma parameters. We classify the excitation mechanisms in the framework of perturbation theory for quantum electrodynamics (QED) based on the order of the Feynman diagram describing the corresponding process (see fig. 4.1.1).

The main purpose of this work is to determine the general properties of the nuclear excitation by plasma photons and electrons. Thus, we make the simplest assumptions regarding the plasma parameters and the spectra of particles: electrons and photons obey Maxwell and Planck energy distributions, respectively. These assumptions are sufficient to qualitatively estimate the efficiency of the processes under consideration

A simple analysis shows that the first-order process results in an effective excitation of the plasma nuclei only in the case of dipole nuclear transitions. The cross section of the photoabsorption of the plasma thermal radiation by a nucleus is strongly resonant:

$$\sigma^{(1)}(\omega) = \frac{\lambda^2}{2\pi} \frac{\Gamma_N^t \Gamma_N^r / 4}{(\omega - \omega_N)^2 + (\Gamma_N^t / 2)^2} . \qquad (1)$$

Here λ is the radiation wavelength, i.e. $\lambda = 2\pi / \omega$ where ω is the photon energy in the system of units $\hbar = c = 1$, Γ_N^r is the radiation width of the nuclear transition from the ground to low-lying isomer state, and ω_N is the energy of the nuclear transition.

The efficiency is calculated using an approximate formula

$$\zeta^{(1)} = \int_0^\infty \sigma(\omega) \tau n(\omega) d\omega , \qquad (2)$$

where τ is plasma's lifetime, and $n(\omega)$ is specrtum of photons.

Let us calculate the efficiency of excitation by the thermal self-radiation of plasma for a few nuclei having a relatively low-lying (no greater than a few keV) first excited state (see Table 4.1.1). Figure 4.1.2 demonstrates the results of the numerical calculation of the nuclear excitation efficiency by plasma selfadiation.

Table 4.1.1.

Nucleus	Ground State $J_i^\pi (T_{1/2})$	Isomeric State $J_i^\pi (E, T_{1/2})$	Transition $E/ML, \Gamma_N^r (J_i \rightarrow J_f)$, eV
^{201}Hg	3/2⁻(stable)	1/2 ⁻(1.561 keV, -)	$M1, 2\times10^{-11} - 2\times10^{-12}$
^{181}Ta	7/2⁺(stable)	9/2 ⁻(6.24 keV, 6.05 µs)	$E1, 1.32\times10^{-12}$
^{73}Ge	9/2⁺(stable)	5/2⁺(13.27 keV, 2.95 µs)	$E2, 8.3\times10^{-14}$
^{57}Fe	1/2⁻(stable)	3/2 ⁻(14.413 keV, 98 ns)	$M1, 1.0\times10^{-9}$
^{169}Tm	1/2⁺(stable)	3/2 ⁺(8.41 keV, 4.08 ns)	$M1, 7.83\times10^{-10}$
^{239}Pu	1/2⁺(24110 y)	3/2 ⁺(7.861 keV, 36 ps)	$M1, 4.26\times10^{-9}$

It follows from the data presented in Fig. 4.1.2 that the ^{239}Pu nucleus is the most promising experimental object.

The diagram of second order with respect to the electromagnetic interaction constant e shown in Fig. 4.1.1 describes two main processes leading to nuclear excitation: inverse electronic conversion (IEC) and inelastic scattering of the plasma electrons by nuclei.

In the course of IEC, a plasma electron populates the ionized atomic level and excites the nucleus by a virtual photon. The mechanism under consideration works only in plasma whose temperature is comparable to the nuclear transition energy. The IEC cross section at completely free atomic shells is calculated using the conventional QED methods:

$$\sigma_{IEC}(E \rightarrow f) \approx \delta(\omega_N - (E - E_f))\frac{\lambda_e^2}{4}\Gamma_c(\omega_N; f). \qquad (3)$$

Here, E is the electron energy in the continuous spectrum, p is the momentum of the electron, E_f is the energy of the bound electron state at the atomic shell populated during IEC, Γ_c is a conversion width of the level, λ_e is the wavelength of an electron with energy E.

Note the resonant character of expression (3). The energies E^r of the working electrons in the plasma spectrum (electrons that excite nuclei) coincide with the difference between the nuclear transition energy ω_N and the absolute value of the binding energy E_f at the populated atomic shell: $\omega_N - |E_f| - \Gamma_c/2 \leq E^r \leq \omega_N - |E_f| + \Gamma_c/2$.

For the nuclei excitation in plasma, the IEC efficiency can be represented as

$$\zeta_{IEC}^{(2)} = \int_0^\infty \sigma_{IEC}(E)n_e f_e(E)\tau v_e \frac{dE}{T}. \qquad (4)$$

After integration in (3) the order-of-magnitude estimate for the efficiency is given by:

$$\zeta_{IEC}^{(2)} \approx \frac{(\lambda_e^r)^2}{4}\frac{\Gamma_c}{T}f_e(E^r)n_e\tau v_e^r, \qquad (5)$$

where $E^r = \omega_N - |E_f|$ is the resonance energy, λ_e^r is the resonant wavelength of an electron, and $v_e^r = \sqrt{2E^r/m_e}$ is the velocity of resonant electrons.

As well as all the remaining mechanisms, IEC exhibits the highest efficiency at a plasma temperature T comparable to the nuclear transition energy ω_N. At such a plasma temperature, the ionization involves the atomic shells for which the probability of the internal electronic conversion is high and the number of electrons at the working part of the spectrum is relatively large. Table 4.1.2 demonstrates the nuclear excitation efficiencies in plasma for the case of IEC at $T \approx \omega_N$.

As a rule, parameter $n_e\tau$ depends on the specific experimental conditions. Therefore, we perform calculations for a single value $n_e\tau \approx 10^{10}$ cm⁻³s corresponding to the solid density and a lifetime of 1 ps. Formula (5) is linear in terms of this parameter, which makes it possible to easily recalculate the data presented in Table 4.1.2 for a more realistic case.

Table 4.1.2.

Nuclei	Transition multipolarity	Energy, keV	Γ_c, eV	$\zeta_{IEC}^{(2)}$ at $T \approx \omega_N$
^{235}U	$E3$	0.0768	3×10^{-19}	$\approx 10^{-18}$
^{229}Pa	$E1$	0.160-0.220	$\approx 10^{-9}$	$\approx 10^{-9}$
^{201}Hg	$M1$	1.561	$\approx 10^{-7}-10^{-8}$	$\approx 10^{-8}-10^{-9}$
^{205}Pb	$E2$	2.329	$\approx 4\times10^{-10}$	$10^{-11}-10^{-12}$
^{181}Ta	$E1$	6.24	7.6×10^{-11}	$\approx 10^{-13}$
^{73}Ge	$E2$	13.275	1.5×10^{-10}	$\approx 10^{-13}$

It is seen from Table 4.1.2 that experimental study of IEC can be realized at least for the ^{201}Hg nucleus. Note that, for the ^{235}U nucleus, the excitation efficiency is very low, which means that substantial efforts are needed to obtain a positive experimental result.

The aforementioned direct photoabsorption and IEC are resonant processes. Photons and electrons taking part in the interactions leading to nuclear excitation leave the plasma: the former are absorbed by the nucleus and the latter populate the ionized atomic levels. The cross sections of the nuclear excitation processes are high and can be estimated as λ^2, where λ is the wavelength of the resonant photons or electrons. However, only narrow parts of the photon and electron spectra equal to the radiation and conversion widths of the excited nuclear level, respectively, are involved in the aforementioned processes.

Inelastic scattering of the plasma electrons by nuclei is a process of another type. All plasma electrons whose energy is greater than the nuclear transition energy take part in the excitation. Thus, the spectrum of the particles involved in the process becomes substantially broader. On the other hand, both the original and the final states of the electron that excites a nucleus belong to the continuous spectrum. Hence, the process is not resonant and its cross section that weakly depends on energy is significantly less than $\left(\lambda_e^r\right)^2$. Mutual compensation takes place: the broadening of the spectrum of particles taking part in the excitation by a few orders of magnitude is compensated by a few orders of magnitude lower cross section of the process. However, the difference in the yield of the excited nuclei can be related to the strong effect of the electron population kinetics of the ionized atomic levels in the presence of plasma cooling on the IEC process. The excitation by inelastic electron scattering is less sensitive to the aforementioned processes, since the (e, e') cross section is often virtually independent of ion charge.

The cross section of the inelastic electron scattering by a nucleus involved in the transition with multipolarity E/ML is represented as:

$$\sigma_{ee'} = a_B^2 \left(\frac{R_0}{a_B}\right)^{2L} \left|\left\langle J_i \left\| E/ML \right\| J_f \right\rangle\right|^2 \xi_e, \tag{6}$$

where a_B is the Bohr radius, $R_0 = 1.2 A^{1/3} 10^{-13}$ cm is the nuclear radius, ξ_e is the electron part of the square of the interaction Hamiltonian matrix element, and $\left\langle J_i \left\| E/ML \right\| J_f \right\rangle$ is the reduced matrix element of the nuclear transition depending on the reduced probability $B(E/ML)$ given by expression $B(E/ML; J_i \to J_f) = e^2 R_0^{2L} \left|\left\langle J_i \left\| E/ML \right\| J_f \right\rangle\right|^2$, ξ_e - representing the electron part of the matrix elements of the inelastic scattering Hamiltonian.

To calculate the electron factor of the scattering cross section, we preliminary calculate the self-consistent field of the nucleus and electron shell for ions with various degrees of ionization using the Hartree–Fock–Slater method. In the presence of the calculated selfconsistent field, we find the radial components of the relativistic wave functions of free electrons.

The excitation efficiency is estimated as:

$$\zeta_{ee'}^{(2)} = \int_0^\infty \sigma_{ee'}(E) n_e f_e(E) v_e \frac{dE}{T} \approx \left\langle \sigma_{ee'} v_e \right\rangle n_e \tau, \tag{7}$$

где where $\left\langle v_e \sigma_{ee'} \right\rangle$ is the reaction rate averaged with respect to the distribution $f_e(E)$.

Table 3 demonstrates the results of numerical calculations of the excitation cross sections of ^{235}U, ^{229}Pa, ^{201}Hg, ^{181}Ta, and ^{205}Pb nuclei; the reaction rates; and the excitation efficiency for the plasma with temperature $T \approx \omega_N$ and $n_e \tau \approx 10^{10}$ cm^{-3}s. The comparison with the data presented in Table 4.1.3 show that the efficiencies of the excitation processes involving IEC and inelastic electron scattering are either equal or of the same order of magnitude.

Table 4.1.3.

Nuclei	Multipolarity of transition	Energy, keV	$\sigma_{ee'}$, cm^2 at $E_e = 2\omega_N$	$\left\langle v_e \sigma_{ee'} \right\rangle$, cm^{3}s^{-1} at $T \approx \omega_N$	$\zeta_{ee'}^{(2)}$ at $T \approx \omega_N$
^{235}U	$E3$	0.0768	$\approx 3 \times 10^{-38}$	$\approx 1.4 \times 10^{-29}$	$\approx 10^{-19}$
^{229}Pa	$E1$	0.160	$\approx 3.5 \times 10^{-29}$	$\approx 2.2 \times 10^{-20}$	$\approx 10^{-10}$
^{201}Hg	$M1$	1.561	$\approx 0.7 \times 10^{-29}$	$\approx 1.5 \times 10^{-20}$	$\approx 10^{-10}$
^{205}Pb	$E2$	2.329	$\approx 3.6 \times 10^{-32}$	$\approx 0.9 \times 10^{-22}$	$\approx 10^{-12}$
^{181}Ta	$E1$	6.24	$\approx 0.9 \times 10^{-33}$	$\approx 3.8 \times 10^{-24}$	10^{-13}-10^{-14}

In the third order of perturbation theory, we consider four processes leading to nuclear excitation in plasma. The three of them shown in Fig. 4.1.1 are IEB, IEC expanded owing to the preliminary scattering of electrons by photons, and the transfer of plasma thermal radiation into the nuclear absorption band owing to the preliminary rescattering of photons by plasma electrons.

In the IEB process we observe a substantial increase in the width of the working interval of the plasma photon spectrum related to the fact that the radiation widths of atomic levels are greater than those of nuclear levels. In the case under consideration, the atomic shell serves as a transfer link (Fig. 4.1.3).

In the initial and final states of the IEB process, an electron occupies one of the shells of the ionized atom. The states of both discrete and continuous spectra serve as transient states. In the case under consideration, two substantially different scenarios can be realized. If the plasma temperature T is comparable to the energy ω_N of the nuclear transition, the nuclear excitation related to IEB predominantly proceeds via the discrete part of the spectrum owing to the ionization of the atomic levels whose energies allow the internal electron conversion. Normally, there exists a transient level with energy E_n for which either the matrix elements of the transitions from the initial state (*i*) to the transient state (*n*) and from the transient state to the final state (*f*) take large values or the energy of the atomic transition *n* *f* is close to the energy of the nuclear transition. Therefore, it is reasonable that the estimates employ the one-level approximation. It is possible that different electronic states serve as the initial and final states in the IEB process. However, the initial state can also be identical to the final state. In the first case, variation in the multipolarity of transitions is always possible. In the second case, such a variation is possible if the state is partly occupied. Thus, it is possible that the atomic absorption of *E*1 photons from plasma initiates a non-electric dipole nuclear transition.

The cross section of the nuclear excitation in the IEB process is given by

$$\sigma_{IEB}^{(3)}(\omega) = \frac{\lambda^2}{2} \delta(E_n - E_i - \omega) \Gamma_A^r(\omega, i \to n) P_{NEET}, \qquad (8)$$

where Γ_A^r is the radiation width of the atomic transition, ω is the plasma photon energy, $\lambda = 2\pi / \omega$, Γ_n is the width of the transient atomic state, and P_{NEET} is a probability of an nuclear excitation by electron transition

$$P_{NEET} \approx \frac{E_{int}^2 (L; \omega_N; n \to f, I \to F)}{\Delta^2}$$

where E_{int} is the energy of electron–nucleus interaction that leads to the electron transition from the transient to final state and nuclear excitation in the NEET process, $\Delta = E_n - E_f - \omega_N$ is the mismatch between the atomic and nuclear transitions shown in Fig. 4.1.3.

Assume that the plasma self-radiation has a continuous spectrum $n(\omega)$. The width of the spectral interval corresponding to the resonant transition in the atomic shell to the transient state in the vicinity of $\omega = \omega_{in} \equiv E_n - E_i$ is $\Gamma_A^r(\omega; i \to n)$. Therefore, the density of the resonant photons is $n(\omega)\Gamma_A^r(\omega; i \to n)$. The transition with nuclear excitation is nonresonant (we consider a typical case where the mismatch is $\Delta \gg \Gamma_n$).

The efficiency of the process is represented as

$$\zeta_{IEB}^{(3)} = \int d\omega \sigma_{IEB}^{(3)}(\omega) \tau n(\omega) \approx \frac{\lambda_{in}^2}{2} \Gamma_A^r(\omega_{in}) P_{NEET} n(\omega_{in}) \tau . \qquad (9)$$

Table 4.1.4 shows the results of calculations using formula (9) for a few of the aforementioned nuclei.
Table 4.1.4.

Nucleui	Multipolarity of Transition	Energy, keV	$\zeta_{IEB}^{(3)}$ at $T \approx \omega_N$
^{235}U	*E3*	0.0768	$\approx 10^{-19}$
^{229}Pa	*E1*	0.160	$\approx 10^{-12}$-10^{-13}
^{201}Hg	*M1*	1.561	$\approx 10^{-10}$
^{205}Pb	*E2*	2.329	$\approx 10^{-14}$
^{181}Ta	*E1*	6.24	10^{-13}-10^{-14}

The comparison of the results presented in Table 4.1.4 to the graphs illustrating the nuclear excitation in plasma in the presence of direct photoabsorption shows that, for the *E*1 and *M*1 transitions, the IEB mechanism exhibits relatively low excitation efficiency. However, for the *E*2 transition, the probability of excitation involving IEB is greater than the probability of direct photoabsorption. For the *E*3 transition, multipole exchange is effective (noncoincidence of the nuclear transition multipolarity with the multipolarity of the atomic transition from the initial to transient (normally, *E*1) state). It follows from the data for ^{235}U that the gain is very high. The result obtained is rather obvious. The reason for this is the small radiation width (0.9×10^{-39} eV) of the level ½$^+$ (76.8 eV) in ^{235}U. A similar scenario is realized for the decay of the level ½$^+$ (76.8 eV) via the electron bridge and owing to the direct photon emission by the nucleus. Here, the probability of the first-order process is also less than the probability of the third-order process involving the electron bridge by about 15 orders of magnitude.

It may seem strange that the processes of high orders with respect to *e* dominate over the processes of low orders. However, this is quite evident. In conventional electrodynamics, the hierarchy of cross sections corresponds to the orders of the Feynman diagram, in which all electronic states belong to the continuous spectrum. In the case under

consideration, at least one electronic state belongs to the discrete spectrum and appears to be localized within the atomic shell at sizes comparable to the Bohr radius a_B. Therefore, the integration with respect to the electron coordinate r is effective at sizes a_B. On the other hand, the multipole expansion of the propagator contains a Hankel function of the first kind $h_L^{(1)}(\omega r)$:

$$D_{\mu\nu}(\vec{r}-\vec{R}) = g_{\mu\nu}\exp(i\omega|\vec{r}-\vec{R}|)/|\vec{r}-\vec{R}| \approx \omega\sum_{LM}...h_L^{(1)}(\omega r)...j_L(\omega R),$$

Here, r and R are the electron and nuclear coordinates, respectively. If $\omega r \ll 1$, the Hankel function is approximated as $1/(\omega r)^{L+1}$. In the presence of the bound state, the working region is $r \leq a_B$. For transitions with low energies ($\omega a_B \ll 1$), the Hankel function not only compensates for the smallness introduced to the amplitude and cross section of the processes by the additional electron–photon vertex but makes the high-order process dominant.

Thus, only the interaction of photons with the bound electrons of an atomic shell (e.g., as in the IEB process) can lead to effective competition of the high-order (with respect to the electromagnetic interaction constant e) processes and the first- and second-order processes. Although the working parts of the spectra broaden and the nuclear excitation involves all plasma photons and electrons, the interaction with the plane wave part of the electron spectrum causes only a decrease in the effective excitation cross section. The fourth-order processes are an example which illustrates this fact. Taking into account the results of the above analysis, we conclude that there exists a single diagram describing the processes that basically differ from those already mentioned. Figure 4.1.4 shows the corresponding fourth-order diagram.

In this diagram, the initial electronic state at the upper line corresponds to the continuous spectrum, whereas the final states correspond to the continuous and discrete spectra, respectively. The electronic states at the second line belong to the discrete spectrum of the atomic shell.

The fourth-order (with respect to e) and inverse Auger processes in the nucleus and atomic shell allow for the ultimate extension of resonance fragments in the spectra of plasma electrons and photons related to nuclear excitation. Adding new electron–photon vertices to the diagrams under consideration is possible only in the plane-wave part of the electron spectrum. In full accordance with the conventional electrodynamics, this does not lead to an increase in the nuclear excitation efficiency. Therefore, there exist no effective mechanisms of an order greater than four with respect to e for the nuclear excitation in plasma to the first excited state. As a whole, the fourth-order processes cross sections of nuclei excitation in plasma are smaller systematically than the third-order cross sections.
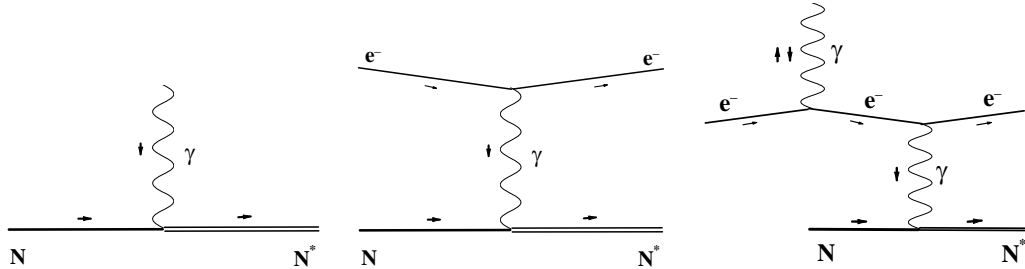

Fig. 4.1.1. Diagrams of main nucleus excitation processes by plasma's photons and electrons.
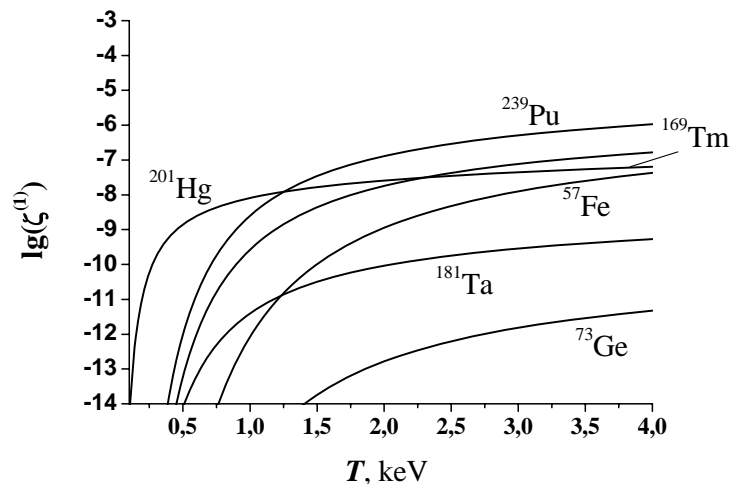

Fig. 4.1.2. Efficiency of the nuclear excitation by the equilibrium thermal radiation of plasma with a lifetime of 1ps.
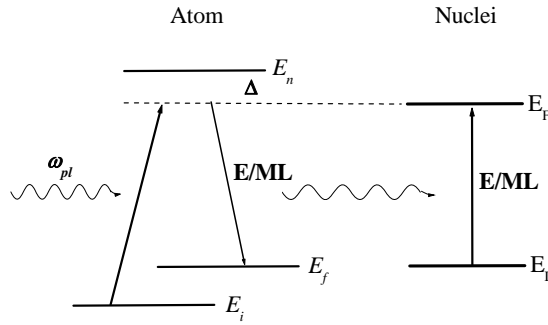
Fig. 4.1.3. Scheme of the nuclear excitation by photons via an atomic shell.
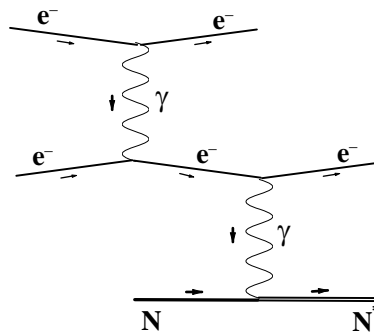
Fig. 4.1.4. Direct diagram of the fourth-order process describing nuclear excitation in plasma.

Induced decay of the isomer ^{178m2}Hf (16^+, 2.446 MeV, 31 y) has a great scientific and public interest. A substance with stored energy and a physical process that ensures the rapid liberation of this energy are two components of any explosive device. In the case of Hf-178m2 the energy is stored in a metastable state and amounts to 2.446 Mev per nucleus, or 1.3 GJ per gram of substance. One can controls the decay rate of the Hf-178m2 isomers using external x-rays. Very promising results were obtained by some scientific teams in experiments on induced decay of Hf-178m2. That is why we investigated all possible processes for induced decay of Hf-178m2 and methods of the isomer accumulation.

The experimental conditions on induced decay of Hf-178m2 allow one to conclude that the process under consideration is purely electromagnetic in nature. No pronounced strong-field effects play any role, because the pump radiation is non-coherent, and has a too low intensity. This leaves only two mechanisms for the induced decay. The first one is the direct interaction of the incident x-rays with the nucleus leading to isomer decay via an intermediate state. The second is the interaction of the incident x-rays with the atomic shell which, in turn, transfers the excitation to the nucleus. An essentially different scenario is also possible. In case of "normal" spontaneous decay the nuclear transitions from the isomeric state occur directly to the lower levels. We considered all these three processes in frame of the QED.

We designed a special model to obtain some estimations on cross sections of the induced decay processes. We introduced a certain additional level into the ^{178}Hf excitation spectrum and suppose that this level has a number of unusual properties. 1. We "forget" about the K forbiddenness, and assume that for unknown reasons the intermediate level is connected both with the isomer state and all other levels of the rotational bands via K-allowed transitions. 2. We suppose that the intermediate nuclear level has spin 15^-, so that an $E1$ transition between this level and the 16^+(2.446 MeV) isomer is possible. 3. We also suppose that the nuclear matrix element of the above-mentioned $E1$ transition has the maximum value possible for the ^{178}Hf nucleus, that is, it equals the matrix element of the collective transition to the giant dipole resonance (GDR) state. 4. We made a similar assumption for all the transitions from the intermediate state to the lower-lying levels. That reduces the probability of the nucleus returning to the isomer level. Thus these assumptions provide conditions for the maximum population of the states that correspond to the transitions with increased intensity observed in experiments. 5. We assume that there is a level in the spectrum of ^{178}Hf below the intermediate 15^- "mixed K" state, such that the partial width of transition to this

level almost exhausts the total width of the intermediate state $G^{tot}_{\text{"mixed }K\text{"}}$. 6. We assume else the transition between the intermediate and the isomer levels should have the energy w_N equal to the atomic transition energy w_A within the vacancy width $G_{L_I}+G_{M_{II}}\sim 10$ eV.

Our calculation gives the following estimations on the induced decay cross section in the frame of this extremely tolerant model. In the case of direct interaction between x-rays and the nucleus the considerations lead to the following upper limit for the integral cross section within the assumptions no 1–4: $\sigma < 10^{-27}$ keV cm^2, and $\sigma < 10^{-23}$ keV cm^2 within the assumptions no 1–5. That is still less than the value $\sim 10^{-21}$ cm^2 keV measured in experiments. In the case of decay due to the photon interaction with the atomic shell one obtains 10^{-25} cm^2 and 10^{-23} cm^2 within the assumptions no 1–6 with and without assumption 6 correspondingly.

We verify the hypothesis that the lifetime decrease of the isomer 16^+(2.446 MeV, 31 yr) is due to the probability increase of the $E3$ transition with energy 12.7 keV to the level13$^-$(2.433 MeV). This nuclear transition is the principal channel for the isomer decay in normal conditions. Such acceleration could be due to the interaction with the atomic shell via an inverse NEET process. We obtain the upper limit of the process probability - 10^{-22}. This result absolutely excludes the possibility of explaining the experimental data with the enhancement of the $E3$ nuclear transition 16^+(2.446 MeV, 31 yr)®13$^-$(2.433 MeV) due to the interaction with the atomic shell. No assumptions about the properties of the nuclear transition (similar to the assumptions no 1–6) can be used here. The intensity of the transition is measured and leaves no room for speculation.

A new 2.457 MeV gamma line was detected in the experiment with a beam of synchrotron radiation with the photon energies 9567 eV. We estimated that the multipolarity of this transition is E15. In this case it will take 10^{50} years of continuous irradiation of the target with about 10^{13} Hf-178m2 isomers in an experiment for at least one transition to occur from the intermediate state to the ground state of the nucleus accompanied by emission of an E15(2.457 MeV) photon.

The production of several grams or more of the isomer Hf-178m2 is an extremely difficult and expensive task. No effective process for such production has been described in the literature. Then cross sections of some of the processes are known. For instance, for the reaction ^{176}Yb(α,2n)^{178m2}Hf the cross section is s~ 7r10^{-27} cm^2 at E_a=36 MeV. In the event of spallation of W-186 by 650 MeV protons the Hf-178m2 production cross section is ~ 5r10^{-28} cm^2, while in the fragmentation of the target containing a natural mixture of isotopes of Ta, s~ 3r10^{-28} cm^2. Despite of relatively large cross sections, commercial production of Hf-178m2 isomers, e.g. several grams per annum, cannot be achieved by these methods, because there are no devices capable of generating a current of protons or alpha particles sufficiently high for operating with large amounts of the initial material. Very large targets can be irradiated in fusion reactors of the future. The cross section of the process ^{179}Hf(n,2n)^{178m2}Hf is $7*10^{-27}$ cm^2 for neutrons with energies 14-15 MeV. If such reactors are built and if a fraction of neutrons produced in the d+t reaction is used to irradiate Hf-179, one can hope that macroscopic amounts of Hf-178m2 will be produced. However, no energy can be liberated from isomers Hf-178m2, because the x-ray induced decay cross section is too small.

The process of Nuclear Excitation by Electron Transition (NEET) is a process of nonradiative nuclear excitation by means of direct energy transfer from the excited atomic shell to the nucleus via a virtual photon. This process is possible, if within the atomic shell there exists an electronic transition close in energy and coinciding in type with the nuclear one. The modern theory of NEET agrees reasonably with experimental results obtained in last years in USA and Japan for nuclei ^{197}Au, ^{193}Ir, and ^{189}Os in the experiments at synchrotron radiation (SR) beams if the photons energy exceeded the K-shell electron binding energy appreciably. We consider here a model of the NEET process near the K-shell ionization threshold of atom.

The process of the nuclear excitation as a result of ionization of the atomic K-shell is described by diagram showed in Fig. 4.1.5. One electron passes from the K-shell to continuum. We consider the case of nuclear excitation by the atomic $M_I\rightarrow K$ transition.

Corresponding cross sections calculated for nuclei ^{197}Au, ^{193}Ir, and ^{189}Os are in Fig.3. The following values of the energies and the widths were used for the cross section calculation at the nucleus ^{197}Au:: $E_K = -80.725$ keV, $E_{MI} = -3.425$ keV, $\Gamma_K = 52$ eV, $\Gamma_{MI} = 14.3$ eV. We use $\omega_N = 77.351$ keV for the nuclear transition energy. The ^{197}Au nucleus is unique because the difference between the energies of the atomic transition and the nuclear transition is 50 eV only, i.e. this difference is commensurable with the atomic widths in K and M_I shells of Au. There are two kinds of lines in Fig. 4.1.6. The solid lines correspond to the excitation by a monochromatic beam. The dashed lines correspond to real SR-beam by Gaussian form with the width 3 eV. It is clear evident in Fig. 4.1.6 that the nucleus excitation begins when the incident photon energy is tuned above threshold by 50 eV approximately. The effective width of the process (the function $d\sigma_N/d\omega_{SR}$ (FWHM)) is closed to the Γ_{MI} width of Au for the monochromatic beam, and it equals 20 eV for the real SR beam. These results are in a reasonable agreement with experimental data obtained in Japan last years. We predict very close dependence for the cross section of the NEET process in ^{193}Ir.
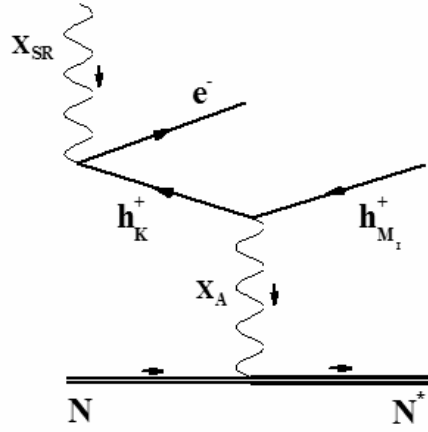
Fig. 4.1.5. NEET process near K-edge.
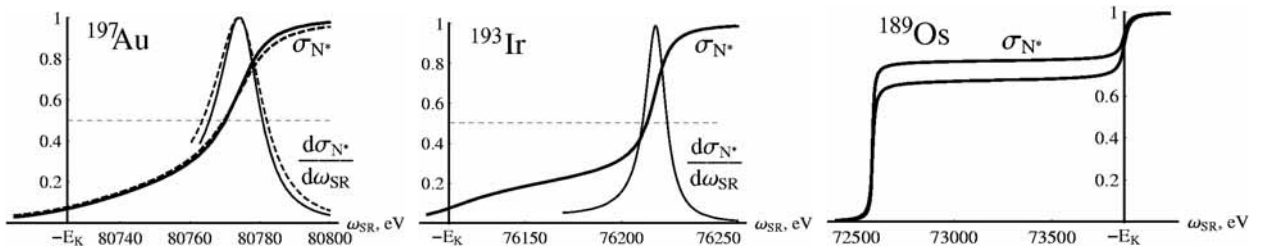
Fig. 4.1.6. Cross sections of NEET process for some nuclei as a function of the SR photon energies.

In ^{189}Os the atomic transition energy $\omega_A = E_{MI} - E_K$ = 70.822 keV exceeds the energy of the nuclear transition ω_N = 69.535 keV in contrast to ^{197}Au and ^{193}Ir. Furthermore, the difference $\omega_A - \omega_N$ = 1287 eV exceed considerably the atomic widths values Γ_K = 42.6 eV, Γ_{MI} = 20.4 eV. The nuclear excitation cross section is shown in Fig.3. We see that the excitation of the nucleus begins when the incident photon energy is tuned below the K-shell ionization threshold: ω_{SR} = $-E_K$ - 1.287 keV. The lower line in Fig.3 corresponds to the width Γ_{MI} = 20.4 eV, the upper line corresponds to the width Γ_{MI} = 12.8 eV. The value of σ_N averages 0.7-0.8 (in the units of the maximal value σ_N far from the K-edge) in the range $-E_K$ - $\omega_A - \omega_N < \omega_{SR} < -E_K$. That means the SR photons excite the nucleus effectively below the ionization threshold.

Subthreshold excitation is a quantum effect. The K-shell vacancy has a sizeable width. As a consequence, incident photons with energy tuned below the binding energy $-E_K$ can ionize the K-shell. In this case the energy of the emitted photon in the electron $M_I \rightarrow K$ transition satisfies the condition $\omega_{X_A} \leq E_{M_I} - E_K$ (see in Fig. 4.1.5). On the other hand the energy of the nuclear transition satisfies the analogous condition $\omega_N \leq \omega_A = E_{M_I} - E_K$. That is why the nuclear subthreshold excitation is possible. This very effect we see in Fig. 4.1.6 for ^{189}Os. The K-shell hole is an intermediate state in such a process. Therefore the parameters of this state are not included to the energy conservation law $1/((\omega_{SR} - E_e + E_{M_I} - \omega_N)^2 + \Gamma_{M_I}^2 / 4)$, which is an analogue of the usual delta-function $\delta(\omega_{SR} - E_e + E_{M_I} - \omega_N)$ connected the initial and the final states in Fig. 4.1.5. Thus we have now the theory for description of the process of nuclear excitation by electron transition in a wide range of the energies of incident beam.

Investigation of the decay channels for the 3/2+(3.5±1.0 eV) isomeric level of Th-229m in a condensed medium was found very hard matter. The stage of optical measurements from 1997 to 1999 showed how complicated it is to observe an isomeric transition. The experiments were relatively similar. In the alpha decay of the 233-U nucleus, the low-lying level 3/2+(3.5±1.0 eV) in 229-Th becomes populated with a probability of about 2%. With a sample containing 100 mg of 233-U, one can expect about 7×10E5 isomeric decays of the 3/2+(3.5±1.0 eV) state of 229-Th to occur every second. Such an activity is sufficient for optical measurements to produce results.

In all the experimental work that we have just mentioned, the researchers dealt not with atomic thorium but with one of its chemical compounds. In due course it became clear that all, or almost all, of the detected optical radiation could be attributed with a high degree of probability to the luminescence of various chemical compounds, initiated by the bombardment of alpha particles. Therefore, it is advisable to examine the decay of the low-lying isomeric state in matter more thoroughly.

Decay in metal.

Let us examine an experiment in which a thin layer of an active substance containing one of the chemical compounds with 233U is deposited on a substrate. Upon alpha decay of 233-U, the daughter 229-Th nuclei, among which, the reader will recall, 2% are in the isomeric state 3/2+(3.5±1.0 eV), may be ejected into the vacuum and decay on the walls of the chamber (usually outside the field of vision of the optical system); they could also slow down and decay in the substrate or in the material of the target proper. The last two cases are the most interesting ones.

If the target layer is thin enough, for instance, it comes out to 30 ± 40 A, most of the thorium atoms are slowed down in the substrate material, for which noble metals such as gold and platinum are usually used. Upon alpha decay of 233-U, the recoil nucleus 299-Th acquires an energy of about 100 keV. The range of such nuclei in metals amounts to several dozen atomic layers (about 200 A). A metal of such a thickness is practically transparent to visible light and is not an obstacle for detecting the photons generated in the decay of the low-lying isomer 229m-Th. At the same time, there is another possible decay channel in a metal, a channel corresponding to the second-order diagram with the photon propagator – de-excitation of the isomer via conduction electrons. This process is similar to inelastic electron scattering by nuclei. The process has no energy threshold in the metal, since the nucleus gives off energy in this case. (Isomer decay in the metal can also be interpreted as conduction electron conversion. But in contrast to conventional internal inversion, here the initial state of the electron is not a bound atomic state.)

To make a qualitative estimate of the decay probability of 229m-Th (3/2+, 3.5±1.0 eV) in what is known as a standard metal, we use the simplest free-electron approximation (in this model, the conduction electrons are interpreted as a gas of free particles). The calculated decay probability is 10E4 1/s, i.e., the lifetime of the thorium isomer in the metal is roughly 10E-4 s. This probability is much higher than the estimate of 0.1 - 10 s for the decay probability of the low-lying level of the 229-Th nucleus through the electron-bridge channel. Hence, the conversion involving conduction electrons may indeed be the dominating decay channel of the 3/2+(3.5±1.0 eV) state in the metal. It is interesting to note that if for the substrate we use a felicitously selected semimetal in which the conduction electron number density is lower by two to three orders of magnitude than that in platinum, the probability of emission of optical photons becomes appreciable.

Decay of recoil nuclei in the semiconductor $^{233}UO_2$.

Especially interesting is the problem of decaying the low-lying isomer ^{229m}Th that forms as a result of alpha decay of 233-U in the material of the target proper, i.e., in the semiconductor $^{233}UO_2$. Such a situation emerges for a large number of recoil 229-Th nuclei if the target thickness exceeds the free path of the recoil nuclei. The semiconductor $^{233}UO_2$ has an energy gap width of 2.8 eV. As a result of alpha decay of 233-U, an excited 229-Th nucleus may at the end of its range occupy an interstitial position in the lattice or take the place of one of the uranium atoms, knocking it out of its position in the crystal. In the latter case, the uranium atom finds itself in an interstitial position.

In all these variants, the initial band structure of the semiconductor $^{233}UO_2$ undergoes a perturbation. As a result, additional levels appear in the forbidden band, and these levels may play an important role in the decay of the thorium isomer. The nuclear transition energy is sufficiently high for an electron to be moved from the valence band to the conduction band. Next, the new levels participate either in radiationless relaxation of energy (into phonons) or in emission of radiation in the IR range. It is quite possible that there is no emission of radiation in the visible range, accompanying the decay of the thorium isomer in the semiconducting crystal $^{233}UO_2$.

Decay in the insulator $^{229}ThO_2$.

Thorium dioxide is a common, well-studied chemical compound. It is an insulator with an energy gap width of 6 eV and a refractive index n = 2 for 3.1-eV photons.

Conversion of the nuclear transition that would involve electrons from the valence band is mpossible: there is simply not enough energy to move an electron to the conduction band. In principle, an electron-bridge process is possible here. However, the forbidden band of an ideal insulator (such an insulator is considered here) contains no electronic states. Hence, in the decay of the low-lying nuclear isomeric state through the electron-bridge channel in $^{229}ThO_2$, states of the continuous spectrum from the conduction band act as intermediate states. The mismatch between the energies of the nuclear and electronic transitions in this case exceeds 1 eV. Moreover, there can be only an elastic electron bridge. The probability of occurrence of such an electron bridge is negligible.

As a result, the main decay channel for the low-lying level 3/2+(3.5±1.0 эB) in $^{229}ThO_2$ may be the direct nuclear emission in the optical range, i.e., "nuclear light". The decay probability of an isolated nucleus in a vacuum can be calculated easily. Without allowance for the effect of the medium, one finds $T_{1/2}$ = 80 min - 8 h in the energy range 4.5-2.5 eV.

Let us to account for the effect of the dielectric medium. The entire difference between the probabilities of magnetic dipole transitions in the medium and in the vacuum is determined by the renormalization of the phase volume. Thus, in the medium the probability of an M1 radiative transition increases n^3-fold. Accordingly, the most probable lifetime of the 3/2+(3.5±1.0 eV) state in $^{229}ThO_2$ is within the 10 min – 1 h range. (We must make a reservation here that this estimate has been given on the assumption that n = 2 not only at ω = 3.1 eV, but also in the entire energy range from 2.5 to 4.5 eV. The numerical result can be corrected somewhat depending on the real value of n.)

The "nuclear light", or the optical emission of the nuclei is absolutely nontrivial and untypical phenomenon for the nuclear spectroscopy. In this sense, the result predicted here has tremendous value for the science. No doubts that this phenomenon will be find if the 3/2+(3.5±1.0 eV) state really exists in the ^{229}Th nuclei.

4.2. Transient isomer excitation in plasma
4.3 Plasma modeling

Numerical calculation of dependencies of hot electron temperature and bremsstrahlung x-ray yield on laser pulse intensity was carried out. For that we used the code, describing femtosecond laser plasma dynamics. To simulate such dependencies we added new module, which calculate temperature of hot electrons and spectral density of bremsstrahlung x-ray radiation. This module simulates temperature of hot electrons in each spatially-temporal cell by means of empirical formula. The formula was introduced so that the final dependence of hot electron temperature on laser pulse intensity corresponds to experimental results. Then we calculated spectral density of x-ray radiation in each cell. We assume that electrons are Maxwellian and interact only with atoms in cell. The final result for spectral density of x-ray radiation we obtained from summation of each cell results. Thus, we obtained numerical dependencies of hard x-ray yield in different spectral bands on laser pulse intensity. The results are qualitative agreed with experiment. So, we obtained for plasma formed at crystalline silicon target under action of laser pulse with time duration 200fs, wave length 616nm and intensity from 10^{16}W/cm^2 to $5 \cdot 10^{16}$W/cm^2 the next dependencies from simulation: $\gamma(E_{x-ray}>2,5\text{keV}) \sim I^{2,3}$, $\gamma(E_{x-ray}>8,7\text{keV}) \sim I^{3,3}$, $\gamma(E_{x-ray}>13,1\text{keV}) \sim I^{3,6}$, and from experiment: $\gamma(E_{x-ray}>2,5\text{keV}) \sim I^{1,7\pm0,1}$, $\gamma(E_{x-ray}>8,7\text{keV}) \sim I^{3,3\pm0,1}$, $\gamma(E_{x-ray}>13,1\text{keV}) \sim I^{4,7\pm0,3}$.

It is known, that processes of excitation of low-energy nuclear states by solid state plasma radiation are very likely. The excited states have two ways of decay. The first way is γ-decay, the second is internal electronic conversion (IEC). In the second case the energy of a nucleus is transferred to the electron of the same ion. The basic problem of registration of the excited nuclear states is radiation of plasma. However, it is possible to eliminate IEC-decay. The IEC-decay is much more effective then γ-decay, it will result in essential prolongation of life time of the excited nuclear states. The IEC-decay is forbidden in strongly ionized plasma when the ionization potential is more than energy of the excited nuclear state.

We made the numerical model which simultaneous solving of the equations of hydrodynamics and the equations describing ionization and recombination. The model describes plasma evolution up to several microseconds. Plasma is represented in one-liquid two-temperature approaching. In the given approximation plasma consists of two component: electronic and ionic. The effects of heat conductivity in electronic and ionic components are taken into account. We have neglected plasma oscillations. Dynamics of plasma depends on pressure of plasma and its viscosity in this approximation. To describe the ionization state we use average charge approaching. We take into account electron impact ionization, three body recombination and electron impact excitation and de-excitation. The special attention is given influence of cascade processes on velocities of ionization and recombination. The ionization from excited states and recombination to these states is taken into account. We show that cascade processes increase by some orders velocity of ionization and recombination.

Quasi 3-dimensional model for the calculation of the expansion into vacuum and background gas and recombination of hot dense plasma, created by femtosecond laser pulse with intensity of $10^{15} \div 10^{16}$ W/cm^2. The initial parameters are as follows: temperature, higher than 100 eV; ion density, higher than 10^{22}cm^{-3}; and ionization multiplicity greater than 10. The numerical model for the evolution of dense hot plasma presented in this work makes it possible to calculate the charge, energy, and time-of-flight spectra of ions at time intervals of up to $10\,\mu s$, which correspond to the characteristic times of the experimental measurements of such spectra. For an adequate description of the evolution of a plasma generated by a femtosecond laser pulse at the surface of a solid target, we need to calculate transient ionization and recombination in this plasma, taking into account bound–bound transitions. In dense plasma with $N_i > 10^{22}$cm^{-3}, we need to take into account a small number of levels (one to five excited states). In plasma with a lower density, the analysis employs a larger number of levels. The primary effect in plasma-gas interaction is recharging.

Plasma generated by a femtosecond laser pulse does not exhibit expansion during the laser pulse. This fact makes it possible to study the plasma evolution in two stages. At the first stage, the interaction of radiation with matter takes place. This interaction is accompanied by the propagation of heat, shock, and ionization waves. At the second stage, the laser-induced plasma expands into vacuum. In this work, we consider a model describing the second stage of the plasma evolution. Thus, we consider hot, strongly ionized laser-induced plasma in two cases: a thin film and plasma at a substrate.

To simulate the plasma expansion, we employ a plane one-dimensional one-liquid two-temperature approximation, in which the plasma motion is described via the motion of ions (the plasma is electrically neutral) at an electron temperature that differs from the ion temperature. In the model, we take into account the following processes: heat conduction inside the plasma (in electron and ion subsystems), viscous friction upon the plasma expansion, heat exchange between the electron and ion components of the plasma, and nonstationary ionization and recombination in the equilibrium plasma.

To describe the variation in the charge state of the plasma, we employ the mean charge approximation with allowances for such processes as the impact ionization from the ground and excited states, the three-particle recombination into the excited and ground states, and the bound-bound electronic transitions in plasma ions. These processes govern the dense plasma kinetics. The model under consideration does not take into account the quantum structure of individual levels in ions, which allows for its application in calculations of the plasma parameters for various chemical elements.

Note that, in hot nonequilibrium plasma, a relatively high population of the excited states affects the ionization rate. A similar statement is valid for the three-particle recombination. The probability of recombination into one of the excited states is significantly higher than the probability of electron capture in the ground state. Therefore, to adequately describe the ionization and recombination processes, we need to take into account such cascade processes as the excitation of the ion followed by ionization and the inverse process of recombination into the excited state followed by relaxation to the ground state.

Thus, to calculate the ionization and recombination rates, it is most important to take into account the bound-bound electronic transitions in the plasma ions. In this approximation, the equation for the variation in the concentration of ions with charge z ($0 < z < Zn$) is represented as

$$\frac{dN_z}{dt} = \sum_n (\kappa_\bigoplus^n(z, T)N_e^2 N_{z+1} - \kappa_i^n(z, T)N_e N_z), \quad (1)$$

where k'' (z, T) is the rate of ionization from the excited state n and $k^\wedge$ (z, T) is the rate of the three-particle recombination to this state. We interpret the excited state as a set of electronic levels in an ion with the same principle quantum number n. Equation (1) is written with allowances for the fact that the rate of transitions between the excited levels in a strongly ionized plasma is substantially higher than the ionization and recombination rates. In this case,the population N_z of the levels in an ion with the charge z is calculated using the Saha-Boltzmann distribution. Ionization and recombination provide a certain perturbation in this distribution. To find the total (effective) ionization rate, we need to sum the rates of ionization from all excited levels of the ion.

To describe the impact ionization, we employ the Seaton formula

$$\kappa_i^n = 4.3 \times 10^{-8} \left(\frac{Ry}{E_z^n}\right)^{3/2} \beta^{-1/2} e^{-\beta} \text{ cm}^3/\text{s},$$
$$\beta = \frac{E_z^n}{T}, \quad (2)$$

where E_z is the ion ionization energy and E_{znn} is the number of excited states.

The principle of detailed equilibrium yields a relationship between the rates of impact ionization and three-particle recombination. Let $/''$ be the concentration of the ionization events from the excited state n for an ion with charge z, and let R_z be the concentration of the three-particle recombination events for this state. Then

$$I_z^n = \kappa_i^n(z, T)N_e N_z^n, \quad (3)$$

where N_z is the concentration of ions with charge N_{znz} in the excited state n and

$$R_z^n = \kappa_\bigoplus^n(z, T)N_e^2 N_{z+1}, \quad (4)$$

where N_{z+1} is the total concentration of ions with charge z + 1 $\left(N_{z+1} = \sum_n N_{z+1}^n\right)$.

For the steady-state plasma, we have $I_z^n = R_z^n$ and,

$$\kappa_\bigoplus^n(z, T) = \kappa_i^n(z, T)\frac{N_z^n}{N_{z+1}N_e}.$$

We calculate the ratio $\dfrac{N_z^n}{N_{z+1}N_e}$ from the Saha-Boltzmann distribution for the equilibrium plasma with a temperature T and an ion concentration $N_i = \sum_z N_z$.

In this work, we consider the plasma expansion in vacuum at time intervals of up to 10 μs. At such a time interval, the ion concentration in the plasma decreases from 1022 to 1014 cm–3. In accordance with the results from [9], the estimates of the recombination rates show that, if the ionization state slightly differs from the steady state, the rates of dielectronic recombination and photorecombination are less than the rate of the three-particle recombination at concentrations higher than 10^{16} cm^{-3}. In addition, in calculations of the electron concentrations at the excited levels, we can neglect the photodecay rate of the excited states, since it is much less than the rate of excitation and excitation quenching upon electron impact.

The below representation of the equations of the model proposed is suitable for numerical integration. We integrate the equations in terms of the Lagrangian mass coordinates. In a plane case, the mass variable is introduced in the following way:

$$z = \int_{x_0}^{x} \rho\, dx,$$

where x0 is the boundary of the medium under consideration and x is the actual coordinate.

In terms of the mass coordinates, the gas-dynamic equation and the variation in the ionization composition are represented as

$$\rho = \frac{\partial z}{\partial x},$$

$$\frac{\partial x}{\partial t} = u,$$

$$\frac{\partial u}{\partial t} = -\frac{\partial}{\partial z}(p_e + p_i - \sigma),$$

$$\frac{\partial \varepsilon_e}{\partial t} = -p_e\frac{\partial u}{\partial z} - \frac{\partial W_e}{\partial z} - \frac{Q_{ei}}{\rho}, \qquad (7)$$

$$\frac{\partial \varepsilon_i}{\partial t} = -p_i\frac{\partial u}{\partial z} - \frac{\partial W_i}{\partial z} + \frac{Q_{ei}}{\rho},$$

$$N_e = z N_i,$$

$$\frac{\partial z}{\partial t} = \kappa_i N_e - \kappa_{th} N_e^2.$$

Here, x is the coordinate, u is the hydrodynamic velocity, and pe and pi are the pressures in the electron and ion subsystems, respectively. The viscosity σ is given by $\sigma = \frac{4}{3}\eta\frac{\partial u}{\partial x} = \frac{4}{3}\rho\eta\frac{\partial u}{\partial z}$, and $W_{e,i} = -k\frac{\partial T_{e,i}}{\partial x} = -k\rho\frac{\partial T_{e,i}}{\partial z}$ is the heat flow caused by heat conduction. In the model proposed, we employ the ballistic thermal conductivity (the Spitzer thermal conductivity limited by the velocity of particles in the medium). In addition, $\varepsilon_e = \frac{3}{2}\frac{k_B z T_e}{m_i}$ and $\varepsilon_i = \frac{3}{2}\frac{k_B T_i}{m_i}$ are the specific internal energies of the electron and ion subsystems, respectively; Qei describes the heat exchange between the electron and ion subsystems; κi and κth are the total rates of the impact ionization and the three-particle recombination, respectively; kB is the Boltzmann constant; z is the mean charge; Ne and Ni are the concentrations of electrons and ions, respectively; Te and Ti are the temperatures of electrons and ions, respectively; and mi is the ion mass.

We carried out the numerical investigation of Si and Hg plasma formed by laser pulse. The initial conditions of numerical simulation were: plasma density, average charge and temperature. The plasma formed by femtosecond laser pulse is not able to spread during a pulse. It is possible to assume, that energy is transferred to plasma instantly. During a pulse the thermal wave propagates on 10^{-5} sm. As the developed model does not consider interaction radiation with solid surface, the conditions describe already created plasma of solid-state concentration. The electronic temperature was set in a range $200 \div 1000\text{eV}$. An average charge for plasma Si is equal to 10, for mercury $z = 35$. Results of work for silicon plasma were compared with experimental data.

Comparison of the data received at numerical integration with experiment has shown, that the model adequately describes plasma spreading. For the exact description of change of ionization state it is necessary to take into account cascade processes through 5 excited electronic conditions of an ion.

The developed model allows us to calculate of initial parameters of plasma by measurements made through several microseconds.

The given model was applied for plasma of mercury (see fig. 1). It is shown, that at strong initial ionization and high initial temperature ($T_e = 1\text{keV}$) the charge at the front ablated plasma is frozen on values from 17 up to 43 (directly at the front) on times of the order $10\mu s$. The necessary charge for elimination of IEC is $z = 21 \div 43$. At $z > 21$ the efficiency of decay on this way starts to reduce, and at $z = 43$ it is switched off completely. Prolongation of life excited states is possible. So it is possible to register of photons, irradiated by nucleus after peak of plasma radiation.

The above described model was extensively used for experimental data treatment (see previous section).
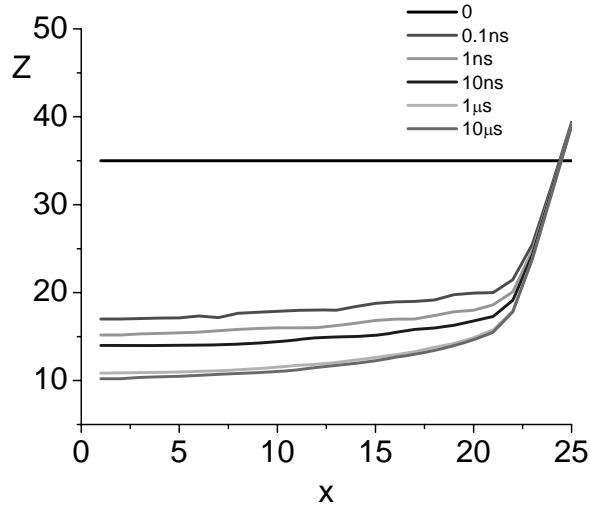
Fig. 4.3.1 Ionization degree of mercury plasma at initial point of time and at 0.1ns, 1ns,10ns, 1us, 10us.

4.4. Low energy nuclear excitation by line plasma emission

The possibility of excitation of low-energy nuclear states by quasi-resonant X-ray line emission of femtosecond laser produced plasmas was investigated. The expression for process efficiency was obtained. It is suggested to "tune" the energy of X-ray line quanta to sharp resonance with energy of nuclear transition by controlling of laser plasma ionization state. Based on the fact that plasma ionization state is determined primarily by the thermal electronic component, while the ionic X-ray line emission with an energy higher than 1 keV is induced by the hot electronic component, we suggest the nuclear excitation scheme with two ultrashort laser pulses, taking $^{201}Hg_{80}$ nucleus (E^*=1561 eV) and quasi-resonant Kα radiation of aluminum ion Al^{+9} ($E_{K\alpha}$=1561 eV) as an example (Fig. 4.4.1). The first pulse produces laser plasma that contains the maximal, in time and space, number of ions with the desired charge, while the second pulse produces hot electrons that are necessary for generating X-ray lines at the moment the fraction of ions with a certain charge reaches its maximum value in plasma.

In order to determine conditions, under which the maximal fraction of ions with a certain charge exists in the plasma, we have created and realized the original model of calculation of laser plasma ionization state which takes into account the transitions between excited states of ions and the presence of hot electrons in plasma. The main peculiarity of our model is based on how we determine the average excited state of the ions in plasma by performing calculations of the kinetics of excitation for just one ion with definite charge. As a result of computer modeling it was determined that steady state population of excited states of ions in solid-state plasma could be reached on times comparable with duration of femtosecond laser pulses. Besides the steady state value of "temperature" of distribution is determined by both the concentration and temperature of plasma thermal electrons. It is shown that presence of hot electrons in laser produced plasma with fraction less than 1% (I~10^{16}-10^{17} W/cm²) has no influence on plasma charge state, but can increase the fraction of highly-excited ions.

We have realized the computational model of X-ray line generation due to inner-shell ionization of atoms and ions by hot electrons in solid-state femtosecond laser produced plasmas. It is obtained that maximal yield of K- and L-line X-ray emission could be reached using targets with thickness d~(0.7-1.1)d_{ph}, where d_{ph} is the absorption length of corresponding X-ray quanta with energy $E_{S\chi}$ in material of target. Besides the temperature of hot electrons $T_{h,opt}$ on the surface of the target must be equal to $T_{h,opt}$~5$E_{S\chi}$ for most intense lines of K-series, and $T_{h,opt}$~(3-4)$E_{S\chi}$ for lines of L-series. In this case the conversion of laser pulse energy into energy of X-ray line emission is estimated to be of the order of $\varepsilon_{S\chi,opt}$ ~10^{-5}-10^{-4} for most intense lines of K- and L-series.

According to the presented scheme of nuclear excitation by quasi-resonant X-ray line emission we estimated the efficiency of excitation of $^{201}Hg_{80}$ nucleus (E^*=1561 eV) by Kα radiation of aluminum ion Al^{+9} ($E_{K\alpha}$=1561 eV) under optimal conditions. In this case the first laser shot with intensity ~10^{15}-10^{16} W/cm² produces the plasma on the surface of solid-state aluminum target with temperature of thermal electrons T_e ~ 90 eV and fraction of Al^{+8} ions ~25%. Then the second laser shot with intensity ~10^{16}-10^{17} W/cm² generates in aluminum plasma the hot electrons with temperature $T_{h,opt}$ ~ 10 keV, which ionize the K-shell of Al^{+8} ions and lead to effective emission of Kα radiation of Al^{+9} ions. It is shown that maximal number of excited nuclei is of the order of ~10^2-10^3 per laser shot with energy ~1 J. This value is several orders higher than yield of excited nuclei in conditions of pumping by Kα radiation of neutral aluminum atoms.
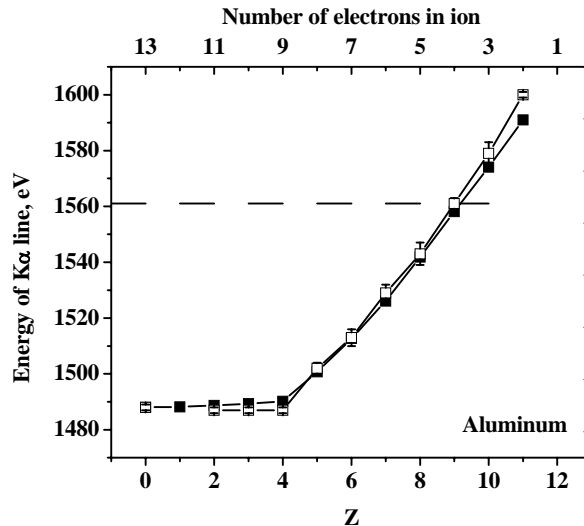
Fig. 4.4.1. Dependence of the aluminum ion Kα quanta energy on ion charge. The dashed line indicates the $^{201}Hg_{80}$ transition energy (1561 eV).

CONCLUSIONS

Laser system design, upgrade and tests:

- Ti:Sa laser system launched into operation during the project has the following parameters: wavelength 805 nm with spectrum bandwidth of 30 nm; pulse duration down to 40 fs with lowest wings at 70 fs; repetition rate 10 Hz, energy per pulse up to 40 mJ with vacuum compressor and 3 mJ with air one; beam quality $M^2\sim1.8$; focused intensity up to 10^{18} W/cm². Contrast of this system at 10 ns is determined by leakage of radiation from regenerative amplifier and was measured as 500.

- Cr:F laser system launched into operation during the project has the following parameters: wavelength 1250 nm; pulse duration 115 fs; repetition rate 10 Hz, energy per pulse up to 0.5 mJ; beam quality $M^2\sim1.3$; focused intensity up to 10^{16} W/cm². Contrast of this system at 1 ps is determined by compressor alignment and was measured as 10^5.

- Raman laser system launched into operation during the project has the following parameters: wavelength 630 nm; pulse duration 10 ps; repetition rate 5 Hz, energy per pulse up to 8 mJ.

Plasma characterization X-rays characterization methods and results:

- The possibility of usage of silicon avalanche photodiodes (APD) (Advanced Photonix, USA) with thickness of sensitive layer ~80 μm as detectors of X-ray and gamma-radiation and for estimations of average energy of hot electrons of laser produced plasma was investigated. The calibration experiments have shown that APDs have efficiency above 50% in the range of photon energy from 2 to 15 keV, energy resolution ~20%, and signal/noise ratio ~10. The obtained parameters are several times better then characteristics of detectors based on photo-multiplying tube (FEU-119) with scintillator NaI(Tl).

- The new x-ray detectors based on photodiode Hamamatsu S8559 and charge amplifier РШ2731Э were tested in real experiment with femtosecond laser plasma. Good correlation between values measured by different detectors is observed. The accuracy of method of multiple absorption foils for determination of the average energy of hot electrons in laser-produced plasma is investigated. The method of estimation of the average energy of hot electrons in every laser shot with accuracy ~25-30% is developed for wide range of laser pulse intensities and X-ray detectors (APD or PMT+scintillator) with different spectral sensitivities. It is shown that accuracy of estimations of the average energy of hot electrons is determined by accuracy of X-ray yield measurements by detectors in the case when low-energy boundaries of transmission of foils used in experiment have difference higher then average energy of hot electrons of plasma.

- In numerous experiments it was shown that Cr:F laser system can be efficiently used in experiments on production of hot dense laser plasma suitable for low energy nuclear level excitation. For example mean hot electron temperature for BaF_2-target at the laser radiation intensity $I=(2\pm0.2)\cdot10^{16}$ W/cm² was $T_e^{hot}=(7\pm1)$ keV using Cr:F laser system. Experiments with Ti:Sa laser system showed that hot electron temperatures as high as 15-20 keV can be easily achieved in plasma.

Ionic plasma diagnostics

- In a given time the method of hot electron mean energy estimation was proposed and developed. It was shown that estimates for hot electrons mean energy obtained by means of ionic method well agreed with estimates obtained by means of early developed x-ray method. And we can exploit the new method in our experiments.

- The effect of an impurity film lying on the surface of a target in a vacuum of up to 10^{-5} Torr on the ion acceleration in a plasma, which is formed by a 2 x 10^{16}-W cm"^{2} femtosecond laser pulse is studied using the time-of-flight and mass spectrometry techniques. It is shown that, under such conditions, the maximum mean energy per unit charge (8 keV) is gained by protons, whereas the ions constituting the target substance (Si, Ti) acquire an energy per unit charge of < 1 keV. The use of a < 10 J cm^2 nanosecond laser pulse applied 0.1-100 ms before a femtosecond laser pulse allows the target surface to be efficiently cleaned due to the removal of H-, C-, and O-containing molecules from it. Unlike a continuous thermal heating of a surface, the pulse laser cleaning ensures higher heating temperatures and can be efficiently applied to any solid targets in both the thermal and plasma cleaning modes.

- We obtain atomic, energy, and charge spectra of ions accelerated at the front surface of a silicon target irradiated by a high-contrast femtosecond laser pulse with an intensity of 310^{16} W/cm^2, which is delayed with respect to a cleaning nanosecond laser pulse of 3-J/cm^2 energy density. A tremendous increase in the number of fast silicon ions and a significant growth of their maximum charge in the case of the cleaned target from 5+ to 12+ have been observed. The main specific features of the atomic, energy, and charge spectra have been analyzed by means of one-dimensional hydrodynamic transient-ionization modeling. It is shown that fast highly charged silicon ions emerge from the hot plasma layer with a density a few times less than the solid one, and their charge distribution is not deteriorated during plasma expansion. A noticeable increase in the charge and energy of ions accelerated from a solid tungsten target irradiated by a femtosecond laser pulse with the intensity higher than 10^{16}W/cm^2 has been found when the target surface is previously cleaned by a nanosecond laser pulse with an energy density of 3 J/cm^2. Tungsten ions with the charge up to +29 and energies up to 1 MeV were detected in this case, while the charge and energy of tungsten ions from a target with the uncleaned surface are not exceed +3 and 12 keV, respectively. It is found that the mean charge of tungsten ions in a solid tungsten target cleaned from the surface layer of hydrocarbon and oxide compounds and exposed to femtosecond laser radiation with an intensity exceeding 10^{16} W/cm^2 attains 22+, while the maximum charge is 29+. The maximum energy of such ions approaches 1 MeV. The corresponding values obtained on a dirty target with the same laser pulse parameters constitute 3+, 5+, and 150 keV. The results of numerical simulation show that such a large maximum charge of ions can be attained owing to the emergence of an electrostatic ambipolar field at the sharp boundary between the plasma and vacuum. The main mechanism of ionization of ions with maximum charges is apparently impact ionization in the presence of an external quasi-static field. In addition, direct above-threshold ionization by this field can also play a significant role. It is also shown that heavy ions in a clean target are accelerated by hot electrons. This leads to the formation of high-energy ions. The effect of recombination on the charge of the ions being detected is analyzed in detail.

- Our experiments revealed strong dependence of ionic current from laser-produced femtosecond plasma on the presence of contamination (or oxide) layer at the top of the target. With relation to internal conversion decay of low energy nuclear levels excited in plasma such a dependence could be crucial at various aspects. From one hand by surface cleaning one can achieve more bulk ions (possessing low energy nuclear state) in hot plasma region thus enhancing excited nuclei yield. Moreover, as it follows from our experiments, at cleaned surface the interaction of hot electrons with bulk ions becomes more efficient – more bulk ions are located in the same plasma volume as hot electrons are. This also should lead to an increase in the number of excited nuclei. From another hand fast light ions, which come mostly from contamination layer have time-of-flight that is comparable to the low energy nuclear level life-time. Thus elimination of contaminant layer greatly decreases the "noise" signal from negative ions. It is this signal mostly preventing IC electrons detection by electrostatic time-of-light separator in the case of ^{57}Fe or ^{181}Ta isomeric levels. Finally the observed increase in the charge multiplicity of fast bulk ions could enhance IC blocking giving rise to gamma decay events. The appropriate candidate to observe this phenomenon could be ^{201}Hg isomeric state.

- Ion acceleration mechanism
  - A numerical simulation of the recombination and ionization processes in expanding plasma generated by an ultrashort laser pulse with an intensity of 10^{15}–10^{16} W/cm ^{2}is carried out. This analysis is based on an original one-dimensional plane hydrodynamic model for the expansion of a nonequilibrium plasma in vacuum. Significant attention is paid to the effect of bound–bound transitions in ions on the rates of ionization and recombination processes and the ionization state of the plasma at long (up to 10^{-6} s) time intervals. It is demonstrated in calculations using examples of Si and Hg plasma that the excited states as functions of the plasma concentration need to be taken into account in a correct analysis of the plasma kinetics. The results of the numerical simulation are compared to the experimental data obtained using the time-of-flight method. It is shown that the model proposed makes it possible to describe the main features of the experimentally observed charge and time-of-flight ion spectra.
  - Based on experiment to numerical simulation comparison we propose the following pattern of formation of fast heavy ions at the sharp boundary of a polyatomic target exposed to femtosecond laser radiation. The initial charge of ions is formed due to impact ionization in a thin surface layer of the dense hot plasma and is determined by the thermal electron component. For a laser pulse intensity above 10^{16} W/cm^2 and a pulse duration of 200 fs, the average charge of tungsten ions attains values of 22+–23+. In this case, a time period of 100−200 fs is sufficient for the ion composition of the plasma to be close to equilibrium for an electron temperature of 100–300 eV. Rapid expansion of the plasma over the same time periods and the substantial

decrease in the electron concentration associated with it lead to an additional increase in the average charge for a small fraction of ions at the front of the expanding plasma (up to 30+). These ions are in the range of action of the ambipolar field determined by thermal as well as hot electrons. This leads to two effects. On the one hand, ions are accelerated to values of energy per unit charge, which correspond to the mean energy of hot electrons (up to 12 keV per unit charge in our experimental conditions). On the other hand, a fraction of ions are subjected to deeper ionization due to a decrease in the ionization potential by an external quasi-static electric field (the maximum charge increase up to 35+). The main mechanism is apparently impact ionization in the presence of the external quasi-static field. However, direct above-threshold ionization by this field can also make a substantial contribution. Subsequently, partial recombination of fast ions takes place due to charge exchange in the residual gas in the interaction chamber. An our conditions (residual pressure of the gas 10^{-5} Torr and the time-of-flight base 70 cm) reduces the average charge of fast ions to 22+ and the maximum charge to 29+.

Gamma decay of Ta-181: methods and results

- We were aimed at experiments on registration of gamma-decay of $^{181}Ta_{73}$ (6.238 keV, 6.05 μs) excited in femtosecond laser plasma. We carried out the test experiments on registration with avalanche photo diode (APD) with preamplifier of gamma-radiation of Co-57 (6.4 keV, 14.4 keV) together with X-ray emission of tungsten W_{74} plasma produced by laser pulses with intensity (5-20)·10^{15} W/cm^2. From results of the lead measurements follows, that: duration of the signals recorded by means of APD makes size of the order of 40-50 ns; average amplitude of the impulses corresponding registration of γ-quantum with energy 6,5 keV for APD 19 mV.

- In the experiment the Ti:Sa laser system with energy of a laser impulse 1 mJ and duration 70 fs was used, allowing to achieve intensity on a surface of a target ~10^{17} W/sm^2 As a result of the experiment 2174 traces have been received and processed. Glitches corresponding to a single 6.238 keV was not revealed. On the basis of the calculations, with probability of 50 % a number of γ-quanta do not exceed 0,2 in a single laser shot.

Internal conversion measurements

- We made experiments on registration of internal conversion of nuclei excited in laser produced plasma the experiments. Special spectrometer with energy resolution of 12% and energy of detected electron easily tuned from 100 eV to 40 keV was designed and thoroughly tested.

- The formation of a high-energy (~35 keV) beam of negative hydrogen ions was observed in the expanding femtosecond laser plasma produced at the surface of a solid target by radiation with an intensity of up to 2 *10^{16} W/cm ^{2}. The energy spectra of the H$^+$ and H$^-$-ions show a high degree of correlation. Such negative prevents efficient detection of IC electrons. To eliminate this signal pulsed laser cleaning was proposed and implemented.

- The experiments on electronic conversion decay of excited *Fe* nuclei (*E=14 keV, t=98 ns*) were carried out. Nuclei were excited in plasma produced by Ti:Sa femtosecond laser radiation (800 nm, *2 mJ*, 60 fs, 10^{17} *W/cm^2*). Measured electronic distribution on energy has a maximum at energy of 7.2 keV. This value is in a good agreement with theoretical energy of internal conversion electrons (estimated value is 7.2 keV). Width of distribution peak corresponds to energy resolution of our spectrometer ~10% (0.7 keV).

Isomer excitation in equilibrium dense plasma

- In calculating the number of excited nuclei in a dense plasma whose temperature is close to the energy of the excited nuclear level, resonant mechanisms are the most important: direct photoabsorption of the plasma radiation by nuclei, inverse electronic conversion (IEC), and inverse electronic bridge. The excitation efficiency determined by the inelastic scattering of plasma electrons by nuclei is of the same order of magnitude as the IEC efficiency. The fourth-order (with respect to *e*) and inverse Auger processes in the nucleus and atomic shell allow for the ultimate extension of resonance fragments in the spectra of plasma electrons and photons related to nuclear excitation. Adding new electron–photon vertices to the diagrams under consideration is possible only in the plane-wave part of the electron spectrum. In full accordance with the conventional electrodynamics, this does not lead to an increase in the nuclear excitation efficiency. Therefore, there exist no effective mechanisms of an order greater than four with respect to *e* for the nuclear excitation in plasma to the first excited state. In the case of exciting isomer nuclei to relatively high-lying states in a plasma whose temperature is a few times lower than the energy of the level excited, one must take into account the processes involving intermediate nuclear states: two-photon excitation, simultaneous excitation by the plasma photons and electrons, some of the fourth-order processes, etc. There exist a few nuclei in which such excitation can be realized in spite of the low efficiency.

- Recently, there have been reports in the mass media about plans to build what became known as an "isomeric bomb" based on Hf-178. What all the publications are speaking about is no less than the possibility of building a radically new weapon that does not fall under a single article of the existing nonproliferation treaties. The publications were based on the sensational results on induced decay of the long-lived isomer Hf-178m2 (16+, 2446 keV, 31 yr), obtained in 1999-2004 by a group of researchers headed by Carl B Collins, the Director of the Center for Quantum Electronics, University of Texas at Dallas. Our results show the following. The production of several grams or more of the isomer 178m2-Hf is an extremely difficult task. So far, no effective process for such production has been described in the literature. The use of only one of the above reactions will require large investments. Actually, such burdensome expenditures from state budgets may prove useless: no energy can be liberated by the method described in Collins's articles. The cross sections of the induced decay of the isomer 178m2-Hf measured by that method do not agree with the current ideas about the physics of the nucleus and the

physics of electromagnetic nuclear processes. Summarizing the obtained results, it would be noted the following. Theoretical calculations and the analysis of the existing experimental data suggest that the hafnium problem, as presented by the works of Collins's group, does not exist. The hullabaloo over the hafnium bomb was due to meaningless experimental data and the incompetence of certain individuals rather than to the real possibility of building a radically new weapon based on 178-Hf.

- Th-229 found in a state with an energy of 3.5±1.0 eV, which is quite unusual for nuclei, could become the object of exciting investigations at the junction of far-apart areas of physics. Some of the possibilities are:
  - o "Nuclear light", or the gamma radiation emitted by an atomic nucleus in the optical range. Nuclear light is produced by the direct nuclear emission of radiation in the optical range in the insulator $^{229}ThO_2$. A test of the chance of increasing the probability of nuclear decay in a dielectric medium by a factor of n^3 in comparison to the probabilities of decay in vacuum. The possibility of studying the properties of a cavity. A highly stable nuclear source of light for metrology.
  - o Creation of population inversion in a system of nuclei via highly effective laser excitation. The acceleration of alpha decay of Th-229 through the excitation of the state $3/2^+(3.5±1.0$ eV) by applying low-intensity laser radiation.
  - o A probe for studying the chemical environment and the properties of condensed media and surfaces.
  - o A verification of the exponential nature of the law of decay of an isolated metastable state in large time intervals.
  - o The moderation of gamma decay of the low-lying nuclear level in the dielectric matrix $^{229}ThO_2$ placed inside a spherical cavity with reflecting walls, between mirrors, etc.

Double pulse isomer excitation

- The scheme of nuclear excitation by the ionic X-ray lines in laser plasma using two femtosecond laser pulses is proposed. The first pulse produces plasma with a given degree of ionization, allowing the X-ray line energies of the target ions to be tuned to resonance with the nuclear transition, while the second pulse generates hot electrons that are necessary for X-radiation. High luminosity of the characteristic X-ray radiation allows for the excitation efficiency of low-lying nuclear states to be increased by four-to-five orders of magnitude. High intensities of X-ray lines emitted by femtosecond laser plasma render it one of the most promising X-ray sources for nuclear excitation. The possibility of controlling the degree of laser- plasma ionization allows the use of X-ray lines from both neutral target atoms and various ions for these purposes. By controlling the degree of ionization, one can tune the ionic X-ray lines to the exact resonance with the nuclear transition energy and, thereby, greatly extend the potentialities of this method. In our opinion, the method with the use of two laser pulses is most promising the heating pulse produces plasma with a given degree of ionization, while the ultrashort pulse generates hot electrons that create vacancies in the ion electronic shells; the latter are subsequently filled to emit X-ray quanta.

REFERENCES
1. L.A.Rivlin - Soviet Inventor's Certificate # 621265 of Jan. 10, 1961. (Sov. Bull. of Inventions # 23, 220, 1979 - in Russian).
2. V.Vali, W.Vali - Proc. IEEE, 51, 182, 1963.
3. G.C.Baldwin, et al. - Proc. IEEE, 51, 1247, 1963.
4. G.C.Baldwin, J.C.Solem - Rev. Mod. Phys., 69, 1085, 1997.
5. L.A.Rivlin - *(invited paper),* Quantum Electronics (Moscow), 29, 467, 1999.
6. C.B.Collins et al. - Phys. Rev. Lett., 82, 695, 1999.
7. D. Belic, et al, Phys. Rev. Lett. 83, 5242 (2000).
8. Rivlin. Gamma-ray lasing by free nuclei and by matter-antimatter beams. Hyperfine Interaction, v. 107, 57, 1997.
9. Rivlin. Inducing nuclear gamma-ray emission by strong-field ignition or without a total population inversion. Laser Physics, v. 5, 297, 1995.
10. Rivlin. Gamma-ray laser operating with the assistance of the recoil of free nuclei (invited paper), Quantum Electronics (Moscow), v. 29, 467, 1999.
11. Rivlin. Self-sustained exothermal reaction of anti-Stokes gamma transitions in long-lived isomeric nuclei. Part I. Quantum Electronics (Moscow), v. 30, 551, 2000.
12. L.A.Rivlin. Self-sustained exothermal reaction of anti-Stokes gamma transitions in long-lived isomeric nuclei. Part II. Quantum Electronics (*Moscow*), v. 30, 937, 2000.
13. E.V. Andreeva, S.D.Yakubovich et al. Picoseconds semiconductor lasers with external fiber resonator. Quantum Electronics, v..30, #2, p.158, 2000.
14. L.A.Rivlin, S.D.Yakubovich. About possibility to increase concentration and extension of laser cooled atomic ensembles. Quantum Electronics, v. 30, #11, pp. 1027-1030, 2000.
15. A.T.Semenov, S.D.Yakubovich et al. (GaAl)As Single Quantum-Well Superluminescent Diodes with extremely low coherence length. Electron Lett., 1995, v. 31, #4, p.314-315.
16. L.A.Rivlin, A.A.Zadernovsky. Induced two-quantum gamma emission under conditions of external ignition. Laser Physics, v. 6, No. 5, pp. 956-962, 1996.
17. L.A.Rivlin, A.A.Zadernovsky. Induced annihilation of positronium atoms under conditions of external ignition. Laser Physics, v. 7, No. 6, pp. 1231-1237, 1997.

18. Zadernovsky A.A. Ignition of burst two-quantum generation of coherent gamma-photons. Laser Physics, v. 10, No. 1, pp. 71–75, 2000.
19. Zadernovsky A.A. Stimulated gamma emission by anti-Stokes transitions of free isomeric nuclei. Laser Physics, v. 11, No 1. pp. 16–22, 2001.
20. Zadernovsky A.A. Stimulated gamma emission of free isomeric nuclei with anti-Stokes transitions. Quantum Electronics (Moscow), v. 31, No. 1, pp. 90-94, 2001.
21. V.I.Balykin, V.G.Minogin, and V.S.Letohov "Electromagnetic trapping of cold atoms" Rep.Prog.Phys. 63 (2000) 1429-1510.
22. C.S.Adams, E.Riis "Laser cooling and trapping of neutral atoms" Prog.Quant.Electr. 21 (1997) 1-79.
23. Vuletic V. et all, Phys.Rev.Lett., 81 (1998) 5768.
24. Davis K.B. et all, Phys.Rev.Lett., 75 (1995) 3969.
25. Wharton K.B., Hatchett S.P., Wilks S.C., et al. // Phys. Rev. Lett., 81 822 (1998).
26. Tatarakis M., Lee P., Davies J.R., et al. // Phys. Rev. Lett., 81 999 (1998).
27. A.V.Andreev, V.M.Gordienko, A.B.Savel'ev "Nuclear processes in high temperature plasma, induced by ultrashort laser pulse" (review paper) // Quantum Electronics, 2001, in press.
28. Abstarcts of 9th Annual International Laser Physics Workshop (LPHYS'2000), Bordeaux, France, July 17-21, 2000
29. Chumakov A.I., Baron A.Q.R., Arthur J., et al. // Phys. Rev. Lett., 75 549 (1995).
30. C.B.Collins, F.Davanloo, M.C.iosif, et.al, "Accelerated emission of gamma-rays from the 31-yr isomer of 178-Hf induced by x-ray radiation" // Phys.Rev.Lett., 82, 695-698 (1999).
31. Attallah F., Aiche M., Chemin G.F., et al. // Phys. Rev. Lett., 75 1715 (1995).
32. Morita M. // Progr. Theor. Phys. 49, 1574 (1973)
33. Letokhov V.S. // Kvantovaya electronica, 4, 125 (1973).
34. Izawa Y., Yamanaka C. // Phys. Lett. B88, 59 (1979).
35. Arutyunyan R.V., Bol'shov L.A., Vikharev V.D., et al // Yadernaya fizika, 53 36 (1991).
36. A.V.Andreev, V.M.Gordienko, A.M.Dykhne, A.B.Savel'ev, E.V.Tkalya, "Excitation of nuclei in a hot, dense plasma: feasibility of experiments with 201-Hg", JETP Letters, 66(5), 331-335 (1997).
37. A.V.Andreev, R.V.Volkov, V.M.Gordienko, A.M.Dykhne, M.P.Kalashnikov, P.M.Mikheev, P.V.Nickles, A.B.Savel'ev, E.V.Tkalya, R.A.Chalykh, O.V.Chutko "Excitation and Decay of low-lying nuclear states in a dense plasma produced by subpicosecond laser pulse" JETP, 91(6), 1163-1175 (2000).
38. A.V.Andreev, R.V.Volkov, V.M.Gordienko, A.M.Dykhne, P.M.Mikheev, A.B.Savel'ev, E.V.Tkalya, R.A.Chalykh, O.V.Chutko "Excitation of low energy nuclear levels in non relativistic dense laser plasma", Quantum electronics, 26, 55 (1999).
39. A.M.Akulshin, V.L.Velichansky et al. "Formation of narrow velocity distribution in an atomic cesium beam by resonant injection-laser radiation" Sov. J.Quantum Electron. 19 (1989) 972.
40. A.M.Akulshin, V.L.Velichansky et al. "Effect of radiation pressure on shape of saturated absorption resonance of cesium vapor" JETP Lett. 50 (1989) 187.
41. B.Tromborg, J.Mork, V.L.Velichansky "On mode coupling and low-frequency fluctuations in external-cavity laser diodes." – Quantum Semiclass. Opt. 9 (1997) 831-851.
42. M.D.Lukin, M.Fleischhauer, A.S.Zibrov, H.G.Robinson, V.L.Velichansky, L.Hollberg, M.O.Scully "Spectroscopy in Dense Coherent Media: Line Narrowing and Interference Effects" – Phys.Rev. Lett. 79(16) (1997) 2959-2962.
43. M.D.Lukin, M.Fleischhauer, M.O.Scully, V.L.Velichansky "Intracavity electromagnetically induced transparency" – Opt. Lett. 23(4) (1998) 295-297.
44. V.A.Sautenkov, M.M.Kash, V.L.Velichansky, and G.R.Welch "Density narrowing in electromagnetically induced transparency" – Laser Physics, 9 (4) (1999), 889-893.
45. I.Novikova, A.B.Matsko, V.A.Sautenkov, V.L.Velichansky, G.R.Welch and M.O.Scully "AC-Stark shifts in the nonlinear Faraday effect" Opt. Lett. 25(22) (2000) 1651-1653.
46. A.V.Yarovitsky, V.L.Velichansky 'Limits of continuos frequency tuning of injection lasers with selective external cavities.' Sov.J.Quantum Electronics 25(8) (1995) 765-769.
47. V.V.Vasil'ev, V.L.Velichansky, M.L.Gorodetsky, V.S.Ilchenko, L.Hollberg, A.V.Yarovitsky 'High-coherence diode laser with optical feedback via a microcavity with "whispering gallery" modes' Quantum Electronics 26(8) (1996) 657-658.
48. V.V.Vasiliev, V.L.Velichansky, V.S.Ilchenko, M.L.Gorodetsky, L.Hollberg, A.V.Yarovitsky 'Narrow-line-width diode laser with a high-Q microsphere resonator' Optics communication 158 (1998) 305-312.
49. E.Mikhailov, N.Senkov, V.Velichansky, A.Yarovitskiy, Y.Rostovtsev, R.Kolesov 'Pump and probe lasers for "blue" inversionless gain measurement in Cs.' Conference "Snow bird" (1999).
50. H.Failache, S.Saltiel, A.Yarovitski, A.Baas, A.Fischer, M.-P.Gorza, M.Fichet, D.Bloch et M.Ducloy 'Couplage quantique resonnant a longue portee entre atome excite et surface dielectrique.' Campus de la Doua, Lyon-Villeurbanne, July 2000, A-6. Colloque de la division de physique atomique, moleculaire et optique de la societe francaise de physique.
51. A.N.Oraevsky, A.V.Yarovitsky, V.L.Velichansky " Frequency stabilization of a diode laser by using whispering gallery mode." To be published in Sov.J.Quant.Electr in 2001.

52. V.V.Vassiliev, V.L.Velichansky, M.L.Gorodetsky, V.S.Ilchenko, L.Hollberg, A.V.Yarovitsky "High-coherence diode laser with optical feedback via a microcavity with 'whispering gallery' modes" Sov.J.Quant.Electr. <u>26</u> (8) (1996) 657-658.

53. V.V.Vassiliev, V.L.Velichansky, P.Kersten, F.Riehle "Injection locking of a red extended-cavity diode laser" Electron.Lett., 33(14) (1997) 1222-1223.

54. V.V.Vassiliev, V.L.Velichansky, P.Kersten, T.Trebst, F.Riehle "Subkilohertz enhanced-power diode-laser spectrometer in the visible." Opt.Lett. 23 (15) (1998) 1229-1231.

55. V.V.Vassiliev, V.L.Velichansky, V.S.Ilchenko, M.L.Gorodetsky, L.Hollberg, A.V.Yarovitsky "Narrow- line-width diode laser with a high-Q microsphere resonator" Opt.Comm. 158 (1998) 305-312.

56. V.N.Belousov, L.A.Bolshov, N.N.Elkin, N.G.Kovalsky, Yu.K.Nizienko, M.I.Persiantsev. "Mechanism of nonlinear distortions in the angular spectrum of radiation under Stimulated Scattering." Zh.Eksp.Teor.Fiz., v. 92, N1, pp. 61-73, 1987.

57. V.N.Belousov, Yu.K.Nizienko "SBS-compressor for powerful laser system. " Preprint of Kurchatov Institute of Atomic Energy 4707/7, Moscow, 1988.

58. Yu.K.Nizienko"Divise for laser beams amplification» Patent of USSR No1671106 from 05.03.1989.

59. V.N.Belousov, A.M.Mamin, Yu.K.Nizienko. A collection of Papers Presented at the IAEA Technical Committee Meeting on Lidar Thomson Scattering at JET, Abingdon, Oxon, UK, 8-10 April 1991, p.103-111, IAEA, Vienna, July, 1991.

60. V.N.Belousov, A.M.Mamin, Yu.K.Nizienko, A.R.Sidorov " Composite aperture Laser with phase conjugation and pulse compression." Izv. RAN, ser. fiz., v.56, pp. 186-190, 1992.

61. V.N.Belousov and Yu.K.Nizienko "Powerful Nd:glass laser with composite active elements incorporating WFR cells and output pulse compressors" Laser and Particle Beams, vol.11, No.3, pp583-585, 1993.

62. Yu.K.Nizienko,A.M.Mamin,P.Nielsen,B.Brawn,Revew of Scientific Instruments,v.65,p.2460,1994.

63. A.V. Andreev, R.V.Volkov, V.M. Gordienko, A.B. Savelev, E.V. Tkalya, O.V.Chutko, A.A.Shashkov, A.M. Dykhne, "Excitation of tantalum-181 nuclei in a high temperature femtosecond laser plasma", JETP Lett., 69(5), pp.371-376, 1999.

LIST OF PUBLISHED PAPERS AND REPORTS WITH ABSTRACTS

1. S.A. Karamian, J.J. Carroll, L.A. Rivlin, A.A. Zadernovsky, F.J. Agee, "Possible ways for triggering of the ^{179m2}Hf isomer", Preprint E15-2003-179 of the Joint Institute for Nuclear Research, Dubna, 2003. p. 1-14.

Realistic approaches to triggering of the ^{179m2}Hf isomer are discussed. The nuclear level scheme of ^{179}Hf suggests three promising ways for triggering, but two of them are seemingly closed by the high multipolarities of the required electromagnetic transitions. New possibilities to overcome such restrictions are deduced by utilizing a model of atomic-nuclear compound states. A new and productive method of observing triggering would base an experiment on the use of an electron cyclotron resonance ion trap, ECRIT. Some quantitative details of the behavior of ^{179m2}Hf and ^{242m}Am atomic-nuclear systems in an ECRIT environment are examined. Many important parameters are as yet unknown and they can be estimated only after the new type of experiments proposed here in which high rates of triggering are possible.

2. A.A. Zadernovsky, "Analysis of the destructive impact of X-ray pumping on the gamma-ray laser medium", Laser Physics, Vol. 13, No. 2, pp. 184–189, 2003.

We discuss in this paper the destructive impact of X-ray pumping radiation on the active medium of cooled free nuclei with hidden inversion of state populations and formulate a set of requirements for the pumping radiation and the amplifying nuclear medium crucial to the development of recoil assisted gamma-ray lasing.

3. D.S. Mamedov, V.V. Prokhorov, S.D. Yakubovich, "Extremely Broad-Band High-Power Superluminescent Diode at 920 nm", Quantum Electronics, Vol. 33, No 6, pp. 471-476, 2003.

Physical characteristics of superluminescent diodes (SLDs) based on single-quantum well (AlGa)As/(InGa)As heterostructure with graded-index waveguide were investigated. Depending on active channel length CW output power ex single-mode fiber was in the range 1 - 10 mW and spectrum FWHM - 100 – 110 nm, that corresponds to 7.6 – 8.8 nm coherence length.

4. L.A. Rivlin, "Two-quantum-induced energy release of isomeric nuclei", Quantum Electronics, Vol. 34, No 1, pp. 23 - 28, 2004.

The possibility of using long-lived isomers with a specific stored energy content more than 10 MJ/g as a new type of nuclear fuel is analyzed. The basic process of energy release is a two-quantum stimulated radiative process of unloading the metastable states in the field of two counter-propagating external beams of gamma-photons with energy equal to the half-energy of isomer excited state.

5. S.A. Karamian, J.J. Carroll, L.A. Rivlin, A.A. Zadernovsky, F.J. Agee, "Possible ways for triggering of the ^{179m2}Hf isomer", Laser Physics, Vol. 14, No 2, pp. 166-174, 2004.

Realistic approaches to triggering of the ^{179m2}Hf isomer are discussed. The nuclear level scheme of ^{179}Hf suggests three promising ways for triggering, but two of them are seemingly closed by the high multipolarities of the required electromagnetic transitions. New possibilities to overcome such restrictions are deduced by utilizing a model of atomic-nuclear compound states. A new and productive method of observing triggering would base an experiment on the use of an electron cyclotron resonance ion trap (ECRIT). Some quantitative details of the behavior of ^{179m2}Hf and ^{242m}Am atomic-nuclear systems in an ECRIT environment are examined. Many important parameters are as yet unknown and they can be estimated only after the new type of experiments proposed here in which high rates of triggering are possible.

6. L.A. Rivlin, J.J. Carroll, F.J. Agee, "Driven energy release of nuclear isomers", Laser Physics, v.14, 435-438, 2004

Progress in the development of high-reflectivity x-ray mirrors makes possible to intensify the stimulated nuclear energy release process due to using of Fabry-Perot resonator that may combine stimulating action of external and intraresonator gamma-photon beams. Here the detailed theoretical analysis of such a combined driving radiative process is presented. It includes investigation of dynamics, CW and pulsed mode operation, stability criteria etc.

7. A.A. Zadernovsky, "Nuclear gamma-ray laser with a Fabry-Pérot resonator", Laser Physics, v.14, 448-454, 2004.

We consider a scheme for the recoil-assisted gamma-ray laser with a Fabry-Pérot resonator which takes advantage of the resonator both for an externally produced pumping X ray and for stimulated gamma radiation emitted by the active nuclei. We formulate a set of requirements for the pump X-ray radiation and the nuclear medium crucial to achieving the threshold condition for the gamma-ray lasing. A comparison with a single-pass regime of self-amplified spontaneous gamma emission is made.

8. L.A. Rivlin, "Quantum nucleonics: Status and prospects", Quantum Electronics, Vol. 34, 606-609, 2004

It is pointed out that use of long-lived nuclear isomers in modern quantum nucleonicsis impeded by a large broadening of the gamma line of metastable nuclear states, which exceeds many times their natural radiative width. This broadening can be eliminated if atoms containing nuclei form a Bose-Einstein condensate.

9. L.A. Rivlin, "On radiative nuclear gamma transitions in a Bose-Einstein condensate", Quantum Electronics, Vol. 34, 736-740, 2004

The unique properties of radiative nuclear gamma transitions in atoms of a Bose-Einstein condensate, in particular, the efficient suppression of the inhomogeneous broadening of gamma lines related to the translation degree of freedom of the atoms are theoretically estimated. The effective temperature characterizing this broadening proves to be many orders of magnitude lower than the real temperature of the atomic ensemble. The phenomena considered in the paper open up new approaches to the problems of quantum nucleonics, for example, the observation of stimulated gamma radiation of long-lived isomeric nuclei.

10. L.A. Rivlin, "On coherent radiative processes in crystallized ion beams", Quantum Electronics, Vol. 34, No 2, pp. 180-184, 2004.

We consider the space-periodical structures formed by deeply cooled free ions of identical signs in traps of different kinds (quasi-crystals). Such a periodically regular positions of nuclei in crystallized ion beams influence on coherent radiative nuclear processes, for instance, on Dicke super-luminescence, direction of gamma-quantum emission, distributed feedback, hidden inversion of state population and so on. The quantitative estimates for needed deep cooling of ion beams are presented.

11. L.A. Rivlin, "Stimulated radiative decay of the metastable state of atomic Helium", Quantum Electronics, Vol. 34, No 11, pp. 1011-1012, 2004.

The possibility is shown to observe stimulated VUV emission by the direct transition from metastable state 2^3S_1 of atomic Helium, incorporated into Bose-Einstein condensate.

12. D.S. Mamedov, A.A. Marmalyuk, D.B. Nikitin, S.D. Yakubovich, V.V. Prokhorov, "Double-pass superluminescent multilayer quantum-well (GaAl)As heterostructure diodes with a reduced power consumption", Quantum Electron., 34 (3), 206-208, 2004.

Superluminescent diodes (SLDs) based on a three-layer quantum-well (GaAl)As heterostructure with a bent active channel emitting in the spectral range from 820 to 840 nm are studied. The diodes can operate without thermal stabilization in the temperature range between -55 and +93 °C emitting 0.1 mW of optical power at the output of a single-mode fiber. They offer a significant advantage in operating currents and power consumption over conventional SLDs based on a bulk separate-confinement double heterostructure.

13. P.A. Lobintsov, D.S. Mamedov, V.V. Prokhorov, A.T. Semenov, S.D. Yakubovich, "High-power superluminescent diodes with non-injection output sections", Quantum Electron., 34 (3), 209-212, 2004

Superluminescent diodes based on a separate-confinement (GaAl)As heterostructure are studied in the 850-nm spectral region. A contact p^+-GaAs layer in the output sections of a narrow active channel of width 4 mm was removed and a metal contact was not deposited. These sections played the role of saturable absorbers. This design provided a significant increase in the catastrophic optical damage threshold and ensured 250 mW of output cw power at the diode facet. The power coupled out through a single-mode fiber in the case of a simplest coupling achieved 110 mW.

14. T.H. Ho, D.C. Adler, S.D. Yakubovich et al. "Ultrahigh resolution OCT imaging with a broad-band SLD light source", Opt. Express, v. 12, #10, p. 2112-2119, 2004

Ultrahigh resolution optical coherence tomography imaging is performed with a compact broadband superluminescent diode light source. The source consists of two multiplexed broadband superluminescent diodes and has a power output of 4 mW with a spectral bandwidth of 155 nm, centered at a wavelength of 890 nm. *In vivo* imaging was performed with approximately 2.3 µm axial resolution in scattering tissue and approximately 3.2 µm axial resolution in the retina. These results demonstrate that it is possible to perform *in vivo* ultrahigh resolution optical coherence tomography imaging using a superluminescent diode light source that is inexpensive, compact, and easy to operate.

15. L.A. Rivlin, "On the super-narrow gamma lines of nuclei in a Bose-Einstein condensate", Quantum Electronics, 35 (4), 390-392, 2005.

It is shown that due to the quantum coherence of atoms in a Bose—Einstein condensate, the width of gamma lines of the long-lived metastable states of isomeric nuclei in these atoms can be close to the natural radiative width. This opens up the possibility of observing super-narrow gamma lines, which are narrower by a few orders of magnitude than the Mössbauer gamma line.

16. L.A. Rivlin, "On the induced release of the energy of isomeric nuclei in a Bose-Einstein condensate", Quantum Electronics, 35 (5), 474-478, 2005.

It is shown that the asymptotic temporal behaviour of the current value of the stimulated emission cross section leads to a complex dynamics of the radiative release of the nuclear energy of long-lived metastable states induced by the external flux of resonance gamma quanta. The stimulated emission cross section of isomeric nuclei in atoms of a

Bose—Einstein condensate becomes sufficient to achieve a comparatively high efficiency of this process, which is manifested in a considerable increase in the decay rate of metastable states.

17. L.A. Rivlin, "Remarks on the trigger induction of the radiative decay of metastable states of isomeric nuclei", Quantum Electronics, 35 (9), 813-81, 2005.

The conditions of known experiments on the trigger acceleration of the radiative decay of isomeric nuclear states are compared. It is shown that in the case of quasi-monochromatic inducing sources, the use of Mössbauer targets can increase the efficiency of the process by a few orders of magnitude. It is pointed out that the asymptotic behaviour of the current value of the absorption cross section requires the comparability of the exposure time with upper-level lifetime of the transition.

18. L.A. Rivlin, "Quantum Nucleonics: Where we are now and where we may go", Laser Physics, v. 15, No. 3, 454-456, 2005.

Current trends in quantum nucleonics (QN) is discussed , in particular, various schemes of eventual nuclear gamma-ray lasing experiments and the driven energy release of long-lived isomers, and point out the common general embarrassments of all the mentioned approaches. Some methods of surmounting these embarrassments are propounded.

19. A.A. Zadernovsky, "Identification of prime nuclides for an active medium of a gamma-ray laser", Laser Physics, v. 15, No 4, pp. 480-486, 2005.

We have screened nuclear isotopes to select the most promising nuclides potentially valuable to realizing a gamma-ray laser based on the concept of hidden inversion of nuclear state populations. Selection procedure relies on a detailed analysis both the internal nuclear structure and the atomic electron shell of a potential candidate. Ranking of the selected nuclides is accomplished in the order of ascending threshold spectral photon flux density of pumping radiation. The first-ranked candidates are identified to be recommended for a further investigation.

20. V.V. Prokhorov, D.S. Shvakov, S.D. Yakubovich, "Broad-band highly bright radiation sources based on SOA and SLD", Quantum Electronics, v. 35, No 7, p.504-507, 2005.

It is shown experimentally that the use of a travelling-wave semiconductor optical amplifier (SOA) significantly improves the output characteristics of a superluminescent diode (SLD), increasing, in particular, its output power or broadening its emission band. By using SOAs based on separate-confinement double (InGa)PAs heterostructures emitting at 1300 nm and different SLDs as input radiation sources, there were obtained up to 50 mW of cw power at the output of a single-mode fibre and the emission band with the half-width up to 70 nm.

21. M. Wojtkowski, P.I. Lapin, D.S. Mamedov, J.G. Fujimoto, S.D. Yakubovich, "Multichannel extremely broadband near-IR radiation sources for optical coherence tomography", Quantum Electronics, v. 35 (7), 667-669, 2005.

The construction and output parameters of two experimental samples of near-IR radiation sources based on the superposition of radiation from several superluminescent diodes are described. The first, three-channel sample emitting 18 mW of cw output power in a spectral band of width 105 nm through a single-mode fibre, is optimised for ophthalmology coherence tomography. The second, four-channel sample emits the 870-nm band of width more than 200 nm, which corresponds to the record coherence length smaller than 4 μm.

22. L.A. Rivlin, "Quantum nucleonics: Outlines and outlook", Proceedings of 2nd International Conference "Frontiers of Nonlinear Physics", pp. 458-461, 2005.

We discuss the current trends in Quantum Nucleonics .It is pointed out that use of long-lived nuclear isomers impeded by a large broadening of the gamma line of metastable nuclear states, which exceedsmany times their natural radiative width. This broadening can be eliminated if atoms containing nuclei form a Bose-Einstein condensate.

23. A.A. Zadernovsky, "Selection of nuclides for an active medium of gamma-ray laser", Proceedings of 2nd International Conference "Frontiers of Nonlinear Physics", pp. 517-529, 2005.

We discuss a selection of the most promising nuclides potentially valuable to realizing a gamma-ray laser based on the concept of hidden inversion of nuclear state populations. Selection procedure relies on a detailed analysis both the internal nuclear structure and the atomic electron shell of a potential candidate. Ranking of the selected nuclides is accomplished in the order of ascending threshold spectral photon flux density of pumping radiation. The first-ranked candidates are identified to be recommended for further investigations.

24. L.A. Rivlin, "Kinematics of bosons in a two-dimensional potential well", Quantum Electronics, 36 (1), 90-93, 2006.

Analysis of the kinematics of bosons (photons, atoms) in two-dimensional potential channels with the transverse eigenvalues slowly varying along the longitudinal axis of the channel reveals the existence of Bose condensation without temperature lowering, the stratification of an atomic flux over phase states, and also processes which

phenomenologically reproduce phenomena in nonlinear media (shock-like waves). These phenomena can form the basis for new experimental methods.

25. A.A. Zadernovsky, "Excitation of nuclei by photon beams carrying orbital angular momentum", Laser Physics, v. 16, No 4, pp.571-575, 2006.

A drop in the efficiency of nuclear excitation through transitions of high multipolarity is related to the increase in the angular momentum difference between the nuclear states involved in the excitation transition. Such transitions need photons with a high angular momentum. It is well known that photon beams carrying a well-defined and arbitrarily high value of angular momentum about the beam axis can be produced. We discuss some features in the excitation of nuclei with the beams.

26. L.A. Rivlin, "On stimulated VUV emission of the atomic helium in a Bose—Einstein condensate: I.", Quantum Electronics, 36 (2), 95-100, 2006.

A scenario of the experiment on the observation of stimulated VUV emission at a wavelength of 62 nm from metastable states of helium atoms in a Bose—Einstein condensate moving along an extended quantum well (trap) is considered. The quantitative estimates of parameters are presented.

27. L.A. Rivlin, "On stimulated VUV emission of atomic helium in a Bose—Einstein condensate: II", Quantum Electronics, 36 (4), 329-332, 2006.

The scenario of the experiment on observation of stimulated VUV emission at a wavelength of 62 nm from metastable states of helium atoms in a Bose—Einstein condensate moving along an extended quantum-well trap is further considered taking into account the asymptotic behaviour of the current value of the stimulated emission cross section. Quantitative estimates are presented.

28. P.A. Lobintsov, D.S. Mamedov, S.D. Yakubovich, "Lifetime tests of superluminescent diodes", Quantum Electronics, 36 (2), 111-113, 2006.

The process of slow degradation of a batch of 48 superluminescent diodes (SLDs) with different active-channel lengths L_a (24 diodes with L_a = 600 μm and 24 diodes with L_a = 1000 μm) made of a heteroepitaxial wafer is studied. The diodes were divided into six groups, each containing eight diodes, and were tested at the stabilised injection current I = 140 mA and the heatsink temperatures 25, 55, and 70°C. The median lifetime of a SLD with L_a = 600 μm was 3000, 2450, and 1900 h at temperatures 25, 55, and 70°C, respectively. The calculated lifetime for a SLD with L_a = 1000 μm exceeds 100000 h at 25°C and is 53000h at 55°C and 30500 h at 70°C. The obtained results confirm that a perspective technical solution providing an increase in the lifetime of high-power SLDs is the design with non-injected ends of the active channel which reduces current and, hence, thermal loads.

29. E.V. Andreeva, L.N. Magdich, D.S. Mamedov, A.A. Ruenkov, M.V. Shramenko, S.D. Yakubovich, "Tunable semiconductor laser with an acousto-optic filter in an external fibre cavity", Quantum Electronics, 36 (4), 324-328, 2006.

A tunable semiconductor laser with a laser amplifier based on a double-pass superluminescent diode as an active element and an acousto-optic filter in an external fibre cavity as a selective element is investigated. A continuous spectral tuning is achieved in a band of width 60 nm centered at a wavelength of 845 nm and the 'instant' linewidth below 0.05 nm is obtained. The sweep frequency within the tuning range achieves 200 Hz. The cw power at the output of a single-mode fibre was automatically maintained constant at the level up to 1.5 mW.

30. P.I. Lapin, D.S. Mamedov, A.A. Marmalyuk, A.A. Padalitsa, S.D. Yakubovich, "High-power broadband superluminescent diodes emitting in the 1000—1100-nm spectral range", Quantum Electronics, 36 (4), 315-318, 2006.

The physical parameters of superluminescent diodes (SLDs) based on a quantum-well heterostructure with two active (InGa)As layers are studied. The optical power coupled into a single-mode fibre was 0.5—30 mW and the width of the emission spectrum was 30—120 nm depending on the SLD active-channel length. The use of such SLDs in BroadLighter combined broadband radiation sources will provide emission covering the near-IR region between 800 and 1100 nm.

31. E.V. Andreeva, A.E. Zhukov, V.V. Prokhorov, V.M. Ustinov, S.D. Yakubovich, "Superluminescent InAs/AlGaAs/GaAs quantum dot heterostructure diodes emitting in the 1100—1230-nm spectral range", Quantum Electronics, 36 (6), 527-531, 2006.

Superluminescent diodes (SLDs) based on a multilayer InAs/AlGaAs quantum dot heterostructure are studied. It is shown that the emission spectra of SLDs strongly depend on the active-channel length and injection current. In particular, the conditions are determined under which the emission spectrum covers the spectral range between 1100 and 1230 nm due to the levelling of the intensities of quantum transitions from the first and second excited states. Commercial SLDs emitting in this spectral range are not available at present. The SLD design provides cw operation and efficient coupling with a single-mode fibre. The output power achieves 1 mW in free space and 0.5 mW when

coupled out through a fibre. Preliminary resource tests have demonstrated a rather high reliability of the developed SLDs.

32. V.V. Vassiliev, S.A Zibrov, and V.L.Velichansky, "Compact extended-cavity diode laser for atomic spectroscopy and metrology" Review of Scientific Instruments 77, 013102 (2006).

We report on a compact, inexpensive and durable extended cavity diode laser (ECDL) of an original mechanical concept. The independent temperature control of a laser diode and an extended cavity provides a low frequency drift. The linewidth of a few hundred kHz was measured by taking a beating of two identical ECDLs. The continuous tuning range of about 1Å is achieved by the synchronous scan of two piezo-transducers translating and rotating an external diffraction grating. The laser has been used in high-resolution spectroscopy, atom cooling, metrology and precise interferometry.

33. A.V. Yarovitskii, O.N. Prudnikov, V.V. Vasiliev, V.L. Velichansky, O.A. Razin, I.V. Sherstov, A.V. Taichenachev, V.I. Yudin, "Tunable frequency-stabilized laser for studying the cooling dynamics of Rb atoms in a magnetoopicaltrap" Quantum Electronics, 34, 341 (2004).

A system is developed which allows one to stabilize the diode frequency at any point in the vicinity of the cycling D2 line transition in Rb in the interval from +40 to – 150 MHz and to switch the laser frequency within this interval for ~ 1 ms. A method is proposed and realized for increasing the contrast of the reference sub-Doppler resonance observed in circularly polarized fields. The ultimate contrast of the resonance is estimated. The system can be used to study the anomalous light pressure force acting on atoms in optical molasses. A magnetooptical trap for Rb atoms is described.

34. A.V. Taichenachev, V.I.Yudin, V.L. Velichansky, A.S. Zibrov, and S.A. Zibrov "Pure superposition states of atoms generated by a bichromatic elliptically polarized field" Phys. Rev. A **73,** 013812 (2006)

We identify the specific polarizations for the two components of a bichromatic field, which produce pure superposition states of atoms with a specific magnetic quantum number m via coherent population trapping. The superposition states are composed of two Zeeman substates magnetic quantum number m of the two ground-state hyperfine levels with arbitrary angular momenta F_1 and F_2. It is established that in the general case of m $\neq 0$, optical fields with elliptical polarizations are needed for the preparation of such a pure state. It is shown analytically that a unique advantage of the D_1 line (over the D_2 line) of alkali-metal atoms is the possibility that pure m-m states may be generated even if the excited-state hyperfine levels are not spectrally resolved.

35. Sergei A. Zibrov, V.L.Velichansky, A.S. Zibrov, A.V.Taichenachev, and V.I.Yudin "Experimental preparation of pure superposition states of atoms via elliptically polarized bichromatic radiation" Optics Letters, **31**, 2060 (2006).

We propose a simple and effective way of creating pure dark superposition states. The generation of pure states is carried out by using bichromatic radiation with controllable polarization ellipticity. We derived analytic formulas for polarization elipticity to obtain pure dark states of different Zeeman sublevels of alkali atoms. Experimentally we accumulated ~60% of the atoms in the 0-0 dark state of the D_1 line of ^{87}Rb.

36. R.V. Volkov, D.M. Golishnikov, V.M. Gordienko, M.C. Dzhidzhoev, I.M. Lachko, B.V. Mar'in, P.M. Mikheev, A.B. Savel'ev, D.S. Uryupina, A.A. Shashkov "Formation of the ion current of high-temperature femtosecond laser plasma on the target surface containing an impurity layer"// Quantum Electronics, **33** (11), 981–986 (2003).

The effect of an impurity film lying on the surface of a target in a vacuum of up to 10^{-5}Torr on the ion acceleration in a plasma, which is formed by a 2×10^{16} W cm^{-2} femtosecond laser pulse is studied using the time-of-flight and mass spectroscopy techniques. It is shown that, under such conditions, the maximum mean ehergy per unit charge (8 keV) is gained by protons, whereas the ions constituting the target substance (Si, Ti) acquire an energy per unit charge of <1 keV. The use of a 10 J/cm^{-2} nanosecond laser pulse applied 0.1-100 ms before a femtosecond laser pulse allows the target surface to be efficiently cleaned due to the removal of H-, C- and O-containing molecules from it. Unlike a continious thermal heating of a surface, the pulse laser cleaning ensures higher heating temperatures and can be efficiently applied to any solid targets in both the thermal plasma cleaning mode.

37. O.V. Chutko, V.M. Gordienko, I.M. Lachko, B.V. Mar'in, A.B. Savel'ev and R.V. Volkov «High-energy negative ions from expansion of high-temperature femtosecond laser plasma», Applied Physics B, **77** (8), 831-837 (2003).

The atomic, charge and energy distributions of ions in expanding femtosecond laser plasmas have been studied by means of time-of-flight mass–charge spectroscopy. High-energy negative and positive ions with energies of up to 35 keV have been detected during the interaction of 200 fs laser pulses (I~2×10^{16} W/cm^2) with silicon, titanium and other solid targets. A high correlation between negative and positive single-charged ions of the identical atomic number is shown. Negative ions are produced as a result of collisions of fast single-charged ions and neutrals with molecules of residual gas.

38. V.V. Bol'shakov, V.M. Gordienko, A.B. Savel'ev, and O.V. Chutko "Excitation of low-lying nuclear states by the ion line emission in femtosecond laser plasma"// JETP Letters, **79** (2), 71–75 (2004).

The scheme of nuclear excitation by the ionic X-ray lines in laser plasma using two femtosecond laser pulses is proposed. The first pulse produces plasma with a given degree of ionization, allowing the X-ray line energies of the target ions to be tuned to resonance with the nuclear transition, while the second pulse generates hot electrons that are necessary for X-radiation.

39. E.V.Tkalya «Mechanisms for the Excitation of Atomic Nuclei in Hot Dense Plasma» Laser Physics **14**, N3 (2004) 360-377.

The most important mechanisms for the excitation of atomic nuclei by photons and electrons of a hot dense plasma are analyzed in the framework of the first four orders of perturbation theory for quantum electrodynamics. Qualitative estimates of the excitation efficiencies in various processes are derived.

40. E.V.Tkalya «Induced decay of ^{178}Hf^{m2}: theoretical analysis of experimental results» Physical Review C**71**, 024606 (2005) (8 pages).

This article reviews experimental results obtained recently on the x-ray-induced acceleration of the decay of the long-lived isomer 178m2-Hf. Two basic mechanisms for the induced decay are considered: (1) direct interaction of the incident x rays with the nucleus and (2) the nucleus-x-ray interaction proceeding via atomic shells. We establish that the absence of K forbiddenness for all transitions to a hypothetical "mixed K" level cannot explain the measured cross sections even if collective nuclear matrix elements, resonant conditions, and so on, are assumed. We also tested, and rejected, the hypothesis that the enhancement is due to normal nuclear transitions in the inverse nuclear excitation by electron transition process. The possibility to make measurements with intense laser radiation is considered too. Thus, there appears to be no explanation of these experimental results within quantum electrodynamics and the contemporary concepts of atomic nuclei.

41. E.V.Tkalya «Induced decay of ^{178}Hf^{m2}: Cross Section Upper Bound and Comparison with Experimental Data» In: Proc. II Int. Conf. Frontiers of Nonlinear Physics, 2005 (6 pages); In: Abstracts II Int. Conf. Frontiers of Nonlinear Physics, Nizhny Novgorod - St. Petersburg, Russia, July 5 - 12, 2004, p.125.

This paper reviews experimental results published in C.B.Collins et al., Phys. Rev. Lett. 82, 695 (1999); Phys. Rev. 61, 054305 (2000); Europhys. Lett. 57, 677 (2002) on the x-ray induced decay acceleration of long-lived isomer Hf-178m2(16+, 2.446 MeV, 31 yr). Two basic mechanisms for the induced decay were considered: direct interaction of the incident x-rays with the nucleus; the nucleus-x-rays interaction via the atomic shell. It was established that the absence of the K forbidenness for all transitions to the hypothetic "mixed K" level cannot explain the measured cross sections even if the collective nuclear matrix elements, resonant conditions, etc. are used. The hypothesis of the normal nuclear transitions enhancement in the inverse NEET process was also tested and rejected. Thus, there are no explanation of C.B.Collins et al. experimental results within quantum electrodynamics and of the contemporary concept of the atomic nuclei.

42. A.V. Andreev "Hyperfine structure of hydrogen and geonium" Laser Phys. Lett. **1**, No. 2, 69–74 (2004)

Here the theory of hyperfine structure of hydrogen and geonium is developed. The theory is based on the new relativistic wave equation for half-spin particle interacting with the electromagnetic field. The proposed equation is Lorentz and gauge invariant and includes three independent material constants: mass m, charge q, and magneton μ of a particle. We present the analytically tractable solutions of this equation for the two problems: electron motion in the Coulomb field and electron motion in the uniform magnetic field.

43. A.V. Andreev, R.A. Chalykh "To the possibility of getting nuclear states population inversion" Bulletin of MSU, .sec. 3: Physics and Astronomy, p.34-38 (2004)

The possible scheme of getting population inversion between first excited and ground state of Ge^{73} nucleus is observed on the base of nuclear selection on the first excited state. We have carried out a numerical research of inversion dynamics in this scheme and analysis of parameters influence on the inversion.

44. A.V.Andreev " Neutron Scattering by an Electrostatic Field and Laser Field of Ultrahigh Intensity", Laser Physics, p.1-8, vol.15, No. 5 (2005)

We examine the interaction of a neutron with an electrostatic and laser field of ultrahigh intensity. The conditions of neutron reflection by the field are determined. The amplitudes of reflected and transmitted waves are calculated. The dynamics of evolution of the neutron electric and magnetic dipole moments in the process of scattering is analyzed.

45. R.V. Volkov, A.A. Vorob'ev, V.M. Gordienko, M.S. Dzhidzhoev, I.M. Lachko, B.V. Mar'in, A.B. Savel'ev, D.S. Uryupina "Influence of pulse laser clearing of a target on ionization and acceleration of ions in the plasma created by femtosecond laser pulse." Quantum Electronics, 2005, v. 35, № 10, p. 953-958.

It is shown, that on characteristics of an ionic current of the laser plasma formed on a surface of a solid-state target under action superintensive femtosecond of radiation, essential influence renders doped layer which is being on a

surface of this target. Application of pulse laser clearing leads to occurrence additional high –energy components in a spectrum of ions of a material of a target. It is shown, that changing time of an advancing of cleaning laser radiation it is possible to operate such parameters of an ionic current of plasma, as an average and maximal charge of ions, the maximal energy of ions of a material of a target.

46. V.M. Gordienko, I.A. Makarov, E.V. Rakov, A.B. Savel'ev "Subsurface generation of rigid x-ray radiation at pulse-periodic influence on a target from BaF_2 radiation of femtosecond chrome-forsterite laser at intensity below 10^{15} W/sm^2" Quantum Electronics, 2005, v. 35, № 6, p. 487-488.
The effect subsurface generation of rigid x-ray radiation ($E > 20$ keV) during formation of the channel by sequence of laser impulses femtosecond duration in a target from BaF_2 is found out at intensity 10^{14} - 10^{15} W/sm^2.

47. R.V. Volkov, V.M. Gordienko, I.M. Lachko, A.B. Savel'ev, D.S. Uryupina "Acceleration of heavy multicharged ions up to energy in 1 MeV at an irradiation of the cleared solid-state target femtosecond laser radiation with intensity 10^{16} W/sm^2 " JETP Letters 81(11) 708-711 (2005)
The effect of essential increase in a charge and energy of the ions accelerated at influence of femtosecond laser radiation with intensity from above 10^{16} W/sm^2 on a solid-state target of tungsten, realized in conditions of preliminary clearing a surface of a target by nanosecond laser pulse with density of energy 3 J/sm^2 is found out. In these conditions ions of tungsten with a charge up to +29 and energy up to 1 MeV are registered. While for a target with the crude surface the charge of ions of tungsten did not exceed +3, and energy - 12 keV.

48. V. M. Gordienko, I. M. Lachko, A. A. Rusanov, A. B. Savel ev, D. S. Uryupina and R. V. Volkov "Enhanced production of fast multi-charged ions from plasmas formed at cleaned surface by femtosecond laser pulse" Applied Physics B: Lasers and Optics 80, №6, 733 – 739.
We present atomic, energy and charge spectra of ions accelerated at the front surface of the silicon target irradiated by the high-contrast femtosecond laser pulse with intensity of 3x10^16W/cm^2, which is delayed with respect to the cleaning nanosecond laser pulse of the 3 J/cm^2 energy density. The tremendous increase in the number of fast silicon ions and significant growth of their maximum charge in the case of the cleaned target from 5+ to 12+ has been observed. The main specific features of the energy, charge and atomic spectra have been analyzed by means of one-dimensional hydrodynamic transient-ionization modeling. It is shown that fast highly charged silicon ions emerge from the hot plasma layer with density few times less than the solid one, and their charge distribution are not deteriorated during plasma expansion.

49. A.A. Rusanov, A.B. Savel'ev, D.S. Uryupina "Ionization and recombination in the extending plasma created by femtosecond laser pulse" Preprint of physics department of MSU №5/2005, Moscow, 2005. A.B. Savel'ev, V. M. Gordienko, I. M. Lachko, A. A. Rusanov, D. S.Uryupina, R. V. Volkov "Enhanced ionization of W ions at a plasma-vacuum boundary in femtosecond laser plasma at moderate intensities" Proc. SPIE Vol. 5975, p. 43-54, Topical Problems of Nonlinear Wave Physics; Alexander M. Sergeev; Ed. Feb 2006.
Experimental and numerical investigations of femtosecond laser plasma at the cleaned surface of W target are carried out. The constructed picture of ionization, acceleration and recombination of ions in plasma well explains main features of atomic, charge and energy spectra of fast and slow ions. It was shown that experimentally measured maximal charge of W ions exceed charge predicted by impact ionization and can be reached due to ambipolar field ionization.

50. A.B. Savel'ev, V.M. Gordienko, I.M. Lachko, A.A. Rusanov, D.S. Uryupina, and R.V. Volkov "Effect of surface cleaning on fast ion ionization and acceleration under femtosecond laser-plasma interaction" Proceedings of International symposium Topical problems of non-linear wave physics, St. Petersburg - Nizhny Novgorod, Russia, 2-9 August 2005, p.104.
Plasma produced by a high-power femtosecond laser pulse at a surface of a solid target has proved out as an effective source of energetic ions. Hot electrons at the front or rear side of the target accelerate mostly ions originating from surface contaminants – protons. The prevalence of contaminant ions in the ion beams, obtained in most of the recent experiments, obstructs understanding the physical picture of the ion origin and acceleration in such laser-solid interactions and makes these ion beams hardly useful for applications requiring pure elemental composition (such as the ion-beam sputtering, implantation, ion sources for heavy ion accelerators, etc.).

The situation is dramatically altered, when the surface is cleaned by either the resistive heating, pulsed laser cleaning, etc. Pulsed laser cleaning makes it possible to heat the surface of the target of any type (metals, semiconductors, and insulators) locally up to much higher temperatures than those obtained through resistive heating, thus removing not only hydrocarbons and water molecules, but also the oxide layer.

In this paper, we present atomic, energy and charge spectra of ions accelerated at the front of the silicon and tungsten targets irradiated by the high-contrast femtosecond laser pulse with the intensity of 3x10^16 W/cm^2, which is delayed with respect to the cleaning nanosecond laser pulse of the 3J/cm^2 energy density. Target (plate made of Si or W) was placed inside the vacuum chamber with residual pressure of 10^-5Torr. Two laser beams were focused at the same spot at the target surface – nanosecond one (10mJ, 308nm, 30 ns) and femtosecond one (0.5mJ, 616nm, 200fs). Nanosecond laser beam advanced femtosecond one by the controlled time delay. Ions currents were

measured using electrostatic time-of-flight spectrometer. We observed tremendous increase in the number of fast primary ions (Si or W) and significant growth of their maximum charge in the case of the cleaned target. In the case of cleaned targets we also observed that the highest charges belong to fast ion components having mean energy of 11 keV per unity of charge. The main specific features of the energy and charge spectra have been analyzed by means of one and two-dimensional hydrodynamic codes with transient ionization.

Finally, we are discussing the physical picture of ionization and acceleration of primary ions at the pre-cleaned vacuum-plasma interface, including origin of deep ionization, role of the cleaning laser pulse parameters (energy density and advance time), influence of the contrast of the femtosecond laser pulse, etc. This picture provides an explanation of main specific features of atomic, charge and energy spectra of fast ions obtained at uncleaned and cleaned targets. We are also discussing the possible impact from above threshold ionization by ambipolar field on the generation of deeply ionized fast ions. Thus, we showed that pulsed laser cleaning of the target surface makes it possible to produce the plasma with mono-elemental ion composition. In addition to the obvious advantages of this approach with respect to applications, it essentially simplifies the general picture of the interaction of femtosecond laser pulse with the dense plasma and allows for easy interpretation of experimental data, which in turn provides a better insight into ionization and acceleration processes in plasmas. Moreover, the pulsed laser cleaning could be an effective means to increase dramatically energy of multi-charged heavy ions produced at relativistic intensities, used to control the plasma ion current and energy spectra. It can be important for many applications including ion implantation, ion-beam sputtering of chemically clean films, producing ion sources for the accelerators et al.

51. D.S.Uryupina, V.M.Gordienko, I.M.Lachko, A.A.Rusanov, A.B.Savel'ev, R.V.Volkov «Acceleration, ionization and recombination of ions in expanding femtosecond laser plasmas» Proceedings of International symposium Topical problems of non-linear wave physics, St.Petersburg-Nizhny Novgorod, Russia, 2-9 August 2005, p.129.

We present the results for comparative study of experimental and numerical research of ionization and recombination dynamics during femtosecond laser plasma expansion.

Due to preliminary laser cleaning of the target we can obtain femtosecond laser plasma containing only target bulk substance ions. The presence of ions with smoothly changed in wide range M/Z ratio permits us to monitor ionization and recombination processes in plasma more carefully. To create plasma in our experiments we used radiation of femtosecond dye-laser system (p-polarization, wave length=616nm, t=200fs, E=0,5mJ, I=3x10^16 W/cm^2). The ionic currents were measured from Si and W plasmas. By means of electrostatic time-of-flight method we registered Si ions with charge of 1-12 and W ions with charge of 1-29. We found also that ions accelerated by hot electrons do not recombine during plasma expansion while slow ions accelerated by thermal electrons recombine strongly. The mean charge of slow ions decreases from 8+ to 4+ in Si plasma and from 22+ to 5+ in W plasma.

To analyze our experimental results we used two numerical codes. First one describes the interaction of high-power ultrashort laser pulse with a solid target on a sub-picosecond time scale. The code takes into account laser-radiation absorption at the moving plasma-vacuum interface, the ionization kinetics, flux-limited Spitzer and ballistic thermal conductivity, electron-ion heat exchange and hydrodynamic plasma expansion. Both codes do not include hot electrons since their contribution to the plasma energy balance does not exceed one percent at our experimental conditions. Second code calculates hydrodynamic plasma expansion into vacuum or low-pressure neutral gas on the nanosecond time scale, taking into account the ionization and recombination kinetics, thermal conductivity and electron-ion heat exchange. It uses the results from the first code as an input data.

So we experimentally found that fast ions do not recombine during plasma expansion and their charge distribution repeats plasma charge distribution at the initial instant. To estimate ion charge distribution in plasma we exploited Saha equation. It is clear that Saha equation is valid for the equilibrium-state plasma and in our case should predict wider charge distribution.

By means of our consecutive numerical simulation we found that in silicon plasma during laser action ions gain mean charge of 9+. Charge distribution of ions also coincides with estimation by Saha equation. Slow ions effectively recombine during plasma expansion and their charge decreases to 4+ while fast ions do not recombine. At the same time for tungsten plasma collision ionization cannot explain measured charge of ions. The calculated mean ion charge is 22+, that coincides with experimental one. At the same time the maximum charge of W ions predicting by Saha equation is 28+ while experimentally measured charge of ions is 29+. Besides the quantity of highest charged ions is much lower then experimentally measured. In that case we connect increasing of ion charge with influence of ionization by electrostatic field at the plasma-vacuum boundary. This field originates from spatial division of electrons and ions. Simple estimations show that electrostatic potential at plasma-vacuum boundary can exceed ionization potential of W ions up to 28+ ion. So, this can cause above threshold ionization of tungsten.

52. Rusanov, A.B. Savel'ev «Numerical Simulation of the Evolution of High-Temperature Dense Plasma Generated by a Femtosecond Laser Pulse» Laser Physics, Vol. 14, No. 12, 2004, pp. 1466–1474 2004

A numerical simulation of the recombination and ionization processes in expanding plasma generated by an ultrashort laser pulse with an intensity of 10^{15}–10^{16}W/cm^2 is carried out. This analysis is based on an original one-dimensional plane hydrodynamic model for the expansion of a nonequilibrium plasma in vacuum. Significant attention is paid to the effect of bound–bound transitions in ions on the rates of ionization and recombination

processes and the ionization state of the plasma at long (up to 10   s) time intervals. It is demonstrated in calculations using examples of Si and Hg plasma that the excited states as functions of the plasma concentration need to be taken into account in a correct analysis of the plasma kinetics. The results of the numerical simulation are compared to the experimental data obtained using the time-of-flight method. It is shown that the model proposed makes it possible to describe the main features of the experimentally observed charge and time-of-flight ion spectra.

LIST OF PRESENTATIONS AT CONFERENCES AND MEETINGS WITH ABSTRACTS

1. S.A. Karamian, J.J. Carroll, L.A. Rivlin, A.A. Zadernovsky, F.J. Agee, "Possible ways for triggering of the ^{179m2}Hf isomer", 12th International Laser Physics Workshop (LPHYS'03), Section on Quantum Nucleonics and Isomer Physics, Hamburg, Germany, August 25-29, 2003. Book of Abstracts p. 69.

Nucleonics and Isomer Physics, Hamburg, Germany, August 25-29, 2003. Book of Abstracts p. 69.

Realistic approaches to triggering of the ^{179m2}Hf isomer are discussed. The nuclear level scheme of ^{179}Hf suggests three promising ways for triggering, but two of them are seemingly closed by the high multipolarities of the required electromagnetic transitions. New possibilities to overcome such restrictions are deduced by utilizing a model of atomic-nuclear compound states. A new and productive method of observing triggering would base an experiment on the use of an electron cyclotron resonance ion trap, ECRIT. Some quantitative details of the behavior of ^{179m2}Hf and ^{242m}Am atomic-nuclear systems in an ECRIT environment are examined. Many important parameters are as yet unknown and they can be estimated only after the new type of experiments proposed here in which high rates of triggering are possible.

2. L.A. Rivlin, J.J. Carroll, F.J. Agee, "Driven energy release of nuclear isomers", 12th International Laser Physics Workshop (LPHYS'03), Section on Quantum Nucleonics and Isomer Physics, Hamburg, Germany, August 25-29, 2003. Book of Abstracts p. 70.

Progress in the development of high-reflectivity x-ray mirrors makes possible to intensify the stimulated nuclear energy release process due to using of Fabry-Perot resonator that may combine stimulating action of external and intraresonator gamma-photon beams. Here the detailed theoretical analysis of such a combined driving radiative process is presented. It includes investigation of dynamics, CW and pulsed mode operation, stability criteria etc.

3. A.A. Zadernovsky, "Nuclear gamma-ray laser with Fabry-Pérot resonator", 12th International Laser Physics Workshop (LPHYS'03), Section on Quantum Nucleonics and Isomer Physics, Hamburg, Germany, August 25-29, 2003. Book of Abstracts p. 74.

We consider a scheme for the recoil-assisted gamma-ray laser with a Fabry-Pérot resonator which takes advantage of the resonator both for an externally produced pumping X ray and for stimulated gamma radiation emitted by the active nuclei. We formulate a set of requirements for the pump X-ray radiation and the nuclear medium crucial to achieving the threshold condition for the gamma-ray lasing. A comparison with a single-pass regime of self-amplified spontaneous gamma emission is made.

4. D.S. Mamedov, V.V. Prokhorov, S.D. Yakubovich "Broad-Band Superluminescent Doide Based on MQW (InGa)PAs Heterostructure at 1550nm", CLEO-Europe2003, Conf. Tech. Digest, Paper CC7W.

Emission spectra of superluminescent diodes (SLDs) at 1450 – 1650 nm based on MQW (InGa)PAs heterostructure are investigated. At certain operation conditions FWHM of these spectra exceeds 120 nm. Light-emitting modules with SM fiber output based on such SLDs ensure output power spectral density > - 45 dBm in the range more than 200 nm centered at 1550 nm. This range covers main bands (S, C and L) of WDM telecommunication systems. The possibilities of further broadening of the emission band of similar SLDs are discussed.

5. L.A. Rivlin, "Quantum Nucleonics: outlines and outlook", 2nd International Conference "Frontiers of Nonlinear Physics", Nizhny Novgorod – St. -Petersburg, Russia, July 5-12, 2004. Book of abstracts, p. 122.

We discuss the current trends in Quantum Nucleonics .It is pointed out that use of long-lived nuclear isomers impeded by a large broadening of the gamma line of metastable nuclear states, which exceedsmany times their natural radiative width. This broadening can be eliminated if atoms containing nuclei form a Bose-Einstein condensate.

6. A.A. Zadernovsky, "Selection of nuclides for an active medium of gamma-ray laser", 2nd International Conference "Frontiers of Nonlinear Physics", Nizhny Novgorod – St. -Petersburg, Russia, July 5-12, 2004. Book of abstracts, p. 129-130.

We discuss a selection of the most promising nuclides potentially valuable to realizing a gamma-ray laser based on the concept of hidden inversion of nuclear state populations. Selection procedure relies on a detailed analysis both the internal nuclear structure and the atomic electron shell of a potential candidate. Ranking of the selected nuclides is accomplished in the order of ascending threshold spectral photon flux density of pumping radiation. The first-ranked candidates are identified to be recommended for further investigations.

7. L.A. Rivlin, "Quantum Nucleonics: where we are now and where we may go", 13th International Laser Physics Workshop (LPHYS'04). Trieste, Italy, July 12-16, 2004. Book of abstracts, p. 70.

We discuss the current trends in Quantum Nucleonics, in particular, various schemes of eventual nuclear gamma-ray lasing experiments; the driven energy release of long-lived isomers; the proposal of nuclear chain reaction of radiative gamma-transitions; and point out the common general embarrassments of all the mentioned approaches. Some methods to surmount these embarrassments will be propounded.

8. A.A. Zadernovsky, "Identification of prime nuclides for an active medium of gamma-ray laser", 13th International Laser Physics Workshop (LPHYS'04). Trieste, Italy, July 12-16, 2004. Book of abstracts, p. 62.

We have screened nuclear isotopes to select the most promising nuclides potentially valuable to realizing a gamma-ray laser based on the concept of hidden inversion of nuclear state populations. Selection procedure relies on a detailed analysis both the internal nuclear structure and the atomic electron shell of a potential candidate. Ranking of the selected nuclides is accomplished in the order of ascending threshold spectral photon flux density of pumping radiation. The first-ranked candidates are identified to be recommended for a further investigation.

9. D.C.Adler, S.D. Yakubovich et al. "Ultrahigh resolution OCT imaging using a broad-band SLDs ", OSA BIOMED 2004, Conf. Digest, SE2 Paper

In vivo OCT imaging is demonstrated using a compact, inexpensive superluminescent diode light source with 155 nm bandwidth centered at 890 nm and 4 mW output power. Resolutions of <2.3 um in tissue were obtained

10. J.G.Fujimoto, S.D. Yakubovich et al. "New technology for ultrahigh resolution OCT imaging using a broad-band diode light source", ARVO 2004, Conf. tech. Digest, 3002/B637 Paper

UHR-OCT imaging that is comparable to current state-of-the-art resolution can be performed using a superluminescent diode light source. To date, UHR-OCT imaging has only been achieved with expensive femtosecond laser light sources, preventing the widespread application of the UHR-OCT technology. The ability to perform UHR-OCT imaging using a low-cost, commercially available, turnkey diode light source may enable future widespread use of ultrahigh resolution OCT technology.

11. P.A.Lobintsov, S.D. Yakubovich et al. "High-power SLD with unpumped output sections", Proc. 12th Int. Symp. "Nanostructures: Physics and Technology", St. Petersburg, 2004, p.91

Superluminescent diodes (SLDs) of spectral range 850 nm based on (GaAl)As separate confinement double heterostructure were investigated. In these SLDs output sections of narrow active channel were not pumped. These unpumped sections played the role of saturable absorbers. Such design increased significantly optical damage threshold and ensured CW output power level up to 250 mW. Optical power coupled to SM fiber reached 110 mW— the highest value ever obtained for SLD-emitters.

12. D.S.Mamedov, S.D. Yakubovich et al. "Extremely broad-band light source based on QW SLDs for OCT", Proc. 12th Int. Symp. "Nanostructures: Physics and Technology", St. Petersburg, 2004, p.93

Emission of two SQW superluminescent diodes (SLDs) in 810–870 and 860–970 nm spectral ranges was combined using original SM-fiber broad-band Y-coupler. The obtained light source exhibits CW output power more than 5 mW and extremely low coherence length about 5 μm. The level of relative intensity noise (RIN) in frequency range 100 kHz–10 MHz was below .135 dB/Hz. Application of such light source in optical coherence tomography (OCT) system ensures *in vivo* recording of tomograms with record spatial resolution of 2–3 um.

13. L.A. Rivlin, "A few notes on results of isomer triggering experiments", 7th AFOSR Workshop on Isomers and Quantum Nucleonics, Dubna, Moscow Region, Russia, June 26 – July 30, 2005. Book of Abstracts p. 26.

Possible reason of disputability of results of isomer triggering experiments is discussed. It may consist in (i) unsatisfactory low spectral density of triggering radiation of broadband, as well as narrowband x-ray sources and (ii) shortage of continuous duration of triggering pulse in comparison with lifetime of upper level of trigger transition. Elimination of discrepancy (ii) shall significantly increase a running value of trigger transition cross-section and consequently a trigger efficiency itself. Another way to increase trigger efficiency is application of Moessbauer type target with isomers embedded into cooled solid matrix in conjunction with bright narrowband x-ray source.

14. A.A. Zadernovsky, "Excitation of nuclei by the photon beams carrying orbital angular momentum", 7th AFOSR Workshop on Isomers and Quantum Nucleonics, Dubna, Moscow Region, Russia, June 26 – July 30, 2005. Book of Abstracts p. 37.

A drop in the efficiency of nuclear excitation through transitions of high multipolarity is related to the increase in the angular momentum difference between the nuclear states involved in the excitation transition. Such transitions need photons with a high angular momentum. It is well known that photon beams carrying a well-defined and arbitrarily high value of angular momentum about the beam axis can be produced. We discuss some features in the excitation of nuclei with the beams.

15. A.A. Zadernovsky, "Excitation of nuclei by the photon beams carrying orbital angular momentum", 14th International Laser Physics Workshop (LPHYS'05), Kyoto, Japan, July 4-8, 2005. Book of Abstracts p. 76.

It is well known that photon beams carrying a well-defined and arbitrarily high value of angular momentum about the beam axis can be produced. We discuss some features in the excitation of nuclei with the beams.

16. S.D. Yakubovich, "Between LEDs and LDs: Superluminescent Diodes. (Invited paper)", 5th Belorussian-Russian Workshop "Semiconductor lasers and systems", 2005, Book of papers, p.86.

It is shown experimentally that the use of a travelling-wave semiconductor optical amplifier (SOA) significantly improves the output characteristics of a superluminescent diode (SLD), increasing, in particular, its output power or broadening its emission band.

17. V.V. Prokhorov, D.S. Shvakov, S.D. Yakubovich, "Study of the system SLD-SOA of the 1300 nm spectral diapason", 5th Belorussian-Russian Workshop "Semiconductor lasers and systems", 2005, Book of papers, p.87.
We discuss using SOAs based on separate-confinement double (InGa)PAs heterostructures and different SLDs as input radiation sources.

18. P.I. Lapin, D.S. Mamedov, M. Wojtkovski, J.G. Fujimoto, S.D. Yakubovich, "Low-coherent light sources of high brightness based on superposition of radiation of SLDs", 5th Belorussian-Russian Workshop "Semiconductor lasers and systems", 2005, Book of papers, p.131.
The construction and output parameters of two experimental samples of near-IR radiation sources based on the superposition of radiation from several superluminescent diodes are described.

19. P.A.Lobintsov, D.S.Mamedov, S.D. Yakubovich, "Lifetime tests of SLDs", 5th Belorussian-Russian Workshop "Semiconductor lasers and systems", 2005, Book of papers, p.135.
We describe SOAs based on separate-confinement double (InGa)PAs heterostructures emitting at 1300 nm and different SLDs with up to 50 mW of cw power at the output of a single-mode fibre and the emission band with the half-width up to 70 nm.

20. P.I. Lapin, D.S. Mamedov, M. Wojtkovski, J.G. Fujimoto, S.D. Yakubovich, "Novel Near-IR Broad-Band Light Sources for OCT Based on SLD", European Conf. On Biomedical Optics, 2005, Munich, Germany, Conf. Program MA8, p.8, SPIE-OSA/Vol.5861 586108 1-4.
The construction and output parameters of two experimental samples of near-IR radiation sources based on the superposition of radiation from several superluminescent diodes are described. The first, three-channel sample emitting 18 mW of cw output power in a spectral band of width 105 nm through a single-mode fibre, is optimised for ophthalmology coherence tomography. The second, four-channel sample emits the 870-nm band of width more than 200 nm, which corresponds to the record coherence length smaller than 4 μm.

21. V.V. Prokhorov, D.S. Shvakov, S.D. Yakubovich, "Broad-Band High-Brightness Light Sources Based on SOA and SLD", European Conf. On Biomedical Optics, 2005, Munich, Germany, Conf. Program MC10, p.11, SPIE-OSA/Vol.5861 586101 1-5
It is shown experimentally that the use of a travelling-wave semiconductor optical amplifier (SOA) significantly improves the output characteristics of a superluminescent diode (SLD), increasing, in particular, its output power or broadening its emission band. By using SOAs based on separate-confinement double (InGa)PAs heterostructures emitting at 1300 nm and different SLDs as input radiation sources, there were obtained up to 50 mW of cw power at the output of a single-mode fibre and the emission band with the half-width up to 70 nm.

22. S.D. Yakubovich, "Between light-emitting and laser diodes: SLDs", (Invited paper), 2nd Int. Conf. on Advanced Optoelectronics and Lasers, 2005, Yalta. CAOL'2005 Proceedings, Vol.1, p.49
The construction and output parameters of experimental samples of near-IR radiation sources based on the superposition of radiation from several superluminescent diodes are described.

23. L.A. Rivlin, "On stimulated radiative decay of metastable states", International Conference on Coherent Control of the Fundamental Processes in Optics and X-ray-Optics (CCFP'2006), Nizhny Novgorod – Kazan - Nizhny Novgorod, Russia, June 29 – July 3, 2006. Conference program and abstracts p. 30.
Some features of stimulated radiative decay of metastable states of nuclei in BEC are discussed.

24. A.A. Zadernovsky, "Stimulated gamma emission in an active medium with hidden inversion", International Conference on Coherent Control of the Fundamental Processes in Optics and X-ray-Optics (CCFP'2006), Nizhny Novgorod – Kazan - Nizhny Novgorod, Russia, June 29 – July 3, 2006. Conference program and abstracts p. 40.
Comparative analysis of different schemes for a gamma-ray laser is made. All schemes take advantage a hidden inversion of nuclear state populations which appears in cooled nuclear ensembles due to assistance of the nuclear recoil in emission and absorption of gamma quanta.

25. A.A. Zadernovsky, "Gamma-ray laser with hidden inversion of nuclear state populations", 15th International Laser Physics Workshop (LPHYS'06), Lausanne, Switzerland, July 24-28, 2006. Book of Abstracts p. 53.
We discuss different schemes for a gamma-ray laser. Among them are: (1) anti-Stokes scheme, which is based on the energy-storage capability of isomeric nuclei, (2) the two-level pump approach, totally forbidden in typical optical lasers, which uses the opportunity, offered again by the nuclear recoil, to pump the first excited state of a nucleus directly from its ground state.

26. A.B.Savel'ev, A.V.Andreev, O.V.Chutko, A.M.Dykhne, V.M.Gordienko, I.M.Lachko, E.V.Tkalya «Spectroscopy of low energy nuclear levels using femtosecond laser plasma» 12th International Laser physics Workshop, Hamburg, Germany, August 25-29, Book of Abstracts, 2003, p.75.

Excitation in hot dense laser plasma could provide for new methods of nuclear spectroscopy of low energy nuclear levels. We discuss various experimental and theoretical aspects while exciting low energy nuclear transitions in solids using moderate intensity laser pulses. We consider different physical mechanisms providing for low energy nuclear processes due to electrons, ions, and X-rays from hot dense laser plasma: electron and ion inelastic scattering, x-ray photo-excitation, etc., taking into account influence of plasma dynamics on those processes.

Finally we overview our recent experimental results on experimental detection of gamma and internal conversion decay of low-energy nuclear levels excited in femtosecond plasma and discuss some further advances in the field.

27. A.V.Andreev, A.M.Dykhne, V.M.Gordienko, A.B.Savel'ev, E.V.Tkalya «Non linear processes in nuclear isomers under femtosecond laser plasma interaction» Technical program of XI Conference on Laser Optics, St.Petersburg, Russia, June 30-July 4, 2003, p.30.

Excitation of low energy nuclear levels under femtosecond laser interaction with hot dense plasma could be strongly non linear and influenced by ionization and recombination plasma processes. For example, partial or even total IC blocking can take place for some stable isotopes. Finally, multi-quanta excitation from metastable levels and other phenomena will be also considered.

28. P.M.Mikheev, V.V.Bolshakov, O.V.Chutko, V.M.Gordienko, A.B.Savel'ev, R.V.Volkov «Efficient pumping of nuclear transitions by hard x-ray pulses from femtosecond laser plasma interaction» Book of Abstracts 12th International laser physics workshop, Hamburg, Germany, August 25-29, 2003, p.77 2003.

The efficiency of nuclear transitions pumping by bremsstrahlung and line hard x-ray radiation from femtosecond laser produced plasma was considered. The spectrum of bremsstrahlung radiation was measured experimentally.

Femtosecond laser plasma is efficient source of incoherent hard x-rays with quantum energy up to tens of keV even for laser pulse intensity of the order of 10^{16}-10^{17} W/cm^2. The possibility of Ta-181 nuclear level (energy 6.24 keV) excitation by x-rays from femtosecond laser plasma was demonstrated experimentally in [1].

We investigated numerically the temporal changes of bremsstrahlung spectrum shape during laser-plasma interaction. The efficiency of low-lying nuclear levels excitation by bremsstrahlung radiation of femtosecond laser plasma was estimated. The experiments on x-ray yield measurements in different spectral ranges were carried out. The temperature of hot electrons estimated from x-ray yield measurements in the frame of classical bremsstrahlung theory is in a good agreement with direct electronic spectrum registration by electrostatic time-of-flight spectrometer.

Another way of nuclear levels excitation in plasma is using of line x-ray emission from one type of elements to pump nuclear transitions of another one. The energy of line x-ray quanta depends on ionization degree of plasma. Thus igniting laser plasma with certain characteristics (ionization degree, temperatures of thermal and hot electrons) it is possible to shift line x-ray emission to the energy of nuclear level. In our calculations we estimated the plasma conditions and efficiency of Hg-201 level (energy 1.56 keV) excitation by line x-ray emission of Al plasma.

[1]. A.V.Andreev, R.V.Volkov, V.M.Gordienko, et al, "Excitation of tantalum-181 nuclei in a high temperature femtosecond laser plasma", JETP Lett., **69** (5), 371-376 (1999).

29. A.B.Savel'ev, O.V.Chutko, M.S.Dzhidzhoev, D.M.Golishnikov V.M.Gordienko, I.M.Lachko, B.V.Mar'in, P.M.Mikheev, A.A.Shashkov, D.S.Uryupina R.V.Volkov «Fast ion production from femtosecond laser plasma interaction:negative ion formation and the role of surface contamination» Book of Absrtacts 12th International laser physics workshop, Hamburg, Germany, August 25-29, 2003, p.106.

The atomic, charge and energy distributions of ions in expanding femtosecond laser plasma were studied with time-of-flight mass-charge spectroscopy. High-energy negative and positive ions with energy of up to 35 keV were detected during femtosecond laser plasma interaction of 200 fs laser pulses (I~2·10^{16} W/cm^2) with solid Si, Ti and other targets. High correlation between negative and positive single-charged ions of the same atomic species is shown. The origin of these negative ions is due to collisions of fast single charged ions and neutrals with residual gas molecules.

We also present results on the influence of the film adsorbed on the target surface at vacuum of 10^{-5}Torr onto ions emission from plasma created by femtosecond laser pulse with intensity of 2x10^{16} W/cm^2. It was shown that the highest energy per charge (8.5 keV) acquire protons, while basic target ions (Si, Ti) gain not more than 1 keV per charge. With the help of heating nanosecond prepulse advancing femtosecond pulse by 0.1-100 ms with energy density up to 10 J/cm^2 allows for effective surface cleaning due to removal of molecules containing hydrogen, carbon and oxygen. By the contrast to the instantaneous resistive heating the pulsed laser cleaning provides for higher heating temperatures and can be used for any solid targets in the regimes of thermal and plasma cleaning.

30. O.V. Chutko, A.B.Savel'ev «The role of hot electrons in populating of ionic excited states, plasma charge state and X-ray line emission in laser-matter interactions» Book of Abstracts of 13th International Laser Physics Workshop (LPHYS'04) (Trieste, Italy, July 12-16, 2004), p.148

It is shown that hot electrons play dominant role in formation of highly excited states of ions and X-ray line emission from femtosecond solid-state laser produced plasma. The spatial and temporal characteristics of X-ray line emission are investigated

31. P.M. Mikheev, V.V. Bolshakov, O.V. Chutko, V.M. Gordienko, Savel'ev A.B. «Nuclear excitation by quasi-resonant X-ray line emission from femtosecond laser produced plasma» Book of Abstracts of 13th International Laser Physics Workshop (LPHYS'04) (Trieste, Italy, July 12-16, 2004), p.64

The double laser pulse scheme of nuclear excitation by X-ray lines of plasma ions is proposed. The first pulse produces plasma with a charge state, providing the energies of X-ray line quanta of plasma ions to be tuned to resonance with nuclear transition, while the second pulse generates hot electrons that are necessary for X-ray emission.

32. D.S.Uryupina, R.V.Volokov, V.M.Gordienko, I.M.Lachko, A.B.Savel'ev, O.V.Chutko Ionic currents from femtosecond laser plasma at at target surface cleaned with preceding laser pulse Third International Symposium on Ultrafst Intense Laser Science, Book of Abstracts, 16-20 september 2004, Palermo Italy, P-28 2004
    A.B.Savelev, A.V.Andreev, V.V.Bolshakov, O.V.Chutko, V.M.Gordienko «Quasi resonant x-ray pumping of a few kev nuclear levels in an expanding laser plasma» Abstracts of Frontiers of Nonlinear Physics, Nizhny Novgorod, Russia, July 5-12, 2004, p.123

Femtosecond laser plasma is efficient source of incoherent hard x-rays with quantum energy up to tens of keV even for laser pulse intensity of the order of 10^{16}-10^{17} W/cm^2. The possibility of Ta-181 nuclear level (energy 6.24 keV) excitation by x-rays from femtosecond laser plasma was demonstrated experimentally.

Since natural linewidth of nuclear transition (less than 10^{-9} eV) is essentially less than nuclear line broadening in hot dense plasma (up to 1 eV) we consider different mechanisms of such broadening as well as their influence on the excitation efficiency of low energy nuclear levels. We also include into consideration huge line shift due ion acceleration in plasma.

Very efficient way of nuclear levels excitation in plasma is in using of line x-ray emission from one type of elements to pump nuclear transitions of another one. The energy of line x-ray quanta depends on ionization multiplicity of plasma. Thus igniting laser plasma with certain characteristics (ionization degree, temperatures of thermal and hot electrons) it is possible to shift line x-ray emission to the energy of nuclear level. In our calculations we estimated the plasma conditions and efficiency of Hg-201 level (energy 1.56 keV) excitation by line x-ray emission of Al plasma.

33. A.B.Savel'ev, V.M.Gordienko, I.M.Lachko, B.V.Mar'in, D.S.Uryupina, and R.V.Volkov «Experimental investigation of ion acceleration from femtosecond laser plasma interaction: role of surface impurities» Abstracts of Frontiers of Nonlinear Physics, Nizhny Novgorod, Russia, July 5-12, 2004, p.137

The atomic, charge and energy distributions of ions in expanding femtosecond laser plasma were studied with time-of-flight mass-charge spectroscopy. We present results on the influence of the film adsorbed on the target surface at vacuum of 10^{-5}Torr onto ions emission from plasma created by femtosecond laser pulse with intensity of 2×10^{16} W/cm^2. It was shown that the highest energy per charge (8.5 keV) acquire protons, while basic target ions (Si, Ti, Ta) gain not more than 1 keV per charge. Heating by nanosecond prepulse advancing femtosecond pulse by 0.1-100 ms with energy density up to 10 J/cm^2 allows for effective surface cleaning due to removal of molecules containing hydrogen, carbon and oxygen. By the contrast to the instantaneous resistive heating the pulsed laser cleaning provides for higher heating temperatures and can be used for any solid targets in the regimes of thermal and plasma cleaning.

34. A.V. Andreev **"**Isomer separation in laser plasma" Abstracts of II International conference "Frontiers of Nonlinear Physics" (Nizhny Novgorod, July 5-12, 2004, Russia), p.112-113 (2004)

The schemes of isomer separation in laser plasma are discussed. Nuclei of Ge^{73} in the excited state are formed by electronic capture decay in atoms As^{73}. Nuclei As^{73} are astable and the only channel of decay – electron capture decay with transformation into nuclei Ge^{73}. This allows suggesting the scheme of selecting Ge^{73} atoms with nuclei in the first excited state. Results of numerical simulation show that vapor density from which selects ions of Ge^{73} with a nucleus in the first excited state, does not influence on selectivity of excited nuclei at constant quantity of vapor. It enables to increase quantity of vapor without increasing of duration of evaporation that will result in growth of population inversion.

35. A.B.Savel'ev "Effect of surface cleaning on decay of low energy nuclear isomers excited during femtosecond laser plasma interaction" Abstracts of 7th AFOSR workshop on isomers and quantum nucleonics, Dubna, Moscow region, Russia, June 26-June 30, 2005, p.29.

Decay of low energy nuclear states excited during femtosecond laser action onto the surface of a target can be much influenced by surface composition. In our recent papers we showed that surface cleaning leads to prominent increase in charge and energy of bulk ions. In this paper we consider how surface cleaning could help to detect nuclear decay through electronic conversion (IEC) process. First case is IEC inhibition due to high ionic states in plasma. Using clean surface one can obtain higher ionization states at the instant of plasma creation and nuclear excitation as well as prolonged ionization freezing due to higher ions velocities. Besides highly energetic negatively charged hydrogen ions emerged from femtosecond laser-plasma interaction prevent IEC electrons to be detected by electrostatic time resolved technique. Surface cleaning nearly eliminates signal from all kind of hydrogen ions.

36. A.B. Savel'ev, V.M. Gordienko, I.M. Lachko, A.A. Rusanov, D.S. Uryupina, and R.V. Volkov "Deep ionization and efficient acceleration of primary ions from front surface of laser-purified target" CLEO®/EUROPE 2005 Conferences on Lasers and Electro-Optics/Europe EQEC 2005 Munich, ICM, Germany 12-17 June 2005 CG3-3-WED, Europhysics Conference Abstracts: Volume 29B.

The plasma produced by a high-power femtosecond laser pulse at a surface of a solid target has proved out as an effective source of energetic ions. Hot electrons at the front or rear side of the target accelerate mostly the ions originating from surface contaminants – protons. The prevalence of contaminant ions in the ion beams, obtained in most of the recent experiments, obstructs understanding the physical picture of the ion origin and acceleration in such laser-solid interactions and makes these ion beams hardly useful for applications requiring pure elemental composition (such as the ion-beam sputtering, implantation, ion sources for heavy ion accelerators, etc.). The situation is dramatically altered, when the surface is cleaned by either the resistive heating or pulsed laser cleaning. The latter approach makes it possible to heat the surface of the target of any type (metals, semiconductors, and insulators) locally up to much higher temperatures than those obtained through resistive heating, thus removing not only hydrocarbons and water molecules, but also the oxide layer.

In this paper, we present atomic, energy and charge spectra of ions accelerated at the front of the silicon and tungsten targets irradiated by the high-contrast femtosecond laser pulse with the intensity of 3×10^{16} W/cm^2, which is delayed with respect to the cleaning nanosecond laser pulse of the 3 J/cm^2 energy density. The tremendous increase in the number of fast primary ions (Si or W) and significant growth of their maximum charge in the case of the cleaned target has been observed. The main specific features of the energy and charge spectra have been analyzed by means of one-dimensional hydrodynamic transient-ionization modeling. We are also discussing the possible impact from above threshold ionization by ambipolar field on the generation of deeply ionized fast ions. The p-polarized 616-nm, 200 fs radiation from the femtosecond dye-laser system was focused onto the target at an angle of 45 degrees, providing the peak intensity at the target of 3×10^{16} W/cm^2. Radiation from the nanosecond XeCl excimer laser (30-ns, 20-mJ, 308 nm) was focused on the target into the spot of 500-mm diameter centered with respect to the femtosecond-laser spot. The UV pulses were synchronized with the exciting femtosecond laser pulses. The optimal energy density of the cleaning nanosecond pulse W=3 J/cm^2 as well as time delay between the leading nanosecond pulse and delayed femtosecond pulse dt = 100 ms were assigned according to our previous experimental results. Ion currents from the plasma were detected by the electrostatic time-of-flight spectrometer.

For the cleaned targets of Si and W we observed that (i) fast ion component exists only in the case of the cleaned target; (ii) fast primary ions are generated very efficiently with mean energy per charge being equal to 12±2 keV independently on the ion charge with maximum observed energy of the W28+ ions above 1 MeV; (iii) mean charge of fast ions rises up to 8+ for Si and 18+ for W; (iv) upper detected charges were 12+ for Si and 28+ for W having ionization potentials as high 600–800 eV.

In order to analyze our experimental data, the numerical simulation of the plasma spatial-temporal dynamics was performed by means of the one-dimensional hydrodynamic numerical code taking into account laser-radiation absorption at the moving plasma-vacuum interface, flux-limited Spitzer and ballistic thermal conductivity, electron-ion heat exchange, ionization kinetics and hydrodynamic plasma expansion. We are discussing the physical picture of ionization and acceleration of primary ions at the pre-cleaned vacuum-plasma interface, including origin of deep ionization, role of the cleaning laser pulse parameters (energy density and advance time), influence of the contrast of the femtosecond laser pulse, etc. This picture provides an explanation of main specific features of atomic, charge and energy spectra of fast ions obtained at uncleaned and cleaned targets.We showed that pulsed laser cleaning of the target surface makes it possible to produce the plasma with monoelemental ion composition. In addition to the obvious advantages of this approach with respect to applications, it essentially simplifies the general picture of the interaction of femtosecond laser pulse with the dense plasma and allows for easy interpretation of experimental data, which in turn provides a better insight into ionization and acceleration processes in plasmas. Moreover, the pulsed laser cleaning could be an effective means to increase dramatically energy of multi-charged heavy ions produced at relativistic intensities, used to control the plasma ion current and energy spectra. It can be important for many applications including ion implantation, ion-beam sputtering of chemically clean films, producing ion sources for the accelerators et al.

37. A.B. Savel'ev, V.M. Gordienko, I.M. Lachko, A.A. Rusanov, D.S. Uryupina and R.V. Volkov "Acceleration and ionization of fast ions in femtosecond laser plasma created at purified target surface" Technical digest ICONO/LAT-2005, May 11-15 2005, St. Petersburg, Russia, IFW3.

We present atomic, energy and charge spectra of ions accelerated at front surface of the silicon and tungsten targets irradiated by high-contrast femtosecond laser pulse with intensity of 3x10^16W/cm^2. This pulse lags by 100 mks behind the purifying nanosecond laser pulse with energy density of 3 J/cm^2. Tremendous, few orders of magnitude increase in the number of fast ions and significant up shift of their maximum charge from 5+ up to 12+ for Si and from 3+ to 28+ for W were observed for purified targets as compared with the case of unpurified ones. The main features of atomic, charge and energy spectra of fast and slow ions obtained both with initial unpurified target and at the cleaned target are explained using one-dimensional hydrodynamic transient-ionization modeling taking into account field ionization. It is shown that fast highly charged ions emerge from the hot plasma layer with density few times less than the solid one, and their charge distribution does not deteriorated during plasma expansion.

38. D.S.Uryupina, V.M.Gordienko, I.M.Lachko, A.A.Rusanov, A.B.Savel'ev, R.V.Volkov "On the Origin of Fast Multi-Charged Ions from Femtosecond Laser Plasma Interaction at Moderate Intensities" Technical digest ICONO/LAT-2005, May 11-15 2005, St. Petersburg, Russia, IThV2.
Experimental and numerical investigations of femtosecond laser plasma at the cleaned surface of crystalline Si and W targets are carried out. The constructed picture of ionization, acceleration and recombination of ions in plasma well explains main features of atomic, charge and energy spectra of fast and slow ions.

39. A.A. Rusanov, A.B. Savel'ev "Numerical Simulation of the Evolution of High- Temperature Dense Plasma Generated by a Femtosecond Laser Pulse" Technical digest ICONO/LAT-2005, May 11-15 2005, St. Petersburg, Russia, IThV43.
Several interrelated processes that depend on plasma heating, ionization, recombination, and expansion take place in laser plasma generated at a solid surface by a high-power femtosecond laser pulse with an intensity of greater than 10^15W/cm^2. At the moment of laser pulse termination, the plasma concentration is close to the solid-state concentration, and the deposition of energy into the plasma is instantaneous (the plasma has no time for expansion). This makes it possible to separate the stages of energy deposition and plasma expansion.

In this work, we present a one-dimensional model for the calculation of the expansion and recombination of hot dense plasma, created by femtosecond laser pulse. The initial parameters are as follows: temperature, higher than 100 eV; ion density, higher than 3x10^22cm; and ionization multiplicity greater than 10. The numerical model for the evolution of dense hot plasma proposed in this work makes it possible to calculate the charge, energy, and time-of-flight spectra of ions at time intervals of up to µs 10 , which correspond to the characteristic times of the experimental measurements of such spectra. For an adequate description of the evolution of a plasma generated by a femtosecond laser pulse at the surface of a solid target, we need to calculate transient ionization and recombination in this plasma, taking into account bound–bound transitions. In dense plasma we need to take into account a small number of levels and three to five excited states. In plasma with a lower density, the analysis employs a larger number of levels. The comparison of the energy and time-of-flight spectra obtained in the calculations with the experimental data shows that the model proposed adequately predicts such characteristic parameters as the maxima in the energy spectra of ions with the given charge and the front of the ion current maximum. This makes it possible to employ the model for the estimation of the parameters of plasma obtained in experiments based on the measurements of various characteristics of the plasma ion current.

40. E.V. Tkalya. Induced decay of ^{178}Hf^{m2} : cross section upper bound and comparison with experimental data. 6th AFOSR Isomer Workshop "Gamma-Ray Optics and Quantum Nucleonics", the International Conference "Frontiers of Nonlinear Physics", July, 5-12, Nizhny Novgorod - St.-Petersburg, Russia.
This paper reviews experimental results published in C.B.Collins et al., Phys. Rev. Lett. 82, 695 (1999); Phys. Rev. 61, 054305 (2000); Europhys. Lett. 57, 677 (2002) on the x-ray induced decay acceleration of long-lived isomer Hf-178m2 (16+, 2.446 MeV, 31 yr). Two basic mechanisms for the induced decay were considered: direct interaction of the incident x-rays with the nucleus; the nucleus-x-rays interaction via the atomic shell. It was established that the absence of the K-forbidenness for all transitions to the hypothetic "mixed K" level cannot explain the measured cross sections even if the collective nuclear matrix elements, resonant conditions, etc. are used. The hypothesis of the normal nuclear transitions enhancement in the inverse NEET process was also tested and rejected. Thus, there are no explanations of C.B.Collins et al. experimental results within quantum electrodynamics and of the contemporary concept of the atomic nuclei.

41. E.V. Tkalya. New x-ray induced decay of ^{178m2}Hf data: "mixed J" instead of "mixed K" interpretation? 7th AFOSR Workshop "Isomers and Quantum Nucleonics". Dubna, June 26 – July 1, 2005.
This report reviews intriguing experimental result published by C.B.Collins et al., at Laser Phys. Lett. **2**, 162 (2005) about induced decay acceleration of long-lived isomer ^{178m2}Hf (16+, 2.446 MeV, 31 yr) by the low energy synchrotron radiation and registration of the 2.457 MeV gamma emission. Theoretical analysis shows that experimentalists has to wait for the 2.457 MeV gamma photon more than 10^{50} years. It was established, that there is only one way to explain of the origin of these photons - to proclaim the intermediate nuclear level is not "mixed K", but is "mixed J".

42. E.V. Tkalya. Process of nuclear excitation by electron transition (NEET) near K-shell ionization threshold of atom. 56 International Conference "Nucleus-2006" on Problems of Nuclear Spectroscopy and Structure of Atomic Nucleus.

We propose a model for description of the process of Nuclear Excitation by Electron Transition (NEET) near the K-shell ionization threshold of an atom. We explain the experimental results for the ^{197}Au cross section excitation σ_{N^*} obtained by S.Kishimoto et al. Phys. Rev. C 74 031301(R) (2006) using synchrotron radiation near the Au K-edge. We predict the behavior of σ_{N^*} as a function of the incident photon energy for nuclei ^{193}Ir and ^{189}Os. We reveal that the ^{189}Os excitation begins when the energy of incident photons is below the K-shell ionization threshold in Os.